



## APPLICATION OF THE LASER VELOCIMETER FOR TRAILING VORTEX MEASUREMENTS

A. E. Lennert, F. L. Crosswy, and H. T. Kalb  
ARO, Inc.

ARNOLD ENGINEERING DEVELOPMENT CENTER  
AIR FORCE SYSTEMS COMMAND  
ARNOLD AIR FORCE STATION, TENNESSEE 37389

December 1974

Final Report for Period October 1970 — July 1973

Approved for public release; distribution unlimited.

Prepared for

ARNOLD ENGINEERING DEVELOPMENT CENTER (DY)  
ARNOLD AIR FORCE STATION, TENNESSEE 37389

## NOTICES

When U. S. Government drawings specifications, or other data are used for any purpose other than a definitely related Government procurement operation, the Government thereby incurs no responsibility nor any obligation whatsoever, and the fact that the Government may have formulated, furnished, or in any way supplied the said drawings, specifications, or other data, is not to be regarded by implication or otherwise, or in any manner licensing the holder or any other person or corporation, or conveying any rights or permission to manufacture, use, or sell any patented invention that may in any way be related thereto.

Qualified users may obtain copies of this report from the Defense Documentation Center.

References to named commercial products in this report are not to be considered in any sense as an endorsement of the product by the United States Air Force or the Government.

This report has been reviewed by the Information Office (OI) and is releasable to the National Technical Information Service (NTIS). At NTIS, it will be available to the general public, including foreign nations.

## APPROVAL STATEMENT

This technical report has been reviewed and is approved for publication.

FOR THE COMMANDER



MELVIN L. GUIOU  
Captain, USAF  
Research and Development  
Division  
Directorate of Technology



ROBERT O. DIETZ  
Director of Technology

**UNCLASSIFIED**

REPORT DOCUMENTATION PAGE		READ INSTRUCTIONS BEFORE COMPLETING FORM
1 REPORT NUMBER AEDC-TR-74-26	2 GOVT ACCESSION NO	3 RECIPIENT'S CATALOG NUMBER
4 TITLE (and Subtitle) APPLICATION OF THE LASER VELOCIMETER FOR TRAILING VORTEX MEASUREMENTS		5 TYPE OF REPORT & PERIOD COVERED Final Report-October 1970 - July 1973
7 AUTHOR/4; A. E. Lennert, F. L. Crosswy, and H. T. Kalb, ARO, Inc.		6 PERFORMING ORG REPORT NUMBER
9 PERFORMING ORGANIZATION NAME AND ADDRESS Arnold Engineering Development Center Arnold Air Force Station, Tennessee 37389		10 PROGRAM ELEMENT, PROJECT, TASK AREA & WORK UNIT NUMBERS Program Element 65802F
11 CONTROLLING OFFICE NAME AND ADDRESS Arnold Engineering Development Center (DYFS) Arnold Air Force Station, Tennessee 37389		12. REPORT DATE December 1974
14 MONITORING AGENCY NAME & ADDRESS (if different from Controlling Office)		13 NUMBER OF PAGES 169
16 DISTRIBUTION STATEMENT (of this Report)		15 SECURITY CLASS (of this report) UNCLASSIFIED
17 DISTRIBUTION STATEMENT (of the abstract entered in Block 20, if different from Report)		15a. DECLASSIFICATION/DOWNGRADING SCHEDULE N/A
18 SUPPLEMENTARY NOTES Available in DDC		
19 KEY WORDS (Continue on reverse side if necessary and identify by block number) lasers                    cells (Bragg)                    signal to noise ratio speed indicators        instruments (electronic) measurements            aircraft density                 vortexes (trailing)		
20 ABSTRACT (Continue on reverse side if necessary and identify by block number) This report summarizes a three-year analytical and experimental program to develop a dual-scatter laser velocimeter system to map the flow fields of trailing vortices stemming from the wingtips of flying aircraft. The basic design parameters ascertaining feasibility of the LV-measuring technique are presented. Included is a discussion and evaluation of a newly developed two-dimensional Bragg cell (TDBC) for resolving direc-		

# UNCLASSIFIED

## 20. Abstract

tional ambiguity. The electronics instrumentation developed for the operation of the TDBC is evaluated in detail. In addition, the development of a direct readout system yielding considerable improvement over the initial instrument is described and evaluated. A number of significant proof-of-principle experiments made at the AEDC runway of trailing vortices created by NASA-operated aircraft are discussed and evaluated. The conclusions derived from the test programs are enumerated, and a conceptual design of a mobile trailing-vortex-measuring system is described.

## PREFACE

The work reported herein was conducted by the Arnold Engineering Development Center (AEDC), Air Force Systems Command (AFSC), at the request of the National Aeronautics and Space Administration (NASA), Langley Research Center, Virginia, under Program Element 65802F. The results were obtained by ARO, Inc. (a subsidiary of Sverdrup & Parcel and Associates, Inc.), contract operator of AEDC, AFSC, Arnold Air Force Station, Tennessee. The work was done under ARO Project No. BF241. Data reduction was completed in April 1973, and the manuscript (ARO Control No. ARO-OMD-TR-73-147) was submitted for publication on November 15, 1973.

Mr. W. M. Farmer, formerly of ARO, Inc., and Mr. L. E. Mauldin, an employe of NASA Langley Research Center, Virginia, are also coauthors of this report.

## CONTENTS

	<u>Page</u>
1.0 INTRODUCTION . . . . .	9
2.0 ANALYSIS OF ATMOSPHERIC LASER VELOCIMETERS	
2.1 Theoretical Evaluation . . . . .	14
2.2 Effect of the Number of Scatter Centers on the Scatter Signal Power . . . . .	15
2.3 Collected Power Scattered as a Function of Range . . . . .	17
2.4 Signal-to-Noise Power Ratios . . . . .	22
2.5 Summary . . . . .	23
3.0 SYSTEMS EVALUATION	
3.1 Basic Performance Equations . . . . .	25
3.2 Determination of the Data Acquisition Rate . . . . .	37
3.2.1 Analysis and Evaluation . . . . .	37
4.0 BRAGG CELL VECTOR VELOCIMETER DESCRIPTION	
4.1 Bragg Cell Vector Velocimeter . . . . .	41
4.2 Principles of Operation . . . . .	42
4.3 Two-Dimensional Bragg Cell . . . . .	45
4.4 Three-Component Laser Vector Velocimeter . . . . .	52
4.4.1 All Dual-Scatter System . . . . .	52
4.4.2 Dual Scatter - Local Oscillator System . . . . .	55
5.0 SIGNAL CONDITIONING REQUIREMENTS AND ELECTRONICS	
5.1 Introduction . . . . .	56
5.2 Bragg Cell Optics . . . . .	58
5.3 Optical Component Constraints . . . . .	58
5.4 Time and Frequency Domain Characteristics . . . . .	61
5.5 Information Spectra . . . . .	65
5.6 Information Spectrum Translation . . . . .	66
5.7 System Accuracy and Precision . . . . .	67
5.7.1 Subsystem 1 . . . . .	67
5.7.2 Subsystem 2 . . . . .	68
5.7.3 Subsystem 3 . . . . .	69
5.7.4 Subsystem 4 . . . . .	69
5.7.5 Overall System Accuracy and Precision . . . . .	69
5.8 Signal-Conditioning Instrument . . . . .	70
5.8.1 Photodetector Assembly . . . . .	71
5.8.2 Signal Separator and Spectrum Translator . . . . .	71
5.8.3 Fabrication and Packaging . . . . .	75

	<u>Page</u>
5.9 System Evaluation . . . . .	77
5.9.1 Laboratory Test . . . . .	77
5.9.2 Field Test . . . . .	78
5.9.3 Summary . . . . .	80
6.0 LV DATA PROCESSOR SYSTEM . . . . .	81
6.1 Selective Capture of Frequency Burst Signal	
Data . . . . .	82
6.2 Laser Velocimeter Data Processor . . . . .	86
6.2.1 Time Interval Comparator . . . . .	89
6.2.2 Dual Time Interval Comparison . . . . .	90
6.2.3 "Data Accept" Recycle Sequence . . . . .	91
6.2.4 "Data Reject" Recycle Sequence . . . . .	91
6.2.5 Data in BCD Form . . . . .	91
6.3 Processor Sample Rate . . . . .	92
6.4 Extended Frequency Coverage . . . . .	92
6.5 Data Handling . . . . .	95
6.5.1 Digital Printer and Mag Tape Recorder . . . . .	95
6.5.2 Data Compression . . . . .	96
6.5.3 Analog Recording of Time-Dependent	
Data . . . . .	97
6.5.4 Multi-Component Processing of Simultaneous	
Data . . . . .	98
7.0 LABORATORY-GENERATED VELOCIMETER	
SIGNALS	
7.1 Video Recorder as a Frequency Burst Test Signal	
Generator . . . . .	98
7.2 LV Burst Signal Synthesizer . . . . .	100
8.0 TRAILING VORTEX EXPERIMENTS AT AEDC	
8.1 Experimental Arrangement . . . . .	104
8.2 System Alignment . . . . .	106
8.3 Probe Volume Determination . . . . .	107
8.4 AEDC Experiments . . . . .	107
9.0 PROPOSED MOBILE LV SYSTEM	
9.1 General Description . . . . .	124
9.2 Telescope Requirements . . . . .	124
9.3 Telescope . . . . .	127
10.0 CONCLUSIONS AND RECOMMENDATIONS	
10.1 Conclusions . . . . .	130
10.2 Recommendations . . . . .	132
REFERENCES . . . . .	133

<u>Figure</u>	<u>ILLUSTRATIONS</u>	<u>Page</u>
1.	Ground-Wind Data From CO <sub>2</sub> Laser Doppler System . . .	10
2.	Photograph of the Trailing Vortex Experiment . . . . .	11
3.	One Velocity Component Long Range Dual-Scatter Backscatter LDV System . . . . .	11
4.	Photograph of the LV System . . . . .	12
5.	Typical Signals for the Trailing Vortex Experiment . .	13
6.	Comparison of Actual and Model Fringe Intensity at the Geometric Center of a Dual-Scatter LDV . . . . .	15
7.	Backscatter Local-Oscillator Long Range LV System . . . . .	25
8.	LV Fringe Visibility for a Spherical Scatter Center . .	28
9.	LV Operation in Turbulent and Quiescent Atmosphere, S <sub>R</sub> <sup>(CW)</sup> . . . . .	34
10.	LV Operation, S <sub>R</sub> <sup>(CW)</sup> . . . . .	35
11.	Burst LV Operation in Turbulent and Quiescent Atmosphere . . . . .	36
12.	LV Operation in Turbulent and Quiescent Atmosphere . . . . .	36
13.	Backscatter Data Rate (N) versus Minimum Signal-to-Noise Power Ratio (SNR) . . . . .	39
14.	Atmospheric Particle Size Distribution . . . . .	40
15.	Comparison of Self-Aligning Interferometer Block and Bragg Cell LDV Systems . . . . .	42
16.	Schematic of a Two-Dimensional Bragg Cell . . . . .	46
17.	Diagram of Possible Beam and Frequency Combinations Using A Two-Dimensional Bragg Cell . . . . .	50
18.	Schematic of an LV System Using a Two-Dimensional Bragg Cell . . . . .	52
19.	Three-Component Laser Velocimeter . . . . .	54
20.	Remote Sensing LDV System (Two Components, Dual Scatter, Third Component Reference Beam) . . . . .	54

<u>Figure</u>	<u>Page</u>
21. Vector Velocity LV Subsystem Functional Block Diagram . . . . .	57
22. Optical Intensity Spectrum at the Output of the Bragg Cell . . . . .	59
23. Photodetected Signal Spectrum for Motionless Scatter Particle Illustrating Velocity Component Carrier Signals . . . . .	61
24. Time Domain Signals-Single Scatter Particle Traversing the Probe Volume . . . . .	62
25. Frequency Domain Signal Representation-Single Scatter Particle Traversing the Probe Volume . . . . .	64
26. Velocity Information Spectra Illustrating Relationship of Adjacent Spectra . . . . .	66
27. Block Diagram of the Photodetection, Signal Conditioning, and Interface Electronics, Subsystem 2 . . . . .	70
28. Photodetection, Signal Conditioning, and Interface Electronics, Subsystem 2 . . . . .	70
29. Schematic Diagram of Signal Separator and Spectrum Translator . . . . .	73
30. Fabrication Details of Signal Separator and Spectrum Translator . . . . .	76
31. Directionality Evaluation - Laboratory Test . . . . .	78
32. Directionality Evaluation - Field Test . . . . .	79
33. Stationary Fringe Dead Zone . . . . .	81
34. Velocimeter Wave Forms . . . . .	83
35. Test Data of S/N = 0.07, Alias Reading Distribution Obtained From Low S/N Signal Data . . . . .	84
36. Test Data of S/N = 0.09 . . . . .	85
37. Processor Performance in Regions of Low S/N . . . . .	86
38. Laser Velocimeter Data Processor (Block Diagram). .	87
39. Time Interval Comparator Block Diagram . . . . .	88

<u>Figure</u>	<u>Page</u>
40. Loud Speaker Modulated Air Particle . . . . .	93
41. Circuit Diagram of Pulse Stretcher . . . . .	94
42. Memory Formatted LV Data Display . . . . .	97
43. Reconstructed Burst Signal from Video Tape . . . . .	99
44. Schematic Diagram of an LV Signal Synthesizer . . . . .	101
45. Synthesized Burst Signal Waveform . . . . .	102
46. Schematic of the Trailing Vortex LV . . . . .	105
47. Telescope Set-Up Trailing Vortex Study . . . . .	105
48. Peak-to-Peak Signal Band Strength from 8 deg Off-Axis, Backscatter LDV with Very High Moisture Content . . . . .	108
49. Photographs of Trailing Vortex Experiment . . . . .	109
50. Trailing Vortex LV Data, Run No. 10, 7/25/72 . . . . .	113
51. Trailing Vortex LV Data, Run No. 8, 7/26/72 . . . . .	114
52. Trailing Vortex LV Data, Run No. 9, 7/26/72 . . . . .	115
53. Trailing Vortex LV Data, Run No. 10, 7/26/72 . . . . .	116
54. Trailing Vortex LV and Anemometer Data, Run No. 12, 7/26/72 (Horizontal Velocity) . . . . .	117
55. Trailing Vortex LV and Anemometer Data, Run No. 12, 7/26/72 (Vertical Velocity) . . . . .	118
56. Trailing Vortex LV Data, Run No. 13, 7/26/72 . . . . .	119
57. Trailing Vortex LV Data, Run No. 2, 7/27/72 . . . . .	120
58. Trailing Vortex LV Data, Run No. 4, 7/27/72 . . . . .	121
59. Trailing Vortex LV Data, Run No. 24, 7/27/72 . . . . .	122
60. Trailing Vortex LV Data, Run No. 26, 7/27/72 . . . . .	123
61. Mobile LV For Vortices . . . . .	125
62. Conceptual Design of the Remote Sensing Velocimeter (Dual-Scatter-LO System) . . . . .	126
63. Laser Power (Watts) Range-Laser Power Relationship . . . . .	126

<u>Figure</u>	<u>Page</u>
64. Remote Sensing Mono-Static Velocimeter . . . . .	128
65. Spherical Mirror Segment . . . . .	128
66. Fringe Spacing (Microns) . . . . .	129
67. Transmitted Probe Volume Length . . . . .	130

## TABLE

1. Selected Values for Input Parameters . . . . .	33
---	----

## APPENDIXES

A. DETERMINATION OF A THIRD, DUAL-SCATTER, VELOCITY COMPONENT . . . . .	139
B. BRAGG DIFFRACTION OF LIGHT BY TWO ORTHOGONAL ULTRASONIC WAVES IN WATER . . . . .	157
C. INVESTIGATION OF TRAILING VORTEX WAKE VELOCITIES AND DISSIPATION PROPERTIES USING THE LV . . . . .	163

## 1.0 INTRODUCTION

Reports of numerous incidents and accidents (Ref. 1) during the past few years indicate that the trailing vortices stemming from the region near the wing tip of large aircraft create a severe hazard to penetrating light aircraft. Attempts have been made to understand the creation and decay of these wing tip vortices; however, substantiating measurements to correlate the theories have not been too satisfactory. Prior to the development of the laser velocimeter (LV) measuring technique, the only quantitative data acquired of the trailing vortices were by means of flying an aircraft down a runway to permit the action of a crosswind to cause the wing tip vortices to drift past a measurement station. The measurement station generally comprised a tower located at some distance from the edge of a runway upon which mechanical anemometers were suspended. Simultaneously, smoke was released to make the vortices visible (Refs. 2 and 3).

A number of such measurements have been made utilizing cup anemometers and compared with a one-component CO<sub>2</sub> LV system. In an experiment a 20-watt CO<sub>2</sub> gas laser (Ref. 1) was used in conjunction with a 12-in. transmitter-receiver telescope system such that the transmitter beam could be focused near a cup anemometer. Radiation scattered from smoke particles traversing the focal region of the laser beam was collected by the same telescope system. The scattered radiation was imaged on a detector. The signal from the detector passed through a signal-conditioning system that yielded the flow velocity. Preliminary data were taken comparing the cup anemometer with the CO<sub>2</sub> LV system and are included in Fig. 1. The top set of curves compares the measurements of both systems under steady wind conditions. It is readily noticed that the velocity changes measured by the LV system are much more sensitive than those acquired by the anemometer. In the lower set of curves, taken under variable wind conditions, the enhanced sensitivity of the LV system over the anemometer data is much more noticeable. In either curve, directionality is not included in the LV data.

Although the use of the CO<sub>2</sub> laser has proven moderately successful, there is still the spatial resolution that must be overcome to effectively perform detailed quantitative measurements of the trailing vortex. For a given transmitting lens the spatial resolution of an LV system is directly proportional to the wavelength and the transmitter optics f number, a shorter wavelength gives better spatial resolution. Furthermore,

it has been shown that for burst-type signals generally encountered in atmospheric measurements the dual-scatter LV system gives better signal-to-noise power ratio (S/N) (Ref. 4) than reference beam systems. For these reasons an argon laser LV system was constructed to perform measurements of trailing vortices at remote distances. Proof-of-principle measurements were made in April 1971 at the AEDC airport under NASA sponsorship and with the assistance of NASA-Langley personnel. As in previous measurements, a tower with three anemometers was erected, to correlate both LV and anemometer data. The vortex, created by a C47 aircraft flying at approximately 50 ft above the ground, was to be measured. Visual contact with the vortex was established by firing smoke bombs mounted on the wing tips of the aircraft. In addition, a smoke bomb tower was erected near the anemometer tower to visually ascertain the vortex flow field (Fig. 2). The LV system, schematically illustrated in Fig. 3 and photographically in Fig. 4, was checked out on the aircraft run-up pad where the flow field measurements were to be made.

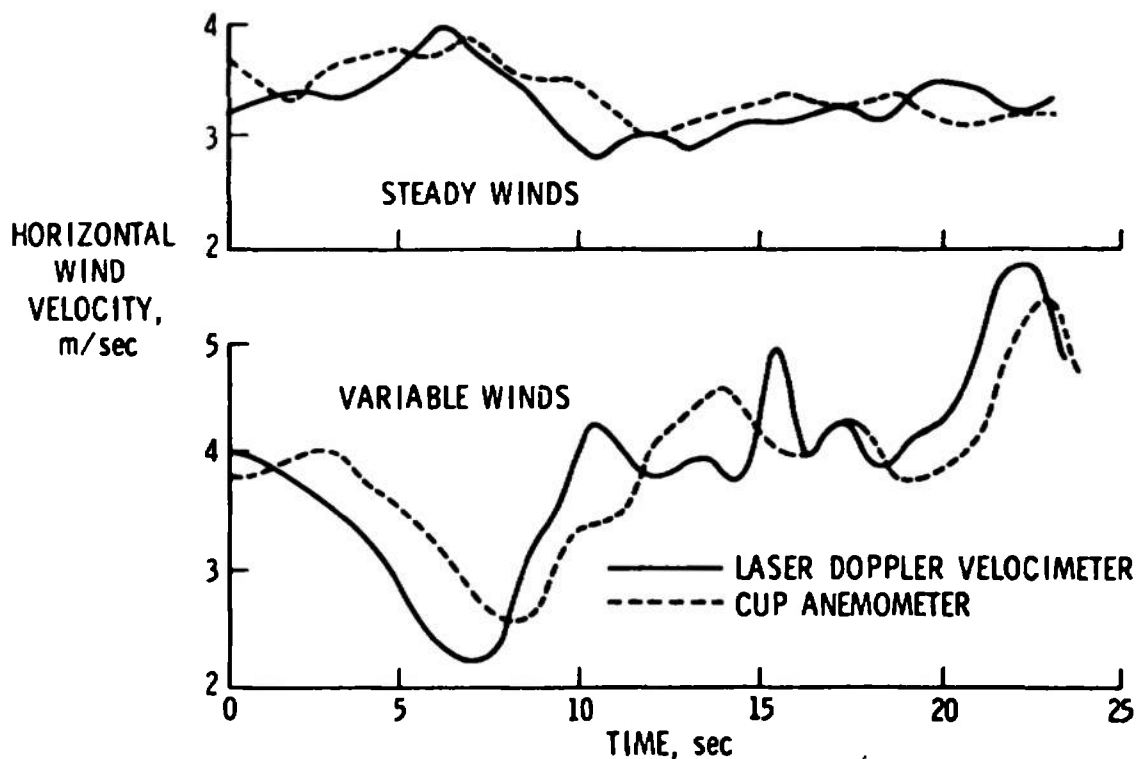


Figure 1. Ground-Wind data from CO<sub>2</sub> laser Doppler system.

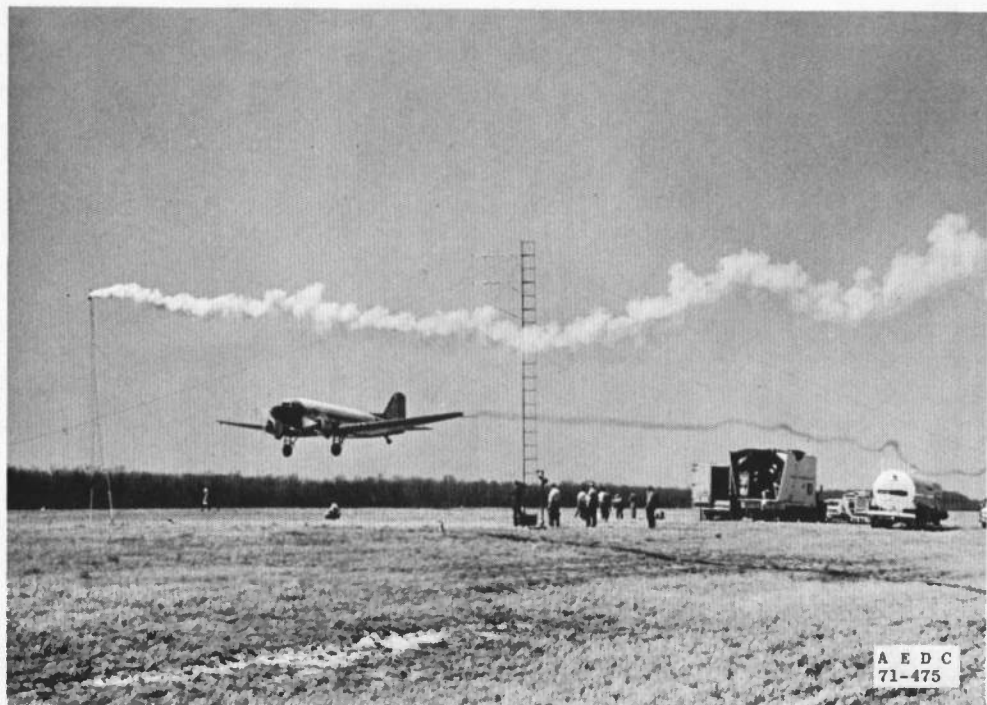


Figure 2. Photograph of the trailing vortex experiment.

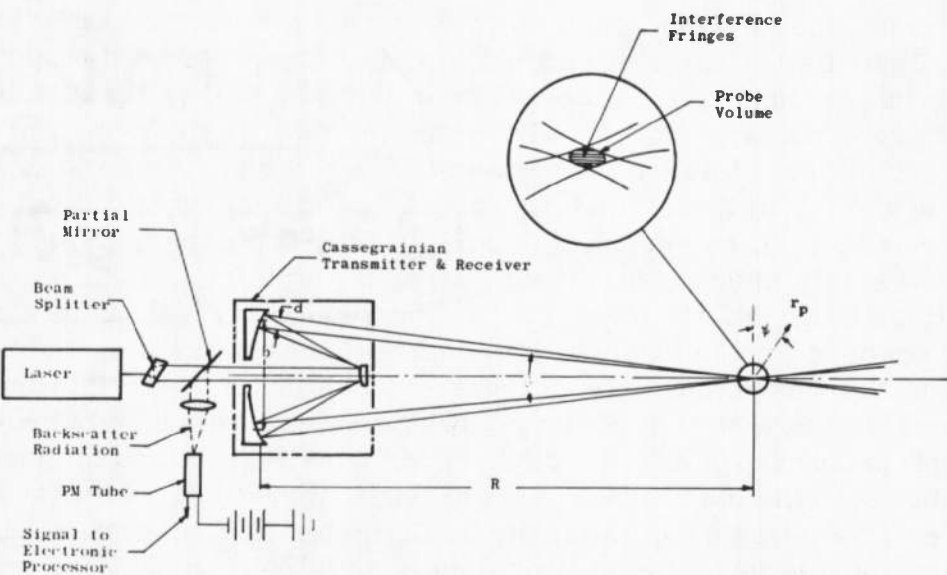


Figure 3. One velocity component long range dual-scatter backscatter LDV system.

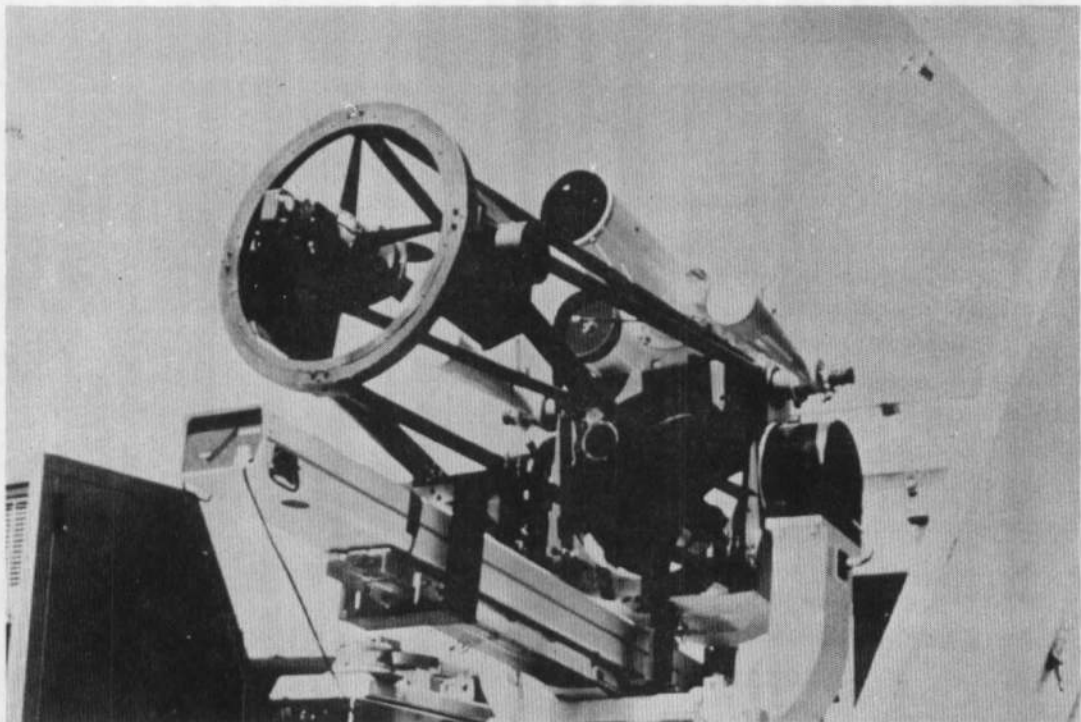


Figure 4. Photograph of the LV system.

Measurements were made at an elevation of approximately 120 ft. The aircraft flew a parallel pattern to the telescope line-of-sight such that the background wind velocity would drift the vortex through both the LV probe volume and a cup anemometer that was mounted on a tower. A major interface problem between the transmitting-collecting optics of the LV unit was such that the automatic readout did not perform, resulting in no rapid data acquisition. The experimental results depended solely upon acquiring photographic data from oscilloscope recordings (Fig. 5). In many cases, the sudden arrival of the trailing vortex produced considerable data such that the analysis of the oscilloscope traces was impossible. It was, therefore, not possible to correlate the LV data with that of the rotating anemometers; nevertheless, proof-of-principle data of the background wind velocities compared favorably with the data acquired from flight operation. Additional work centered about modifying the laser velocimeter (LV) with particular emphasis placed upon the development of the directionality measuring capability in addition to improving the data processor system. During the course of this work, a two-component self-aligning Bragg cell subsystem was developed to acquire directionality, and its performance was verified in both laboratory and field experiments. In addition, the

data processor system was improved such that high data acquisition rates could be processed in the event that the signals were available. Another series of experiments was performed in July 1972 at the AEDC runway with the assistance of NASA-Langley personnel. In the latter experiments two simultaneous velocity components, including directionality, were measured.

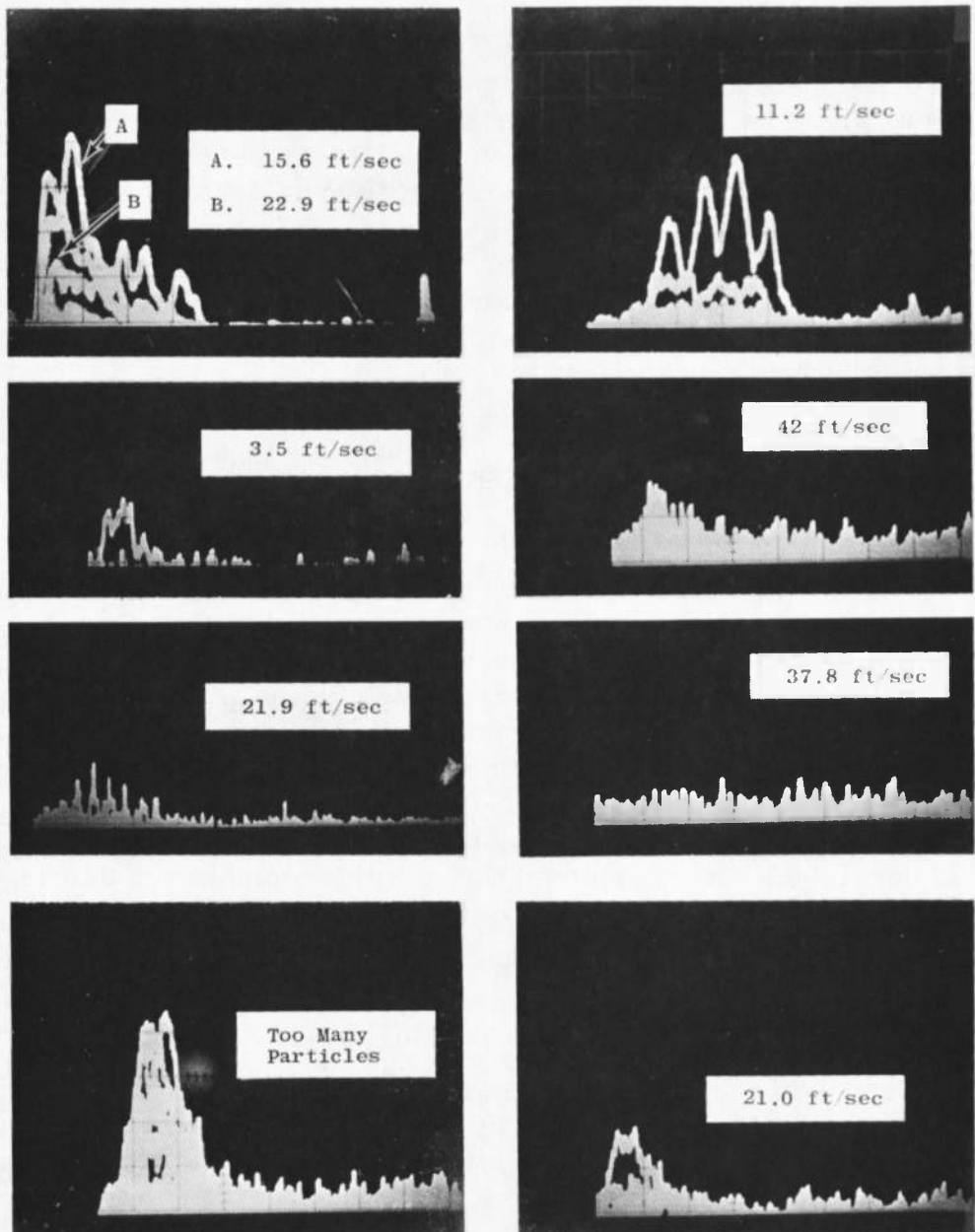


Figure 5. Typical signals for the trailing vortex experiment.

The purpose of this report is to present the theory and results of an evaluation of the pertinent parameters affecting the performance of the two major LV systems. Both the local oscillator and the dual-scatter LV system are evaluated to determine their capability for effecting detailed measurements of the characteristics of trailing vortices. A description of the two-component LV experimental apparatus, including an analysis of the Bragg cell subsystem that was used to perform the experimental program conducted on the AEDC runway, is described and evaluated. A prototype, dual-scatter three-component LV system which has been operated in the laboratory is described. The sub-systems, particularly the electronics, inherent with the operating LV are evaluated and discussed in considerable detail. The basic requirements and conceptual design of a full-scale mobile remote sensing dual-scatter LV system are outlined. The mobile unit is not limited solely to remote detection and evaluation of trailing vortices but may be used for other applications such as remote pollution detection, meteorological applications, etc.

## 2.0 ANALYSIS OF ATMOSPHERIC LASER VELOCIMETERS

Self-aligned laser velocimeter optical systems developed at AEDC (Refs. 5 and 6) have been applied in a number of different flow measurements (Refs. 7 and 8). The current application is a dual-scatter, back-scatter, LV system for use in atmospheric studies at relatively long ranges ( $500m > R > 10m$ ). To determine the performance of such a system, it is necessary to ascertain the dependence of the signal power as a function of range, wavelength, and number of scatter centers in the probe volume. In this section, the analysis of the required parameters is developed. It is assumed that the instrument operates in a quiescent atmosphere.

### 2.1 THEORETICAL EVALUATION

For purposes of clarity, an atmospheric LV system is shown in Fig. 3. The velocity is measured at the point where the beams cross. All Doppler signals are generated within an ellipsoid formed by the crossed beams (Ref. 5). Part of the power scattered by particles moving through the ellipsoid is collected by the transmitting optics where the backscattered power is electronically converted into velocity information. It will be convenient to consider that an LV system is essentially an

interferometer with the interference fringes formed within the probe volume (Ref. 5). The Doppler frequency may then be interpreted in terms of a scatter center moving across this fringe set.

## 2.2 EFFECT OF THE NUMBER OF SCATTER CENTERS ON THE SCATTER SIGNAL POWER

For mathematical simplification, consider only the infinite contrast fringes in the probe volume and assume that the fringes have rectangular intensity distributions. The actual and model intensity distributions are shown in Figs. 6a and b, respectively. Assuming rectangular shapes for the fringe intensity is not a necessary assumption but simplifies the mathematics considerably.

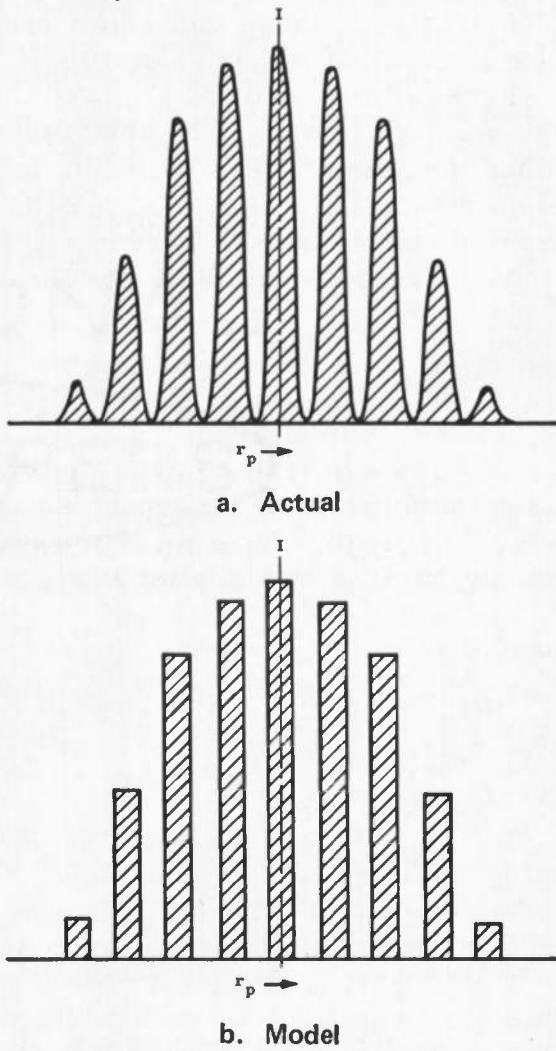


**Figure 6. Comparison of actual and model fringe intensity at the geometric center of a dual-scatter LDV.**

Suppose there are  $n$  scatter centers (SC) moving across the fringes with identical velocities. When an SC traverses a bright fringe, it scatters light; when it traverses a dark fringe, it does not. At any instant of time, the probability of an SC scattering is  $1/2$ . Since the positions of the scatter centers are independent of each other, the probability that light is scattered by all  $n$  scatter centers is  $(1/2)^n$ .

Let  $m$  be the total effective number of scatter centers whose scattered power adds to give a Doppler signal. Let  $P$  be the number whose signals add "in phase" to give a signal, i.e., the number simultaneously in a bright fringe. That we can assign a "phase" to an SC on a particular fringe follows when it is recalled that an SC generates a sinusoidal power output as it traverses the fringe set (Fig. 6). Hence, as a number of SC traverse the probe volume, they are all "phased" in time with respect to each other. The significance of these phase relationships becomes clear when we consider two SC traversing the probe volume with a phase difference of  $\pi$ , i.e., one is always on a bright fringe and one on a dark fringe. The resultant signal has no cyclic information since the sum of the two signals is constant (to within the overall Gaussian modulation of the gross intensity). Let  $g$  be the number whose signals add "out of phase" to reduce the signal, i.e., the number in a dark fringe. The constraints on the phases are then

$$P + g = n \quad (2-1a)$$

$$P - g = m, \quad m > 0 \quad (2-1b)$$

The total number of ways  $n$  SC can be arranged to give  $m$  is the number of different ways  $n$  objects can be separated into two groups, i.e.,  $n! / P! g!$ . Since all sequences have the same probability  $(1/2)^P (1/2)^g$ , the total probability of  $n$  scatter centers adding to give an effective signal due to  $m$  is

$$P_{n,m} = \frac{n!}{P!g!} (1/2)^P (1/2)^g \quad (2-2)$$

or using Eq. (2-1a)

$$P_{n,m} = \frac{n!}{P!g!} (1/2)^n \quad (2-3)$$

For  $n$  reasonably large ( $n > 20$ ), Stirling's approximation can be used

$$n! \approx (2\pi n)^{1/2} \left(\frac{n}{e}\right)^n \quad (2-4)$$

Applying Eq. (2-4) to Eq. (2-3) and making use of Eq. (2-1a) and (2-1b), then

$$P_{n,m} \approx \frac{1}{\left(1 + \frac{m}{n}\right)^{P-1/2} \left(1 - \frac{m}{n}\right)^{P+1/2}} \left[ \frac{2}{\pi n} \right]^k \quad (2-5)$$

Taking the natural logarithm of both sides of Eq. (2-5) and expanding forms of  $\ln(1 \pm \frac{m}{n})$  in a series to second order results in

$$\begin{aligned} \ln \left[ \left( \frac{n\pi}{2} \right)^k P_{n,m} \right] &\approx \frac{-m^2}{2n} \\ \text{or } P_{n,m} &\approx \left( \frac{2}{n\pi} \right)^k e^{-m^2/2n} \quad m \ll n \end{aligned} \quad (2-6)$$

The probability of  $m$  lying between  $m$  and  $m + dm$  is  $P_{n,m} dm$ . Therefore, the mean square value of  $m$ ,  $(\bar{m})^2$ , is

$$(\bar{m})^2 = \int_0^\infty m^2 P_{n,m} dm \quad (2-7)$$

Substituting Eq. (2-6) into Eq. (2-7), one finds that

$$\sqrt{\bar{m}^2} = \sqrt{n} \quad (2-8)$$

which agrees with results previously published. (Refs. 5, 9, and 10).

The RMS value of  $m$  is the desired result since the SC signals must add as phasors, i.e., vector quantities. That only  $\sqrt{n}$  SC give a velocity signal, has significant effects on the parametric performance of LV systems. These effects are pointed out in the next sections. Before proceeding, it should be noted that this statistical result applies also to reference beam LV systems since such systems may be thought of as having virtual fringes in the probe volume. (Refs. 9 through 14).

### 2.3 COLLECTED POWER SCATTERED AS A FUNCTION OF RANGE

To determine the appropriate expressions for signal-to-noise power ratios of the electronic processor in an LV system, the power scattered from the probe volume and collected by the receiving optics

in the LV is calculated for three different cases: (1) gross scattered power for a large number of SC in the probe volume, (2) power scattered by a single SC in the probe volume, and (3) effective signal power for a large number of SC in the probe volume. It is assumed that the instrument operates in a quiescent atmosphere which has a Junge particle size distribution, that fringes in the probe volume are of infinite contrast, that the SC sizes are much less than a fringe spacing, and that the SC are widely separated. In the analysis only one velocity component of the dual-scatter LV system is considered. Extension to include the other components is straightforward. Also, polarization vectors for the two transmitted beams are assumed linear, identical, and normal to the plane of the transmitted beams.

**Case 1. Gross scattered power collected by the LV for a large number of SC in the probe volume.**

The gross power scattered from the probe volume and collected by the optics of the LV,  $P_s$ , is given by

$$P_s = \langle I_o \rangle \sigma V_p T \Omega \quad (2-9)$$

where  $I_o$  is the illuminating intensity at the probe volume,  $\sigma$  is the volumetric scattering cross section,  $V_p$  is the probe volume,  $\Omega$  is the solid angle subtended by the collection optics to the probe volume,  $T$  is the atmospheric transmissivity, and  $\langle \rangle$  indicates a time average assuming  $e^{-ar_p^2}$  is approximately unity.  $I_o$  is then

$$I_o = \frac{2P_o T}{\frac{1}{4}\pi D^2} \cos^2(k \sin \frac{\theta}{2} \cos(\psi) r_p) e^{-ar_p^2} \quad (2-10)$$

where  $P_o$  is the laser input power to the transmitter and  $D$  is the diameter of the focused Gaussian beam measured to the  $1/e^2$  intensity point.  $k$  is  $(2\pi\eta)/\lambda$ , where  $\eta$  is the index of refraction of the atmosphere surrounding the SC, and  $\lambda$  is the wavelength of the light used.  $\theta$  and  $\psi$  are defined in Fig. 3.  $r_p$  is the radial distance from the geometric center of the probe volume, and "a" is the  $1/e^2$  minimum intensity radius in the focal region of the transmitter. The time dependence of  $I_o$  follows directly upon substituting  $r_p = |\mathbf{V}| t$ , where  $|\mathbf{V}|$  is the magnitude of the SC velocity.  $D$  is given by

$$D = \frac{4\lambda R}{\pi d} \quad (2-11)$$

$R$  is the distance from the transmitter to the probe volume, and  $d$  is the beam diameter at the transmitter. Note that "a" in Eq. 2-10 is  $(D/2\sqrt{2})^{-2}$ .

The volumetric scattering cross section is given by

$$\sigma = \sigma_R + \sigma_m \quad (2-12)$$

where  $\sigma_R$  is the Rayleigh scattering cross section and  $\sigma_m$  is the Mie scattering cross section. For the  $R$  and  $P_o$  factors under consideration, we need to consider only  $\sigma_m$  in the calculation of  $P_s$ . The backscatter cross section for Mie scattering per particle is

$$\sigma_{Mie} = \frac{\lambda^2}{4\pi^2} \sum_r i\left(\frac{2\pi r}{\lambda}, \eta, \pi\right) N_{Mie}(r, z) \quad (2-13)$$

where  $i[(2\pi r)/\lambda, \eta, \pi]$  is the Mie intensity backscatter function;  $\eta$  is the index of refraction of the SC,  $\pi$  is the backscatter angle, and  $N_{Mie}(r, z)$  is the number density of particles within  $\Delta r/2$  or radius  $r$  at altitude  $z$ . (Note that  $N(r, z)$  is a probability distribution, thus, the probability of finding a number density of exactly  $r$  size is vanishingly small and can only be specified within a  $\Delta r/2$  increment.)  $z$  is related to the range through

$$z = R \sin \phi \quad (2-14)$$

where  $\phi$  is the angle between the transmission axis and the horizontal. It has been shown (Ref. 15) that the  $z$  dependence of Eq. (2-14) may be separated from the summation for a Junge SC size distribution (which assumes  $[dN(r, z)]/dr$  is proportional to  $C(z)r^{(-\nu + 1)}$ ), and the result specialized (for  $\nu = 3$ ) to

$$\sigma_{Mie} = N_{Mie}(0) \left( e^{-\beta R \sin \phi} \right) \frac{3\pi r_1^3}{\lambda} \phi\left(i\left(\frac{2\pi r_1}{\lambda}, \bar{n}, \pi\right)\right) \quad (2-15)$$

where  $r_1$  is the radius of the smallest SC considered in  $N(r, z)$ .  $\beta$  may be considered essentially constant when  $z$  is less than 2km.  $N_{Mie}(0)$  is the number of Mie SC at  $z = 0$  and is about 450 SC/cc ( $0.125 \mu m \leq r \leq 1.0 \mu m$ ), and  $\phi(i)$  is an integral function of the parameters indicated (Ref. 15).

The  $1/e^2$  intensity probe volume,  $V_p$ , is given by

$$V_p = \frac{\pi}{6} \frac{D^3}{\sin \theta} \quad (2-16)$$

where  $\theta$  is the angle made by the transmitted LV beams as they cross to form the probe volume (Ref. 5). For most LV systems

$$\sin \theta \approx \theta = \frac{b}{R} \quad (2-17)$$

where  $b$  is the beam separation at the transmitter.

The solid angle  $\Omega$  is given by

$$\Omega = \frac{A_R}{\pi R^2} \quad (2-18)$$

where  $A_R$  is the backscatter collection area of the receiver.

The atmospheric transmission factor  $T$  is given by

$$T = e^{-\beta' R} \quad (2-19)$$

where  $\beta'$  may be taken as constant for  $R \lesssim 2\text{km}$ . A more detailed calculation would show its dependence on  $z$ ,  $r$ ,  $N(r, z)$ , etc. (Ref. 15).

Combining Eqs. (2-10) through (2-18) the gross scattered power collected by the receiver is

$$P_s = \frac{8}{db} P_o N_{Mie}(0) A_R r_1^3 \phi \left[ i \left( \frac{2\pi r}{\lambda}, \frac{n}{n_0}, \pi \right) \right] e^{-(\beta \sin \phi + 2\beta')R} \quad (2-20)$$

From Eq. (2-20), noting that for most LV systems  $d$  and  $b$  are essentially independent of  $R$  and therefore constant it may be concluded that for short ranges, ( $R \leq 0.5 \text{ km}$ , which is the case of interest), and at low altitudes ( $z \lesssim 1 \text{ km}$ ) there is practically no  $P_s$  dependence on range. In fact, for  $(\beta \sin \phi + 2\beta')R \ll 1$  there is no dependence on range at all. This effect becomes understandable when it is recalled that as range increases power density decreases as  $1/R^2$ , while the probe volume increases as  $R^4$ , and the solid collection angle is decreasing as  $1/R^2$ .

It is noted that  $P_s$  depends on wavelength only through  $\phi(i)$ , (change in  $\lambda$  small).

Case 2. Power scattered by a single SC in the probe volume.

The instantaneous power scattered by a single SC in the probe volume is given by

$$P_s^1 = I_o \sigma_1 T \Omega \quad (2-21)$$

where  $I_o$ ,  $\Omega$ , and  $T$  are the same as defined previously.  $\sigma_1$  is the average Mie backscattering cross section for a single particle in the Junge distribution. From Eq. (2-15),  $\sigma_1$  is written as

$$\sigma_1 = \frac{3\pi r_1^3}{\lambda} \phi \left[ i \left( \frac{2\pi r}{\lambda}, \bar{n}, \pi \right) \right] \quad (2-22)$$

then using Eqs. (2-10), (2-18), (2-19), and (2-22),  $P_s^1$  is

$$P_s^1 = \frac{3\pi^2 d^2 A_R r_1^3 P_o}{2} \frac{\phi \left[ i \left( \frac{2\pi r}{\lambda}, \bar{n}, \pi \right) \right] e^{-2\beta' R}}{\lambda^3 R^4} \cos^2 \left( k \sin \left( \frac{\theta}{2} \right) \cos(\psi) r_p \right) e^{-ar_p^2} \quad (2-23)$$

Note that  $P_s^1$  depends to a much greater degree on wavelength and range than does the gross scattered power. It is seen from Eq. (2-23) that the magnitude of  $P_s^1$  is increased by two mechanisms dependent on decreasing wavelength, namely the increase in the cross section function  $\phi(i)$  and the explicit inverse cube dependence. Finally, observe that  $P_s^1$  increases as  $d^2$  which is to be expected since the more  $d$  increases, the smaller  $D$  is and, therefore, the greater the input power density at the probe volume.

Case 3. Signal power for a large number of SC in the probe volume.

The signal power,  $P_s^S$ , can now be determined for a large number of SC in the probe volume. Using Eq. (2-8)  $P_s^S$  is

$$P_s^S = \sqrt{n} P_s^1 \quad (2-24)$$

where as before  $n$  is the number of SC in the probe volume

$$n = N(z) V_p \quad (2-25)$$

From Eq. (2-25)  $N(z)$  is written as

$$N(z) = N_{Mie}(0) e^{-\beta R \sin \phi} \quad (2-26)$$

Using Eq. (2-26) in Eq. (2-25) with the previous assumptions concerning  $V_p$ ,  $n$  becomes

$$n = \frac{64 N_{Mie}(0)}{3\pi^2 d^3 b} \lambda^3 R^4 e^{-\beta R \sin \rho} \quad (2-27)$$

Using Eqs. (2-23), (24), and (25)  $P_s^S$  is then

$$P_s^S = \frac{6\pi P_o A_r r_l^3}{\lambda^{3/2} R^2} \left[ \frac{d}{b} \frac{N_{Mie}(0)}{3} \right]^{1/2} \frac{\phi(i) \exp \left[ -R \frac{2\beta}{\lambda} + \frac{\beta \sin \phi}{2} \right]}{\lambda^{1/2} R^2} \times \cos^2 \left[ k \sin \frac{\theta}{2} \cos(\psi) r_p \right] \exp \left[ -a r_p^2 \right] \quad (2-28)$$

When compared to  $P_s$  it is seen that  $P_s^S$  increases directly as  $\lambda^{3/2}$  decreases, whereas  $P_s$  depends on  $\lambda$  only through  $\phi(i)$ . Furthermore,  $P_s^S$  decreases as the inverse square of the range.

## 2.4 SIGNAL-TO-NOISE POWER RATIOS

It is of interest to calculate the signal-to-noise power ratio at the output of a photomultiplier tube using the values of scattered power previously derived. If shot noise due to dark current and thermal effects can be neglected (this is a good assumption) the S/N can be written as

$$S/N \approx \frac{q}{h f_1 \Delta f} \left[ \frac{\langle P_s^S \rangle^2}{P_s + \langle P_{BG} \rangle} \right] \quad (2-29)$$

where  $q$  is the quantum efficiency (electrons per photon) of the photomultiplier,  $h$  is Plank's constant,  $f_1$  is optical frequency of the input radiation,  $\Delta f$  is the shot noise limiting electronic bandwidth, and  $P_{BG}$  is the stray background light power striking the photocathode.

Two cases of S/N using Eq. (2-29) are considered: (1) S/N for a single SC in the probe volume; and (2) S/N for multiple SC in the probe

volume. First, Eq. (2-29) is arranged in the form

$$S/N \approx \frac{q}{hf_1 \Delta f} \left[ \frac{1}{1 + \langle P_{BG} \rangle / P_s} \right] \frac{(\langle P_s \rangle)^2}{P_s} \quad (2-30)$$

Now consider S/N for the first case of a single SC in the probe volume. In this case

$$P_s = \langle P_s^1 \rangle$$

Then using Eq. (2-23), the S/N becomes

$$S/N \approx \frac{q}{hf_1 \Delta f} \left[ \frac{1}{1 + \langle P_{BG} \rangle / P_s} \right] \left( \frac{3\pi^2 d^2 A_R P_o r_1^3}{2} \right) \frac{\phi \left[ i \left( \frac{2\pi r}{\lambda}, \bar{n}, \pi \right) \right] e^{-2\beta' R}}{\lambda^3 R^4} \quad (2-31)$$

For the case of multiple SC in the probe volume, using Eqs. (2-20) and (2-28) yields

$$S/N \approx \frac{q}{hf_1 \Delta f} \left[ \frac{1}{1 + \langle P_{BG} \rangle / P_s} \right] \left( \frac{3\pi^2 d^2 P_o A_R r_1^3}{2} \right) \frac{\phi \left[ i \left( \frac{2\pi r}{\lambda}, \bar{n}, \pi \right) \right] e^{-2\beta' R}}{\lambda^3 R^4} \quad (2-32)$$

If  $P_{BG}$  is completely negligible ( $P_{BG} \ll P_s^1$ ), the S/N for both cases has identical  $\lambda$  and  $R$  dependence for short range and low or constant altitude. More specifically, S/N is the same for both cases. If  $P_{BG}$  is not negligible, then the multiple SC S/N must give inherently better S/N than the single SC S/N because  $P_s \gg P_s^1$ . This implies that S/N would not be improved by using artificial seeding materials.

## 2.5 SUMMARY

The necessary equations to evaluate the parametric performance of an atmospheric long-range LV system have been developed. It is shown that of the number of SC,  $n$ , in the probe volume,  $\sqrt{n}$  contribute to a Doppler signal. This limitation leads to a number of unexpected results in the performance of dual-scatter velocimeters. These results may be summarized as:

1. Signal power from  $n$  SC in the probe volume is inversely proportional to  $\lambda^{3/2} R^2$ , while signal power from a single SC in the probe volume is inversely proportional to  $\lambda^3 R^4$ .
2. The S/N power ratios for both single and multiple SC are identical (inversely proportional to  $\lambda^3 R^4$ ) if the stray background light power is much less than the signal power from a single SC.
3. The multiple SC S/N quickly becomes better than the single SC S/N when stray background light power is comparable in magnitude to that of a single SC.
4. When variation in number density of SC and atmospheric transmission factors can be neglected, gross scattered power detected by the LV is independent of range for any wavelength of light used in the system.

The results presented in 1 and 2 above suggest that improved performance of any LV system can be obtained by decreasing the wavelength of the input illumination. Statement 2 shows that when stray background power is negligible compared to power scattered by a single SC, addition of artificial seeding materials can contribute nothing to the dual-scatter S/N. In the following section the major types of LV systems will be compared operationally for trailing vortex measurements.

### 3.0 SYSTEMS EVALUATION

In determining atmospheric applications of an LV, two distinct methods have been reported (Refs. 2, 7, 10, 16, and 17). The first method utilizes light with a wavelength of about 0.5 micrometers in conjunction with dual-scatter (DS) LV illuminating techniques (Refs. 6, 7, 11, and 17). The second method uses light of 10.6-micrometer wavelength and local oscillator (LO) LV illuminating techniques (Refs. 18, 11, 16). To determine the most feasible technique to pursue as a diagnostic tool for this application, the characteristics of both techniques are evaluated, under similar operating conditions, to ascertain some quantitative basis for LV system selection and determination of performance criteria for atmospheric research. In this section, comparisons are made and the results show that specific ranges and conditions exist where the performance of one method is superior to that of the other.

The analysis under consideration will specifically compare the systems shown in Figs. 3 and 7. It is convenient, for a basic understanding of the instrument, to interpret the Doppler signal in terms of the frequency of a scatter center crossing a set of interference fringes, either real or virtual, generated by the LV optics (Refs. 5 and 14). In the DS system (Fig. 3) two parallel, collimated beams entrance into a transmitter-receiver telescope and are brought to focus. Near the geometric center of the focus the wavefronts are parallel and tilted an angle  $\theta$  with respect to each other. Hence, they generate interference fringes which are planes parallel to the optical axis and perpendicular to the plane defined by the intersecting beams. Light scattered from the fringes by particles traversing them is collected by the receiver and imaged on a detection device. The LO transmitter-receiver telescope system (Fig. 7) also images two beams at the focal region, although only one beam is real while the second is virtual and propagates in a direction opposite to the real beam (Ref. 10). In this case, the virtual interference fringes are perpendicular to the optical axis.

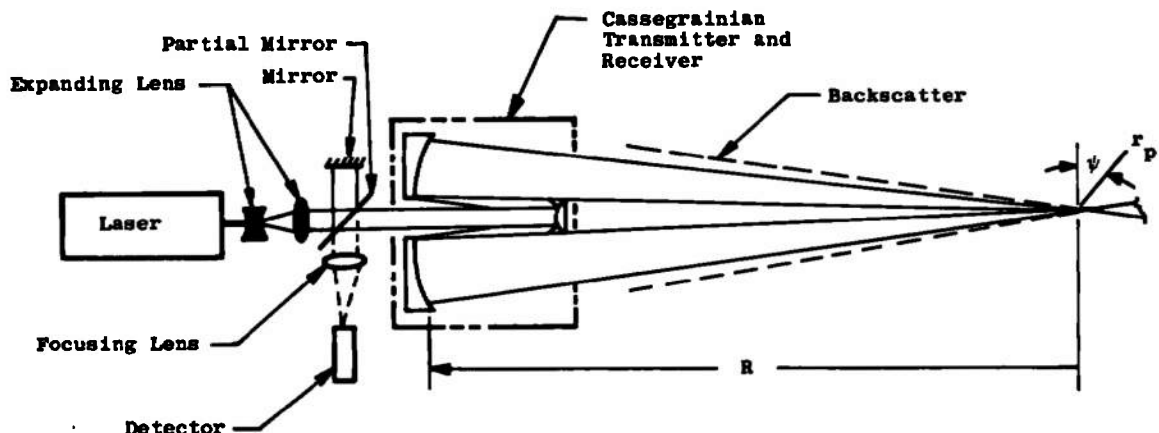


Figure 7. Backscatter local-oscillator long range LV system.

In the following sections, the result of the analyses will compare the relative effects of optical system parameters, radiation alignment, number of scatter centers in the scattering volume, atmospheric turbulence, and signal visibility on the operation of DS and LO LV systems.

### 3.1 BASIC PERFORMANCE EQUATIONS

The signal-to-noise power ratio is indicative of the performance of any electro-optical system. To gain a comparative basis for the

relative performance of LO and DS LV systems, the basic comparative performance figure,  $S_R$ , of the two systems is defined as

$$S_R = \frac{(S/N)_{DS}}{(S/N)_{LO}} \quad (3-1)$$

where the subscripts are used to denote dual-scatter (DS) and local oscillator LV systems.

The S/N values to be evaluated are those at the output of the signal detector, and are, therefore, heavily biased towards the optical and detector performance for each system. Furthermore, numerical values presented in the examples should be taken only as indicative of trends, since, particularly those dealing with atmospheric parameters, the data are open to question or somewhat sparse.

It is assumed that all scatter centers in the probe volume, defined by the  $1/e^2$  intensity points in the focal region of the LV, are moving with the same velocity. Fourier spectrum broadening due to the limited residence time of the scatter center in the probe volume or finite solid collection angle will not be considered. Also, poor detector statistics due to limited photon collection will be neglected, i. e., it is assumed sufficient power is available to detect the signal. The shot noise limited S/N for dual-scatter systems can be written, as from Ref. 19, as

$$(S/N)_{DS} = \frac{q_{DS} \lambda_{DS}}{h c \Delta f_{DS}} \left\{ \frac{1}{1 + \left[ \frac{\langle P_{BG} \rangle}{\langle \bar{P}_s \rangle_{G-DS}} \right]} \right\} \langle \bar{P}_s \rangle_{G-DS}^1 \bar{C}_{DS}^2 \quad (3-2)$$

For local oscillator systems the S/N is given, as from Ref. 19, by

$$(S/N)_{LO} = \frac{q_{LO} \lambda_{LO}}{h c \Delta f_{DS}} \left\{ \frac{1}{1 + \left[ \frac{\langle \bar{P}_s \rangle_{G-LO} + P_{BG}}{\langle P_{LO} \rangle} \right]} \right\} \sqrt{n} \langle \bar{P}_s \rangle_{G-LO}^1 \bar{C}_{LO} \quad (3-3)$$

where all terms with the exception of subscripts are the same as defined for the DS system.

For the LV systems shown schematically in Figs. 3 and 7, the power scattered by a single scatter center in the probe volume is approximately given by

$$P_s^1 = \frac{4P_o \bar{\sigma}_1 T^2 \Omega}{\pi D^2} \quad (3-4)$$

A Junge aerosol size distribution is assumed for the atmosphere (Ref. 15) and Rayleigh scattering from the probe volume is neglected on the grounds that its magnitude is much less than the Mie scattering by the aerosol particles. For a wide size range,  $\bar{\sigma}_1$  is given, as from Ref. 15 and 20, by

$$\bar{\sigma}_1 = \frac{3\pi r_1^3}{\lambda} \phi \left[ i \left( \frac{2\pi r_1}{\lambda}, \bar{n}, \pi \right) \right] \quad (3-5)$$

The  $1/e^2$  intensity diameter was previously given (Eq. (2-11)); therefore, the one particle visibility function can be written (from Ref. 19) as

$$C = \frac{A(\gamma) \int_{A_p} \cos[a \cos(\psi) r_p - a] dA_p}{\int_{A_p} dA_p} \quad (3-6)$$

where

$$A(\gamma) = \frac{2\sqrt{I_1 I_2} \cos(\gamma)}{I_1 + I_2} \quad (3-7)$$

Assuming spherically shaped scatter centers, Eq. (3-6) gives

$$C = 2A(\gamma) \cos(a) J_1(ar)/ar \quad (3-8)$$

$J_1(\cdot)$  is a first order Bessel function,  $r$  is the particle radius, and the values of "a" for DS and LO systems are:

$$a = \frac{4\pi\eta \sin\left(\frac{\theta}{2}\right)}{\lambda} \text{ (DS System)} \quad (3-9)$$

$$a = \frac{4\pi\eta}{\lambda} \text{ (LO System)} \quad (3-10)$$

where  $\eta$  is the index of refraction of the atmosphere surrounding the scatter center. As with the scattering cross section  $C$  will be the ensemble averaged over a Junge size distribution. Figure 8 graphically shows the  $C$  dependence on scatter center size and fringe spacing.

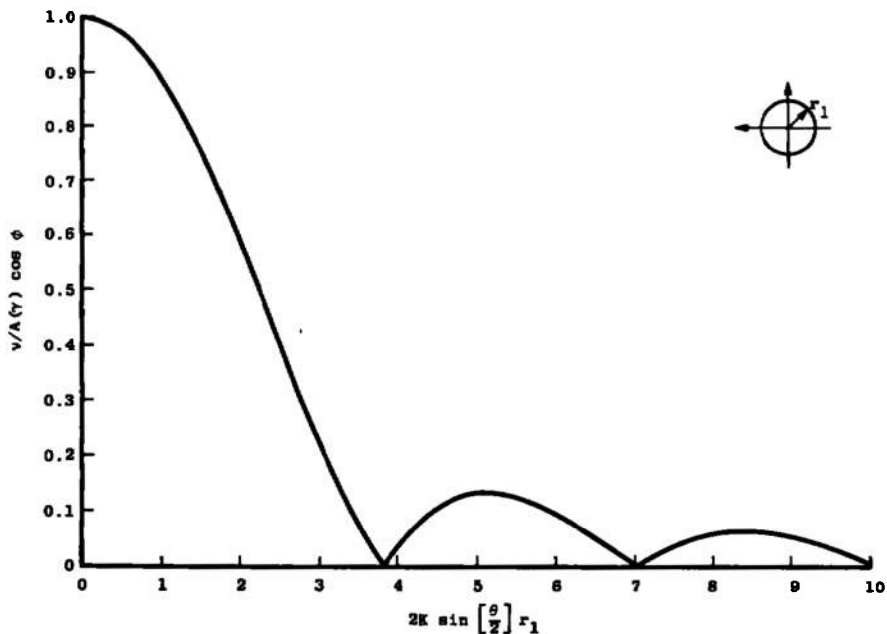


Figure 8. LV fringe visibility for a spherical scatter center.

For future reference it will be convenient to define a system function of wavelength

$$C(\lambda) = \frac{q_{DS} \Delta f_{LO} \langle P_o \rangle_{DS} \phi^{(i)}_{DS} \pi/4}{q_{LO} \Delta f_{DS} \langle P_o \rangle_{LO} \phi^{(i)}_{LO}} \quad (3-11)$$

also, let

$$\bar{C} = \frac{\bar{C}_{DS}}{\bar{C}_{LO}} \quad (3-12)$$

Then using Eqs. (3-1 through 6, 11, and 12 and assuming that

$$P_{LO} \gg \langle \bar{P}_s \rangle_{G-LO} + \langle P_{BG} \rangle \text{ and that } \langle \bar{P}_s \rangle_{G-DS} \gg \langle P_{BG} \rangle$$

then the general comparative performance equation can be written as

$$S_R = \frac{4}{\pi} C(\lambda) \left( \frac{\lambda_{LO}}{\lambda_{DS}} \frac{d_{DS}}{d_{LO}} \right)^2 \left[ \frac{\Delta_{DS}^2}{\Delta_{LO}^2} \frac{\bar{C} \exp(-2\Delta\beta' R)}{\sqrt{n}} \right] \quad (3-13)$$

Equation (3-13) clearly outlines the parametric dependence of  $S_R$ .  $C(\lambda)$  gives the functional dependence of relative detection capability and wavelength scattering characteristics. Two points, not immediately obvious, should be made. First, note that the collector diameter of the dual-scatter system can be made as large as desired (Ref. 5), while that of the LO system is no greater than  $d_{LO}$  due to the radiation alignment (Ref. 18) and can be limited to smaller values due to turbulent degradation of the returning wavefront. However, Eq. (3-14) shows that an increase in  $n$  can compensate for a relative reduction in  $\Delta_{LO}$ . Secondly, visibility is not large in LO systems since the fringe spacing is  $\lambda/2$  and the beam intensities are not equal. This is not the case for long-range DS systems where the beam intensities are equal and fringe spacing is about  $\lambda/\theta$ ,  $\theta$  being small. This means DS systems can accommodate a much larger particle size with  $C_{DS}$  very nearly one.

Atmospheric transmission effects are accounted for in the exponential term where the attenuation constant  $\Delta\beta'$  is given by

$$\Delta\beta' = \beta'_{DS} - \beta'_{LO} \quad (3-14)$$

Usually  $\beta'$  decreases with increasing wavelength. Thus, a gain in scatter cross section due to a decrease in wavelength is offset by a reduction in transmittance through the atmosphere. It should be noted that  $\Delta\beta'$  is a function of altitude and range. However, for ranges and altitudes of the order of 1 km,  $\Delta\beta'$  may be taken as approximately constant (Ref. 15).

The  $n$  dependence of  $S_R$  denotes a point of division in  $S_R$  calculations. In order to calculate  $S_R$ , it must be known whether the signal is continuous (CW) due to  $n$  always being large, or if the signal is a "burst" due to single particles passing through the probe volume.

For burst signals  $n$  becomes 1 and Eq. (3-13) reduces to

$$S_R^{(B)} = \frac{4}{\pi} C(\lambda) \left( \frac{\lambda_{LO} d_{DS}}{\lambda_{DS} d_{LO}} \right)^2 \left[ \frac{\Delta_{DS}^2 \bar{C} \exp(-2\Delta\beta' R)}{\Delta_{LO}^2} \right] \quad (3-15)$$

where the superscript denotes  $S_R$  for burst signals. Note that in a quiescent atmosphere where  $\Delta_{LO}$  is unaffected by atmospheric turbulence, the range dependence enters only through the transmittance term.

For CW signals where  $n$  is large,  $n$  is given by

$$n = n(z)V_{p-LO} \quad (3-16)$$

where  $n(z)$  is the number density of scatter centers as a function of altitude  $z$  and  $V_p$  is the  $1/e^2$  intensity probe volume. The size of probe volume is a function of wavelength. To obtain a fair comparison of the two systems requires both system probe volumes to be identical. Practically speaking, this corresponds to suitable aperturing of the return signal. With this constraint,  $V_{p-LO}$  is given by

$$V_{p-LO} = \frac{\pi^2}{24} \left( \frac{d_{LO}}{b} \right)^{4/3} \frac{D_{DS}^4}{\lambda_{LO}} \quad (3-17)$$

where  $b$  is the DS beam separation at the transmitter.  $n(z)$  was previously written, as from Eq. (2-26), as

$$\rho(z) = N_{MIE}(0) \exp(-\beta \sin(\phi) R) \quad (3-18)$$

Thus, on using Eqs. (3-16) and (3-18) in Eq. (3-13),  $S_R$  for CW signals is given by

$$S_R^{(CW)} = C(\lambda) F(n, L) \left( \frac{\lambda_{\mu LO}^{5/2}}{\lambda_{\mu DS}^4} \right) \exp \{ [\beta \sin(\phi) R - 2\Delta\beta'] R \} \quad (3-19)$$

where  $\lambda_{\mu}$  indicates  $\lambda$  written in micrometers.  $F(n, L)$  is a function of the lens,  $L$ , and "n" parameters given by

$$F(n, L) = \Delta_{DS}^2 \bar{V} \sqrt{\frac{3}{2N_{MIE}(0)}} \frac{d_{DS}^4 b^{2/3}}{d_{LO}^{8/3}} \times 10^9 \quad (3-20)$$

(all linear dimensions given in meters).

It is seen that  $S_R^{(CW)}$  has a much stronger range dependence than  $S_R^{(B)}$  and is also much more sensitive to slight variations in wavelength differences in the two systems.

### Turbulence Dependence of $S_R$

In this section, Eqs. (3-15) and (3-19) are modified to account for the effects of atmospheric turbulence on the LDV signal. It is assumed that atmospheric turbulence produces little or no effect on the input beams during transmission to the probe volume. This suggests that DS systems signals are not significantly affected by atmospheric turbulence since the signal radiation is mixed before it is scattered. Work previously presented indicates that as long as the transmitter beam separation in the DS system or the beam size in the LO system is at most one-half of the outer scale of turbulence, or equivalently the turbulence correlation length, relative beam quality is unaffected by turbulence (Refs. 21, 22, and 23). However, in the LO system, the scattered wave is perturbed by turbulence as it returns to the collector prior to mixing the unperturbed LO reference beam. In this case, there can be no correlation between the wavefronts and phase variation. It has been shown that lack of correlation leads to a limiting aperture effect for the LO system (Ref. 21). Increasing the diameter of the LO collection aperture beyond the turbulence limited aperture diameter contributes nothing to the S/N and, in fact, may degrade the signal (Ref. 22). In the present analysis, it is assumed that the solid collection angle is sufficiently small such that the scattered light may be considered composed of plane wavefronts. For calculation of the limiting aperture diameter, Fried's approach (Ref. 21) is used with his calculations modified to account for finite propagation distances through the atmosphere.

It can be shown that for finite propagation distances through a turbulent atmosphere two cases of limiting aperture must be considered. Case one corresponds to signal propagation parallel to the ground, while case two corresponds to angular path propagation.

For propagation paths parallel to the ground the square of the limiting aperture diameter is given by

$$\Delta_{LO}^2 = 1.44 \times 10^{-16} \lambda_{\mu LO}^{12/5} R^{-6/5} C_N^{-12/5} \left(\frac{1}{4}\right) \quad (3-21)$$

where  $C_N$  is the so-called structure constant for various levels of turbulence and the one-column matrix accounts for daylight (upper element) and night time (lower element) use.

For angular path propagation the square of the limiting aperture diameter is given by

$$\Delta_{LO}^2 = 1.06 \lambda_{\mu LO}^{12/5} \sin^{2/5}(\phi) \gamma^{*6.5} \left[ \frac{2}{3}, \frac{R \sin(\phi)}{h_0} \right] R^{-4/5} \quad (3-22)$$

where  $\gamma^*( )$  is a single-valued analytic function of the incomplete Gamma function (Ref. 4), and  $h_0$  is the 1/e decay point with altitude of the variance of the atmospheric refractive index (Ref. 21).

Substituting Eqs. (3-22) and (3-23) into Eqs. (3-16) and (3-17), complete parametric performance equations for  $S_R$  can be written. Hence for horizontal path propagation,

$$S_R^{(B)} = \frac{\frac{4}{\pi} C(\lambda) \left( d_{DS}/d_{LO} \right)^2 \Delta_{DS}^2 \bar{C} C_N^{12/5} \times 10^{16} R^{6/5} \exp(-2\Delta\beta' R)}{1.44 \lambda_{\mu DS}^2 \lambda_{\mu LO}^{2/5} \left( \frac{1}{4} \right)} \quad (3-23)$$

$$S_R^{(CW)} = \frac{C(\lambda) F(n, L) C_N^{12/5} \times 10^{16}}{1.44 \frac{1}{4}} \left( \frac{\lambda_{\mu LO}^{1/10}}{\lambda_{\mu DS}^4} \right) \frac{\exp(-2\Delta\beta' R)}{R^{4/5}} \quad (3-24)$$

while for angular path propagation

$$S_R^{(B)} = \frac{\frac{4}{\pi} C(\lambda) \left( d_{DS}/d_{LO} \right)^2 \Delta_{DS}^2 \bar{C} \gamma^{*6/5} \left[ \frac{2}{3}, \frac{R \sin(\phi)}{h_0} \right] R^{4/5} \exp(-2\Delta\beta' R)}{1.06 \sin^{2/5}(\phi) \lambda_{\mu DS}^2 \lambda_{\mu LO}^{2/5} \left( \frac{1}{4} \right)} \quad (3-25)$$

$$S_R^{(CW)} = \frac{C(\lambda) F(n, L) \gamma^{*6/5} \left[ \frac{2}{3}, \frac{R \sin(\phi)}{h_0} \right] \left( \lambda_{\mu LO}^{1/10} / \lambda_{\mu DS}^4 \right) \exp \left\{ \left[ \frac{\beta \sin(\phi)}{2} - 2\Delta\beta' \right] R \right\}}{1.06 \sin^{2/5}(\phi) R^{6/5} \frac{1}{4}} \quad (3-26)$$

The primary differences in the horizontal and angular path propagation  $S_R$  equations are that turbulence effects are greatest near the ground and drop off quickly with altitude, and variation of  $n$  with altitude.

## Examples

To graphically illustrate the effects described by Eqs. (3-23) and (3-26), two comparisons are made. The first involves a common wavelength ( $0.5 \mu\text{m}$ ) where an LO system is used in the backscatter mode of operation (Fig. 7) and compared with a dual scatter system (Fig. 3). The second application compares a DS system operating at a wavelength of  $10.6 \mu\text{m}$  where 5 percent of the input power is used for the reference beam. The chosen system parameters are shown in Table 1.

Table 1. Selected Values for Input Parameters

Parameters	Example One	Example Two
$q_{DS} \Delta f_{LO} / q_{LO} \Delta f_{DS}$	1	1
$P_{o_{DS}} / P_{o_{LO}}$	1	0.05
$\phi_{DS(i)} / \phi_{LO(i)}$	1	7.12
$\lambda_{\mu_{LO}} (\mu\text{m})$	0.5	10.6
$\lambda_{\mu_{DS}} (\mu\text{m})$	0.5	0.5
$\Delta_{DS} (\text{m})$	1	1.0
$\Delta_{LO} (\text{m})$	0.1	1.0
$v_{DS}$	1.0	1.0
$v_{LO}$	0.211	0.33
$N_{Mie}(0) (\text{m}^{-3})$	$4.5 \times 10^8$	$4.5 \times 10^8$
$d_{DS} (\text{m})$	0.1	0.1
$d_{LO} (\text{m})$	0.1	1.0
$b (\text{m})$	0.8	0.8
$\beta (\text{Km}^{-1})$	0.885	0.885
$\beta'_{DS} (\text{Km}^{-1})$	0.28	0.28
$C_n (\text{m}^{-1/3})$	$1.414 \times 10^{-7}$	$1.414 \times 10^{-7}$
$I_1, I_2$ DS	1, 1	1, 1
$I_1, I_2$ LO	0.1, 0.9	0.1, 0.9
$\alpha, \gamma$	0, 0	0, 0

The results of the common wavelength comparison for operation at various propagation angles in a turbulent and quiescent atmosphere are shown in Figs. 9 and 11. For CW signals one sees (Fig. 9) that in a quiescent atmospheric operation the DS system can outperform the LO system until the probe volume of the LO system becomes large enough to accommodate enough scatter centers to offset the difference in collection aperture area. As the altitude begins to increase, and  $n$  to decrease, it can be seen that performance increases in favor of the DS system. For the turbulent cases, the  $\Delta_{LO}$  decrease is apparent due to the high  $S_R$  increase. As the propagation angle increases,  $S_R$  decreases as expected, due to the turbulence being most pronounced near ground level.

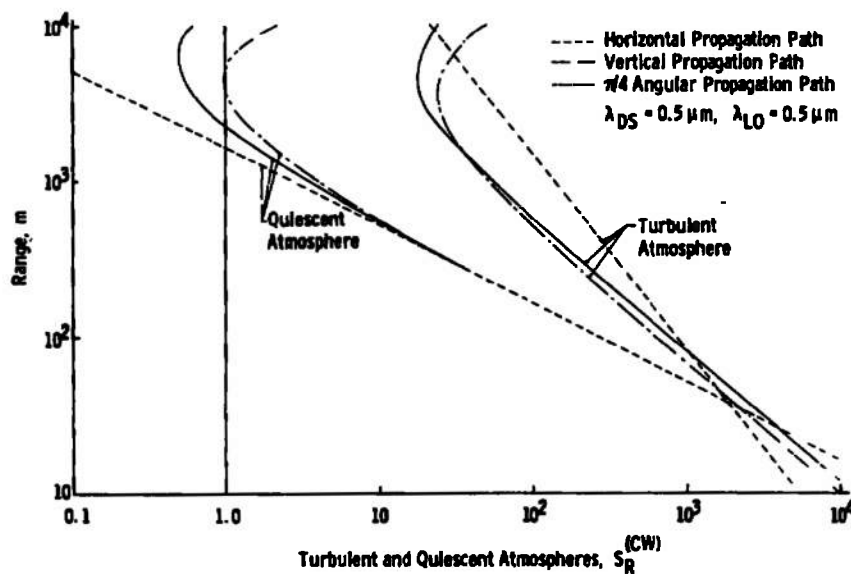
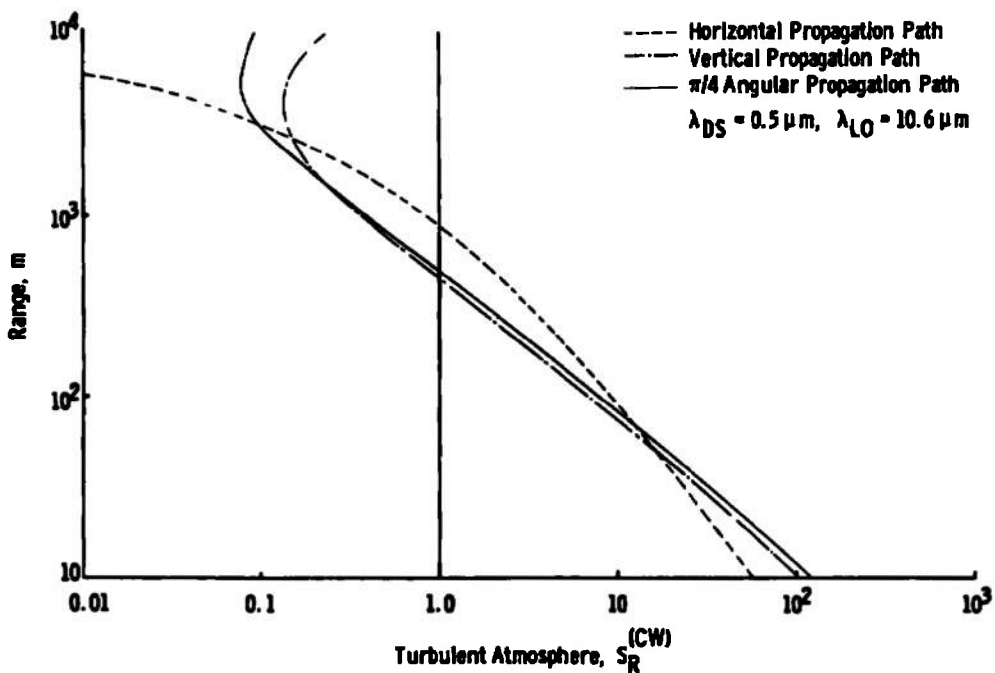
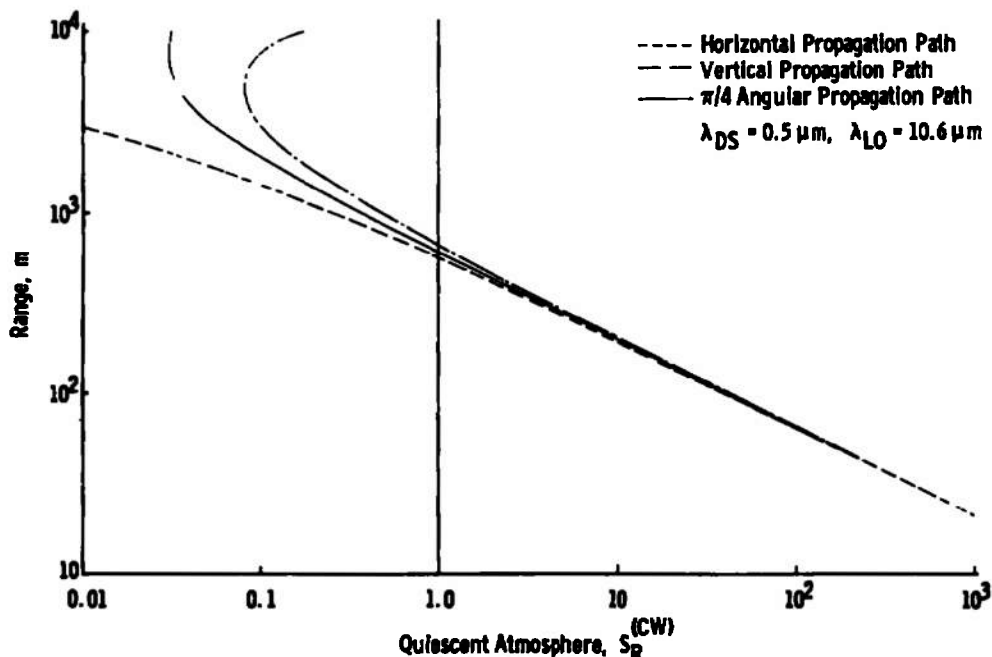


Figure 9. LV operation in turbulent and quiescent atmosphere,  $S_R$  (CW).

In the second comparison shown in Figs. 10a and b, turbulent effects on the LO system are much smaller due to the wavelength increase in the LO system. It is well known that turbulent effects on electromagnetic wave propagation decrease with increasing wavelength (Ref. 25). In this case, solid collection angles are identical. Therefore, the only advantage the DS system has over the LO system is greater scattering efficiency and higher power density at the probe volume. The LO system compensates for these disadvantages with increased power input, higher values of atmospheric transmittance, and large values of  $n$  in the probe volume. Even so, the DS system can be seen to outperform the LO system up to ranges of about 500 m.



a. Turbulent atmosphere



b. Quiescent atmosphere

Figure 10. LV operation,  $S_R^{(CW)}$ .

When the signals are of a burst nature one can see that the DS system outperforms the LO system in the first comparison beyond 50-m range (Fig. 11). In the second comparison (Fig. 12), at relatively long ranges, the DS system considerably outperforms the LO system.

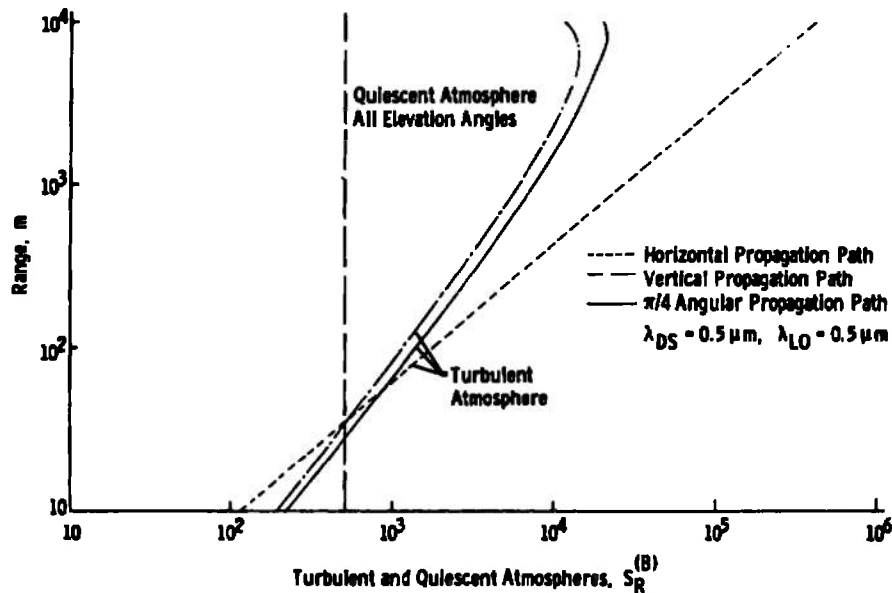


Figure 11. Burst LV operation in turbulent and quiescent atmosphere.

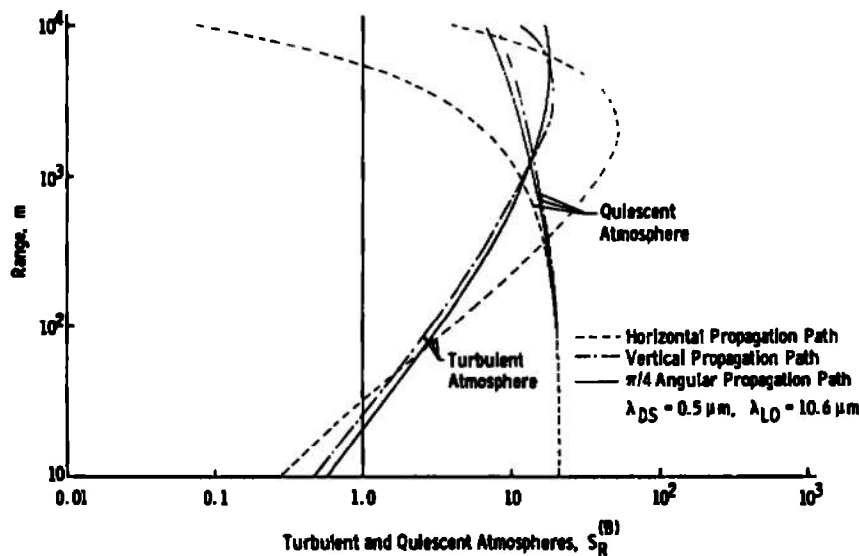


Figure 12. LV operation in turbulent and quiescent atmosphere.

### 3.2 DETERMINATION OF THE DATA ACQUISITION RATE

To evaluate the design of this specific laser velocimeter system for trailing vortex applications, the data acquisition rate of the system is an important criteria to be determined. A theoretical analysis was performed to determine the data acquisition rate as a function of the operating parameters in the system. In this particular analysis, emphasis was placed on determining the rate that signal particle bursts can be acquired (minimum 100/sec) so that the system design could be optimized. In the event that continuous signals are available, the results of the analysis would be somewhat conservative. In a similar manner, the application of the Bragg cell concept of a vector velocity measuring system, the results will also be conservative. This is true since the net count effective, traveling, fringes is greater than the stationary fringe technique. Thus, the time to determine a period count is reduced considerably.

#### 3.2.1 Analysis and Evaluation

In the following analysis, it is assumed that the aerosol particles contained within the earth's atmosphere, between 0- and 3,000-meters vertical range, are essentially spherical in nature and are characterized by a constant index of refraction. Three parameters are required to determine the light scattering characteristics of such an atmosphere. These are: (1) the particle index of refraction,  $\eta$ , (2) the particle size distribution function  $dN/dr$ , and (3) the single particle Mie scatter intensity function  $i(\theta_s)$ .  $dN/dr$  has been experimentally measured and is relatively constant throughout the earth's lower atmosphere (Refs. 26, 27, and 28) and is plotted in Fig. 15 of Ref. 29.  $i(\theta_s)$  has been theoretically determined (Ref. 29); however, since  $i(\theta_s)$  depends upon the dielectric constant and conductivity of the scatterer, an average index of refraction,  $\eta = 1.5$  (Ref. 28) representative of atmospheric aerosol was chosen.

For  $\eta = 1.5$ ,  $i(180 \text{ deg})$  has been conveniently tabulated, as a function of the particle size parameter  $\alpha = 2\pi r/\lambda$ , Ref. 15. Thus, the light scattering characteristics of the atmospheric aerosol are specified.

The number of particles per unit volume within the size range  $\Delta r/2$  of particle radius  $r$  is  $(dN/dr) \Delta r$ . Assuming  $\Delta r$  is small, each of these particles has a differential scattering cross section

$$\frac{d\sigma}{d\Omega}(\theta_s) = i(\theta_s) \left(\frac{\lambda}{2\pi}\right)^2 \quad (3-27)$$

such that when illuminated by a beam of intensity  $i$  it will scatter a power  $(d\sigma/d\Omega)(\theta_s) \Delta\Omega$  into a small solid angle  $\Delta\Omega$  about  $\theta_s$ .

Collectively, particles of all sizes will scatter illuminating radiation to provide a mean photocurrent at the detector which will determine the magnitude of the mean shot noise. The differential scattering cross section per unit volume (power scattered  $\times$  Solid Angle $^{-1}$   $\times$  volume $^{-1}$   $\times$  intensity $^{-1}$ ) is

$$\frac{d\beta}{d\Omega}(\theta_s) = \int_{r_L}^{r_u} \frac{d\sigma}{d\Omega}(\theta_s) \frac{dN}{dr} dr = \int_{r_L}^{r_u} i(\theta_s) \left(\frac{\lambda}{2\pi}\right)^2 \frac{dN}{dr} dr \quad (3-28)$$

where  $r_L$  and  $r_u$  are the lower and upper limits of the extent of the particle size distribution function  $dN/dr$  as shown in Fig. 13. It is assumed that a dual-scatter LV collects backscattered light ( $\theta_s \approx 180^\circ$ ) only from the beam crossover region. Furthermore, the radiation collection optics are set such that they do not directly view a bright background and/or very narrow (e.g., 2A) bandwidth laser line filters are used to reject background radiation. Under such conditions, the mean photocathode current,  $I_c$ , is mainly dependent on the scattered laser light collected from within the probe volume described by

$$I_c = \frac{d\beta}{d\Omega}(180^\circ) P_L \left(\frac{\pi\theta_R^2}{4}\right) \left(\frac{2N_F\lambda}{\theta^2}\right) \frac{\eta e\lambda}{hc} \quad (3-29)$$

The  $\exp(-2)$  length of the probe volume is  $2N_F\lambda/\theta^2$ , the solid collection angle is  $\pi\theta_R^2/4$ , and  $\eta e\lambda/hc$  converts watts to cathode amperes.  $I_c$  of Eq. (3-29) is the time-averaged d. c. (photo) cathode current due to scatter centers of all sizes. The total d. c. shift due to the known presence of a particular particle size is

$$I_{\text{total}} \approx i_c + I_c$$

where  $i_c$  is contributed by the known particle and  $I_c$  is the background light current. The signal-to-noise ratio is then

$$\text{SNR} \approx \frac{1/2 i_c^2}{2e(i_c + I_c)f_e} \quad (3-30)$$

Assuming the electronic bandwidth  $f_e$  is adjusted to be

$$f_e = f_D = v\theta/\lambda$$

then Eq. (3-30) becomes

$$\text{SNR} = \frac{\lambda}{4ev\theta} \times \frac{i_c^2}{(i_c + I_c)} \quad (3-31)$$

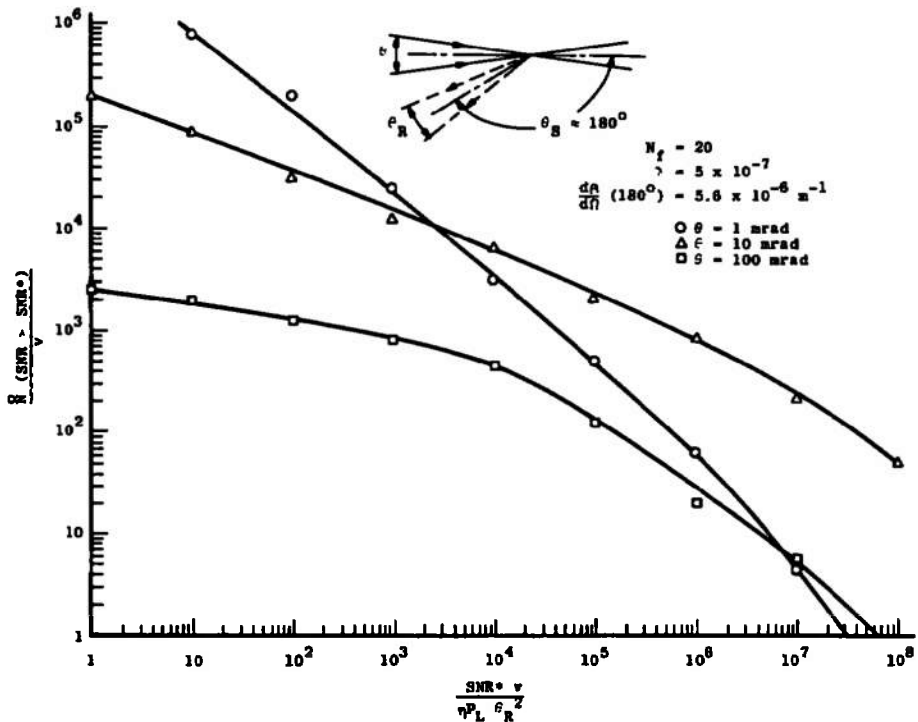


Figure 13. Backscatter data rate  $\overset{\circ}{N}$  versus minimum signal-to-noise power ratio (SNR).

Additionally, a knowledge of the fringe intensity distribution (Ref. 19) allows one to predict the data rate,  $\overset{\circ}{N}$ , as a function of the SNR or the  $\text{epf}^*{}^1$  rate of a dual-scatter, backscatter, LV. These are given by

$$\overset{\circ}{N}(\text{SNR} > \text{SNR}^*) = \frac{\pi v}{\theta} \left( \frac{N_F \lambda}{2\theta} \right)^2 F(i_o^*) \quad (3-32)$$

$$\overset{\circ}{N}(\text{epf} > \text{epf}^*) = \frac{\pi v}{\theta} \left( \frac{N_F \lambda}{2\theta} \right)^2 F(j_o^*) \quad (3-33)$$

---

<sup>1</sup> $\text{epf}^*$  is the electrons per fringe generated at the photocathode by light scattered by a particle in traversing one fringe.

where

$$F(x) = \int_{y=x}^{y=\infty} \frac{N(i > y)}{y} dy, \quad (3-34)$$

$$i_o^* = \frac{4\pi^2 h c N_F^2 \text{SNR}^* v}{\eta \lambda^2 \theta_R^2 \theta P_L} \left( 1 + \sqrt{1 + \frac{\pi \lambda^3 \sigma P_L \theta_R^2 N_F \eta}{2 h c \theta^3 v \text{SNR}^*}} \right) \quad (3-35)$$

and

$$j_o^* = \frac{2\pi^2 h c N_F^2 e p f^* v}{\eta \lambda^2 \theta_R^2 \theta P_L} \quad (3-36)$$

$F(i_o^*)$  was evaluated numerically with a computer.  $N(i > y)$  was obtained by computing on both  $dN/dr$  (Fig. 14) and  $i(180^\circ)$ , where numerical values for the latter were obtained from Appendix II of Ref. 15. Figure 13 contains the results of the analysis (Eqs. (3-32) and (3-33)) in a generalized manner where  $N/v$  is plotted against  $\text{SNR}^* v/\eta P_L \theta_R^2$ . Note since  $dF(x)/dx > 0$  then  $\text{SNR}^* v = (epf^*/2)v$  and the abscissa arguments  $\text{SNR}^*$  and  $EPF^*/2$  can be interchanged provided

$$\frac{\text{SNR}^* v}{\eta P_L \theta_R^2} < \frac{\pi \lambda^3 \frac{d\beta}{d\Omega} (180^\circ) N_F}{2 h c \theta^3}$$

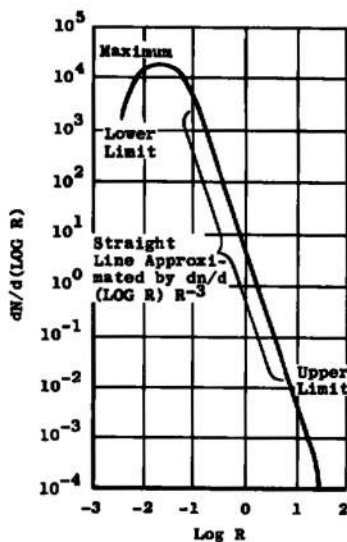


Figure 14. Atmospheric particle size distribution.

## 4.0 BRAGG CELL VECTOR VELOCIMETER DESCRIPTION

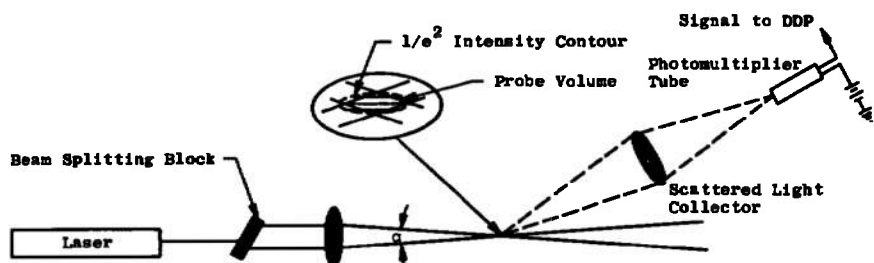
### 4.1 BRAGG CELL VECTOR VELOCIMETER

In this section, a newly developed Bragg cell velocimeter which is self-aligning, can measure two velocity components simultaneously, including directionality, and requires only one detector for both components, is described. In addition the characteristics of a three component measuring system to be applied to velocity measuring systems will also be presented.

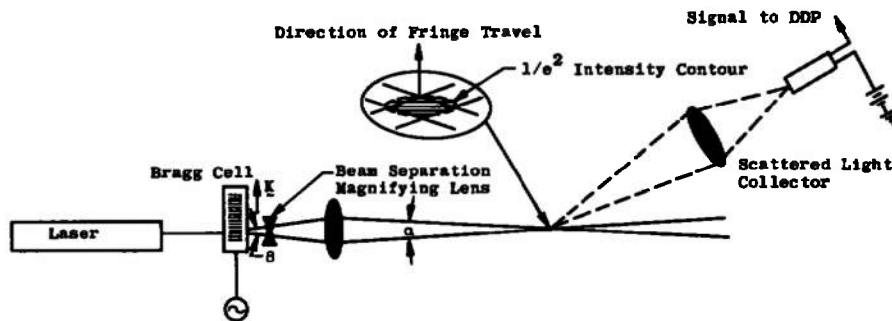
Self-aligning laser velocimeters using the dual-scatter or differential Doppler techniques have been used successfully in a number of applications (Refs. 6, 7, 30, and 31). For measurements of one velocity component, such instruments are simple to construct and straightforward to use. All that is required is a beam splitter of reasonably high quality, a laser, lenses, and a signal detector. A self-aligning velocimeter capable of measuring two velocity components is considerably more difficult to construct, especially since care must be taken to eliminate the so-called cross-talk between components and to match optical paths in the transmitting portion of the instrument to maintain a high signal-to-noise ratio. Furthermore, some complex means such as polarization separation must be used to separate the signals for each velocity component and then direct the respective signals to two different detectors (Ref. 5). Such velocimeter systems suffer from a basic drawback—the velocity signal for each component has a 180-deg directional ambiguity. This presents no difficulty when the velocity direction is known *a priori*. However, in certain applications, such as atmospheric wind studies or in subsonic wind tunnels, the directional ambiguity severely limits the utility of the instrument. Previous work has shown how the directional ambiguity can be removed through the use of ultrasonic Bragg cells, rotating diffraction gratings, etc., to frequency shift a portion of the transmitted light such that a carrier frequency can be generated for the Doppler signal (Refs. 32 through 35). Frequency shifts about the carrier frequency can then be shown to be related to the direction of the velocity vector. The former LV systems have not been self-aligning and have been used only to measure a single instantaneous velocity component.

A standard dual-scatter optical arrangement is shown in Fig. 15a. The laser beam is split into two collimated beams of equal intensity. A lens brings the beams to a common cross-focus point. In the region of focus, the wavefronts in each beam are planar, and a Huygens diagram of the wavefronts in the focus region will show that interference fringes will be generated which are planes parallel to the bisector of

the angle between the two beams and perpendicular to the plane formed by the two beams. Since a particle alternately crosses bright and dark fringes as it crosses the region of focus, a detector will observe the corresponding variations in light intensity and will generate a Gaussian-modulated sinusoidally varying current of the same frequency as that calculated using a Doppler frequency analysis (this assumes the laser operated in a  $TEM_{00}$  mode). The type of LV system shown in Fig. 15a will henceforth be referred to as a "stationary fringe" LV system to distinguish it from a "moving fringe" LV system which uses a Bragg cell to frequency shift one beam (Refs. 34 and 35) or as a simultaneous beam splitter and frequency shifter (Fig. 15b).



a. Stationary fringe LDV system



b. Moving fringe LDV system

Figure 15 Comparison of self-aligning interferometer block and Bragg cell LDV systems.

#### 4.2 PRINCIPLES OF OPERATION

The diffraction of light by ultrasonic waves is well understood (Ref. 36). In a liquid-filled (or solid state) ultrasonic cell, a quartz crystal oscillating at a predetermined frequency generates a traveling wave (although by changing the cell geometry, a standing wave can also be generated).

Since the wave is a longitudinal oscillation, sinusoidal variations in the index of refraction of the liquid are produced. Hence, the device may be visualized as a phase diffraction grating; for standing waves the diffraction grating is imagined to be stationary, while for traveling waves the grating may be imagined as moving at the speed of sound in the direction of the wave propagation. The diffraction characteristics of the grating are a sensitive function of the orientation of the grating relative to the input illumination (Ref. 36). Only Bragg reflection (ultrasonic wave vector nearly perpendicular to the wave vector of the input light) will be considered. Other diffraction modes, e.g., in the so-called Raman-Nath region (Ref. 36), can be used in self-aligning two-component LV systems, but with considerable difficulty. By carefully adjusting the driving crystal electronics and the cell orientation, the cell may be made to diffract one-half of the input light by the Bragg effect, into a first order "Bragg mode", while the other half of the light passes through the cell unaltered. The angle between the beams,  $\beta$ , satisfies the Bragg equation

$$\sin \beta = \frac{\lambda}{\Lambda} \quad (4-1)$$

where  $\lambda$  is the wavelength of the light and  $\Lambda$  is the wavelength of the ultrasonic wave in the diffracting medium.  $\Lambda$  is given by

$$\Lambda = C/f_m \quad (4-2)$$

where  $C$  is the speed of sound in the diffracting medium and  $f_m$  is the modulation frequency of the cell-driving crystal and, therefore, the frequency of the ultrasonic wave. It is well known (Ref. 36) that, if the diffracted light is shifted in a direction opposite the traveling wave, the frequency of the light is decreased by  $f_m$ , while if the light is shifted in the same direction as the traveling wave, the light frequency is increased by  $f_m$ . The grating model of the ultrasonic Bragg cell fits well with the fringe interpretation of the LV. The fringe spacing,  $\delta$ , for stationary fringe LV systems is given by

$$\delta = \frac{\lambda}{2 \sin (\alpha/2)}$$

$$\delta \approx \frac{\lambda}{\alpha} \quad \alpha \ll 1 \quad (4-3)$$

where  $\alpha$  is the angle between the beams transmitted to the probe volume. In a moving fringe LV system, the Bragg cell can act as the beam splitter. The angle between the beams (Eq. (4-1)) is usually quite small and must be magnified for practical applications. In any case, a lens system images the dispersive origin of the two beams, the image of the origin then forms the probe volume for the moving fringe LV system (Fig. 15b). With recourse to geometrical optics, it is straightforward to show that for a moving fringe LV system

$$\delta = m\Lambda \quad (4-4a)$$

$$\frac{\lambda}{\alpha} = m\Lambda \quad (4-4b)$$

where  $m$  is the magnification of the system. Equations (4-4a) and (4-4b) show that the stationary and moving fringe systems are fully equivalent and that the probe volume in the moving fringe case may be thought of as containing the image of the moving diffraction grating. The movement of the grating image,  $\vec{V}_m$ , is given by

$$\vec{V}_m = \vec{mC} \quad (4-5)$$

where  $\vec{C}$  is the velocity vector of the wave in the Bragg cell. Hence, the observed velocity component,  $\vec{V}_{sc}$ , normal to the fringes, is given by

$$\vec{V}_{sc} = \vec{V}_m \pm \vec{V}_D \quad (4-6)$$

where  $\vec{V}_D$  is the velocity component which would be observed if the fringes were stationary. The (+) sign is used if  $\vec{V}_D$  is in a direction opposite to the travel of the grating image, while the (-) sign is used if  $\vec{V}_D$  is in the same direction of travel as the image. Transformation of Eq. (4-6) into one specifying only the frequency is accomplished by

$$\vec{V}_{sc} = \delta f_{sc} \quad (a) \quad (4-7a)$$

$$\vec{V}_m = \delta f_o \quad (b) \quad (4-7b)$$

$$\vec{V}_D = \delta f_D \quad (c) \quad (4-7c)$$

which are forms of the usual equations used for determining velocity components from an LV signal. Using Eqs. (4-7a), (b), and (c) in Eq. (4-6) one obtains

$$f_{sc} = f_m \pm f_D \quad (4-8)$$

Equation (4-8) shows the well-known result that the "Doppler" signal is centered about a carrier frequency  $f_m$  and that the value of this frequency can be used to remove the directional ambiguity (Refs. 32 through 36).

#### 4.3 TWO-DIMENSIONAL BRAGG CELL

The primary difficulty in using Bragg cells (Ref. 32) in a two-component dual-scatter LV system is that considerable effort must be expended to properly align the system. The light input into a focusing lens from the cells must be parallel or the respective components will focus at different points. This could lead to considerable errors in attempting to resolve the measured velocity components into a two-dimensional velocity vector. The optics required for maintaining parallel inputs into the transmitting lens is cumbersome, and it is tedious to align with sufficient accuracy for a coincident focus. These difficulties have been circumvented with the development of a two-dimensional Bragg cell (TDBC). The device is shown schematically in Fig. 16. The cell consists of two legs. At the base of each leg is an X-cut quartz transducer. The transducer consists of a quartz disc, a mounting structure for the quartz disc, and impedance matching electronics.

The X-cut quartz has polished faces and a sputtered metallic coating on each face. When an alternating voltage is applied across the disc, compressive and tensile stresses are produced in the crystal. Thus, the transducer vibrates like a piston, radiating longitudinal waves into the medium. For maximum amplitude of vibration of the quartz disc, the electrical driving frequency and mechanical vibrating frequency must be matched. Accounting for edge effects, the thickness of the quartz disc should be (in cm)  $t = 2.87 \times 10^5/f$  (Ref. 38) where  $f$  is the electrical driving frequency.

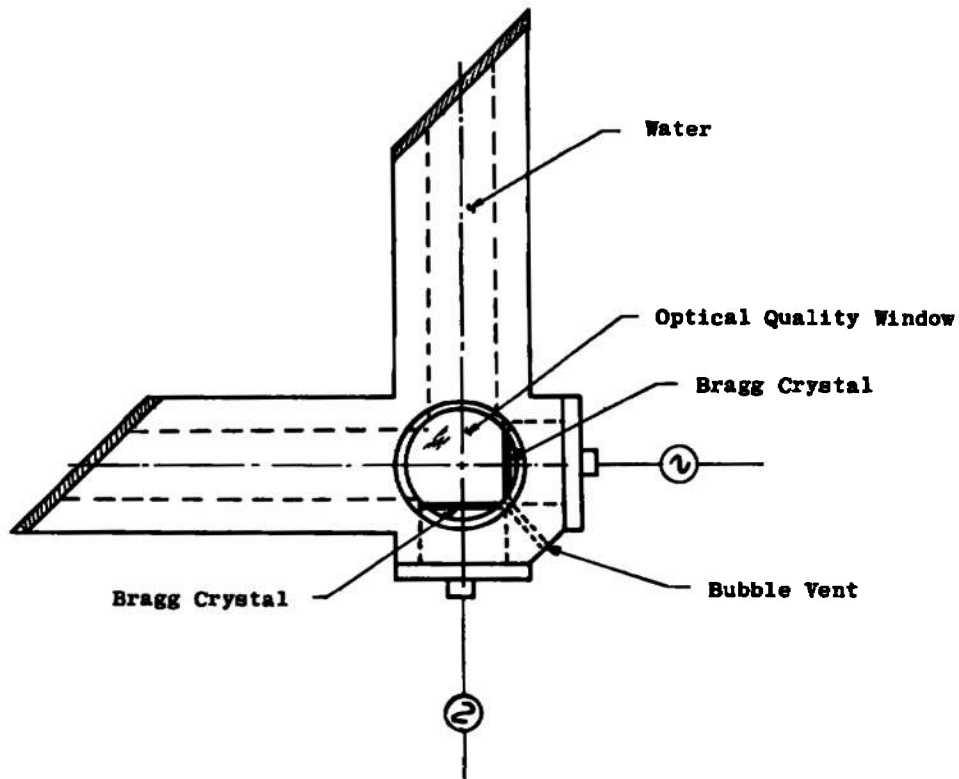


**Figure 16. Schematic of a two-dimensional Bragg cell.**

Since the natural frequency is inversely proportional to the disc thickness, at high frequencies, the disc is thin and brittle. A 10-MHz fundamental frequency is about the limit that can be achieved in most practical cases. However, crystal operation up to 500 MHz can be achieved by operating the crystal at one of its odd overtones. Only odd overtone operation is possible because of the piezo-electric effect. Since ultrasonic frequencies of 15 and 25 MHz were desired in the ultrasonic modulator for reasons that will be discussed later, third overtone operation of a 5-MHz fundamental crystal and an 8.33-MHz fundamental crystal were chosen. The amount of deformation of the expanding and contracting crystal is very small. For longitudinal deformation in quartz,

$$\delta = 2.3 \times 10^{-10} \text{ V(cm)}$$

where  $\delta$  is the deformation of the crystal thickness and  $V$  is the potential difference across the disc (Ref. 38). In a typical ultrasonic modulator, application of  $V = 10$  volts results in a deformation of only  $2.3 \times 10^{-9}$  cm.

The transducer consists of a hollow cylinder with the quartz disc mounted at one end. A flange with electrical feedthrough is attached to the other end of the cylinder so that the seal between the transducer and the water cell is watertight.

The disc transducer radiates into the liquid on one surface and into the air inside the hollow cylinder on the other surface. Because the acoustic resistance for water is much greater than that for air, total reflection occurs at the quartz-air interface. Also, since the boundary is a soft boundary (pressure release boundary), the phase of the acoustic pressure will be reversed, at reflection, and the reflected wave will arrive at the quartz-liquid interface in phase with the acoustic radiation into the liquid. The mode of operation is referred to as air-backed or half-wave resonance and is more efficient than other mounting schemes.

Because electrical energy must be transferred to the crystal, consideration must be given to electrically matching the 50-ohm transmission line to the quartz transducer. This is best done by measuring the equivalent transducer impedance at the driving frequency while the transducer is loaded with the water column in the cell. For this application, the 15-MHz transducer had a  $246 - \cancel{88}^\circ$  ohm impedance and the 25-MHz transducer had a  $94 - \cancel{80}^\circ$  ohm impedance. These were matched to the 50-ohm transmission line by line -Q, L pad, impedance matching circuits.

The water cell is constructed so that the water columns for the transducers are perpendicular and intersect near the transducers. The end of each column opposite the transducer is sealed so that the traveling wave is not reflected back onto itself. This prevents a standing wave from forming. Since the compressive waves are rapidly damped and absorbed in liquids, standing wave formation is not a problem if the liquid column is sufficiently long. It was found that a 10-cm water cell is sufficient to assure a traveling wave in the region near the transducers.

The absorption of the ultrasonic wave (amplitude) in the liquid is given by the standard exponential decay equation where the absorption coefficient for water in the frequency range of interest (15 to 25 MHz) is  $X = 5 \times 10^{-16} f^2$  neper / cm (Ref. 39). Thus, at a frequency of 15 MHz the ultrasonic intensity is down by  $e^{-2}$  after propagating 3.2 cm in water. The less viscous the liquid, the greater the absorption of the acoustic wave. For example, the  $e^{-2}$  propagation distances in methyl alcohol at 15 and 25 MHz is 1.5/cm and 0.5/cm, respectively.

Heat is created as the ultrasonic wave is absorbed due to viscous forces. As the temperature of the liquid medium increases, the velocity of the acoustic wave varies. In all liquids except water the velocity decreases as temperature increases. In water, however, the acoustic velocity increases with increasing temperature and reaches a maximum at about 80°C. The acoustic velocity in water is  $1.43 \times 10^3$  meters/sec at 17°C and increases about 250 cm/sec/°C (Ref. 38). Thus, the small velocity increases due to increasing temperature can be ignored and the water temperature does not have to be monitored. However, laser beam distortion problems can arise due to the thermal gradients; therefore the power input to the cell should be minimized. The minimum power requirements are discussed in detail in Appendix B.

The acoustic wave is also attenuated due to scattering by particles in the water. If the particle is much smaller in diameter than the acoustic wavelength,  $\Lambda$ , then the loss is proportional to  $(1/\Lambda)^4$ . This is the well-known Rayleigh scattering criteria. When the particle size approaches the acoustic wavelength, a complicated process similar to Mie scattering in optics occurs. Finally, when the particles are extremely large, the reflected energy is proportional to the particle diameter squared and is independent of acoustic wavelength. Specular reflection then takes place. The liquid medium used in the ultrasonic modulator should be completely deionized to prevent losses and interferences by scattering. Although not a problem at the acoustic pressure required for ultrasonic modulator operation, deionization also decreases the possibility of cavitation which would cause severe scattering losses and liquid perturbation. For this application, an excellent grade of distilled, deionized water was chosen for the acoustic medium.

The Bragg cell can be used both as a beam splitter and as a frequency shifter. From the previous discussion, the device may be imagined as two superimposed, linearly independent, diffraction gratings. Hence, for the configuration shown in Fig. 16, light from the TDBC appears to disperse from a common origin. This eliminates any possibility of focusing errors for the respective components.

It is convenient for the detection and separation of the respective velocity components to drive the crystal oscillators in the TDBC at two different frequencies. This allows both components of velocity to be detected by a single detector thereby simplifying the optics required for collecting the scattered light. When the TDBC is properly adjusted, the cell produces four equally intense beams—three diffracted beams and the original input beam. Details of the analysis are included as

Appendix A. Since the Bragg cells are linearly independent, the diffracted beams may be independently upshifted or downshifted in frequency. Figure 17 indicates the possible frequency combinations for the four beams which may be chosen. The respective Bragg orders are shown in parentheses with the horizontal value shown first below the dot representing the diffracted beam. The frequency of the diffracted beam is shown above the dot. The set of vortices for each rectangle represents a possible set of beams which may be selected for transmission. The interference fringes generated by any two beams are perpendicular to the line connecting the reference frequency of the two dots. The direction of the fringe travel is specified by the ultrasonic wave vector,  $K(i)$ . The relative lengths of the sides of the rectangles are determined by the ratio of frequencies of the driving crystals. For example, if the driving frequencies are identical, the rectangular array of beams reduces to the special case of a square. It is interesting to observe in this case that stationary interference fringes can be generated by sets of diagonal beams, e.g.,  $(-1, 1)$  and  $(0, 0)$ , when the two driving crystals are driven electronically using a common oscillator reference for the power amplifiers. Examination of Fig. 17 shows that, for any four-beam set chosen, two sets of beams contribute interference fringes for any one component. For example, in the beam set  $(0, 0)$ ,  $(-1, 0)$ ,  $(-1, 1)$ , and  $(0, 1)$ , beams  $(-1, 1)$ ,  $(-1, 0)$  and  $(0, 1)$ ,  $(0, 0)$  generate interference fringes and both measure the same velocity component and move at the same rate,  $f_m^{(2)}$ . Similarly, interference fringes from beams  $(-1, 1)$ ,  $(0, 1)$  and  $(-1, 0)$ ,  $(0, 0)$  both measure the same velocity component (that perpendicular to the other beam set) and move at the same rate,  $f_m^{(1)}$ . Furthermore, interference fringes are generated by beams across the diagonals of the rectangle which move at rates which are either sums or differences of  $f_m^{(1)}$  and  $f_m^{(2)}$  (the so-called "cross-talk" components). These components present no problem per se since they can be eliminated or separated, electronically, along with the orthogonal components. However, to make the system more efficient, i.e., to increase the laser power available for each orthogonal velocity component, the cross-talk can be eliminated using polarization rotators on three of the beams prior to entering the transmitting lens.

Several practical advantages in using the TDBC in a LV system are evident. One may immediately observe that, since all four beams appear to originate from a common source, the system is automatically self-aligning, i.e., the transmitted beams will have a common focus without further beam adjustment. Furthermore, since the respective beam path length differences are negligible, the fringe contrast at focus will

be high, thereby eliminating the need to path compensate the beams prior to transmission and focus.

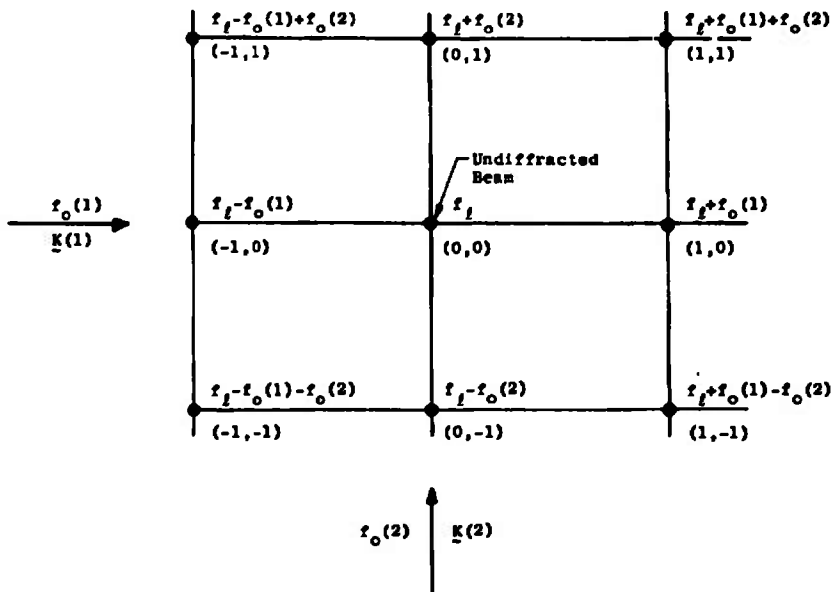


Figure 17. Diagram of possible beam and frequency combinations using a two-dimensional Bragg cell.

Compared to stationary fringe LV systems, the TDBC system can give an increased number of cycles of information in the Doppler signal. This increase has significant ramifications in the choice of the type of signal-processing electronics to be used in a particular application (Ref. 40). An estimate of the maximum number of cycles of information one may expect to observe can be made as follows. Assume that a scatter center with velocity  $V_{sc}$  traverses the probe volume with a trajectory which is normal to the fringe planes and passes through the geometric center of the beam cross point (the condition for the maximum number of cycles of information). The signal observed in real time will have a pulse duration time,  $\tau$ , which will be assumed to be the scatter center time of flight between the  $1/e^2$  intensity points in the probe volume. The number of cycles of information in the detected signal,  $N$ , is then given by

$$N = \tau f_{sc} \quad (4-9)$$

It should be noted that  $f_{sc}$  as given by Eq. (4-8) will not necessarily be the frequency of the signal available to the information processor (Ref. 34). For example, experimentally, a more convenient frequency range could be selected by heterodyning the detected signal current with

that of a local oscillator in the signal conditioning electronics (Ref. 41). However, to compare the number of cycles of information for the moving fringe system with that of the stationary fringe system, it will be assumed that  $f_{sc}$  is given by Eq. (4-8).  $\tau$  is the same for both the moving and stationary fringe systems. Therefore,  $\tau$  may be written as

$$\tau = \frac{N_s \delta}{f_D} \quad (4-10)$$

where  $N_s$  is the number of stationary fringes within the  $1/e^2$  points of the fringe intensity distribution. Using Eqs. (4-7c), (4-8), (4-9) and (4-10), the number of cycles of information observed from the moving fringe system relative to that for the stationary fringe system is

$$\frac{N}{N_s} = \left[ \frac{f_m}{f_D} \pm 1 \right] \quad (4-11)$$

Thus, by always choosing  $f_m \gg f_D$ , a considerable increase in the number of cycles available for the signal processor can be obtained.

One advantage in using a two-frequency TDBC is that the respective, velocity component, frequencies are centered about the Bragg cell modulation frequencies. This allows a multiplicity of components to be detected by a single photodetector and separated electronically, rather than optically, after detection (Refs. 41 and 42). This characteristic of the TDBC simplifies the optics design of an LV system.

A schematic of the type of TDBC velocimeter system investigated for the trailing vortex experiment is shown in Fig. 18. Light from a laser operating in a  $TEM_{00q}$  mode is beam split and frequency shifted by the TDBC. Not shown in Fig. 18, but usually used, is a set of lenses to magnify the relative separation of the beams in order that the probe volume generated by the transmitting lens be made small. Polarization rotation plates are used to increase the laser power available in the orthogonal fringe set and eliminate "cross-talk". Light scattered from the probe volume is collected with a lens system and focused on a photomultiplier tube. The signal is then processed through a series of low-pass frequency filters to separate the carrier frequencies for the respective velocity components (Ref. 41). These signals are in turn heterodyned into a frequency range suitable for analysis using previously developed Doppler Data Processing (DDP) electronics which were originally designed to process signals from a

stationary fringe LV system (Ref. 41). The DDP determines the period of the signal which is displayed or stored on magnetic tape for computation of the velocity components. Details of the processing system used in the experiment are presented in a later section.

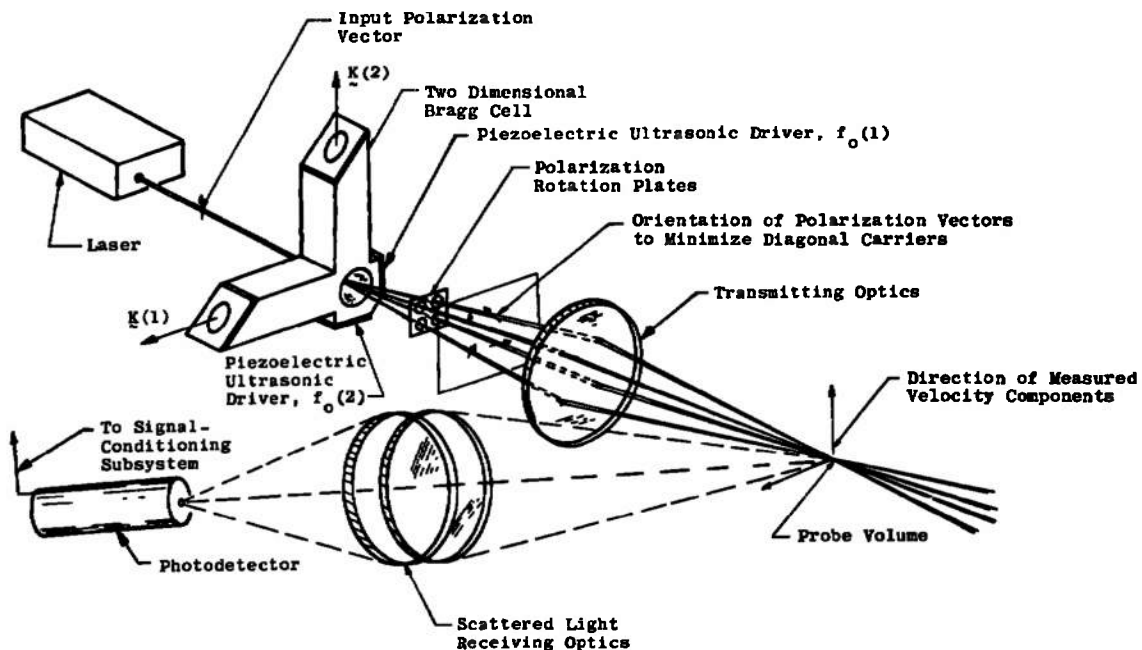


Figure 18. Schematic of an LV system using a two-dimensional Bragg cell.

#### 4.4 THREE-COMPONENT LASER VECTOR VELOCIMETER

There are two major techniques that are being evaluated for use as a three-component dual-scatter system. The second technique utilizes a two-component dual-scatter system for both the vertical and horizontal velocity components. The third velocity component, parallel to the transmitting beam, would be a local oscillator system. The latter system would be, essentially, a three-dimensional orthogonal system. The three-component dual-scatter system comprises two orthogonal components, whereas the third component would be either an x-z or y-z component depending upon the geometric orientation of the optical system.

##### 4.4.1 All Dual-Scatter System

In the proposed all dual-scatter concept, Bragg cells would be incorporated so as to acquire not only directionality but also the magnitude

of the velocity simultaneously. The two cases are schematically illustrated in Figs. 19 and 20. Figure 19 is the three-component all dual-scatter system. In Fig. 19, an argon laser is used for the source and transmits multi-color light through the two-dimensional Bragg cell. From the two-dimensional Bragg cell a color separator reflects the 4880 $\text{\AA}$  line, frequency modulated, light beam to a front surface mirror. The 5145 $\text{\AA}$  line continues from the Bragg cell, which is also modulated at two frequencies similar to those of the 4880 $\text{\AA}$  line and is transmitted through an expansion collimation lens combination into the focal lens. Prior to entrance into the focal lens, one of the four beams, generally the upper right beam, will be removed from the system to reduce the probability of cross-talk among the components. The three beams are then focused to a focal point in space. The 4880 $\text{\AA}$  beams are also directed through an expansion-collimation lens system. In the latter case two beams may be removed, if it is desired, by means of a reflecting front-surface mirror, as schematically illustrated in Fig. 19. The two beams then traverse the focal lens and are brought to the common focal point with the 5145 $\text{\AA}$  lines. Three different sets of fringes are formed and a particle traversing the focal volume scatters light which is collected by the collecting lens collimation combination shown between the two sets of transmitting lens subsystems. The scattered radiation, comprising both 4880 $\text{\AA}$  and 5145 $\text{\AA}$  lines, impinges upon a color separator where the 4880 $\text{\AA}$  line is reflected to a mirror and then through an aperture-lens combination into the photomultiplier tube. The 5145 $\text{\AA}$  line passes through the color separating lens and is collected on its photomultiplier tube and lens-aperture combination. The 5145 $\text{\AA}$  line contains two components of velocity information, whereas the 4880 $\text{\AA}$  line contains a y-z or an x-z velocity combination. In this manner, all three components are simultaneously detected and processed by means of an electronics subsystem comprising frequency separators, translators, and data processing system.

There are some fundamental problems that arise in the use of the planar (x-z or y-z) component velocity measurements for longe-range operations. Transformations are required to establish a set of planar fringes in space as shown in Appendix A. However, the accuracy of the measurement will be functionally dependent upon the separation between the planar dual-scatter component and those of the orthogonal two-component systems. The greater the separation distance, the greater the improvement in accuracy. Details of the analysis for the transformation are included as Appendix A (Ref. 43) in this report.

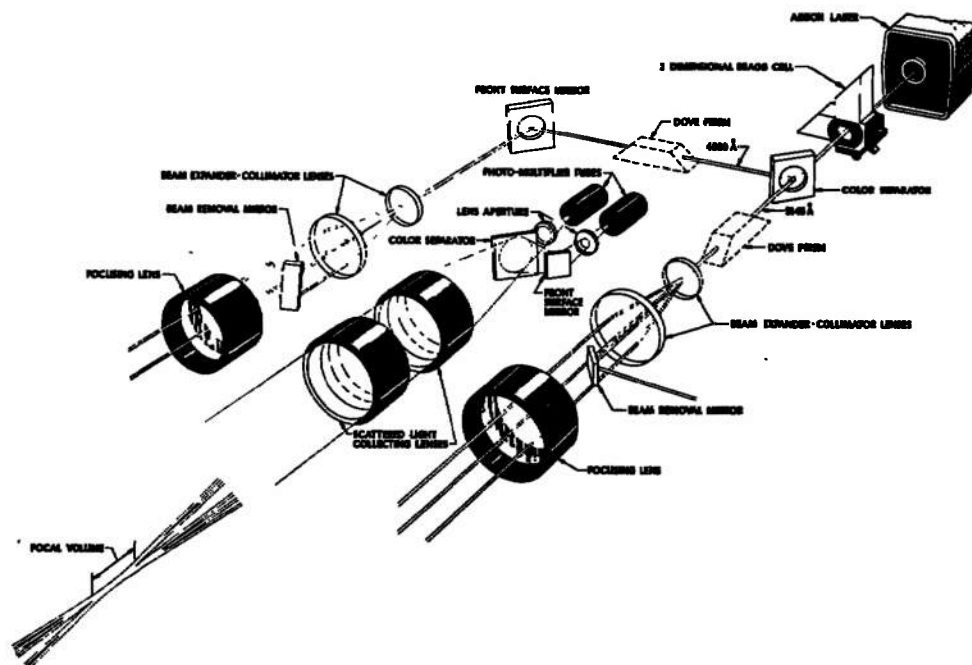


Figure 19. Three-component laser velocimeter.

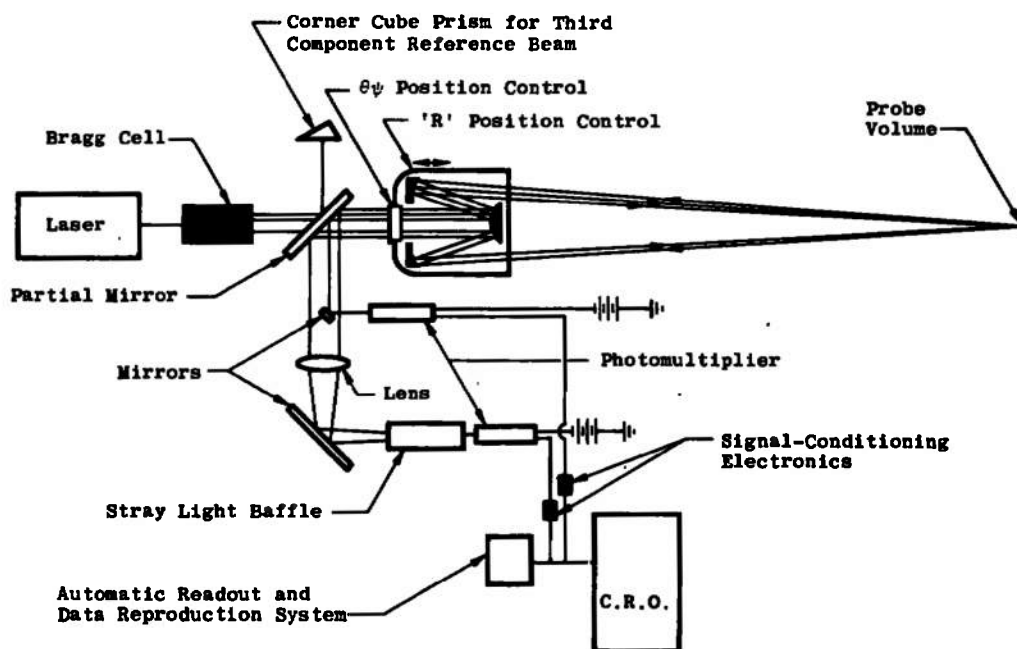


Figure 20. Remote sensing LDV system (two-components, dual scatter, third component reference beam).

#### 4.4.2 Dual-Scatter - Local Oscillator System

In the event artificial seeding of flow is permitted, then the local oscillator system can be used to determine the third velocity component. The dual-scatter-local oscillator system is schematically illustrated in Fig. 20. In this particular case the 4880 Å line will be used for the local oscillator subsystem to yield the third component directly and the two-component, dual-scatter subsystem will determine both the x and y component of velocity. The local oscillator system has been operating in the backscatter mode and can be made operational in the trailing vortex system provided that sufficient seeding is available. This technique is also being operationally checked out at other laboratories (Refs. 36, 44, and 45).

Another technique, which is called an optical diffraction velocimeter or reticle velocimeter (Refs. 46, 47, and 48), has been under investigation to acquire three components of velocity simultaneously. In this particular technique, the optics are extremely simplified in that only one transmitting beam is required for the measurement of the velocity components. The unit can use any type of light source including sunlight; however, in order to adequately filter extraneous light sources a laser beam is preferred. A suitably focused laser beam produces a backscatter pattern on the face of the photomultiplier tube. Placing an optical grating in front of the photocathode and a narrow band interference filter, to exclude extraneous light, produces the necessary means by which velocities can be acquired. The optical grating is a Ronchi ruling which comprises alternate transparent and opaque bars which simulate the fringe characteristics of the dual beam system.

As the particle sweeps through the focused laser beam, the backscatter pattern on the Ronchi ruling is interrupted and a train of pulses similar to those acquired in the dual beam system is generated and these, in turn, can be analyzed to yield velocity information. The technique is quite similar to the fringe type of velocimeter system where the aperture at the detector plays the same role as the fringes generated in the focal volume of a fringe velocimeter. The Ronchi ruling can be such that one of the rulings is thicker than the others in the series, thus directionality can be acquired. By superimposing two different gratings, orthogonal to each other, then two components can be readily resolved. Again, the fundamental problem is concerned with the means of determining directionality of the third component.

As in the dual-scatter system, a fundamental problem exists concerning the directionality of the third component. This is not too critical a problem with regard to the vertical and horizontal components. Several techniques are being pursued to determine the most feasible method for determining the true velocity.

A dish-collector, not having the stringent requirements as the dual-scatter transmit-receive telescope system, could probably be used for collection of light for the third component. The technique is being evaluated in detail for another application. The characteristic of this new technique, including performance and applications for remote sensing, will be published upon completion.

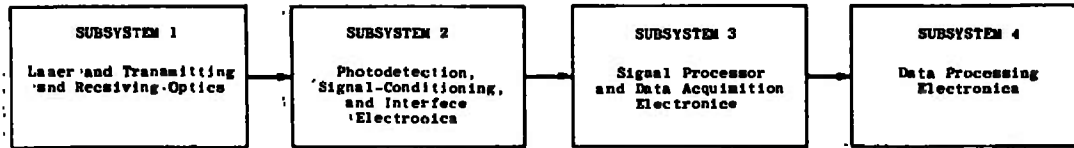
## 5.0 SIGNAL CONDITIONING REQUIREMENTS AND ELECTRONICS

### 5.1 INTRODUCTION

In the previous section, the operation of the newly developed two- and three-dimensional, Bragg cell, laser velocimeter systems were described.

In this section, the signal conditioning requirements for the Bragg cell system will be defined. In addition, the signal-conditioning instrument that has been developed to interface the Bragg cell to the signal processor and the data acquisition system will be described and evaluated.

The newly developed velocimeter system comprises four major subsystems as shown in the functional block diagram in Fig. 21. Subsystems 1, 3, and 4 are presented to define the interface design constraints imposed upon subsystem 2—the signal-conditioning subsystem. Time and frequency domain signal characteristics, essential for the design of the subsystem 2, are analyzed and compared with those of conventional velocimeter systems. The Bragg cell electronics subsystem and velocimeter system evaluation, including accuracy and provision, are discussed. The signal conditioning circuitry is outlined in detail including circuit schematic, fabrication, and packaging. Finally, the directionality capabilities of the Bragg cell vector velocimeter system are evaluated from data acquired both in the laboratory and in field tests.



#### SUBSYSTEM 1 FUNCTIONS

- (1) Provide proper laser power and polarization
- (2) Split input laser beam into four equal power output beams
- (3) Shift the optical frequency of three of the output beams in order to ultimately provide four velocity information carrier signals
- (4) Optionally rotate the polarization of three of the output beams to eliminate two of the four carriers
- (5) Define the probe volume by transmitting and intersecting the four output beams at a common cross and focus point
- (6) Provide scattered laser radiation receiving optics
- (7) Provide receiver aperture and interference filter discrimination against spurious light

#### SUBSYSTEM 2 FUNCTIONS

- (1) Photodetect the scattered laser signal radiation
- (2) Amplify the photodetected signal
- (3) Bandpass filter the signal to separate the carrier-centered velocity information spectra from each other and from wideband noise outside the information bandwidth
- (4) Translate the velocity information spectra to low frequency carriers to accommodate the accuracy specification of Subsystem 3
- (5) Provide selectable cutoff frequency low-pass filters to accommodate the information bandwidth and attenuate noise and spurious signals outside this bandwidth
- (6) Provides above functions for up to three velocity components

#### SUBSYSTEM 3 FUNCTIONS

- (1) Simultaneously accept up to three velocity component signals
- (2) Apply logic decision circuitry to accept valid signals but reject spurious signals
- (3) Determine period of valid signals
- (4) Encode period information and record on paper tape and/or magnetic tape
- (5) Record other experiment variables - time, temperature, position, etc., as required

#### SUBSYSTEM 4 FUNCTIONS

- (1) Convert signal period information to velocity information
- (2) Compute mean velocity, rms deviation, turbulence intensity, etc., as required
- (3) Tabulate and/or plot velocity data

Figure 21. Vector velocity LV subsystem functional block diagram.

## 5.2 BRAGG CELL OPTICS

The principal component of the new technique is the two-dimensional, ultrasonic, Bragg cell system, developed at the AEDC, which inherently contains (1) a self-aligning system, and (2) simultaneous vector velocity measurements for two orthogonal velocity components. A schematic of the optical subsystem is shown in Fig. 18. The incoming laser beam is diffracted by orthogonal ultrasonic traveling waves in the Bragg cell. When properly adjusted, the output of the cell produces four equally intense beams, three diffracted beams, and a portion of the original beam which is undiffracted. These four beams originate from the same region inside the cell, traverse equal optical paths, and are brought to a common focus by the transmitting optics resulting in a self-aligning system. The optical frequency of the diffracted beam can be up-shifted or down-shifted by proper orientation of the Bragg cell with respect to the incoming laser beam. In Fig. 17, the possible four beam combinations that may be selected for transmission are illustrated. The respective Bragg orders are shown in parentheses, with the horizontal value shown first, below the dot, representing a diffracted beam. The optical frequency of the diffracted beam is shown above the dot. Moving interference fringe planes produced in the probe volume by any two beams are perpendicular to the line connecting the two dots representing the two beams. The direction of the fringe travel in the probe volume is the same as that of the ultrasonic wave vector  $K(i)$  for non-inverting transmitting optics, whereas the direction of fringe travel is opposite to  $K(i)$  for inverting transmission optics. Any four-beam set, shown in Fig. 17, can be used to implement the true vector laser velocimeter. For the present analysis, the beam set is assumed to be at  $(0, 0)$ ,  $(1, 0)$ ,  $(1, 1)$  and  $(0, 1)$ .

## 5.3 OPTICAL COMPONENT CONSTRAINTS

As discussed in Section 4.2, the diffraction cell producing the four-beam pattern is operated in the Bragg mode as opposed to the Raman-Nath mode since Bragg mode operation permits concentration of the diffracted light in a single order. Bragg mode operation requires (Ref. 49) that

$$n\lambda = 2\Lambda \sin \phi = 2\Lambda \sin \theta \quad (5-1)$$

and also

$$wf_m^2 = 2\eta v^2 N / n\lambda = 1.2(10^{15}) \quad (5-2)$$

where  $\phi$  and  $\theta$  are the angles of the incident and reflected laser beams with respect to the ultrasonic wavefronts,  $\lambda$  and  $\Lambda$  are the laser light and sound wavelengths respectively,  $n$  is the diffraction order,  $w$  is the diameter of the ultrasonic beam in cm.,  $f_m$  is the ultrasonic frequency in hertz,  $\eta$  is the index of refraction for water,  $v$  is the velocity of sound in water, and  $N$  is the number of ultrasonic wavefronts traversed by a laser light ray in passing through the Bragg cell. For the system shown in Fig. 18,  $n = 1$ ,  $N = 1$ , and  $\lambda = 5145 \text{ \AA} (10^{-4}) \text{ cm.}$

The maximum practical dimension,  $w$ , is dictated by the diameter of the ultrasonic driving device and is 2.54 cm for the piezoelectric quartz crystal driver used in the system described in Fig. 18. This constraint on  $w$  then necessitates the use of an ultrasonic drive frequency,  $f_m$ , in the range of tens of megahertz (Eq. (5-2)). The frequencies that were chosen were (Fig. 17)  $f_m(1) = 25 \text{ MHz}$  and  $f_m(2) = 15 \text{ MHz}$ . The optical spectrum at the output of the Bragg cell is shown in Fig. 22. A more detailed analysis and evaluation is included in Appendix A. Each of the four beams is represented in the frequency domain by a frequency impulse function. The intensities of the four beams can easily be made equal by adjusting the input power to the piezoelectric drivers.

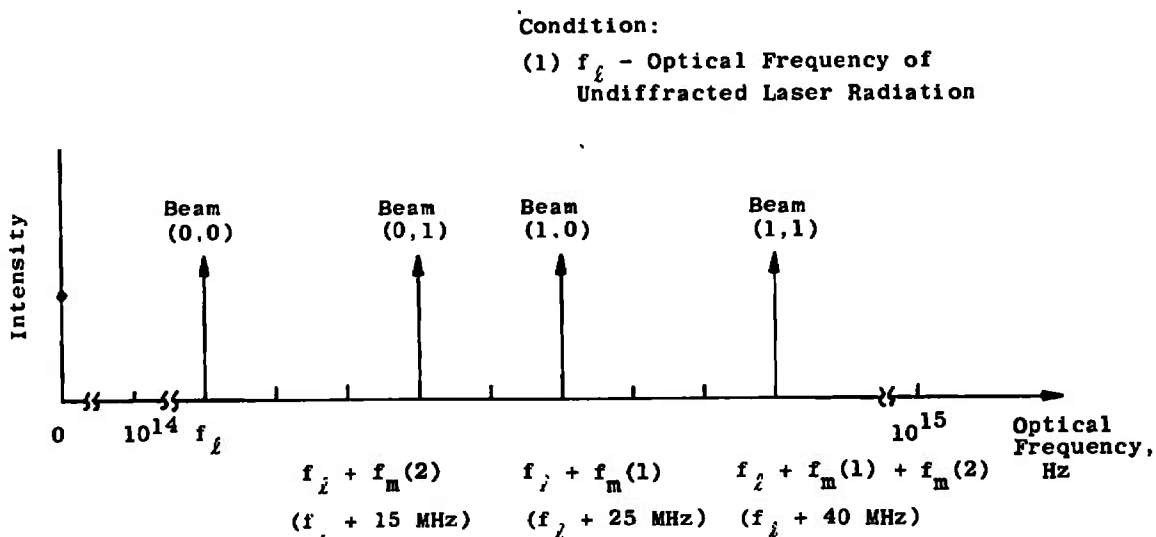


Figure 22. Optical intensity spectrum at the output of the Bragg cell.

The LV system can be successfully operated with or without the polarization rotation plates (Fig. 18). In either case, each set of two

beams with a non-orthogonal polarization relationship will form moving interference fringes in the probe volume. The fringes formed by beam pairs (0, 0) with (1, 0) and by (0, 1) with (1, 1) propagate horizontally across the probe volume at the rate

$$|f_l - [f_l + f_m(1)]| = |f_l + f_m(2) - [f_l + f_m(1) + f_m(2)]| = f_m(1) = 25 \text{ MHz}$$

and are, therefore, used for the horizontal velocity component measurements. By the same considerations, beam pairs (0, 0) with (0, 1) and (1, 0) with (1, 1) produce fringes which travel vertically at the rate  $f_m^{(2)} = 15 \text{ MHz}$ . When the polarization rotation plates are not used, beams (0, 0) and (1, 1) interfere to produce fringes which move diagonally at the rate  $f_m^{(3)} = 40 \text{ MHz}$  and beams (1, 0) and (0, 1) produce fringes which move diagonally at the rate  $f_m^{(4)} = 10 \text{ MHz}$ . The polarization rotation plates produce an orthogonal polarization relationship between the diagonal beams and thereby minimize the diagonal fringes (Ref. 37).

A light scattering particle passing through the probe volume produces a unique signal for each fringe set with frequency,  $f_{SC}$ , given by

$$f_{SC} = f_m \pm f_D \quad (5-3)$$

where  $f_D$  is directly proportional to the velocity magnitude of the particle and is the "Doppler" frequency of the conventional type LV. A motionless scatter particle in the probe volume produces a sinusoidal signal with frequency  $f_{SC} = f_m - f_D$ , while a particle traveling in a direction opposite that of the moving fringes produces a signal with frequency  $f_{SC} = f_m + f_D$ . The photodetected signal spectrum produced by a motionless particle is shown in Fig. 23 which illustrates the velocity component carrier signals when polarization rotators are not used. Use of the polarization rotators eliminates the diagonal velocity component carrier signals at 10 and 40 MHz and thereby eliminates possible interference with the signals centered at 15 and 25 MHz. The diagonal carrier signal amplitudes are half that of either the vertical or horizontal since only two of the four beams are used to form the diagonal fringes, whereas all four beams are used to form the vertical and horizontal fringes.

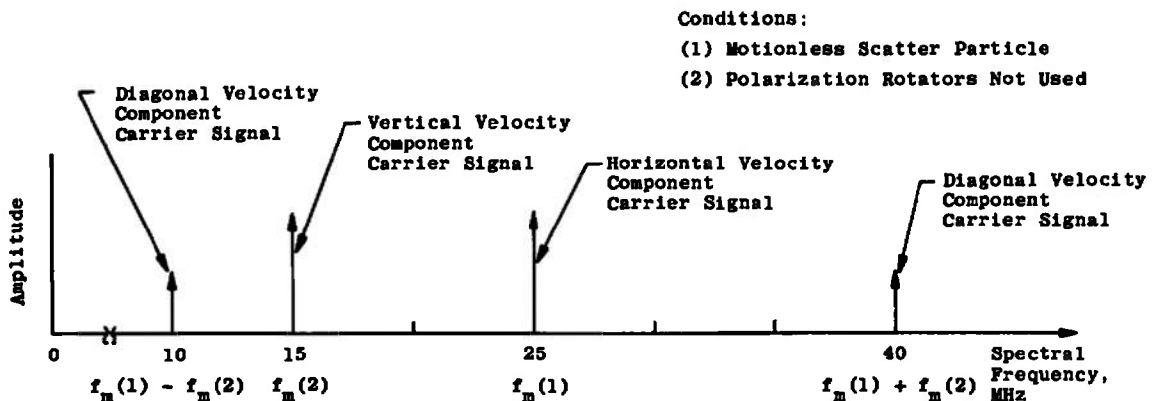


Figure 23. Photodetected signal spectrum for motionless scatter particle illustrating velocity component carrier signals.

#### 5.4 TIME AND FREQUENCY DOMAIN CHARACTERISTICS

The scattered radiation intensity envelope for scatter particle trajectories close to the geometric center of the probe volume is Gaussian for laser operation in the  $TEM_{00}$  mode, the preferred mode for LV applications. The corresponding photodetected time domain signal for a single scatter particle traversing a fringe set for the conventional dual scatter LV is given by

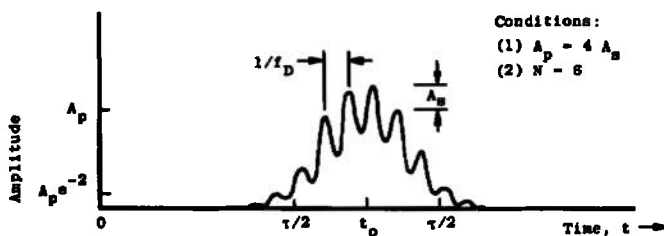
$$X_1(t) = A_p \exp \{-[2\sqrt{2}(t - t_o)/\tau]^2\} + A_s \exp \{-[2\sqrt{2}(t - t_o)/\tau]^2\} \cos 2\pi f_D t \quad (5-4a)$$

while the time domain signal for the same scatter particle and trajectory for a dual-scatter LV with an optical frequency translator is given by

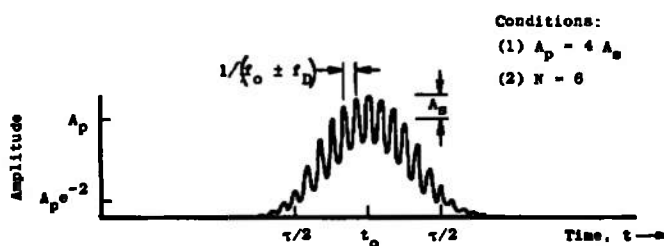
$$X_2(t) = A_p \exp \{-[2\sqrt{2}(t - t_o)/\tau]^2\} + A_s \exp \{-[2\sqrt{2}(t - t_o)/\tau]^2\} \cos 2\pi(f_m \pm f_D)t \quad (5-4b)$$

where  $f_D$  is the "Doppler" frequency,  $f_o$  is the carrier frequency, and  $\tau$  is the time required for the scatter particle to transit the probe volume outer boundaries. This boundary is defined by the surface of that ellipsoid where the laser radiation intensity is  $e^{-2}$  times the maximum intensity near the geometric center of the probe volume (Ref. 5). Equations (5-4a) and (5-4b) are represented in Figs 24a and b respectively. The signals are seen to consist of two distinct summed waveforms, (1) a Gaussian pulse or "pedestal" waveform with peak amplitude  $A_p$  and (2) a Gaussian pulse amplitude modulated sinusoid with peak amplitude  $A_s$ . Note that the signal parameters  $A_p$ ,  $A_s$ ,  $\tau$ , and

$f_D$  are the same for both LV systems provided that the intensity of the laser radiation in the probe volume, probe volume dimensions, and fringe spacings are set up to be identical.



a. Conventional LV system



b. LV system with optical frequency translator

Figure 24. Time domain signals—single scatter particle traversing the probe volume.

The "Doppler" frequency is given (Ref. 5) by

$$f_D = v/d = \frac{2v \sin \theta/2}{\lambda} \quad (5-5)$$

where  $v$  is the magnitude of the scatter particle velocity,  $d$  is the probe volume fringe spacing,  $\theta$  is the angle between the crossed laser beams, and  $\lambda$  is the wavelength of the laser radiation. The parameter  $\tau$  is related to  $f_D$  by

$$\frac{1}{\tau} / f_D = 1/N = \frac{\lambda}{2b_o \tan \theta/2} \quad (5-6)$$

where  $N$  is the number of fringes set up within the probe volume ( $e^{-2}$ ) maximum intensity contour and  $2b_o$  is the Gaussian diffraction limited laser beam diameter in the probe volume.

The signal amplitudes  $A_p$  and  $A_s$  are directly proportional to the peak laser radiation intensity within the probe volume. The ratio  $A_s/A_p$  is related to scatter particle size with respect to the fringe spacing (Ref. 19). In general, large particles produce small  $A_s/A_p$

ratios and vice versa. In wind tunnel LV applications using intrinsic aerosol scatter particles, the  $A_s/A_p$  ratio has been observed to vary from 0 to 0.5.

An important requirement of an LV signal conditioner is to attenuate the pedestal waveform but enhance the sinusoidal waveform. The frequency of the sinusoid contains the velocity information, and the presence of the pedestal waveform interferes with frequency or period information making it difficult to design adequate circuitry. The pedestal waveform can be practically eliminated by utilizing a relatively sophisticated balanced optical photodetector scheme instead of the conventional photo-detector circuitry (Ref. 50). However, simple electronic filters can be used to separate the sinusoid from the pedestal provided that

$$e/2r \ll f_{sc} \quad (5-7a)$$

and

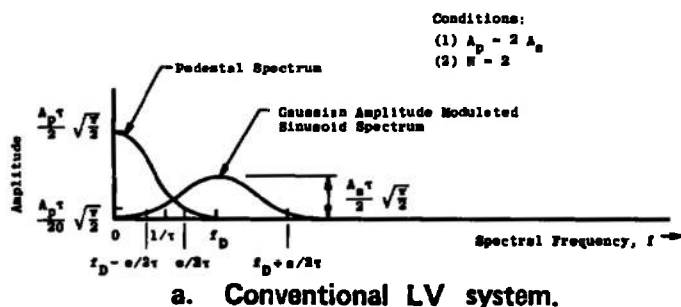
$$2A_s \approx A_p \quad (5-7b)$$

The significance of conditions (Eqs. (5-7a) and (5-7b)) in comparing the conventional LV and the LV with optical frequency translation can be deduced by analyzing the Fourier transforms of Eqs. (5-4a) and (5-4b). Using the frequency translation theorem and the Gaussian function transform pair relationship, the Fourier transforms of Eqs. (5-4a) and (5-4b) are found to be respectively

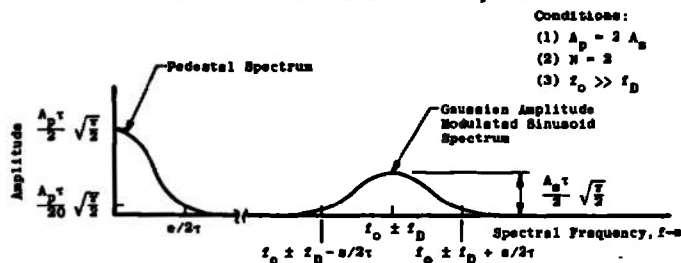
$$X_1(f) = \left(\frac{A_p r}{2}\right) \left(\sqrt{\frac{\pi}{2}}\right) \exp \left\{ -\left[\frac{\pi f r}{2\sqrt{2}}\right]^2 \right\} + \left(\frac{A_s r}{4}\right) \left(\sqrt{\frac{\pi}{2}}\right) \exp \left\{ -\left[\frac{\pi(f + f_m)r}{2\sqrt{2}}\right]^2 \right\} + \left(\frac{A_s r}{4}\right) \left(\sqrt{\frac{\pi}{2}}\right) \exp \left\{ -\left[\frac{\pi(f - f_D)r}{2\sqrt{2}}\right]^2 \right\} \quad (5-8a)$$

$$X_2(f) = \left(\frac{A_p r}{2}\right) \left(\sqrt{\frac{\pi}{2}}\right) \exp \left\{ -\left[\frac{\pi f r}{2\sqrt{2}}\right]^2 \right\} + \left(\frac{A_s r}{4}\right) \left(\sqrt{\frac{\pi}{2}}\right) \exp \left\{ -\left[\frac{\pi(f + f_m \pm f_D)r}{2\sqrt{2}}\right]^2 \right\} + \left(\frac{A_s r}{4}\right) \left(\sqrt{\frac{\pi}{2}}\right) \exp \left\{ -\left[\frac{\pi(f - f_m \pm f_D)r}{2\sqrt{2}}\right]^2 \right\} \quad (5-8b)$$

Equations (5-8a) and (5-8b) are plotted in Figs. 25a and b respectively.\* The sinusoid signal bandwidth (10-percent amplitude points) is  $\epsilon/\tau$ , while the pedestal bandwidth (10 percent) is  $\epsilon/2\tau$  for both the conventional LV and the LV with frequency translator. However, Fig. 25a shows that the conventional LV can violate the inequality set forth in Eq.(5-7a) and produce overlapping spectra. This in turn negates the possibility of using simple filter techniques to separate the sinusoidal signal from the pedestal. For example, Eq. (5-6) shows that  $1/\tau$  becomes a larger percentage of  $f_D$  as  $N$  is reduced so that when  $N = 2$  the  $1/\tau$  point is 0.5  $f_D$  and spectra separation by simple filter techniques is impossible. This particular case is shown in Fig. 25a. Filter techniques are effective for  $N \geq 5$  approximately, except when condition (5-7b) is violated. This condition is violated when scatter particles, large compared to the fringe spacing, pass through the probe volume and produce a significant portion of the pedestal spectra within the sinusoid spectral bandwidth ( $A_p \gg 2A_s$ ).



a. Conventional LV system.



b. LV system with optical frequency translator

Figure 25. Frequency domain signal representation—single scatter particle traversing the probe volume.

Figure 25b shows that the LV with optical frequency translator produces a signal which can always be made to satisfy inequality (Eq. (5-7)) and can be made impervious to conditions in Eq. (5-7b)

\*Only the positive frequency spectrum is shown since the negative frequency spectrum contributes nothing to the explanations.

by choosing  $f_m$ , the Bragg cell driving frequency, high enough to adequately separate the pedestal and sinusoid spectra. The most fundamental form of filter, an RC high pass section, can now be effectively used to separate the spectra.

Two additional advantages, from a signal-conditioning point of view, are gained by using an LV with optical frequency translator. A minimum number of eight sinusoid cycles per scatter particle transit is required for operation of subsystem 3 shown in Fig. 21. Particle trajectories nearly parallel to one of the orthogonal LV measurement axis can produce fewer than eight cycles in the second velocity component signal. This is a brief statement of the "flow direction dead zone" problem discussed in some detail in Ref. 39. The net effective number of sinusoid cycles per particle transit of the moving fringe system,  $N_e$ , produced by the Bragg cell LV relative to the stationary fringe LV system,  $N_s$ , is in the most general case given by

$$\frac{N_e}{N_s} = \left( \frac{f_{IF}}{f_D} \pm 1 \right) = \left( \frac{f_m - f_{ho}}{f_D} \pm 1 \right) \quad (5-9)$$

where  $f_{IF}$  is the output frequency generated by an electronic frequency heterodyne device given the input signal frequency  $f_m \pm f_D$ , then the effective number of signal cycles of the moving fringe system,  $N_e$ , can be made much greater than  $N_s$ , and the requirements of subsystem 3 can be satisfied. The second additional advantage is that  $N_s$  can be made as small as unity, using optical techniques, in a Bragg cell LV system in order to concentrate the available laser power into as few fringes as possible which in turn produces maximum scattered intensity per scatter-particle fringe crossing.

## 5.5 INFORMATION SPECTRA

Figure 23 shows the spectra of the four carrier signals produced by a motionless scatter particle or scattering surface inserted into the probe volume, whereas each particle of a dynamic particle field will produce a signal spectrum as shown in Fig. 25b. Those particles with the maximum velocity deviation from the mean value of the particle field velocity distribution will dictate the bandwidth,  $W$ , of the velocity information spectrum. It follows from this discussion and Fig. 25b that the velocity information bandwidth is given by

$$W = 2 \left| f_{D \text{ mean}} - \left( f_{D \text{ max}} + \frac{e}{2\tau} \right) \right| \quad (5-10)$$

where  $f_D$  mean is the mean "Doppler" frequency produced by the dynamic particle field and  $f_D$  max is the maximum "Doppler" frequency produced by this same field. This bandwidth,  $W$ , is the bandwidth which must be accommodated by the signal-conditioning instrument, subsystem 2.

Information spectra for the special case of an isotropic velocity distribution with zero mean is depicted in Fig. 26. Bandpass filter techniques are used to separate the four information spectra prior to further signal conditioning and data acquisition operations. Simple filters can be used as long as adjacent information spectra are sufficiently attenuated. Overlapping information spectra represent the ultimate limits on component velocity magnitudes which can be accommodated regardless of the type filter used. Figure 26 shows that the first limit is reached when the spectrum centered at 10 MHz overlaps the one centered at 15 MHz. However, this problem can be resolved by use of the polarization rotators (Fig. 18) to minimize the spectra centered at 10 and 40 MHz. The next limit is reached when the spectra centered at 15 and 25 MHz begin to overlap. At this point, accommodation of still greater velocities obviously requires that the velocity information spectra be further separated by using a greater frequency interval between the carriers.

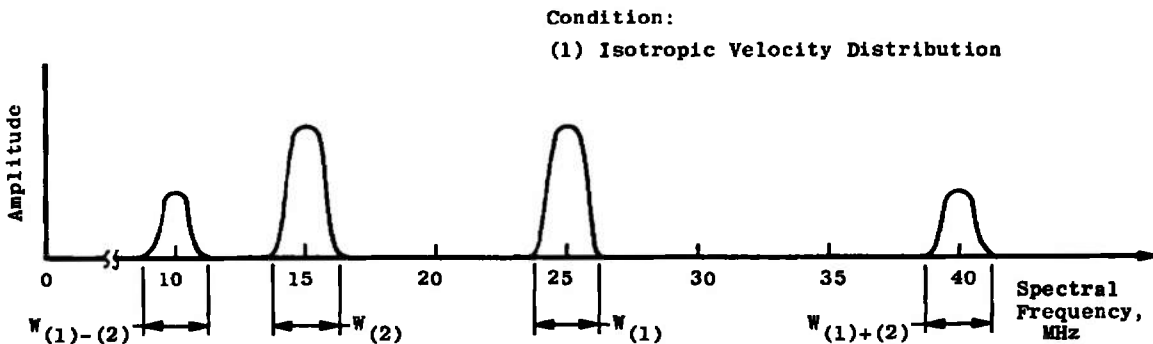


Figure 26. Velocity information spectra illustrating relationship of adjacent spectra.

## 5.6 INFORMATION SPECTRUM TRANSLATION

Equation (5-2), given the practical constraint that  $w \leq 2.54$  cm, shows that proper Bragg cell operation requires a drive frequency (carrier frequency),  $f_m$ , in the order of  $10^7$  Hz. On the other hand, low velocity LV applications such as atmospheric wind velocity measurements may produce signal frequency deviations about the carrier in the  $10^3$ -Hz range. This situation requires a signal frequency (or period) measurement accuracy in the order of 0.01 percent. Subsystem 3, shown in Fig. 21, has a nominal accuracy specification of

one percent of its full-scale setting which is not compatible with the 0.01-percent requirement. Subsystem 2 solves this problem, utilizing electronic heterodyning techniques, by translating the velocity information spectra to a lower carrier frequency. Translation by two decades in frequency results in a carrier of order  $10^5$  with the same  $10^3$ -Hz deviation. The measurement accuracy requirement is now one percent which is compatible with the subsystem 3 specifications.

## 5.7 SYSTEM ACCURACY AND PRECISION

The accuracy and precision to be discussed are definitely not intended to be taken as limits, rather they are specifications attainable by calibration procedures and equipment available at the AEDC.

### 5.7.1 Subsystem 1

The accuracy and precision specifications for subsystem 1 (Figs. 21 and 18) are determined solely by the accuracy and precision associated with the measurements of  $\theta$  (Eq. (5-5)), the orientation of the probe volume fringe planes with respect to the velocity measurement plane and the frequencies of the Bragg cell drivers. The velocity measurement plane is defined by the two orthogonal velocity components to be measured. For a horizontal wind tunnel, this plane is usually defined by the local vertical and the longitudinal axis of the tunnel.

The angle  $\theta$  can be calculated from  $\theta/2 = \tan^{-1} d/2L$  where  $L$  is the distance from the center of the probe volume to a reference plane situated to intercept the beams diverging from the probe volume and  $d$  is the distance between two applicable beams at the surface of this plane. The reference plane is oriented parallel to the velocity measurement plane.

The orientation of the probe volume fringes with respect to the measurement plane can be determined by observing the angular orientations of the lines defined by appropriate pairs of beams projected onto the reference plane. For example, the pair of beams which is used for the vertical velocity component measurement should define a vertical line on the reference plane, whereas the pair of beams used for the horizontal velocity component measurement should define a horizontal line on the reference plane.

Conventional optical tooling techniques utilizing horizontal and vertical tooling bars and optical transits can be exploited to determine  $L$  and  $d$  with a systematic error no greater than one part in  $10^4$ . However, the random error of these measurements can be as much as one part in  $10^3$  because of the uncertainties in the location of the geometric center of the probe volume and the centers of the beams intersecting the reference plane. Given the accuracy specification 0.01 percent and the precision specification 0.1 percent in determining  $L$  and  $d$ , the angle  $\theta$ , and therefore, the relation of  $v$  to  $f_D$  should be determinable to within 0.2 percent.

Optical tooling techniques can also be used to angularly align the probe volume fringes with respect to the reference plane with a systematic error or resolution specification better than one part in  $10^5$ . Again, however, the uncertainties in locating the centers of the beams projected upon the reference plane can produce random errors as great as one part in  $10^4$ .

The Bragg cell drive signal frequency can be determined with a systematic error no greater than one part in  $10^8$  and a random error less than five parts in  $10^9$  by using an electronic frequency counter. The counter can be calibrated to within three parts in  $10^{10}$  by a calibration system referenced to an NBS frequency standard signal transmitted by radio station WWVB. The counter time base aging rate specification is less than five parts in  $10^{10}$  per 24 hours and its short term (1-sec average) fractional frequency deviation, or random error, is less than five parts in  $10^{11}$ . These specifications show that the introduction of the Bragg cell into an otherwise conventional LV system does not degrade the overall system accuracy and precision.

The accuracy and precision specifications for measurement of the probe volume fringe orientations and the Bragg cell driver frequencies are at least an order of magnitude greater than those for determination of the angle  $\theta$ . Therefore, considering only subsystem 1, the velocity component vectors should be within 0.2 percent of the actual values.

### 5.7.2 Subsystem 2

The primary functions of subsystem 2 are listed in Fig. 21. The photodetection, amplification, and bandpass and lowpass filtering operations do not alter the velocity information signal frequencies, and therefore, do not degrade the LV system accuracy and precision. On the other hand, the spectrum translation function requires that the entire

velocity information spectrum be translated to a lower frequency carrier. This function can be executed with high accuracy and precision by using a crystal-controlled oscillator in the heterodyning process. An ultimate systematic error of one part in  $10^8$  and a random error less than five parts in  $10^9$  can be achieved by monitoring the crystal oscillator with the same type frequency counter used to monitor the Bragg cell driver frequency. Therefore, when properly utilized, subsystem 2 should introduce no negligible error into the overall LV system.

### 5.7.3 Subsystem 3

The primary functions of subsystem 3 are listed in Fig. 21. This subsystem is termed the Doppler Data Processor (DDP). Given a signal of high signal-to-noise (S/N) ratio ( $S/N > 20$  db) such as provided by a laboratory oscillator, the DDP will determine the signal period with a combined systematic and random error less than two parts in  $10^3$  (Ref. 42). However, dependent upon a complexity of factors including available laser power, scatter particle size, scattering angle, background light level, etc., an LV system may produce signals with S/N ratios much less than 20 db. Error logic circuitry in the DDP is relied upon to limit the combined systematic and random error to less than two parts in  $10^2$  by sensing and rejecting low S/N ratio signals (Ref. 42).

### 5.7.4 Subsystem 4

Subsystem 4 is a digital computer accepting up to seven significant digit data. Therefore, barring programming errors, this subsystem will not degrade the overall LV system accuracy and precision specifications.

### 5.7.5 Overall System Accuracy and Precision

Given high S/N ratio signals the combined systematic and random error of the overall LV system is dictated by subsystems 1 and 3 and can be as low as 0.4 percent.

As with any opto-electronic measurement device, low S/N ratio conditions ultimately limit the usefulness of the entire LV system. The DDP is presently adjusted to limit the overall LV system systematic and random error to less than two parts in  $10^2$  for poor S/N ratio signals. Data from poor S/N ratio signals are rejected by the DDP and are not recorded.

## 5.8 SIGNAL-CONDITIONING INSTRUMENT

A block diagram of subsystem 2 is shown in Fig. 27, and a photograph is shown in Fig. 28. This subsystem consists of three major assemblies: (1) a photodetector assembly, (2) a set of nine crystal-controlled, heterodyne or spectrum translation oscillators, and (3) an instrument termed a Signal Separator and Spectrum Translator (SSST).

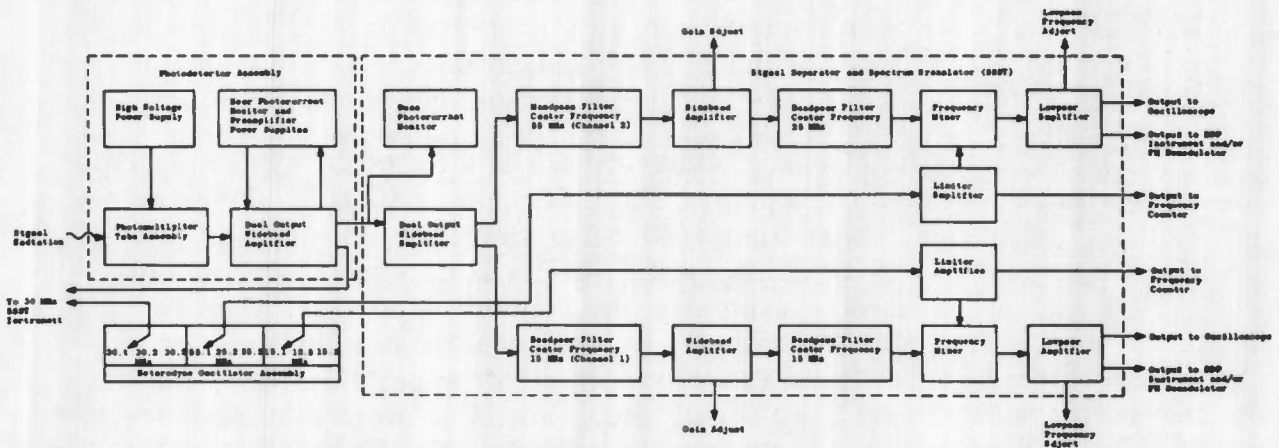


Figure 27. Block diagram of the photodetection, signal conditioning, and interface electronics, subsystem 2.

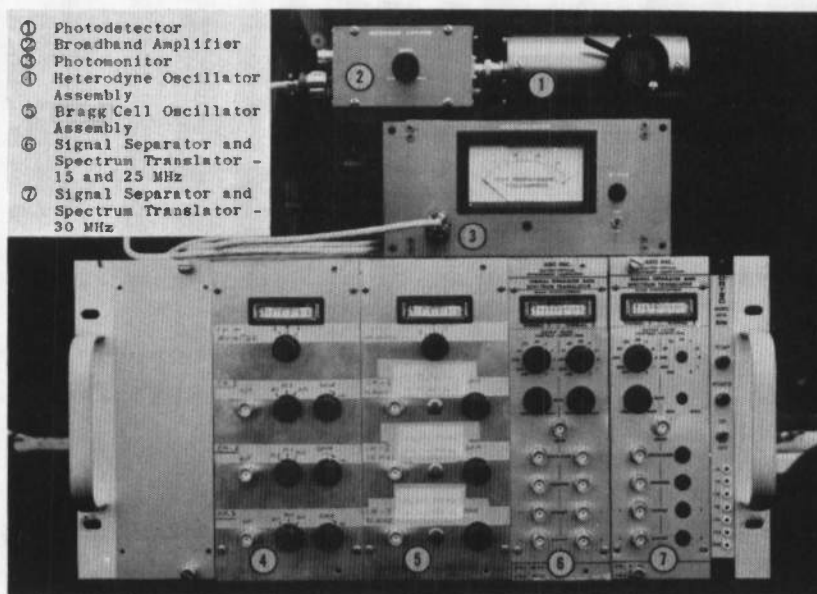


Figure 28. Photodetection, signal conditioning, and interface electronics, subsystem 2.

### 5.8.1 Photodetector Assembly

The photodetector assembly consists of a 931A photomultiplier (PM) tube, its enclosure and high voltage power supply, a dual output pre-amplifier and an instrument to monitor the mean photocurrent level. The PM tube enclosure provides electrostatic, magnetic and electromagnetic shielding, contains an optical interference filter to attenuate spurious radiation and an iris diaphragm type of variable aperture.

The preamplifier provides three primary functions: (1) connects directly to the PM tube enclosure to minimize the parasitic capacitance loading the PM tube anode and thereby maximize frequency response, (2) boosts the signal level before introduction onto a transmission line where noise pickup might occur, and (3) provides required frequency response bandwidth and output impedance to drive a 50-ohm transmission line (Ref. 6). These functions can be provided by any one of several integrated circuit video amplifiers. We presently use the UA733 amplifier which provides a gain variation from 10 to 100 and a usable bandwidth beyond 100 MHz.

Because of spectra separation (Fig. 25b) the "Doppler" signal is passed, but the pedestal waveform is effectively eliminated by a simple RC highpass section coupling the photodetector signal into the preamplifier input. The preamplifier passband is presently required to pass 15-, and 25-MHz carriers and are being used to convey two orthogonal components of velocity information. The 30-MHz carrier is used to convey a third nonorthogonal component of velocity information in a two-laser frequency technique described in the previous section and in Ref. 41. Each SSST instrument is designed to accommodate two different carrier signals. One of the preamplifier outputs provides the input signal for the 15- and 25-MHz SSST instrument while the other output drives the 30-MHz SSST instrument. The following descriptions of the SSST instrument will be solely in terms of the 15- and 25-MHz unit since the operating principles of the 30-MHz unit are identical. The crystal-controlled oscillators used in subsystem 2 are commercially available and will not be discussed further.

### 5.8.2 Signal Separator and Spectrum Translator

A schematic diagram of the 15- and 25- MHz SSST instrument is shown in Fig. 29. The operational amplifier circuit (IC1-MC1539L) is used to monitor the mean photocurrent level when the separate photocurrent monitoring device (Figs. 28 and 29) is not used. The separate device is not required when the photodetected signals are large amplitude.

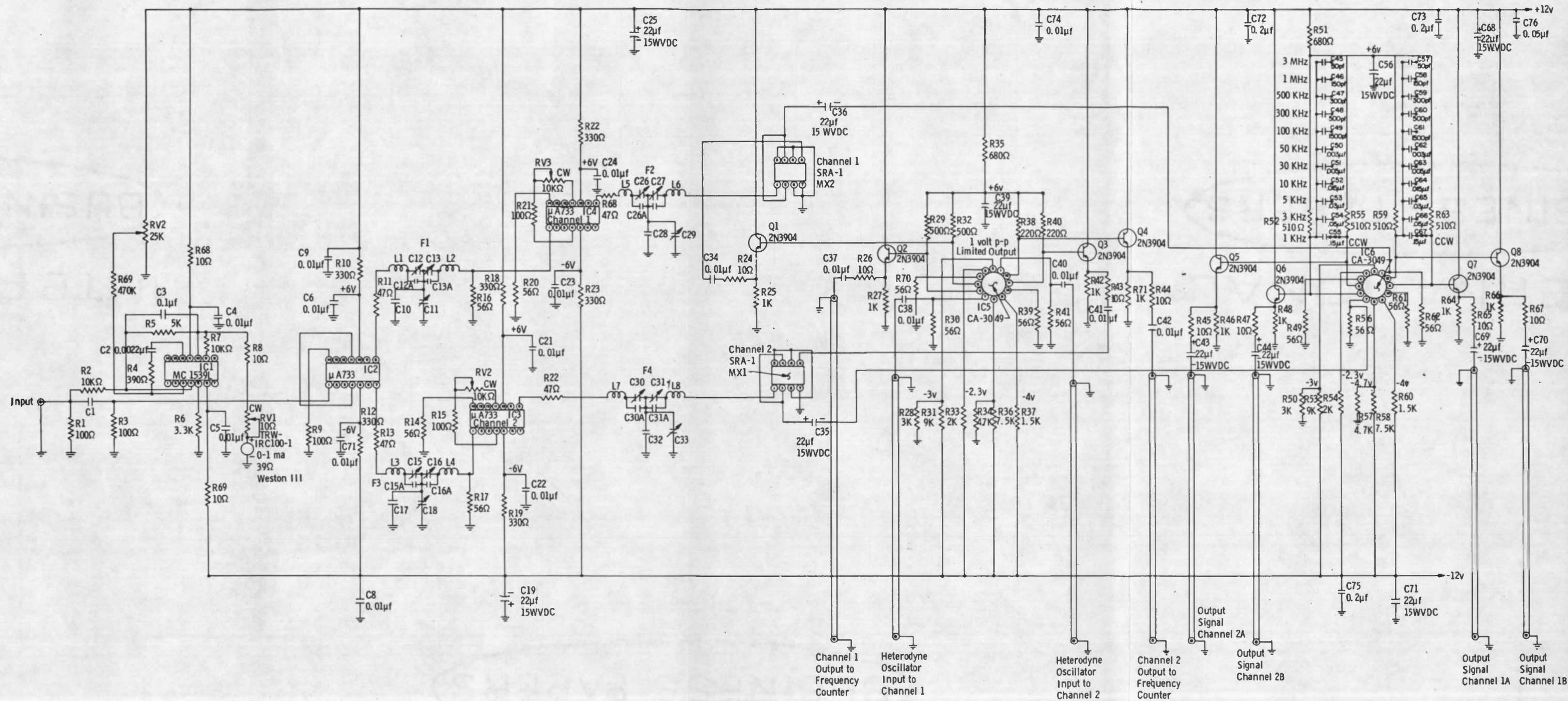


Figure 29. Schematic diagram of signal separator and spectrum translator.

The integrated circuit, IC2, is a UA733 video amplifier with a nominal gain of 100. The output at pin 8 is used for the 15-MHz channel while the output at pin 7 is used for the 25-MHz channel. Separation of the velocity information spectra (Fig. 29) is accomplished by the T-section filters F1, F2, F3, and F4. Filters F1 and F2 are tuned to pass 25 MHz. All filters have a nominal 1-MHz, 3-db bandwidth and 50-ohm input and output impedances. Since the 15- and 25-MHz channels are identical except for the filters, the remaining discussion is in terms of the 15-MHz channel only.

A nominal gain variation of 10 to 50 is provided by IC4. The output of filter F2 drives the 50-ohm signal port of mixer MX2 while the local oscillator port is driven by emitter follower Q1. The emitter follower in turn is driven by a limiter amplifier implemented by the CA3049 integrated circuit, IC5. The limiting level is set at 1.2 volts peak-to-peak which is optimum for operation of the mixer. A second limiter output drives emitter follower Q2 which in turn provides a front panel output for precise counter monitoring of the heterodyne oscillator frequency. The input signal to the limiter amplifier is furnished by one of the three external heterodyne oscillators at 15.1, 15.2, or 15.5 MHz. The velocity information signals at the input to the mixer are centered at 15 MHz, whereas these same signals are centered at 100, 200, or 500 KHz at the mixer output depending upon which heterodyne oscillator is selected.

The output of mixer MX2 is coupled to the input of a lowpass amplifier implemented by the CA3049 integrated circuit IC6. The lowpass cutoff frequency is selected by an eleven-position switch and can be varied in a 1, 3, 5 sequence from 1 KHz to 3 MHz (Fig. 29). The lowpass frequency is always set as low as possible in order to reject noise outside the frequency bandwidth of interest. The lowpass cutoff frequency,  $f_2$ , is given by  $f_2 = (2\pi RC)^{-1}$ , where R is the value of resistor R59 or R63 and C is the value of the capacitor selected by the eleven-position switch. The differential outputs of the lowpass amplifier drive emitter followers Q7 and Q8 which in turn furnish two front panel outputs. One of these outputs normally serves as input to an oscilloscope, while the second output provides the input signal to the DDP instrument.

### 5.8.3 Fabrication and Packaging

Figure 30 shows the front panel and the printed circuit board for the SSST instrument. Ground plane printed circuit board construction was exploited to minimize interaction of the 15- and 25-MHz channels.

Standard Nuclear Instrument Module (NIM) enclosures were used to package the SSST instruments as well as the Bragg cell reference oscillators and the heterodyne oscillators. These NIM modules plug into a NIM bin power supply assembly which fits a standard 19-in. rack. The NIM module-NIM bin approach has been found to be quite practical and economical for prototype or finished instrument packaging. A photographic film positive of the front panel lettering is attached to the prototype SSST to label the switch and connector functions.

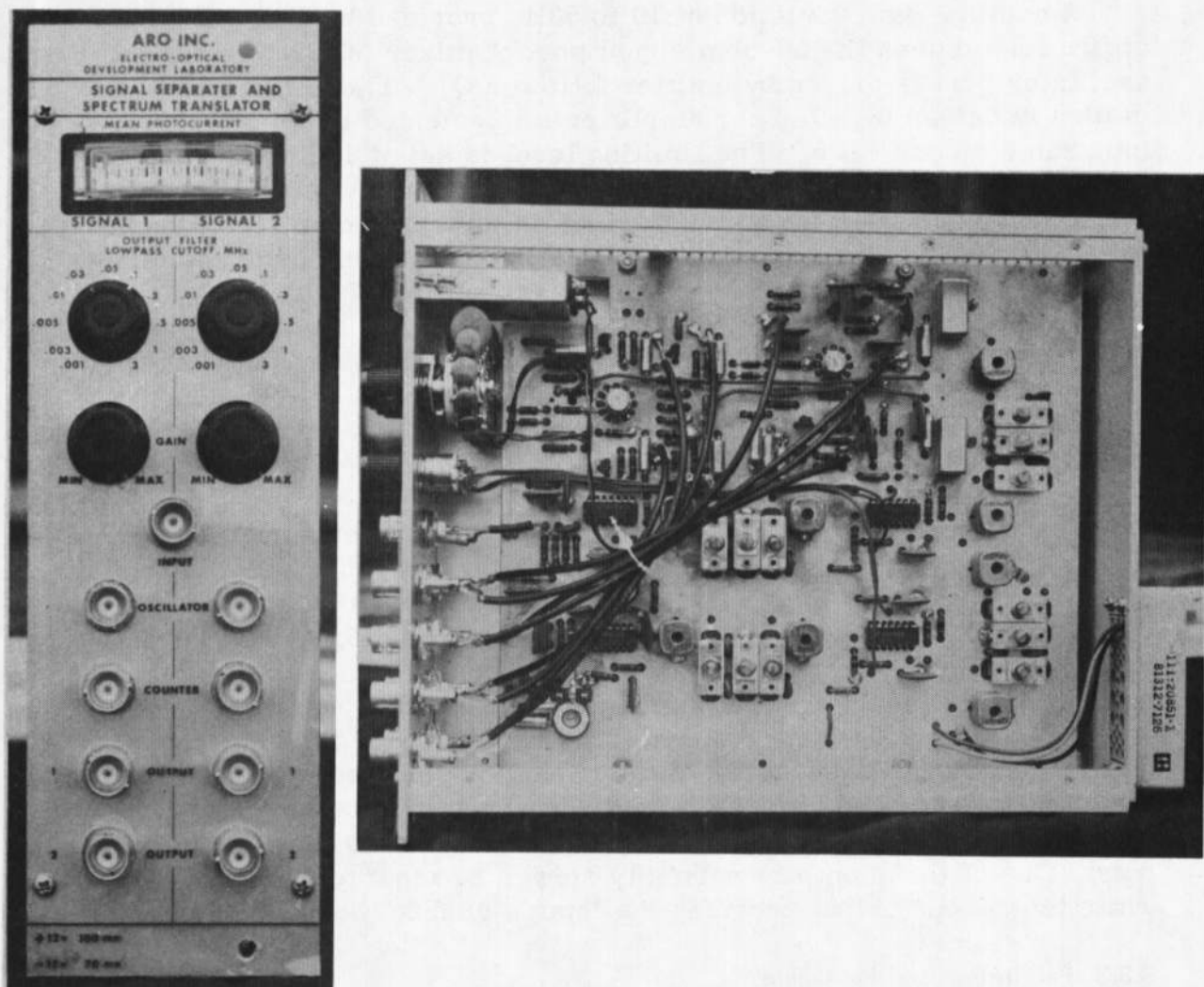


Figure 30. Fabrication details of signal separator and spectrum translator.

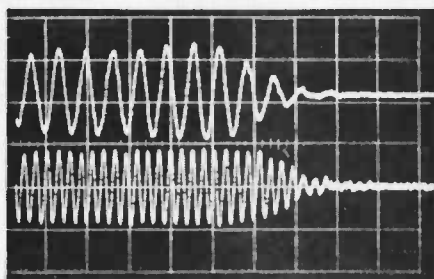
## 5.9 SYSTEM EVALUATION

Two initial evaluations of the system concept shown in Fig. 21 were conducted: (1) a laboratory test using an LV system suitable for wind tunnel applications, and (2) a field test using an atmospheric research-type LV system. The primary purpose of the two tests was to demonstrate that the new LV systems could simultaneously resolve the 180-deg directional problem for two orthogonal velocity components. Precise determination of the velocity component magnitudes were not considered for these evaluations. Therefore, the angles in Eq. (5-5) and the orientation of the two orthogonal measurement axes with respect to the local vertical were not precisely determined.

### 5.9.1 Laboratory Test

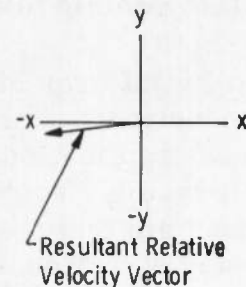
The LV system was set up in the forward scatter configuration (Fig. 15b) with the geometric centerline of the transmitting and receiving optics intercepting at a 12-deg angle at the probe volume. The transmitting optics focal length was 1.1 meters and the receiving optics were located 0.7 meters from the probe volume. The laser power was 10 mw at 4880 Å. The system was set up to simultaneously detect the vertical and horizontal velocity components of intrinsic room aerosols. The translated carrier frequency was set at 20 MHz for both output signals and the SSST lowpass amplifier cutoff frequencies were set at 30 KHz.

The air velocity vector was expected to fluctuate somewhat randomly in direction and magnitude and this was verified by observation of oscilloscope displays of the two output signals from the SSST. Figure 31 is typical of the signals produced by the LV system and the directional capabilities are clearly demonstrated. Figure 31a shows that the vertical component is in the -x direction, whereas Fig. 31b shows that the vertical component is still in the -y direction, but the horizontal component has shifted to the +x direction. The quality of the oscilloscope displays was somewhat degraded by the effects of the chopper technique used to simultaneously display the two waveforms, but the actual S/N ratios were compatible with the DDP instrument.

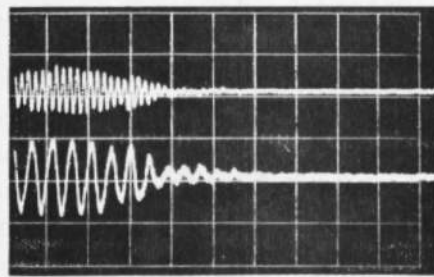


Horizontal, 7.6 kHz

Vertical, 18.3 kHz

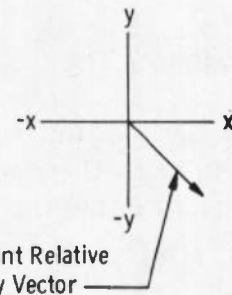


a. Vertical component in  $-y$  direction, horizontal component in  $-x$  direction.



Horizontal, 30 kHz

Vertical, 10.6 kHz



Conditions:

- (1) Translated Carrier Frequency - 20 kHz Both Traces
- (2) Vertical Scale - 0.5 v/div.
- (3) Horizontal Scale - 0.2 msec/div.
- (4) Intrinsic Room Aerosol Scattering Particles

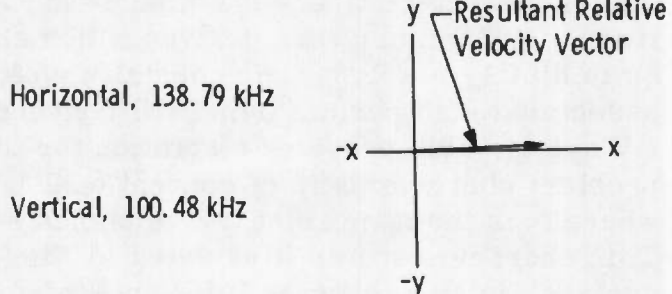
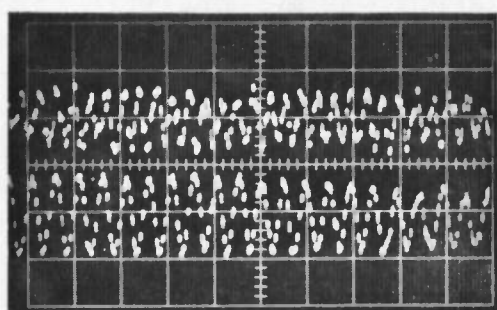
b. Vertical component in  $-y$  direction, horizontal component in  $+x$  direction

Figure 31. Directionality evaluation - laboratory test.

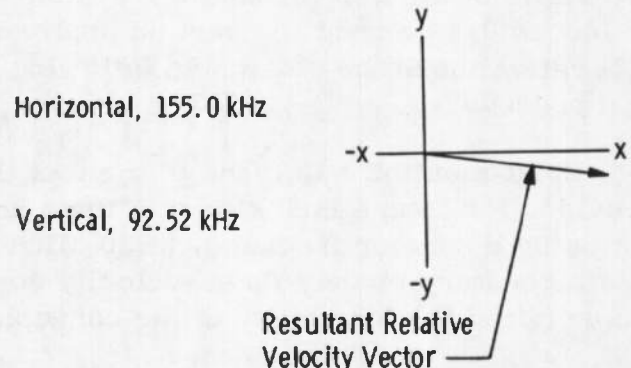
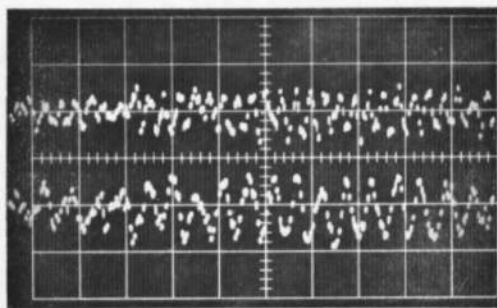
### 5.9.2 Field Test

The atmospheric research LV consisted of a 20-cm-diam telescope for the transmitter system and a 25.4-cm-diam telescope for the receiver. The receiver was mounted directly above the transmitter and operated in a backscatter mode. The laser power was set so that 2 watts were contained in the 5145 $\text{\AA}$  line. The system was set up to simultaneously detect the vertical and horizontal velocity components of atmospheric impurities at a range of 3.5 meters at an elevation of 2.2 meters above the ground. The translated carrier frequency was set at 100 KHz for both output signals, and the SSST lowpass amplifier cut-off frequencies were set at 100 KHz.

Figure 32 is typical of the signal waveforms recorded during the field test. The fluctuation of the vertical velocity component from the  $+y$  direction in Fig. 32a to the  $-y$  direction in Fig. 32b clearly demonstrates the directional measurement capabilities of the LV system. The quality of the oscilloscope displays shown in Fig. 32 was again degraded by the chopper technique used to simultaneously display the two waveforms. The signal frequencies in Fig. 32 are closer to the 1-MHz oscilloscope chopper frequency than are the signal frequencies in Fig. 31. Therefore, the waveform presentation in Fig. 32 is poorer than that in Fig. 31. However, the actual S/N ratios of the signals typified by Fig. 32 were compatible with the DDP instrument.



a. Fluctuation of the vertical velocity component from the  $+y$  direction.



**Conditions:**

- (1) Translated Carrier Frequency - 100 kHz Both Traces
- (2) Vertical Scale - 0.5 v/div.
- (3) Horizontal Scale - 20  $\mu$  sec/div.
- (4) Intrinsic Atmospheric Scattering Particles

b. Fluctuation of the vertical velocity component to the  $-y$  direction

Figure 32. Directionality Evaluation - Field Test.

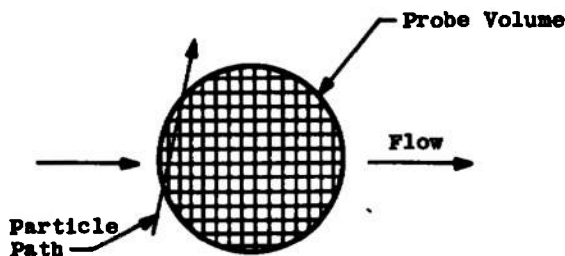
### 5.9.3 Summary

A newly developed LV system which simultaneously measures the magnitude and direction of two orthogonal velocity components of light scattering particles has been summarily described. Functional descriptions of the four major subsystems comprising the LV system were provided. Only subsystem 2, the photodetection and signal-conditioning subsystem, has been described in detail since the other subsystems are treated in other literature. The signal-conditioning problem was defined in terms of the basic physical aspects of laser velocimetry, subsystem-dictated constraints, and accuracy and precision characteristics. The signal characteristics in the time and frequency domains were derived which showed that the new system quite simply resolves the pedestal waveform suppression problem associated with certain (small N) conventional LV systems. The new LV system also provides a solution for the "flow direction dead zone" problem characteristic of conventional LV systems with small N, where N is the number of fringe planes set up in the probe volume. This characteristic is illustrated in Fig. 33. Conventional LV systems are restricted to a lower limit on N of 5 to 10, whereas the new system can function with an N value as low as N = 1. Detailed circuit schematic diagrams of the signal-conditioning subsystem were provided. Data from initial evaluation tests were presented to show that the system is capable of resolving the 180-deg directional ambiguity problem characteristic of all conventional LV systems. An overall system error as low as 0.4 percent for certain applications (those producing a high S/N ratio) should be obtainable following careful alignment and calibration procedures.

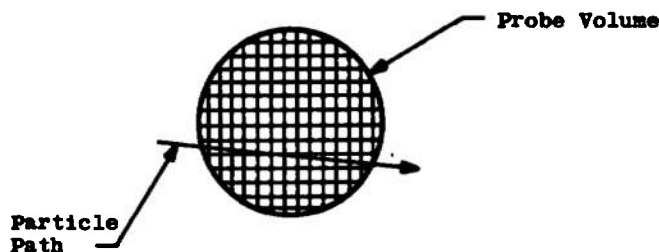
Brief mention was made of the fact that initial LV design criteria provided for future inclusion of a third nonorthogonal velocity component using a carrier frequency at 30 MHz. Recent successful operation of a laboratory model, three-velocity component, Bragg cell-type LV has verified the feasibility of the concept.

The atmospheric wind velocity measurement applications to date have produced relatively low data rate frequency burst samples (<10 samples per second) of velocity. This rate is well below the Nyquist rate required for comprehensive fluid flow turbulence measurements. However, recent experiments with a relatively high power, 10-w, argon laser and an LV optical subsystem defining a quite small probe volume shows promise of producing at least an order of magnitude increase in the data sample rate when using atmospheric aerosols

as scatter particles. The addition of artificial scatter particles, however undesirable, can produce essentially continuous wave signals. To take full advantage of the increased velocity sample rate, FM demodulator and spectrum analysis instrumentation is being assembled to operate in parallel with the DDP instrument.



a. Insufficient number of cycles, no data for the horizontal component



b. Insufficient number of cycles, no data for the vertical component

Figure 33. Stationary fringe dead zone.

## 6.0 LV DATA PROCESSOR SYSTEM

With the use of the dual-scatter LV, producing a fringe set in the focal volume, the velocity of the inherent atmospheric impurities (Refs. 7, 8, 41, and 42) traversing normal to the fringe plane can be determined from the fringe spacing and the average time interval required to traverse them. A data processor has been developed to condition the signals from a detector to provide the velocity data. This section is concerned with a description of these newly developed LV data processors.

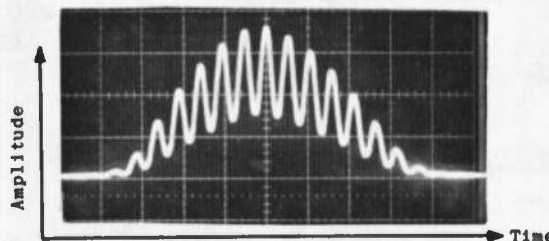
## 6.1 SELECTIVE CAPTURE OF FREQUENCY BURST SIGNAL DATA

The data processor samples eight periods of the limited duration "burst" waveform and digitizes the resultant time interval via period counter techniques. Time intervals as short as 80 nsec may be quantized at rates of 50,000 samples/sec. In the presence of poor signal-to-noise ratios, the burst waveform sustains severe waveform aberrations which make it difficult to extract the desired time period data. The signal suffers both pulse dropouts and pulse additions due to noise mixing with signal information (Ref. 42).

The new processor employs high-speed digital computing circuitry to test the data pulse train for periodicity; it compares the time intervals of both four and five data pulses (or periods of oscillation) to the time interval of eight data pulses. The eight-pulse interval has been chosen to accommodate the short duration signal type dictated by the velocimeter optics design. A two-stage time interval comparison is necessary when sampling low S/N data since pulse dropouts and pulse additions can, in certain combinations, produce pulse trains that appear to be periodic when using only one comparator. With a single test comparison, low S/N data produces alias or false readings that differ widely from the true readings. For example, the 4/8 time interval test typically permits alias readings that are  $\pm 25$ ,  $\pm 50$ ,  $\pm 75$ , and  $\pm 100$  percent of the true reading; the 5/8 test typically permits alias readings of  $\pm 37.5$ ,  $-18$ ,  $-31$ ,  $+62.5$ , and  $+100$  percent. With a dual time interval test, simultaneous, erroneous readings seldom occur thereby permitting dual test rejection to be highly successful.

The advantages of a data acquisition system employing a dual time interval test are clearly indicated in Figs. 34 through 37. Figure 34a illustrates an ideal frequency burst waveform. Figures 34b and c show a progressively increasing noise content added to the burst signal waveform. Figure 34d illustrates the data pulse train output from the zero crossing detector when the signal such as shown in Fig. 34c is processed. It is this type of signal, with dropout and added noise pulses, from which the printed data distributions shown in Figs. 35 and 36 were obtained. In each test a series of 1,000 samples was presented simultaneously to three processors equipped with different error-detecting logic. One processor was equipped with a 4/8 time interval comparator (TIC) test only, a second processor was equipped with a 5/8 TIC test only, and a third processor was equipped with a dual two-step (4/8 and 5/8) TIC test. The resultant distribution of true and false (or alias) readings obtained from the three processors are plotted in Fig. 36. It

can be seen that the dual comparator system shows a marked improvement in the resulting data quality by rejecting most of the false or alias readings. Figure 37 illustrates the performance of the dual comparator processor as a function of signal-to-noise ratio. The processor data capture ratio begins to drop sharply for S/N ratio values below 0.20; however, the quality of the printed data remains high for capture ratios below one percent of total sample cycles.



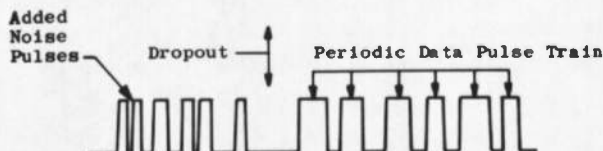
a. Ideal velocimeter frequency burst waveform



b. Noise superimposed on waveform



c. Large amplitude noise on burst signal



d. Zero crossing detector output for low S/N signal

Figure 34. Velocimeter wave forms.

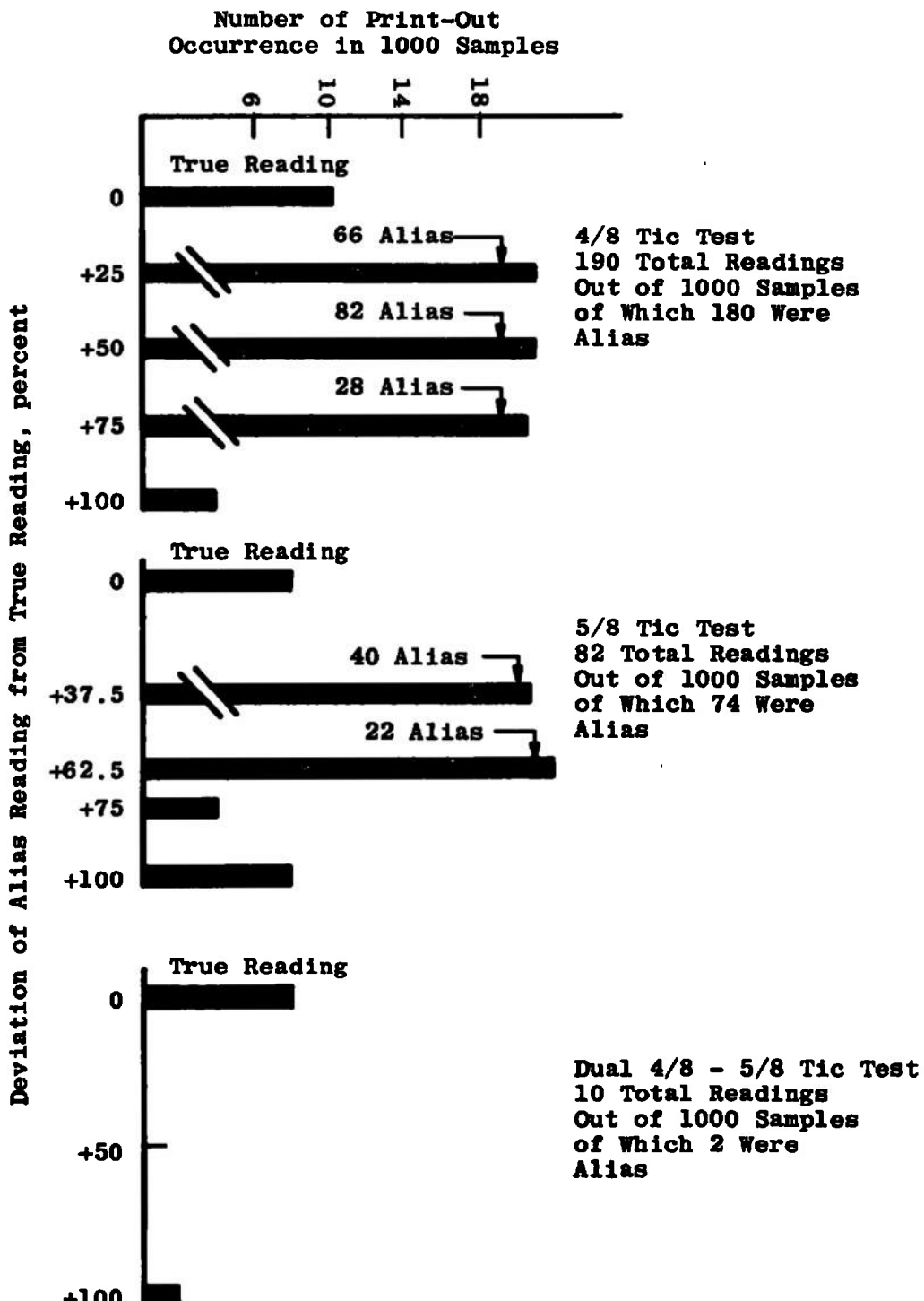
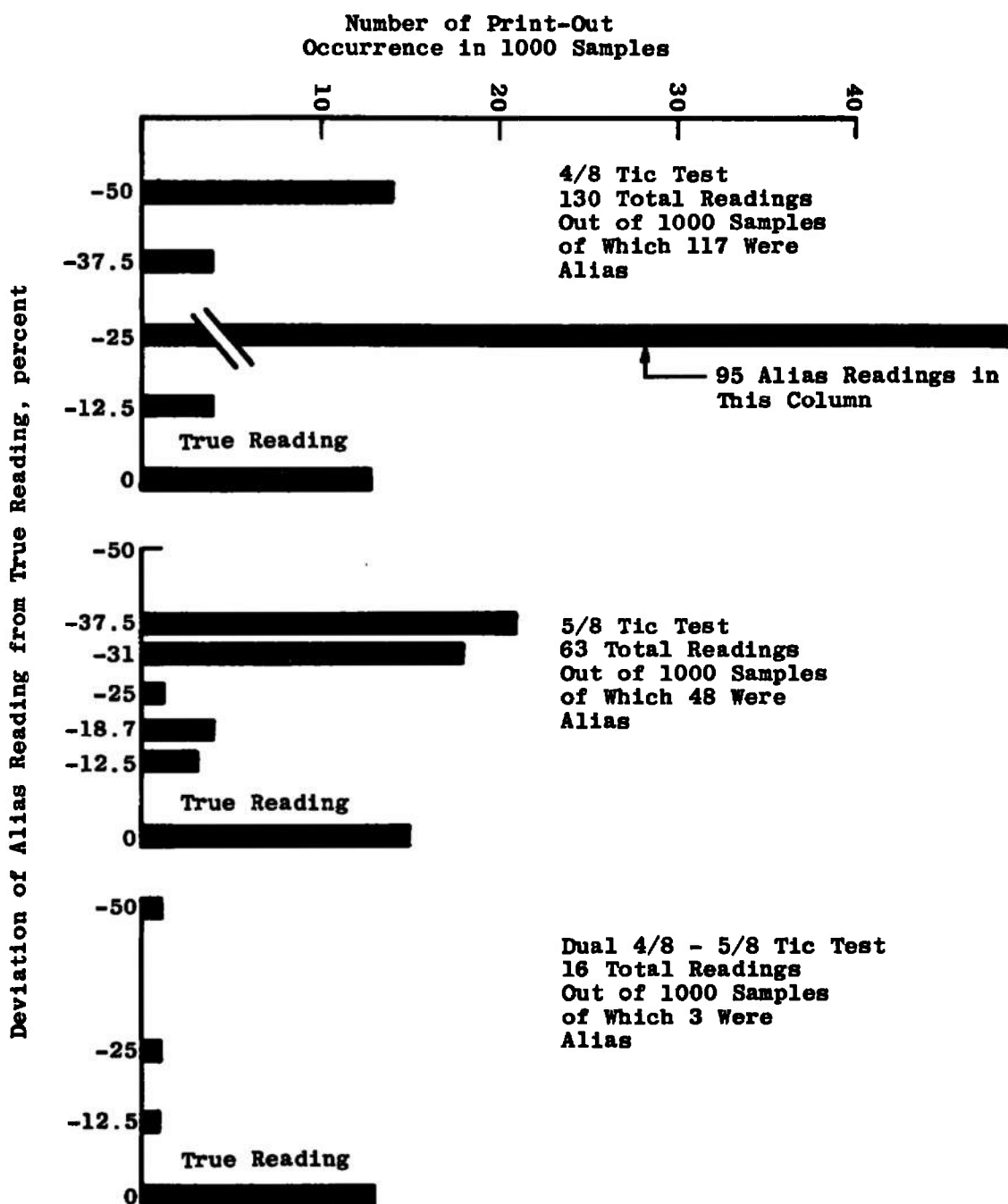


Figure 35. Test data of  $S/N = 0.07$ , alias reading distribution obtained from low  $S/N$  signal data.

Figure 36. Test data of  $S/N = 0.09$ .

## Dual Test Processor Performance in Low S/N Regions

Data Capture Ratio (DCR) =  $\frac{\text{Total Times Processor Prints}}{\text{Total Sample Cycles Made}}$

Data Quality Ratio (DQR) =  $\frac{\text{Total "True" Readings Printed}}{\text{Total Times Processor Prints}}$

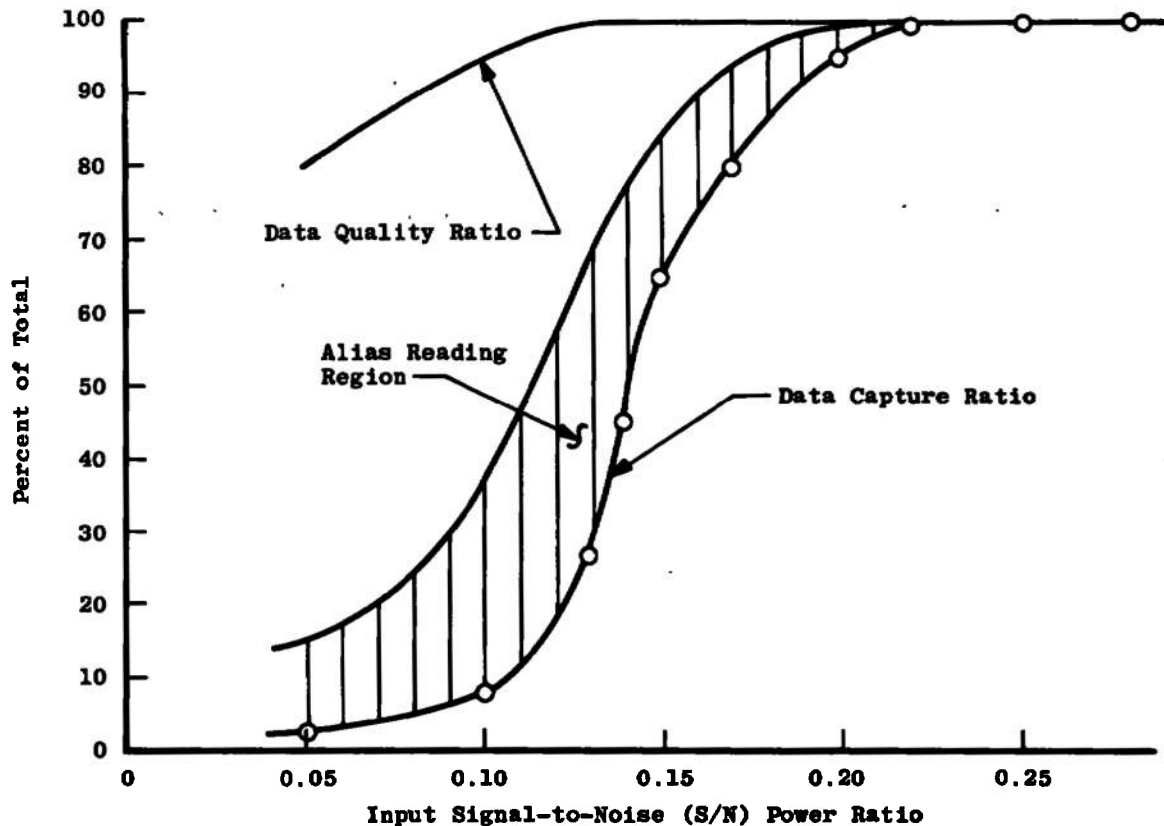


Figure 37. Processor performance in regions of low S/N.

## 6.2 LASER VELOCIMETER DATA PROCESSOR

The data processor is schematically illustrated in Figs. 38 and 39. The circuit is usable for acquiring frequency burst and CW data over the range of 1 KHz to 500 KHz. For frequencies above 500 KHz, a different technique is utilized and will be discussed in another section. The operation of this portion of the processor follows.

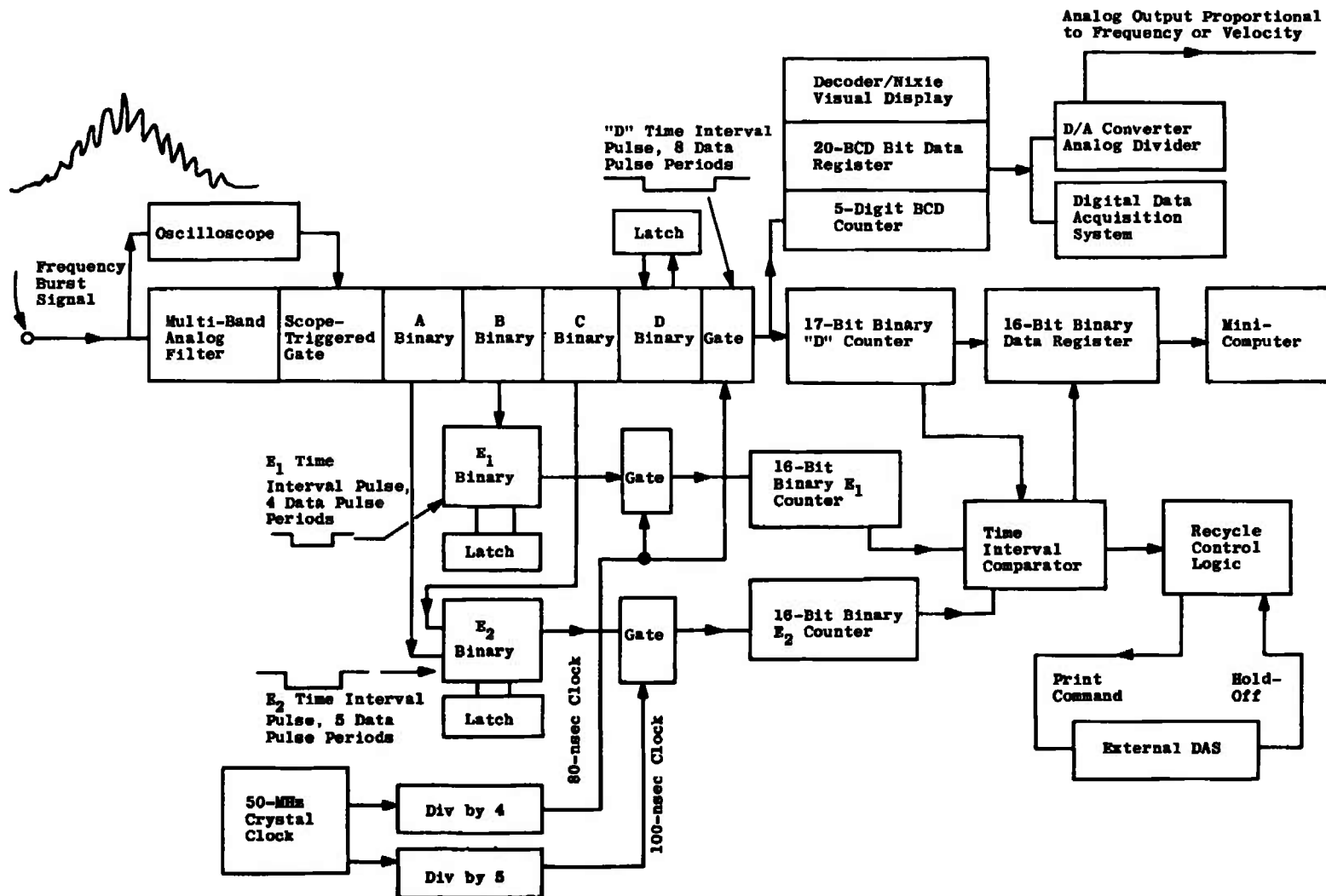
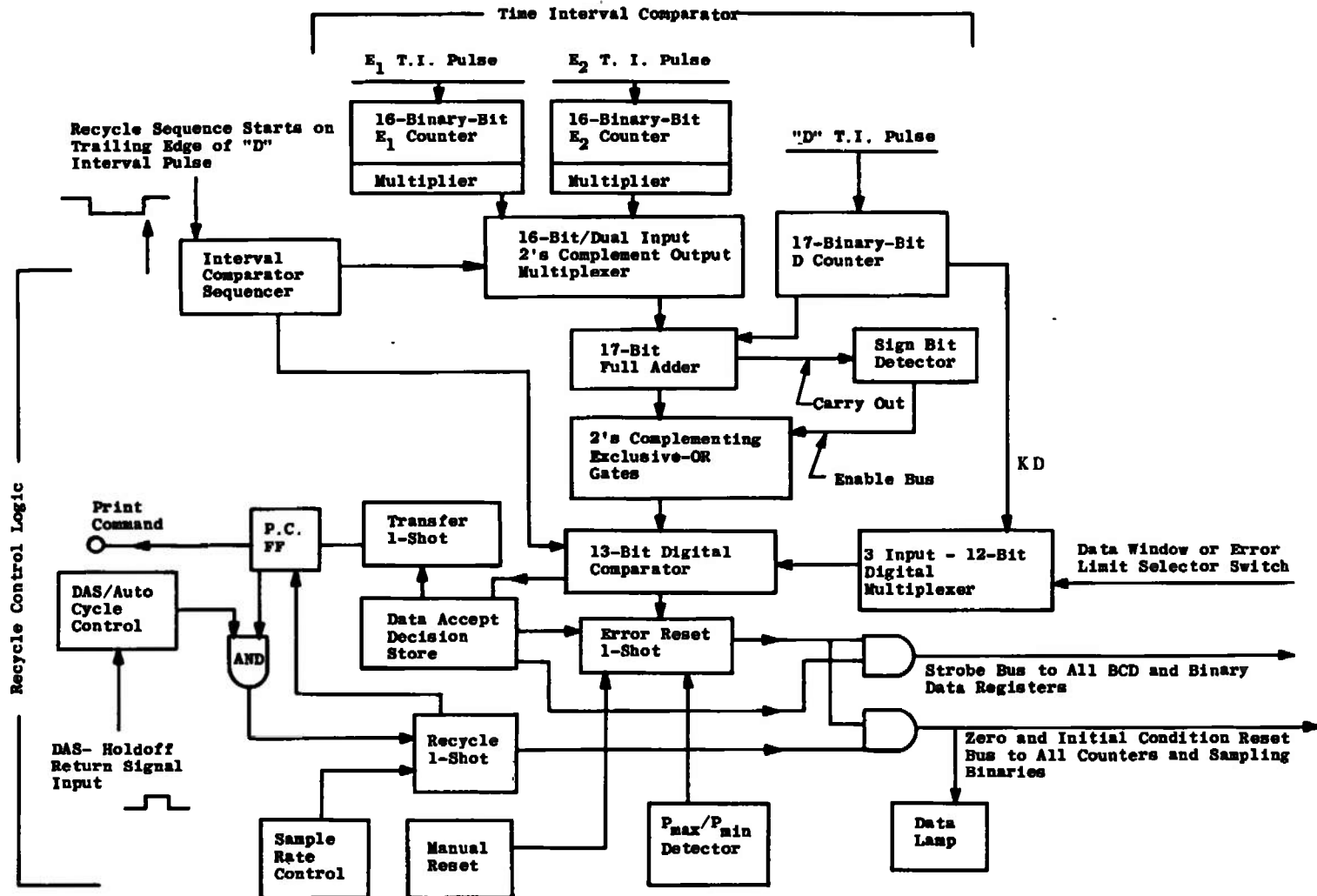


Figure 38. Laser velocimeter data processor (block diagram).



**Figure 39. Time interval comparator block diagram.**

The burst data enter the multiband analog filter and are simultaneously displayed on an oscilloscope. The filter removes the pedestal (lower frequency component) and provides nine filter bands from 1-KHz to 50-MHz frequency coverage. High-speed, emitter-coupled-logic, integrated circuitry is employed in both the filter output zero crossing detector and the sampling binaries A through D. The latter converts the eight signal oscillations into an equivalent time interval pulse (rectangle wave) denoted as the "D" pulse. Simultaneously, time interval pulses are generated by the  $E_1$  and  $E_2$  binaries. The  $E_1$  pulse is equal to the period of the first four data pulses, and the  $E_2$  pulse period equals the period of the first five data pulses.

The three time interval pulses, denoted as the D,  $E_1$ , and  $E_2$ , gate three independent counters bearing the same respective designation. These counters serve to quantize the three time intervals; each counter contains a natural binary number representing the corresponding time interval.

### 6.2.1 Time Interval Comparator

The binary numbers are applied to a hardwired computing circuit (Figure 39) that first compares the eight-pulse interval "D" to the scaled four-pulse interval  $E_1$ , and subsequently compares the eight-pulse interval to the scaled five-pulse interval  $E_2$ . A scale factor of eight to four is applied to the four-pulse interval, by hardwire multiplying the binary number contained in the  $E_1$  (four pulse) counter by two. Thus, for an ideally periodic input data pulse train the multiplied  $E_1$  counter number is equal to the D counter number. To detect the difference in the scaled  $E_1$  pulse time duration with respect to the D pulse time duration, the two binary numbers are applied to a 17-bit full adder. The  $E_1$  counter number is applied in 2's complement form, causing the adder to perform as a subtractor and produce at its output the quantity  $|D - 2E_1|$  or the complement of this number. If D is the larger number entered, then the true quantity is obtained from the subtractor; if  $2E_1$  is the larger number, then the result must be recomplemented to obtain the true value.

As the desired result from the subtractor is the magnitude  $|D - 2E_1|$ , (the sign of the number is unimportant in the final time interval comparison test), it is necessary to detect when the complement of the number is outputted by the subtractor. This is done by the sign bit detector (Fig. 38) which monitors the carry out terminal of the subtractor. It can be shown that the true value exists when a carry out signal is present. Thus, in the absence of a carry signal, the sign bit detector raises the enable bus to a

row of exclusive-OR gates which serve as a programmed inverter. When the enable bus is high, the gates recomplement the subtractor output and input to the 13-bit digital comparator the quantity  $|D - 2E_1|$ . With a carry signal present, the Ex-OR gates pass the subtractor output direct to the comparator without inversion.

The digital comparator performs a comparison of the magnitude of two numbers producing, at appropriate output terminals, a signal denoting which is the larger. The second number input to the comparator is a preselected percentage of the eight-pulse interval D counter binary number obtained by simple binary division. This number, designated as "KD" (Fig. 39), becomes the "data window" or the maximum acceptable limit value that the doubled  $E_1$  time interval pulse may differ from the D time interval pulse. "KD" is obtained by a divide by two sequence in which each time the number receives a right shift of one place (or bit), the resultant number is one-half the quantity of the original number. As an example, the number 16 expressed in binary form is 010000 and becomes 001000 or eight with a one place right shift. The "KD" binary number has been wired to the digital comparator input through a multiplexer to permit a selective division by 32, 64, or 128. The resultant number represents 3.0 percent, 1.56 percent, and 0.78 percent, respectively, of the original D counter binary number. When  $|D - 2E_1| \geq KD$ , the digital comparator outputs a signal onto a "data reject" bus. When "KD" is the larger quantity, the comparator outputs a signal onto a "data accept" bus.

The time interval comparison test can easily be made within a two-microsecond interval with existing standard TTL integrated circuit logic.

### 6.2.2 Dual Time Interval Comparison

At the termination of the 4/8 pulse time interval test, the data accept decision is stored and the comparator multiplexer automatically proceeds with the 5/8 time interval comparison test. The 16-bit multiplexer (Fig. 38) switches the contents of the  $E_2$  counter into the subtractor in place of the  $E_1$  counter number. Procedures similar to the 4/8 test then follow. The  $E_2$  counter binary number is multiplied by 1.6, then 2's complemented and entered into the subtractor. The percentage of the D counter number "KD" applied to the comparator decision  $KD > \text{or } \leq |D - 1.6E_2|$  now appears on either the "data accept" or the "data reject" signal line, respectively.

The decisions from the two tests are then compared. If both tests indicate acceptable data, then the "AND" decision is applied as a strobe pulse to the data registers within the processor, simultaneously causing (1) the binary register to transfer and store the D counter binary, and (2) the 20-bit binary coded decimal (BCD) register to transfer and store BCD data from an auxiliary BCD counter. The purpose of the dual registers shall presently be discussed.

#### 6.2.3 "Data Accept" Recycle Sequence

At the completion of the data transfer strobe pulse, a transfer 1-shot (Fig. 39) and a print command flip-flop are triggered. The flip-flop issues to an attached data acquisition system (DAS) a print command and the processor reverts to a standby mode until a further signal ("flag" pulse) is received from the DAS. The termination of the "flag" pulse from the DAS releases the recycle sequence latch by triggering the recycle 1-shot. This 1-shot resets the print command flip-flop, issues a zero reset pulse to all counters, and resets the A through E sampling binaries to their required initial condition state. At reset pulse termination, the processor must further await the reception of a +A gate signal from the oscilloscope before a new sample interval may begin.

#### 6.2.4 "Data Reject" Recycle Sequence

The recycle sequence is altered when either (1) one or both comparator tests issue "data reject" signals or (2) the input time interval pulse to the D counter does not lie between preselected  $P_{min}$  and  $P_{max}$  values. Provision is made through the error reset 1-shot to abort the sample interval as soon as one of these data reject signals occur. In this mode of recycle, a print command issue is inhibited, counters are reset to zero, and the oscilloscope-triggered gate is given control of the binaries pending a subsequent frequency burst signal event. The  $P_{max} - P_{min}$  detector directly monitors the D counter time interval pulse duration and permits only data that lie between the analog filter minimum and maximum breakpoint frequencies to be passed for time interval comparison.

#### 6.2.5 Data in BCD Form

Five numeric indicator (Nixie) tubes are used for the purpose of visually displaying the average period of the sampled data. Data conversion to decimal form can more conveniently be done "on line" when

the data exists in binary coded decimal form rather than natural binary form. Further, many DAS are equipped to receive BCD rather than binary. Data in binary form, however, more efficiently uses storage bit capacity and can be employed to advantage when data transfer is made to systems such as mini-computers or magnetic tape recorders. As indicated in Fig. 38, the processor employs a five-digit BCD counter operating in parallel with the 17-bit D counter. Thus, at the termination of a sample interval, register-stored data exist in both natural binary and 8421 weighted BCD. The parallel binary BCD counters and registers are implemented with standard MSI digital logic and printed circuit board techniques. The same procedure applies to the time interval comparator and sampling binaries.

### 6.3 PROCESSOR SAMPLE RATE

The rate at which the processor may sample is determined by (1) the signal burst density (number of bursts per unit time), (2) the time interval of eight signal burst oscillations, (3) the processor recycle time, and (4) the DAS transfer time. For example, if continuous wave (CW) signal information were available at 500 KHz, a sixteen-microsecond sample interval for eight data pulses and an eight-microsecond recycle time would provide a processor sample rate of approximately 40,000 per second.

Figure 40 illustrates a typical data acquisition rate of the processor. In this figure, the velocity of air was measured at a 5-KHz rate. The measurements were taken at a fixed point adjacent to a speaker cone oscillating at 146-Hz using a dual-scatter velocimeter employing a Bragg cell to acquire directionality (Ref. 41). Note that the sampled data are time dependent. Data acquisition was accomplished by direct transfer to an on-line mini-computer with subsequent data reconstruction by a Cal-Comp Plotter.

### 6.4 EXTENDED FREQUENCY COVERAGE

The limited sample interval of eight data pulses imposed by the short duration frequency burst-type signals places severe demands on counter resolution at signal frequencies much above 500 KHz. Precision pulse stretchers are employed to extend the time duration of the D and E<sub>1</sub> and E<sub>2</sub> interval pulses producing resultant counter gating pulses 100 times the duration of the unstretched pulse. This permits the extension of the processor upper limit frequency to 50 MHz.

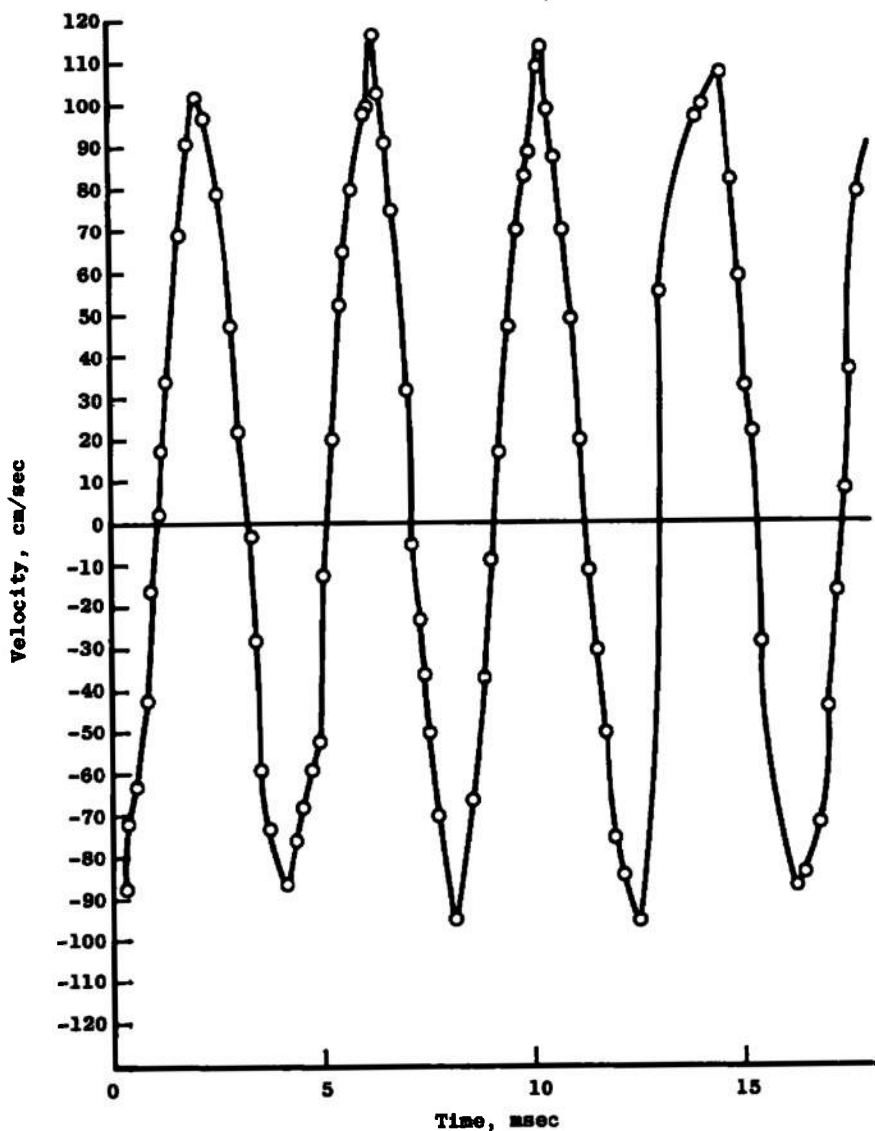


Figure 40. Loud speaker modulated air particle.

The pulse stretcher is schematically shown in Fig. 41.  $Q_1$  and  $Q_2$  are high-speed current switches, direct coupled to the true-complement terminals and an ECL flip-flop. Two precision constant current sources,  $I_1$  and  $I_2$ , and a reference voltage at the collector of  $Q_1$  provide the initial conditions for stretch sequence.  $Q_1$  is on,  $Q_2$  off, permitting  $I_2$  to cause  $Q_3$  to conduct. The initial positive voltage appearing across resistance  $R$  has caused the comparator to set the latch with  $Q$  at logic "1". At the beginning of a sample interval, the  $E_1$  binary (complement terminal) delivers a reset pulse to the latch causing  $Q$  to go to "0". The same  $E_1$  pulse simultaneously is applied to the other two pulse stretcher latches. Thus, the start of the  $D$ ,  $E_1$ , and  $E_2$  stretch interval begins at

at the same time instant. Current source  $I_1$  (chosen to be 100 times  $I_2$ ) is diverted through  $Q_2$  and timing capacitor  $C$  into  $V_{REF}$  as the "D" binary interval pulse occurs. The resultant waveform seen at the collector of  $Q_2$  is a negative going ramp with the voltage-time relation expressed as

$$\frac{\Delta e}{t_1 - t_0} = \frac{I_1 - I_2}{C}$$

where  $I_1$ ,  $I_2$ , and  $C$  are constant. The negative ramp causes  $Q_3$  to switch off; then  $I_3$  through resistor  $R$  produces a negative voltage input to the comparator. The comparator's output changes from "1 to 0". The latch, however, remains unchanged at this time. At the D binary pulse termination,  $I_1$  is again directed through  $Q_1$  and sunk into  $V$  reference. Current source  $I_2$  now removes the charge stored within capacitor  $C$ , producing the positive going ramp portion of the waveform at the collector of  $Q_2$ . As the ascending ramp approaches +0.5 volts with respect to  $V$  reference,  $Q_3$  turns on diverting  $I_2$  through  $R$ . The comparator now sees a positive voltage input and responds by producing a "0 to 1" transition at its output. The positive edge from the comparator sets the latch causing  $Q$  to output a "0 to 1" transition. The positive edge from the latch becomes the terminal point in the "stretched" time interval pulse applied to the D,  $E_1$ , and  $E_2$  counters.

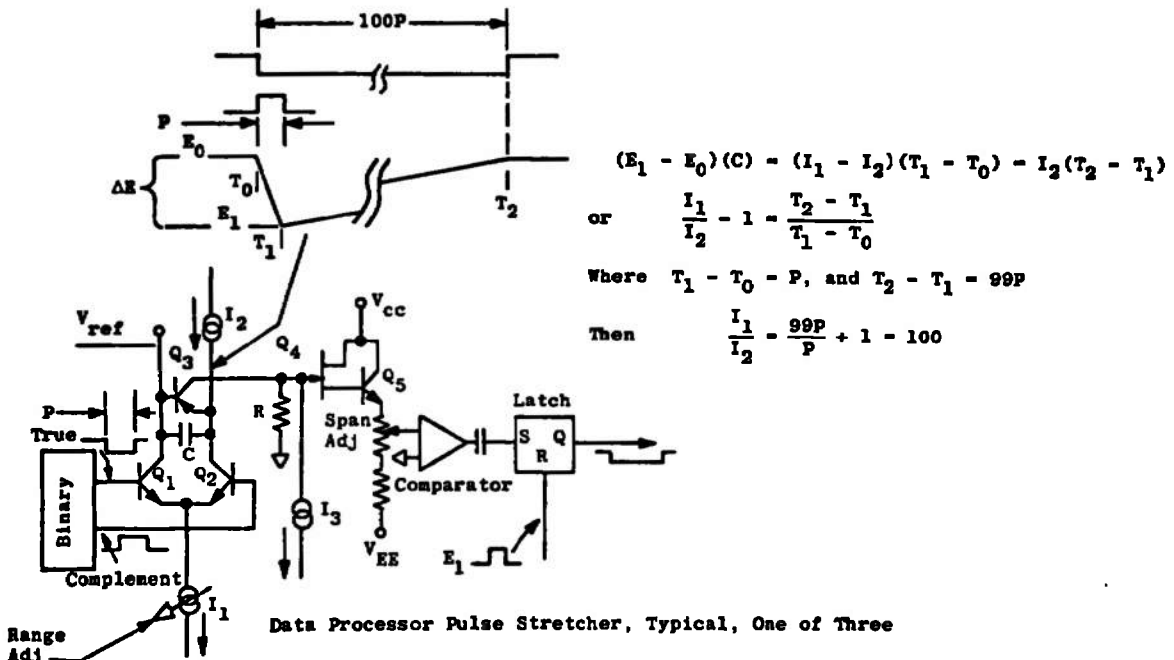


Figure 41. Circuit diagram of pulse stretcher.

The ramp expression for the positive slope is

$$\frac{\Delta e}{t_2 - t_1} = \frac{I_2}{C}$$

By equating the ramp expressions for the negative and positive slopes, it is found that the time interval expansion is directly related to the ratio of the current sources  $I_1$  and  $I_2$ . The dual ramp technique applied in the time interval stretcher offers freedom from certain common mode error sources. Absolute voltage start-stop value determinations are not required; thus, initial condition voltages as well as the value of the timing capacitor may vary with time and ambient conditions without affecting the stretch interval. Precision current sources may be simply constructed and referenced to Zener diodes having negligible temperature coefficients. Calibration of the pulse stretcher is accomplished by applying a stable frequency source and monitoring the BCD counter/visual display while adjusting calibration potentiometers. Two calibration adjustments are available for each stretcher on each range to achieve best linearity. On-board gating permits routing the three interval pulses to the BCD counter individually during the calibration cycle.

## 6.5 DATA HANDLING

A wide variety of digital handling peripheral equipment exists for acquiring, transferring, storing, manipulating and compressing digital data. The large amount of data that can be produced by a laser velocimeter coupled data processor makes some form of automatic data handling system mandatory.

### 6.5.1 Digital Printer and Mag Tape Recorder

The simplest approach employs a digital line printer. This instrument can typically produce a twenty-column, twenty-line per second printout. It has the advantage of producing an on-line hard copy. It has the disadvantages of leaving the printed data in an awkward form for further processing and is inadequate for fast data rates.

A buffered incremental digital tape recorder can increase the data rate to in excess of 1,000 five digit data point groups per second. The buffer memory of the recorder can accept short duration signal bursts at the maximum rate of 50,000 per second. The incremental feature

is useful since the velocimeter data rate is often subject to erratic variations. A high-speed, continuous run, tape system can continuously acquire 6,000 five digit data points per second and with fast memory buffering achieve rates in excess of 100,000 data points per second for short intervals. The digital tape recorder offers the advantage of large static storage capacity of data with some ease in recovering the data for digital computer reduction. The method does suffer the disadvantages of not providing a quick look at the data in progress.

An on-line mini-computer offers a means of short time duration high data acquisition. It may also serve as a buffer for a digital tape system. The computer is versatile in the type of on-line manipulation it can perform on small data groups. The computer can convert the period data of the processor directly to frequency or to velocity units. Data grouping such as rms averaging can be performed, and time correlation of data points for subsequent tape storage can be achieved.

#### 6.5.2 Data Compression

A form of data compression may conveniently be exercised upon large data blocks by the use of a "stand alone" memory. Data outputted by the processor over a given frequency range occupies a known range of numbers. A word location in memory is assigned to each number; the number becomes the address for that specific word location. If the memory word is made to store or totalize the number of times it has been addressed, then at the end of a data taking interval the memory contains a distribution of data that can be displayed along a frequency or period scale. The contents of the memory can be serially read out by a counter sequentially addressing each word location within the original range of numbers. The memory formatted data might typically appear as in Fig. 42. Data in this form can be block transferred to tape or computer at a considerable savings in data quantity handled. The data period and number of occurrences completely describe the data block when time averaged data are permitted. This is significant at high data rates where the limiting factor is the acquisition speed of the recorder or the memory capacity of the computer. A sequence counter and a pair of D/A converters would permit the stored data to be displayed on an oscilloscope. The histogram display provides an on-line look at mean velocity variations. Sixty-four thousand occurrences of a given data period can be stored in one 16-bit memory word opposed to only one if the period value is individually recorded. Typical memory cycle time permits recording at a rate in excess of 1 MHz providing S/N ratios are greater than 2.

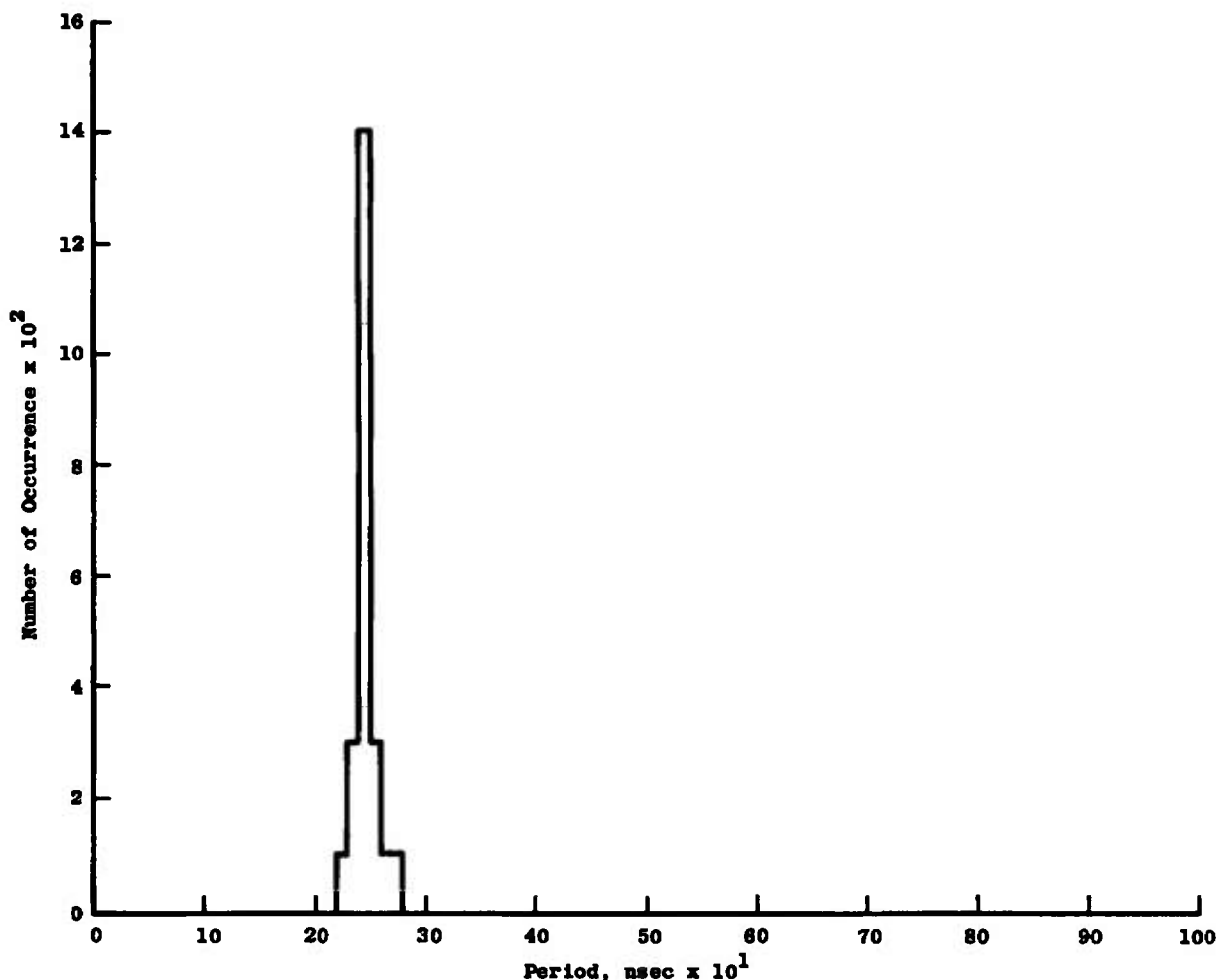


Figure 42. Memory formatted LV data display.

### 6.5.3 Analog Recording of Time-Dependent Data

Time-dependent data recording at high data rates for extended intervals becomes a major task if done digitally. The task becomes worse if three velocity components plus positional data are required. A trade-off can be made by outputting processor data in analog form, employing analog computing techniques to produce velocity information with subsequent data storage in a multi-channel analog recorder. Existing D/A converters and analog dividers provide for conversion rates through 50 KHz. This technique has been locally used for a "quick look" oscilloscope display of a velocimeter system at rates to 30,000 samples per second. The register stored data from the processor directly applied to the D/A converter provides for a zero drop sample and hold technique.

#### 6.5.4 Multi-Component Processing of Simultaneous Data

The processor is a single component data sampling device. Simultaneous capture of multi-component velocimeter data has been accomplished by multiple processors sampling individual data channels. A common gating signal may be applied to the multiple processors permitting simultaneous sampling of a common particle passage through the probe volume. This method has successfully been employed at AEDC for two-component data. A Hewlett Packard digital scanner and magnetic tape system was used to handle the data. The scanner was programmed to channel code the data and provide for transfer to the tape only when both component channels produced data.

### 7.0 LABORATORY-GENERATED VELOCIMETER SIGNALS

In this section, two techniques that have been developed to bench test the LV system are described. Their operational characteristics are discussed in some detail.

#### 7.1 VIDEO RECORDER AS A FREQUENCY BURST TEST SIGNAL GENERATOR

This device has been used within the lab for the analog reconstruction of velocimeter data. Sample information from an operational velocimeter is first recorded and may later be reconstructed as a test signal for performance testing the processor on the bench. The tape recorded video information offers a wealth of frequency burst signal types and waveform variations. Selection of a specific test signal involves the recorder being operated in an unorthodox manner. The tape is maintained stationary and the video reproduce head is permitted to repeatedly scan the same narrow slice of tape. The information contained on this slice is equivalent to one horizontal scan on a conventional video picture tube, yet it can contain numerous frequency burst signals. The horizontal sync pulse generated by the video recorder is used to trigger the "B" time base of an oscilloscope. The oscilloscope is then operated in an "A delayed by B" time base mode. Selectable segments of the tape video information are then displayed against the A time base. The B time base delay control permits the dialing in of new video information. Thus, a frequency burst signal is selected on the scope display and the scope gate signal to the processor permits the processor to initiate a sample interval. The point along the burst signal where sampling begins is easily changed by the B delay control. Figure 43 illustrates a tape reconstructed waveform.

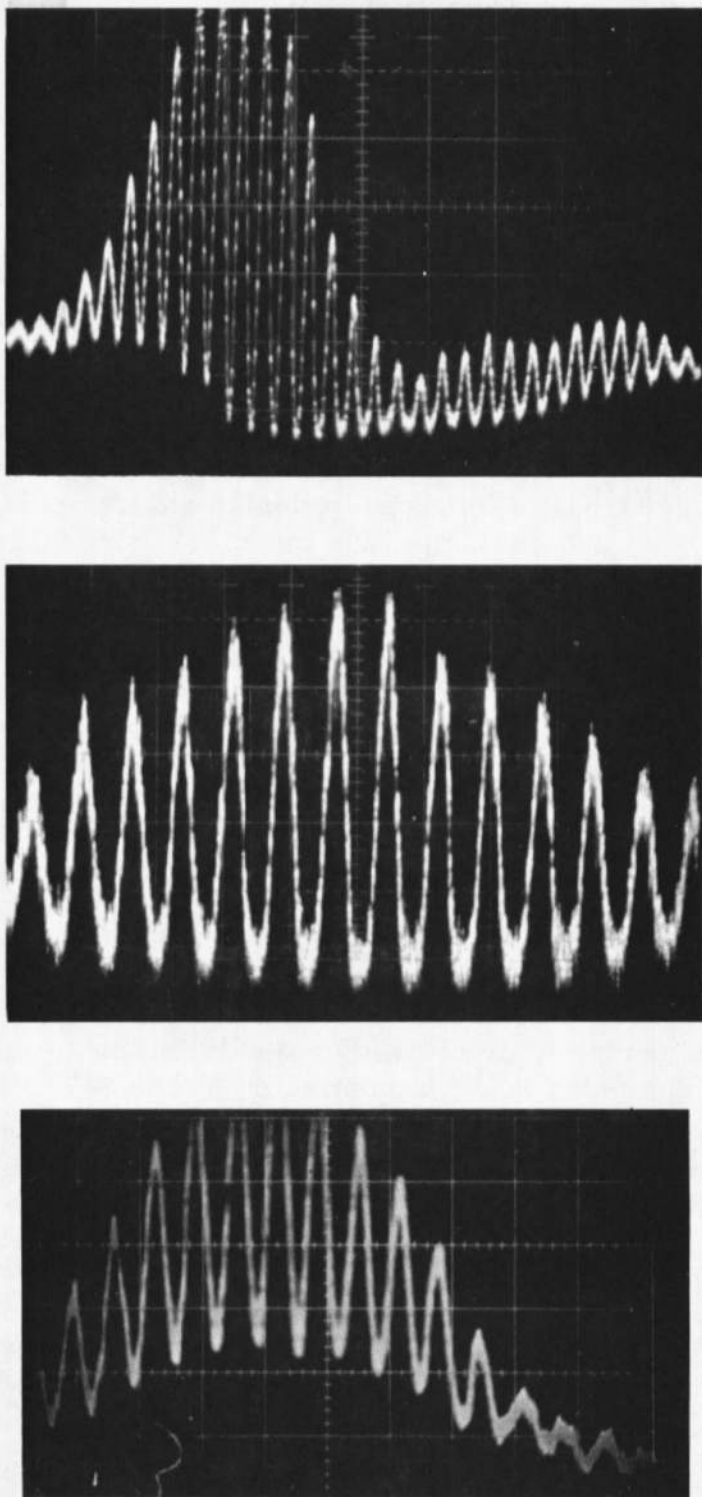


Figure 43. Reconstructed burst signal from video tape.

## 7.2 LV BURST SIGNAL SYNTHESIZER

The photodetected time domain signal for a single scatter particle traversing a fringe set for the conventional dual scatter LV is given in the previous section, Eq. (5-4), as

$$N(t) = A_p e^{-(2\sqrt{2}(t - t_0)/\tau)^2} + A_s e^{-(2\sqrt{2}(t - t_0)/\tau)^2}$$

where  $f_D$  is the Doppler frequency and  $\tau$  is the time required for the scatter particle to transit the probe volume outer boundary. The boundary is defined as the surface of an ellipsoid where the laser radiation intensity is  $e^{-2}$  times the maximum intensity at the geometric center of the probe volume. The signal is seen to consist of two distinct summed waveforms: (1) a Gaussian pedestal waveform with peak amplitude  $A_p$ , and (2) a Gaussian amplitude modulated sinusoid with peak amplitude  $A_s$ .

A circuit used to synthesize the waveform described is shown in Fig. 44. Linear and digital integrated circuits are employed where possible to provide a low cost high performance signal simulator. The synthesized signal produced by this circuit is shown in Fig. 45. The figure illustrates the visibility ratio variations possible in the real time LV signal. Reference to Fig. 44, a voltage-tunable oscillator furnishes the Doppler sinusoid signal source  $E_1$  which is attenuated and applied to a transconductance analog multiplier. Amplitude control by  $R_3$  varies the visibility ratio of the LV burst signal. The sinewave source is squared, frequency counted, and applied to a frequency divider consisting of three 7490 decade dividers, a 1-shot and a J-K flip-flop. The impulse train, of period  $t$ , drives either the divide by 10 or divide by 100 counters. The pulse route is controlled by the 7473 flip-flop, which inhibits one counter path while permitting the alternate counter to function. The 1-shot triggers the flip-flop at the end of a 10- or 100- pulse period, causing input pulse path diversion. The output of the counter circuit is an asymmetrical pulse train which is applied to a switched constant current source  $I_B$ . This source is directed away from timing capacitance  $C_T$  during the  $10t$  logic "1" state of the pulse train. During this interval, current source  $I_A$  linearly charges  $C$  producing a positive slope ramp at the capacitor terminals. At the end of the  $10t$  period, the source  $I_B$ , which is set equal to  $2I_A$ , extracts the charge from  $C$ , producing a negative slope ramp. The resultant triangle wave may be altered by a piecewise diode-resistor wave-shaping circuit to function as a Gaussian approximated pedestal  $E_2$ . More simply, the triangle wave may be used to simulate the pedestal.

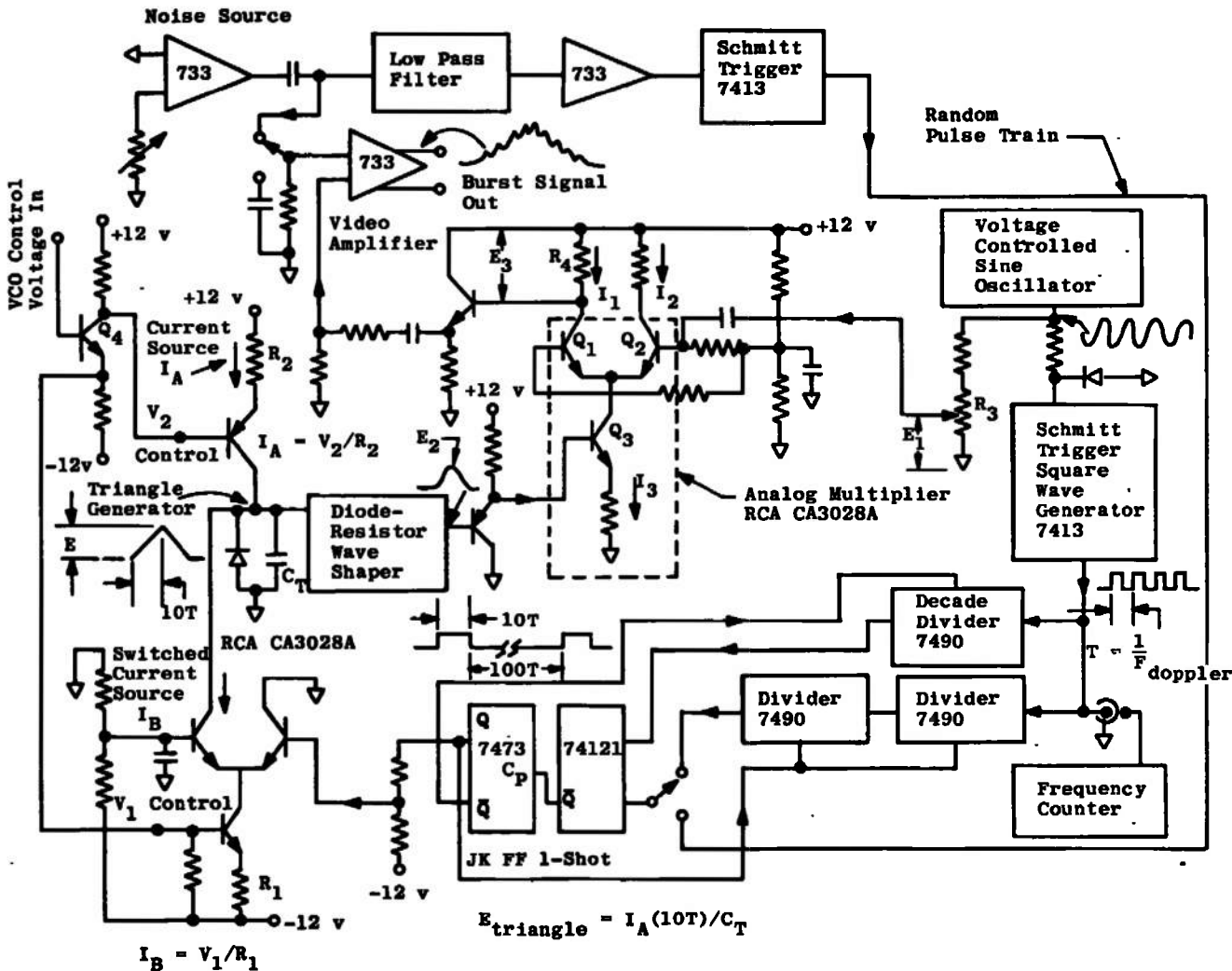


Figure 44. Schematic diagram of an LV signal synthesizer.

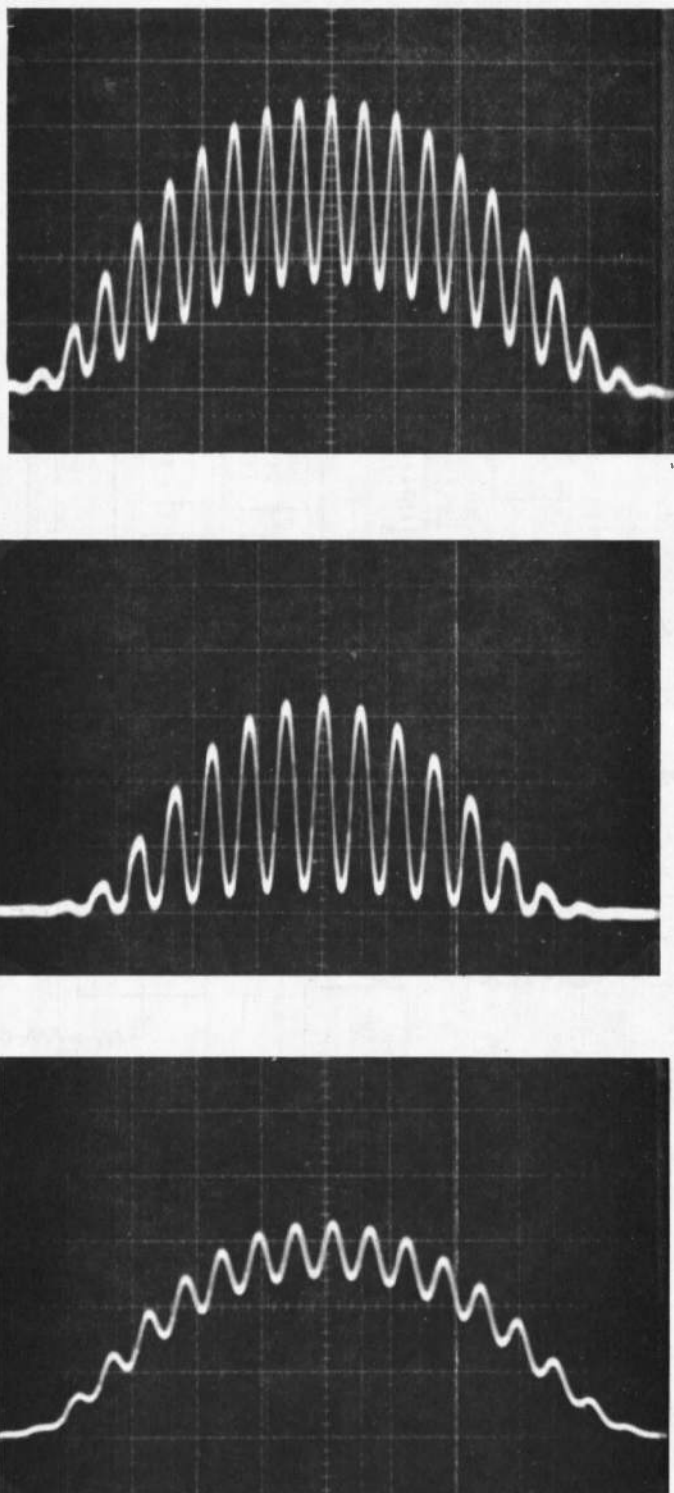


Figure 45. Synthesized burst signal waveform.

$E_2$  enables the voltage-controlled current source  $I_3$  causing the output voltage  $E_3 = I_1 R_4$  to exhibit the same Gaussian waveform as  $E_2$ . This is true since the circuit is symmetrical and  $I_3 = I_1 + I_2$ .

The differential pair  $Q_1$  and  $Q_2$  amplify the Doppler frequency sinusoid input voltage  $E_1$ . The differential gain is proportional to the amplifier transconductance  $dI_1/dE_1 = gm$ . The output current swing  $I_1$  due to  $E_1$  is known to be equal to  $gm E_1$ . If the amplifier is restricted to operation in its linear region, the transconductance  $gm$  (and therefore the gain) increases linearly as  $E_2$  causes the collector current  $I_1$  to increase. The output voltage attributed to  $E_1$  is multiplied by a term proportional to  $E_2$  and contributes a Gaussian amplitude modulated sinusoid burst. The composite output signal is that of a Gaussian modulated sinusoid super-imposed upon a Gaussian pedestal. Variation in the amplitude of  $E_1$  will vary the signal visibility ratio since the pedestal is controlled only by  $E_2$ .

The inverted burst signal  $E_3$  is now applied to the video amplifier which provides dual polarity waveforms at its output. The amplifier further serves as a transmission line driver and adder for incorporating the wide band noise source with the burst signal.

If the circuit is to be used over a wide frequency range, then the current source  $I_B$  and  $I_A$  may be voltage controlled and timing capacitor  $C$  switch selectable. Voltage control can be implemented by a phase splitter  $Q_4$  driven by the oscillator control voltage. This provides for triangle wave amplitude compensation as the Doppler frequency is changed.

The analog multiplier may be used for frequency burst synthesis to 50 MHz. The counter circuit coupling the VCO with the triangle generator provides for phase locking the Doppler sinusoid with the burst event for a stable oscilloscope display. The single divide by 10 counter may be programmed to divide by less than 10 and thus change the number of sinusoids within the burst signal. The decade counter as shown will produce a signal having a nominal 20 cycles per burst. The burst train generated by the circuit can be caused to occur at random intervals by applying a random pulse source to the 1-shot in lieu of the divide by 100 counters. The random pulse source is obtained by low-pass filtering the white noise source.

## 8.0 TRAILING VORTEX EXPERIMENTS AT AEDC

Trailing vortex experiments were run using a three cup anemometer installed at the AEDC runway by NASA Personnel. A Gulfstream aircraft, operated by NASA personnel, was used to create the vortex fields. The LV mobile unit was set on the apron and measurements were made during the period July 25 through July 27, 1972. A description, and the results, of the experiments are discussed in this section.

### 8.1 EXPERIMENTAL ARRANGEMENT

A bistatic transmitter-receiver configuration was used in the latter trailing vortex experiment performed on the AEDC runway. The primary mirror, on the transmitting telescope, was 45.7 cm in diameter with an approximate 10-m focal length. The telescope was operated in a Cassegrain focus mode with the closest, near field, focus being approximately 25 m. The Laser (operated at 4 watts of power at the 514.5-nm wavelength) was mounted, as schematically shown in Fig. 46, on the front of the frame of the transmitting telescope with the longitudinal axis of the laser orthogonal to the optical axis of the telescope and parallel to the ground. A photograph of the experimental arrangement is shown in Fig. 47. This arrangement permitted the telescope and laser to move in a common reference system with the laser rotating about its longitudinal axis. Operating with this configuration also eliminates the possibility of any particles breaking off the interior surface of the laser plasma tube and fusing to the brewster windows while the laser is operating and the telescope tilted. The Laser beam was then folded into a 2X beam reducer and then entranced into a two-dimensional ultrasonic Bragg cell. The four beams produced by the Bragg cell were frequency shifted by 15 and 25 MHz. The 25-MHz frequency difference beam pairs defined the velocity component parallel to the ground. Those pairs of beams with 15-MHz frequency difference defined the velocity component orthogonal to the optical axis of the transmitter and the velocity component parallel to the ground.

Immediately after the Bragg cells, a 4X beam expander in combination with F/4, 20-cm focal length lens was used to magnify the divergence angles between the beams and then collimate the entire beam set. A 20-cm aperture Schmidt-Cassegrain telescope, used as a diverging lens (to expand the beam separation and to determine probe volume position), was used as the final input lens to the 45.7-cm transmitting aperture.

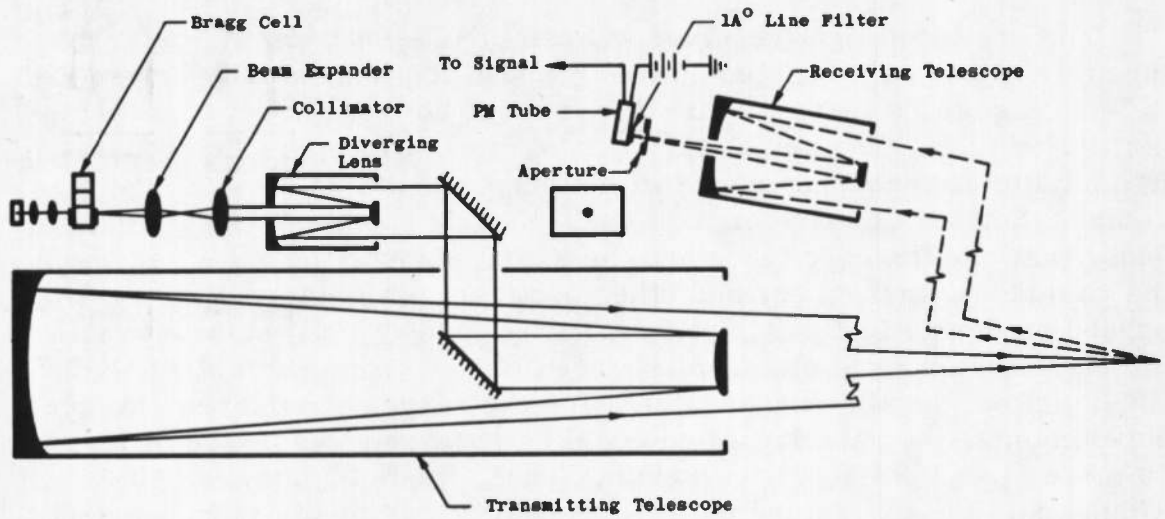


Figure 46. Schematic of the trailing vortex LV.

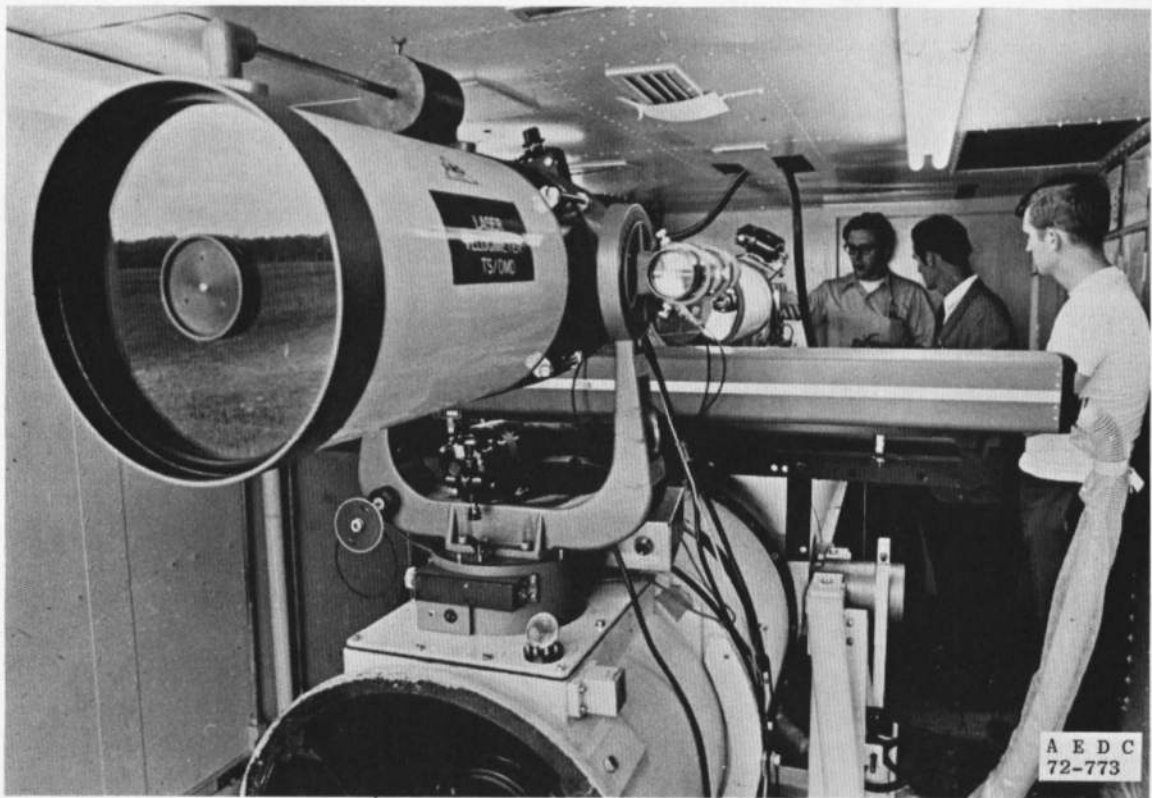


Figure 47. Telescope set-up trailing vortex study.

The scattered light receiver (a Schmidt-Cassegrain, 25-cm aperture telescope) was mounted on the front of the transmitting telescope. A 1-nm laser line filter was used in front of an RCA Model 931A photomultiplier tube. The signal output from the PM tube was heterodyned into a suitable frequency range with electronic circuits previously described (Section 6). The signals could then be observed visually on a dual beam oscilloscope trace and the signal period, the relative time the period was measured, and other pertinent parameters were recorded on magnetic tape. Optimum signal quality was obtained when the signal heterodyne electronics were set for a bandwidth of 100 KHz (the smallest possible bandwidth). For the ranges considered, in these experiments, the velocity which could be observed was on the order of 10 m/sec per 100 KHz of bandwidth. Thus, the maximum velocity which could be determined with the present experimental arrangement was 30 m/sec (300-KHz bandwidth).

## 8.2 SYSTEM ALIGNMENT

The following procedure was used to align the optical system. The geometric center of the probe volume was determined by visually locating the most intense portion of the probe volume by light scattered from a white card. The receiving telescope was manually focused to the white card position. With the laser power set to its lowest setting, the signal from the white card was observed with the detection electronics and the a-c signal (for zero velocity) amplitude maximized by small positional changes of the white card in the probe volume. In this manner, the geometric center of the probe volume could be located within  $\pm 0.5$  cm for a probe volume approximately 40 cm long. The receiving telescope was focused to this region and locked in place.

Typical dimensions for the probe volume at a 30-m range were approximately 0.08 cm in diameter and 40 cm long. The probe volume for such a range is approximately 0.2 cc (for  $e^{-2}$  signal contour). At this range, the receiver telescope was approximately 1.9 deg off the transmission axis and could detect the entire transmitted probe volume. When the optical axis of the transmitter was parallel to the ground, the transmission path was 2.5 m above a grassy ground cover. For these experiments the transmitter was oriented approximately 10 deg WSW. The maximum tilt angle of the system relative to the ground plane was 17.5 deg.

### 8.3 PROBE VOLUME DETERMINATION

The theoretical determination of the probe volume, and in particular the effective depth of field, has been experimentally verified. The sensitive length (or depth of field) of the probe volume was experimentally determined for a dual-scatter LDV with an off-axis, backscatter, collection system. The cross over region was saturated with steam to provide continuous scatter sources. The voltage amplitude, peak-to-peak, from the photodetector was monitored on an oscilloscope as a movable mask varied the length of the beam exposed to the photodetector. The results are shown in Fig. 48 with a schematic of the experimental set up included (Ref. 51). The maximum visable length exposed to the photomultiplier tube was calculated to be 19 mm. It is seen that 92 percent of the voltage increase or 99.3 percent of the backscatter laser signal power is contained within the calculated length. Approximately 0.7 percent of the total power is due to contributions outside the focal depth of field. The scattered power from a distance of 3.2 cm and less is attributed to light scattered from the front edge of the mask. The sensitive length or effective depth of field shown is considerably larger than the actual length of the region from which data are acquired; however, the contribution is low, and as a first approximation the theoretical value may be considered valid for design purposes.

During the trailing vortex experiments the probe volume was positioned at an altitude of approximately 10 m and located approximately 12 cm under and 50 cm from the end of the vane mount of the middle arm of the three-component NASA wind vane anemometer. Photographs of the experimental arrangement are included in Fig. 49.

### 8.4 AEDC EXPERIMENTS

The experimental program, at the AEDC runway, was initiated on July 25, 1972. The weather was partly cloudy, hazy, with intermittent light rain. The 12 runs that were completed on this date were mainly calibration runs and only Run No. 10 is included as Fig. 50. It is seen from this figure that very little data were acquired during the first 26 sec of the run. At approximately 57 sec after initiation of the experiment, the data rate increased for approximately 40 sec. It is seen that the vertical component of velocity is essentially the rotational component of the vortex field and the horizontal component is that due to the oscillation in the core.

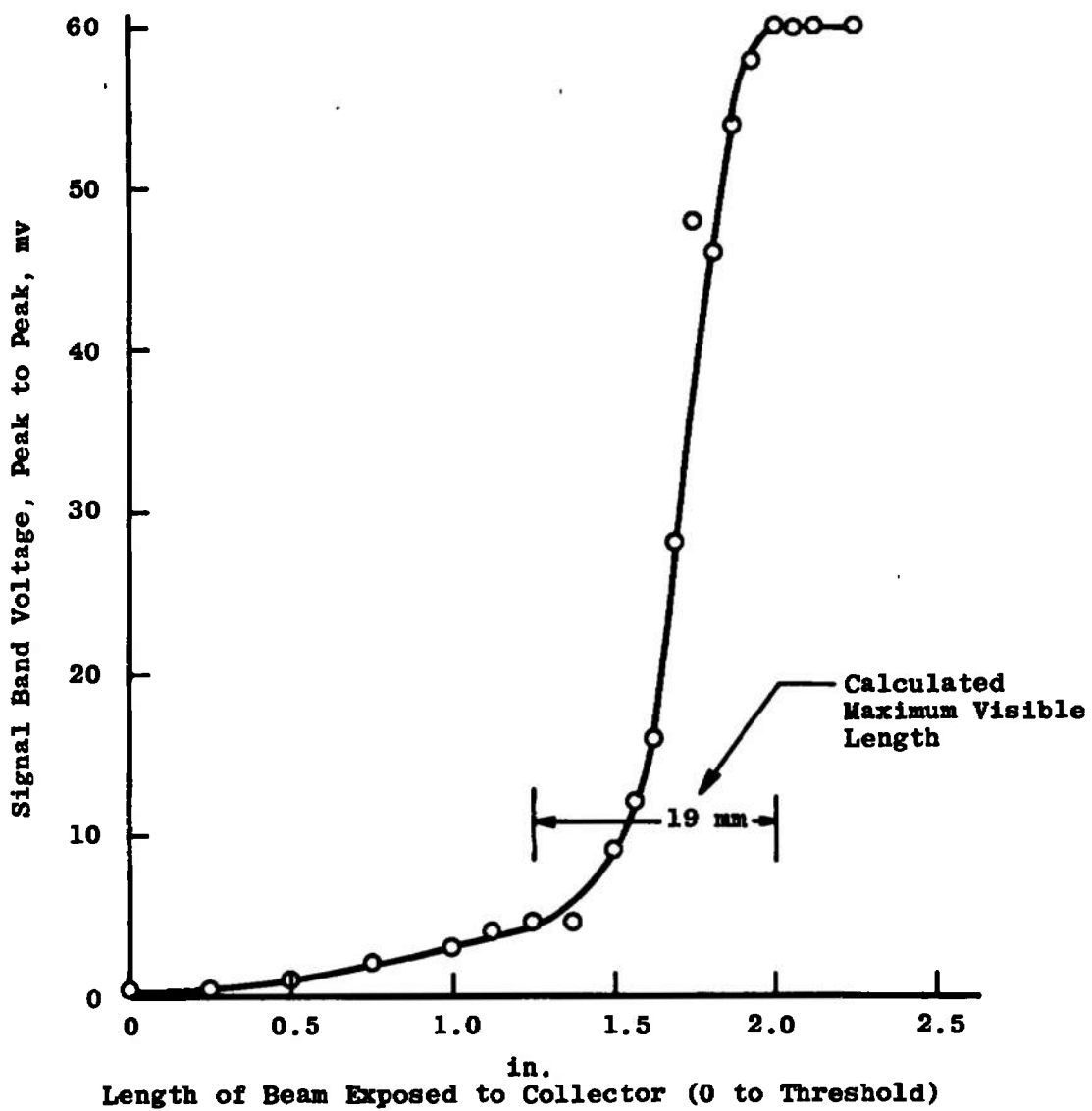
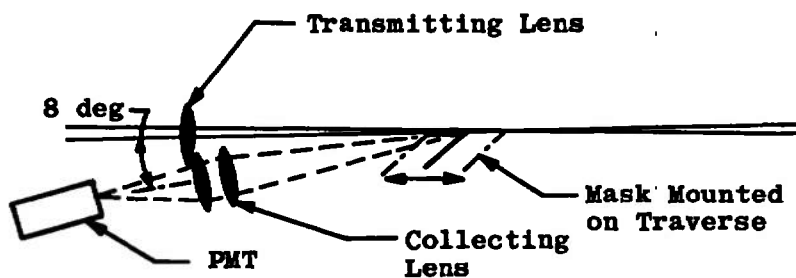
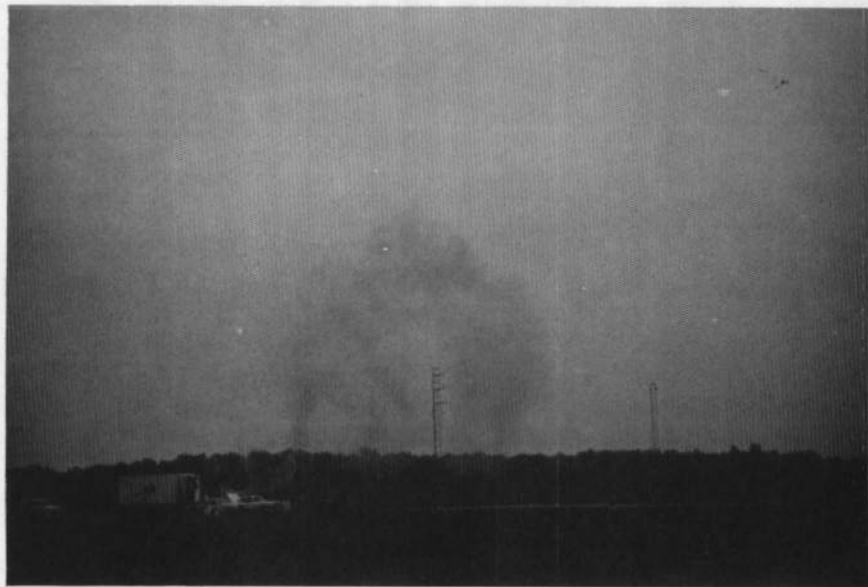


Figure 48. Peak-to-peak signal band strength from 8 deg off-axis, backscatter LDV with very high moisture content.



Figure 49. Photographs of trailing vortex experiment.



**Figure 49. Concluded.**

On July 26 approximately 19 runs were made. Runs 1 through 7 were essentially aborted due to problems associated with either the velocimeter or the anemometer, and no data were acquired. Run No. 8 on the 26th of July is included as Fig. 51. In this particular run a red smoke bomb was placed on the runway. It is seen (Fig. 51) that both the horizontal and vertical component exhibit positive and negative velocities and the maximum LV data acquisition rate occurred approximately one minute from initiation of the experiment. The data rate approached 10 data points per sec; however, on the average, the data rate was approximately 3 to 4 data points per sec. On Run No. 9 a red smoke bomb was placed on the runway; however, it appears that the vortex field missed the anemometer tower. Some data were taken however, and these are included in Fig. 52. The data acquisition rate was approximately 1 data point per sec during this run. On Run No. 10, included as Fig. 53, a purple smoke bomb was placed on the runway and considerable data were acquired approaching 9 data points per sec and exhibiting both negative and positive velocities for both the horizontal and vertical components.

Run No. 12 was made with a yellow smoke bomb on the runway, and the results are included in Figs. 54 and 55 for the vertical and horizontal components of velocity, respectively. In these figures, both the anemometer data and the velocimeter data are recorded. It is seen in the regions where the anemometer data were high very little velocimeter data were acquired, and considerable amount of LV data scatter is evident. In Fig. 54, where the lateral velocity component was measured during the first 50 or 60 sec of the run, the data rate was extremely low and did not increase beyond approximately 1 to 2 data points per sec at any given instant in time. Figure 55 contains the vertical component of velocity acquired by both the LDV data and the anemometer data. Approximately 50 sec after the initiation of the experiment the LV data rates increased to approximately 8 to 9 data points per sec. On the average, during this period approximately 6 to 7 LV data points per sec were acquired. In both of the figures, vertical and horizontal components of velocity went through positive and negative velocity fields. In Fig. 56 another run was made using a yellow smoke bomb on the runway, and the data exhibit the same characteristics as in Fig. 55. On Run No. 13, the data rate increased to approximately 9 data points per sec at approximately 50 sec after experiment initiation.

On July 27, the elevation angles were rechecked and the telescope realigned to approximately 3 to 5 in. below the location where data were taken on the previous day. The elevation angle was found to be  $17^{\circ}4''$ .

The sky was heavily overcast when the experiments were initiated at approximately 7:15 a.m. Of the series of data taken on the 27th, a number of instrumentation and operational difficulties were again encountered and only four sets of data were acquired which could be evaluated. Runs 2 and 4 were taken in the morning, whereas Runs 24 and 26 were taken in the afternoon. Again, as in previous cases, both components of velocity exhibited positive and negative variations which characterize the trailing vortex. However, the data acquisition rate was still too low to affect any major correlation between LV and anemometer data.

Data taken on Run No. 2, early in the morning on July 27, are shown in Fig. 57. The maximum data acquisition rate of the vertical component velocity reached approximately 10 plus data points per sec at 45 sec after the experiment was initiated. The horizontal component of velocity exhibited extremely low data acquisition rates, reaching approximately 6 data points per sec at 46 sec. Figure 58 contains the data taken on Run No. 4 on the morning of July 27, 1972. The horizontal component of velocity again exhibited extremely low data acquisition rate, whereas the vertical component of velocity contained spurts of data initiated at approximately 15 sec after the experiment was started. The data rate then subsided at approximately 25 sec after initiation of the experiment. There was a lag for a period of approximately 7 sec with another little spurt in the data. From 35 to 40 sec there was a lag and then another spurt of data for 5 sec. From 45 to approximately 66 sec after the experiment was started, there was another lag in the data rate, and thereafter considerable data were acquired. In each of these cases, the vertical component of velocity exhibited positive and negative velocity fluctuations and the data acquisition rate was relatively high. The data acquisition rate for the horizontal component velocity was extremely poor throughout the run as seen in Fig. 58. Figure 59 contains data acquired at 32 sec after the experiment was initiated. The vertical component of velocity data rate increased, reaching maximum at approximately 44 sec to 10 data points per sec with an average value of approximately 7 data points per sec. This data rate was sustained for a period up to approximately 70 sec after initiation of the experiment. The horizontal component of velocity again exhibited very poor data acquisition rates. Run No. 26, the final run, was made to determine the background wind velocity by both the LV and a single anemometer positioned on a barrel. The range was 25.6 m horizontally and the data acquisition rate was, on the average, approximately 6 data points per sec, although, not continuous as can be seen in Fig. 60. Again, as in all previous cases, the data acquisition rate of the horizontal component was extremely low, approaching only one data point per second. Upon completing this run, the experimental activities were terminated. In these latter, and final, series of runs no anemometer data were available to attempt further correlation.

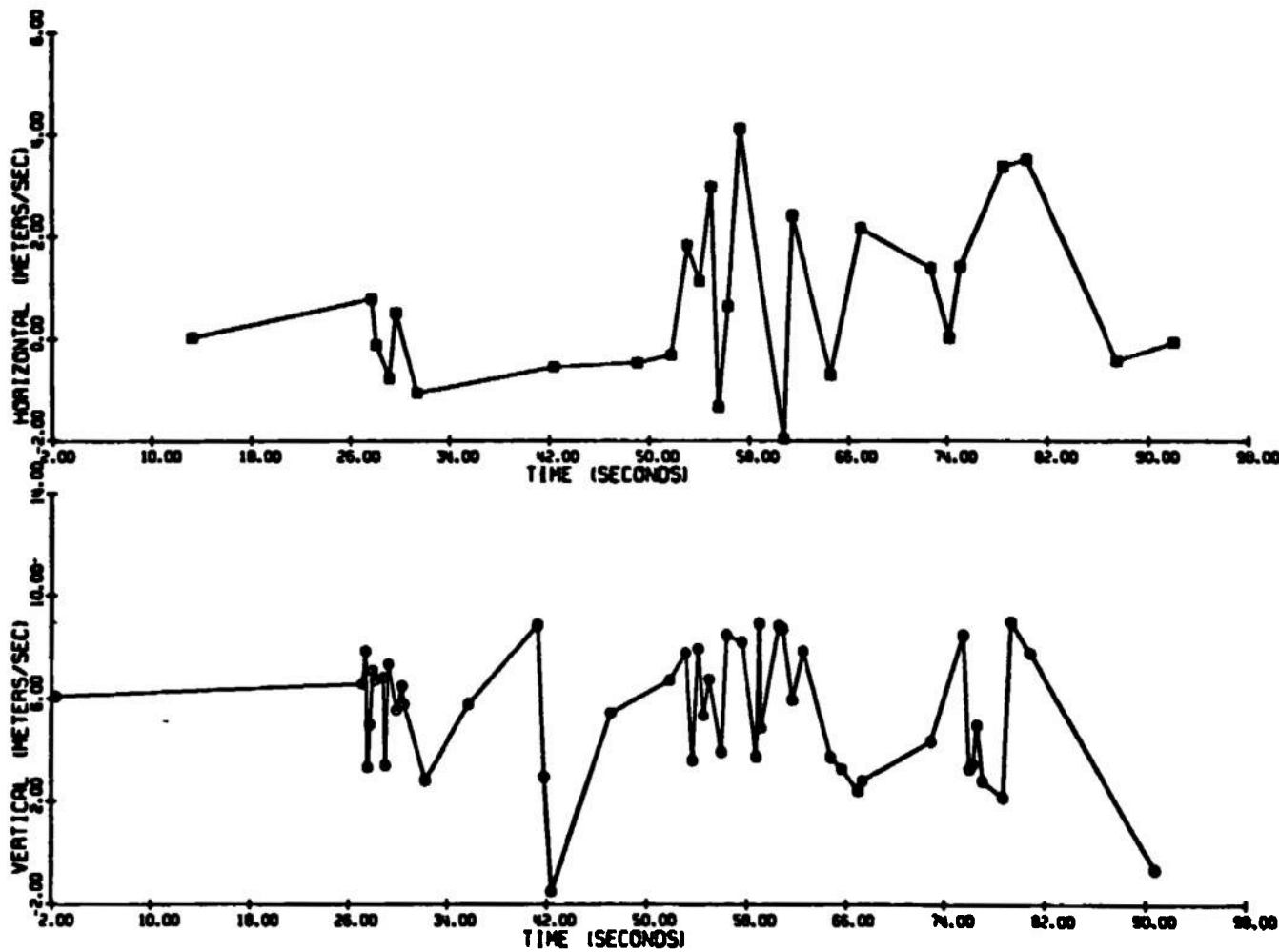


Figure 50. Trailing vortex LV data, run no. 10, 7/25/72.

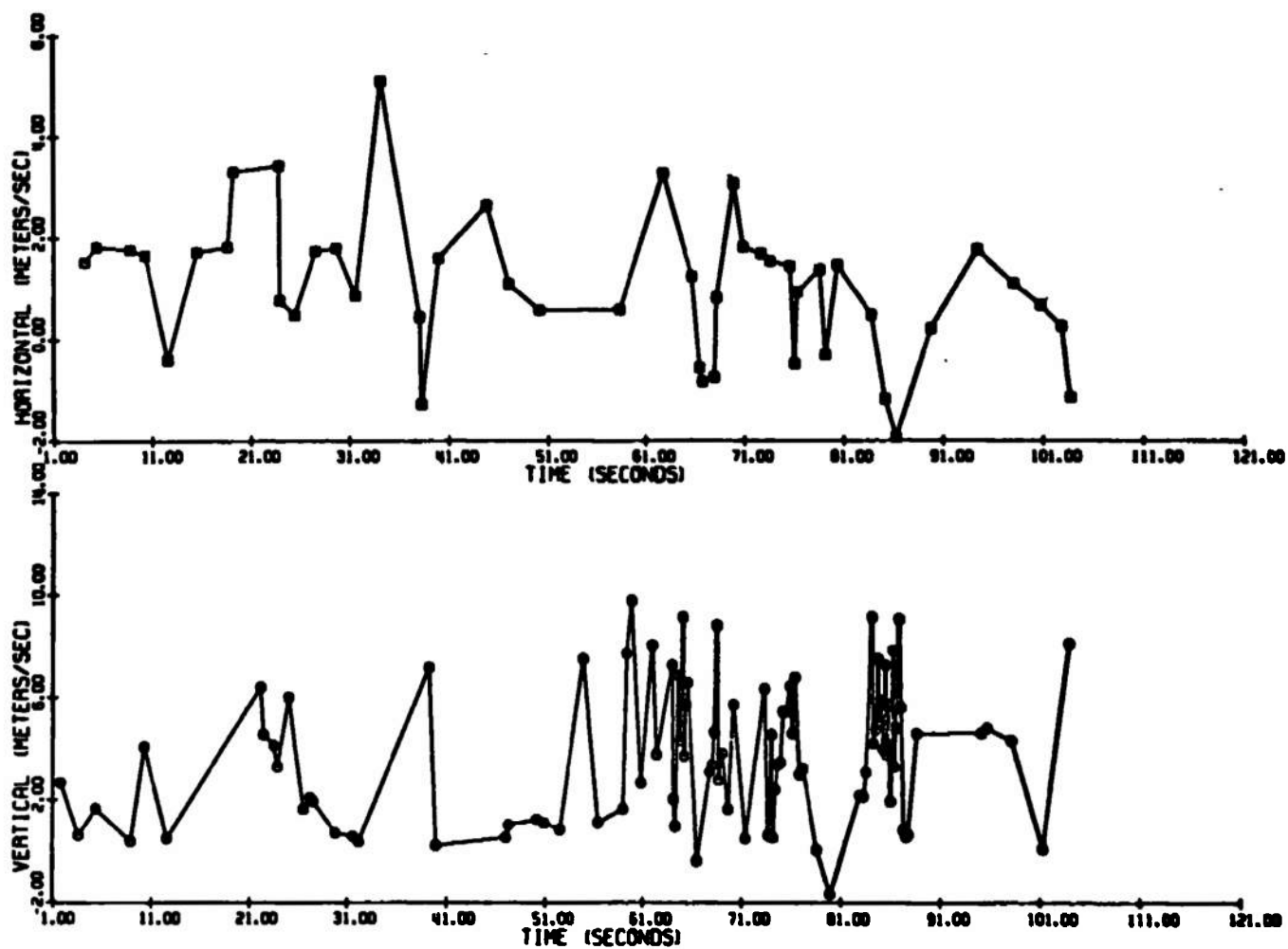


Figure 51. Trailing vortex LV data, run no. 8, 7/26/72.

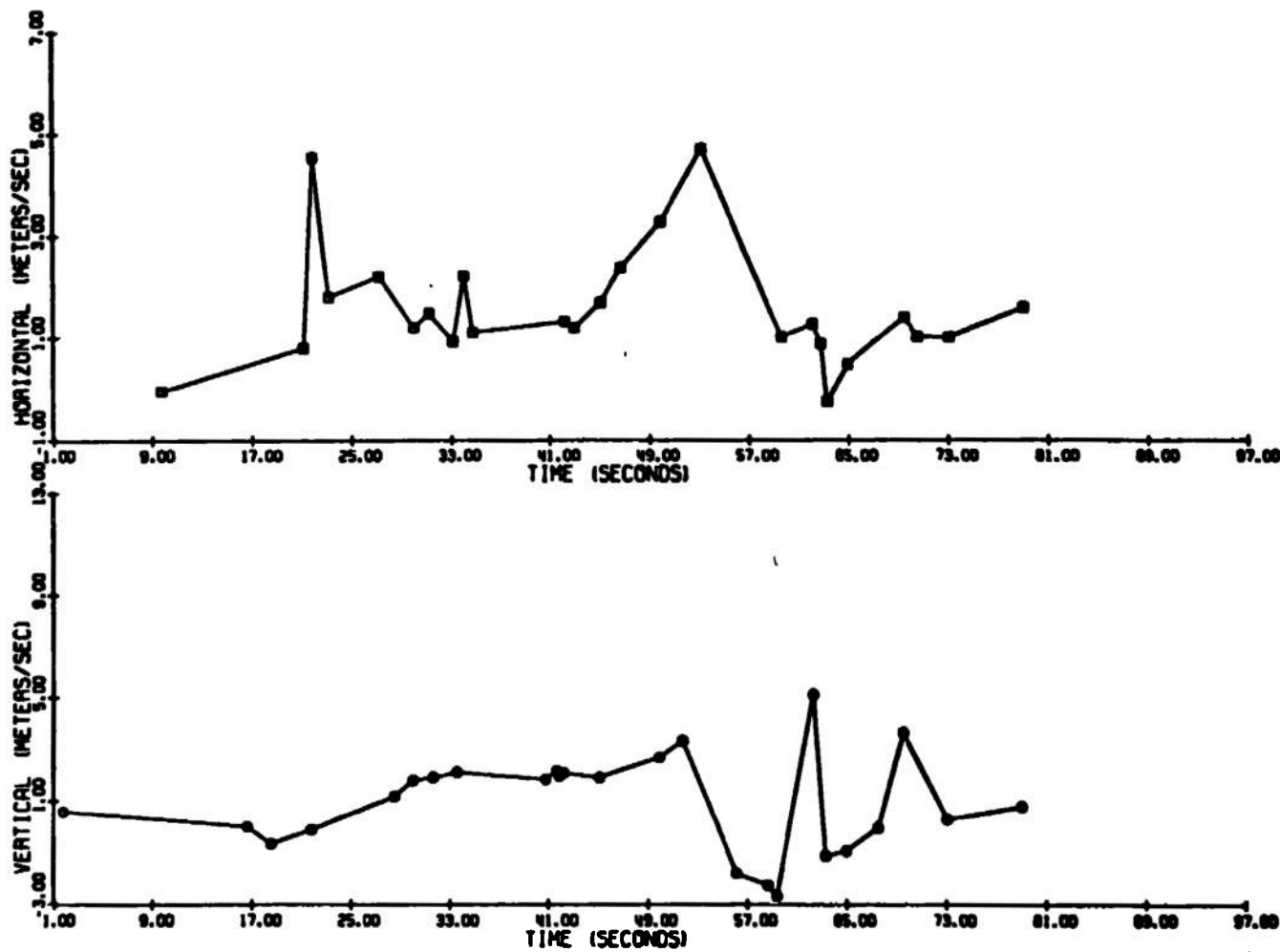


Figure 52. Trailing vortex LV data, run no. 9, 7/26/72.

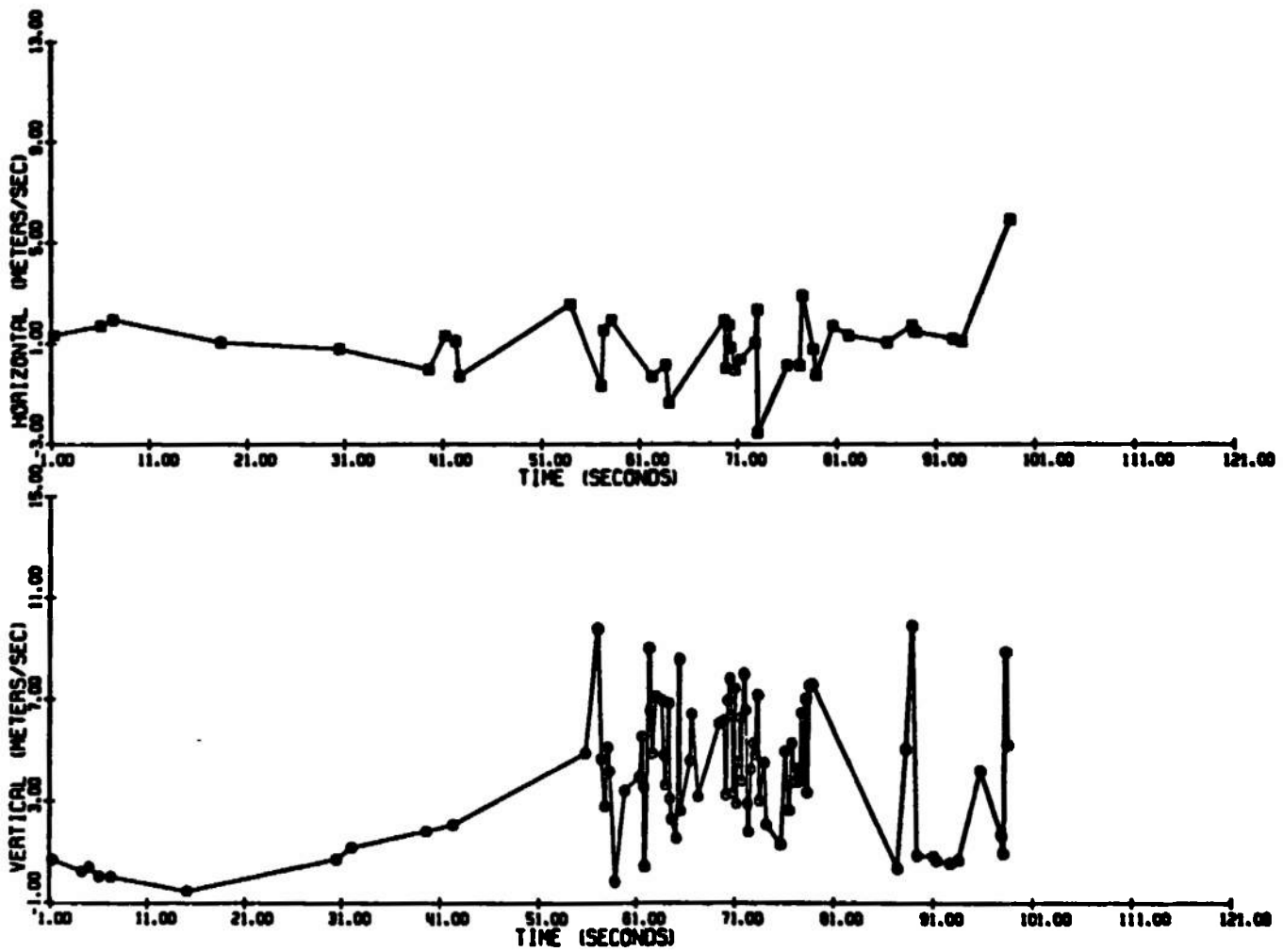


Figure 53. Trailing vortex LV data, run no. 10, 7/26/72.

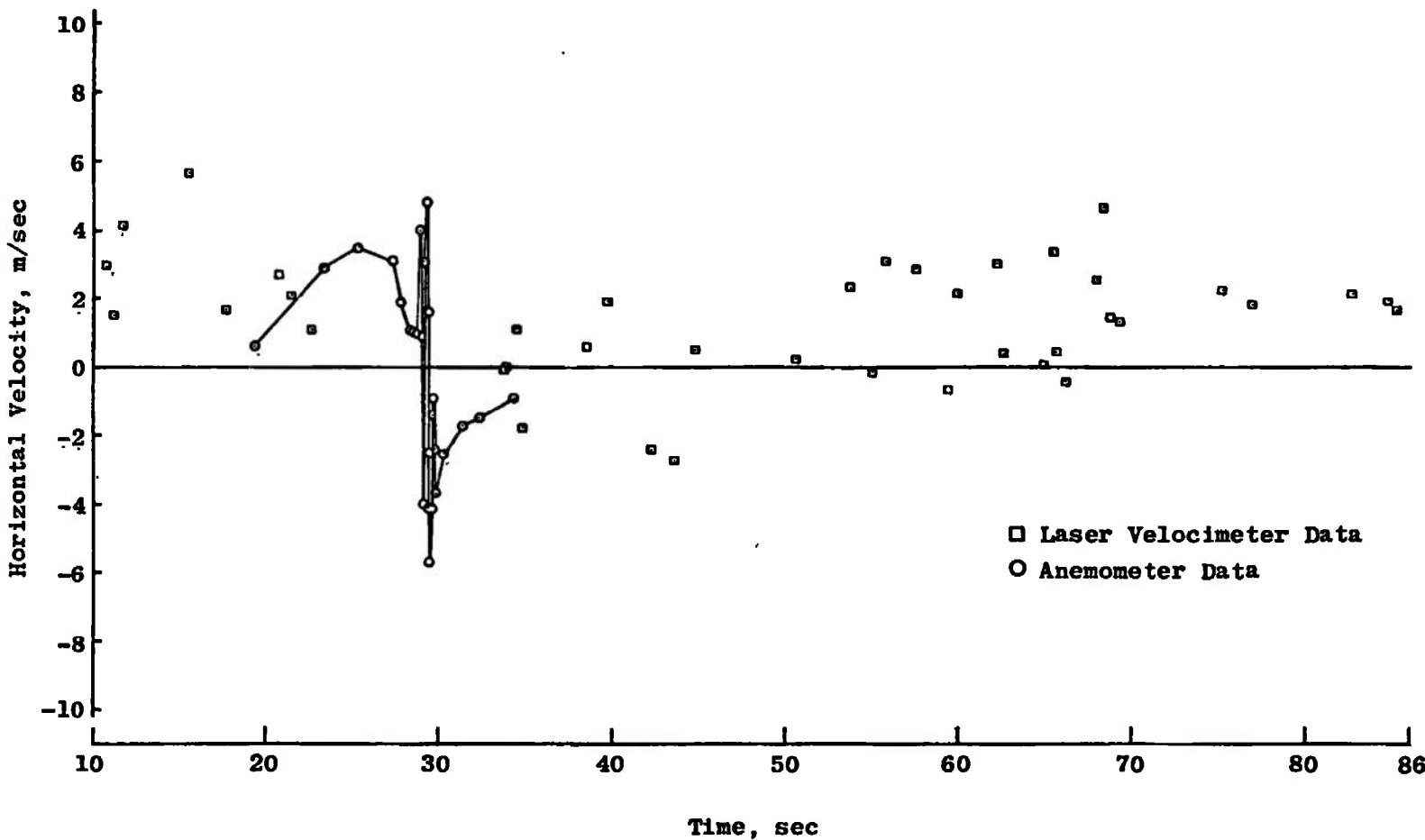


Figure 54. Trailing vortex LV and anemometer data, run no. 12,  
7/26/72 (horizontal velocity).

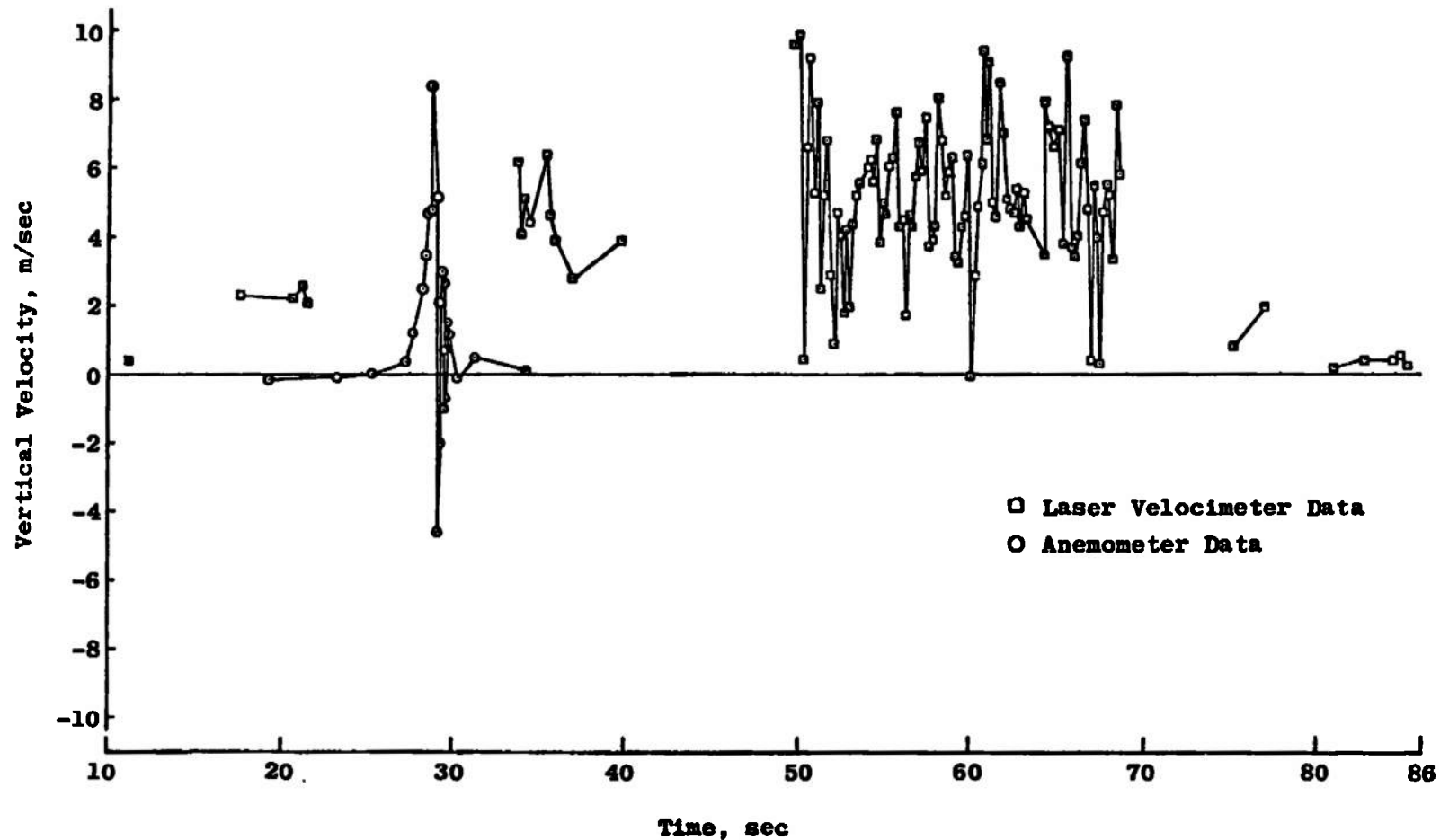


Figure 55. Trailing vortex LV and anemometer data, run no. 12,  
7/26/72 (vertical velocity).

611

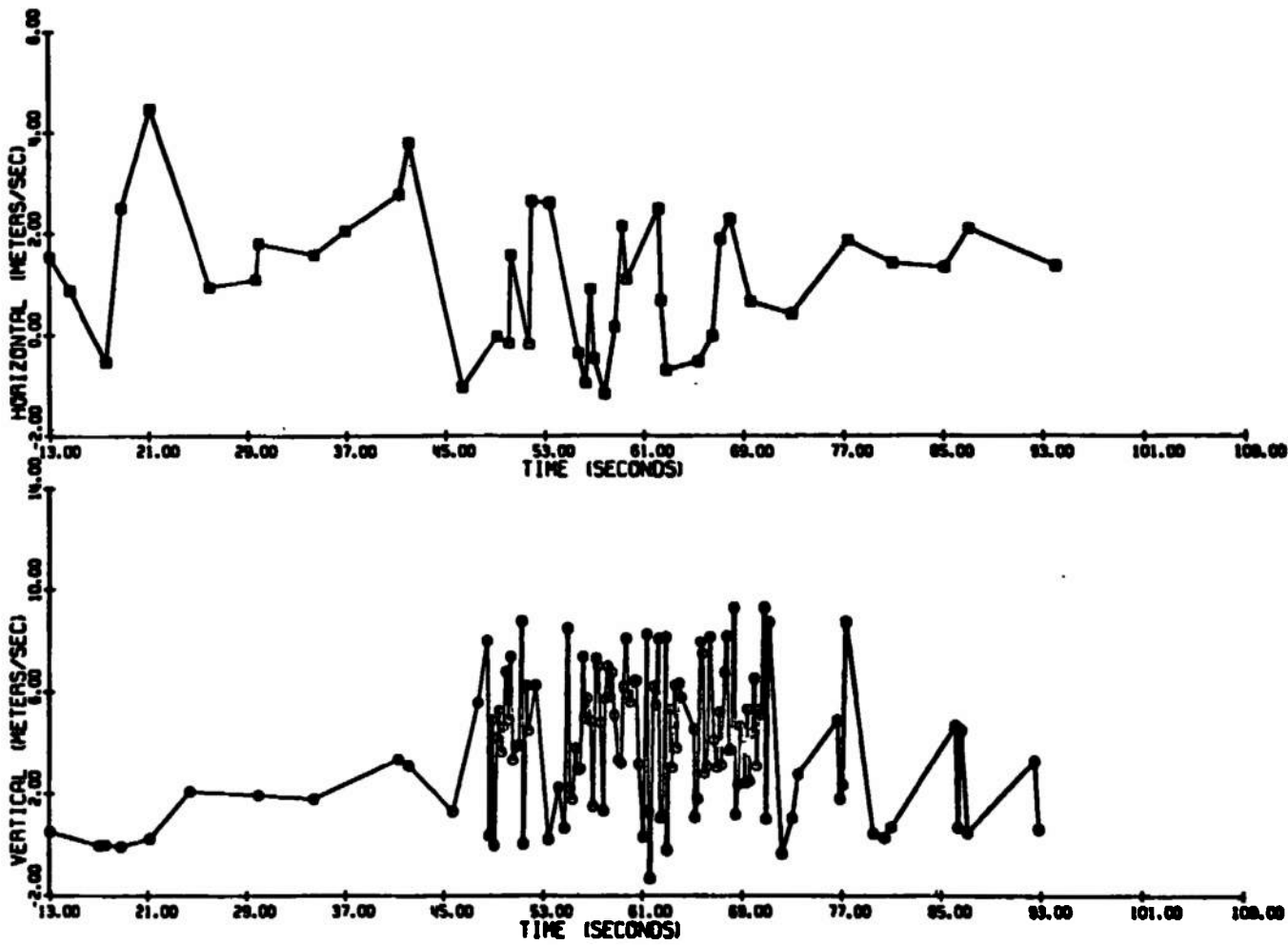


Figure 56. Trailing vortex LV data, run no. 13, 7/26/72.

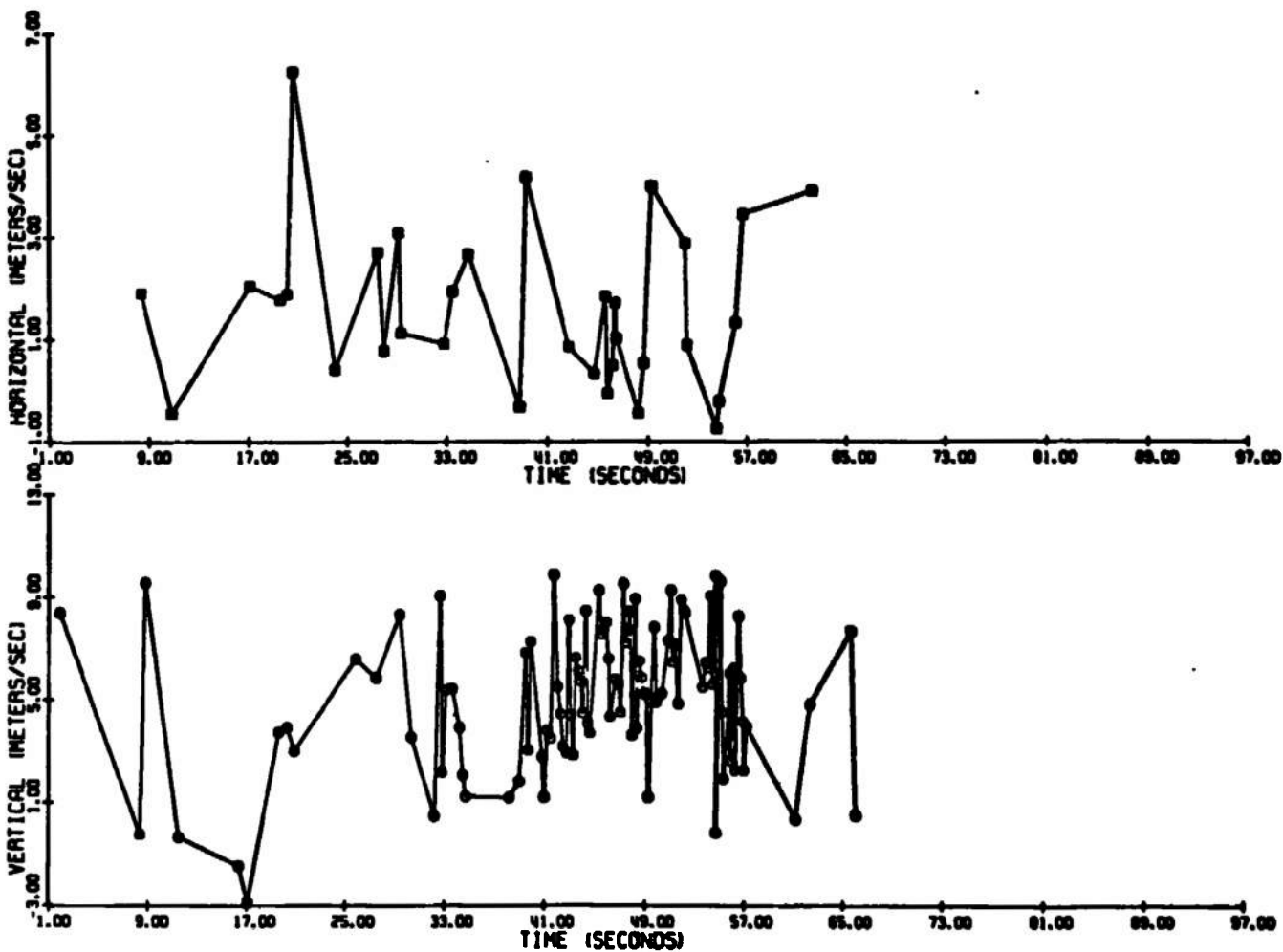


Figure 57. Trailing vortex LV data, run no. 2, 7/26/72.

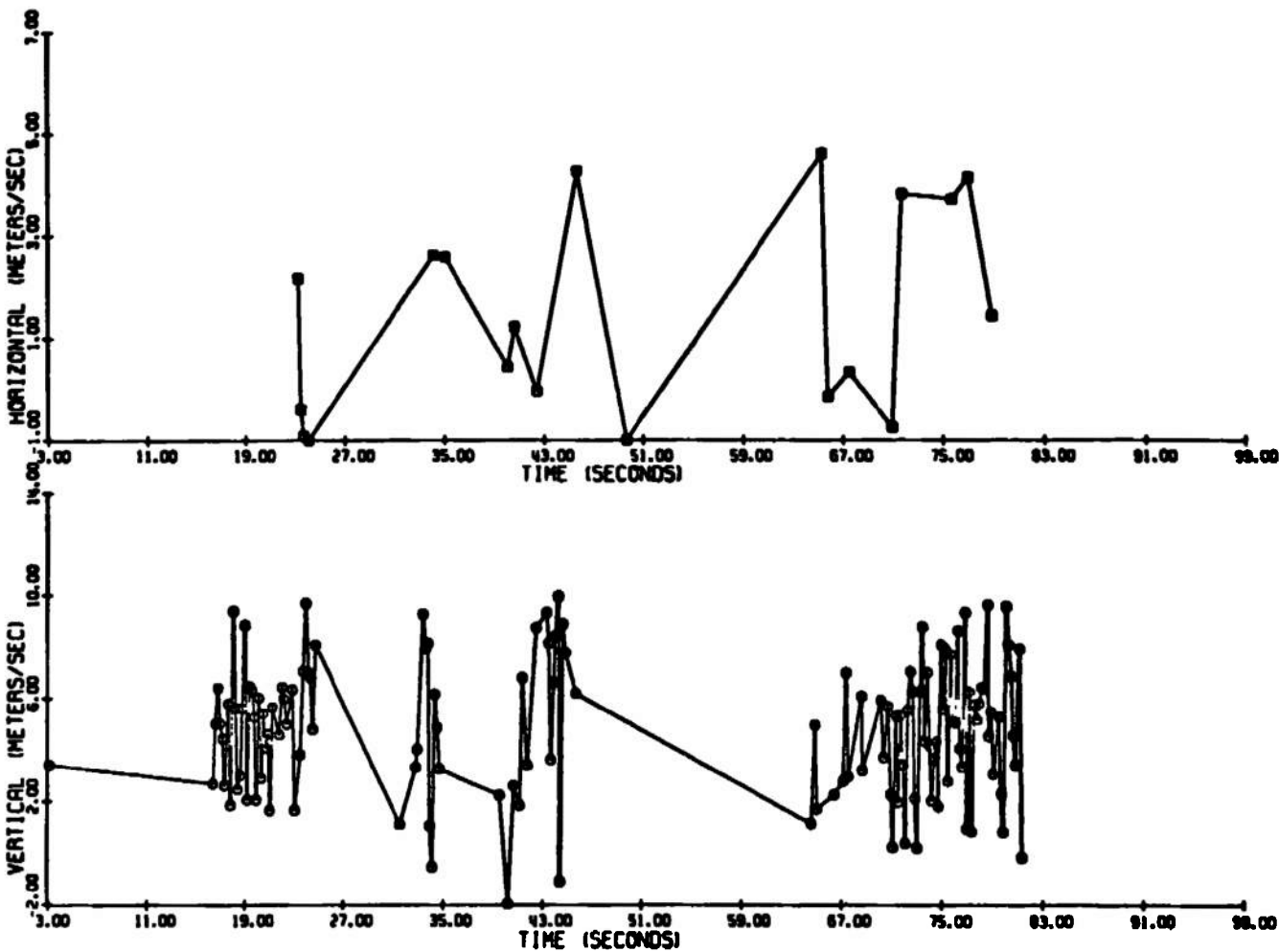


Figure 58. Trailing vortex LV data, run no. 4, 7/27/72.

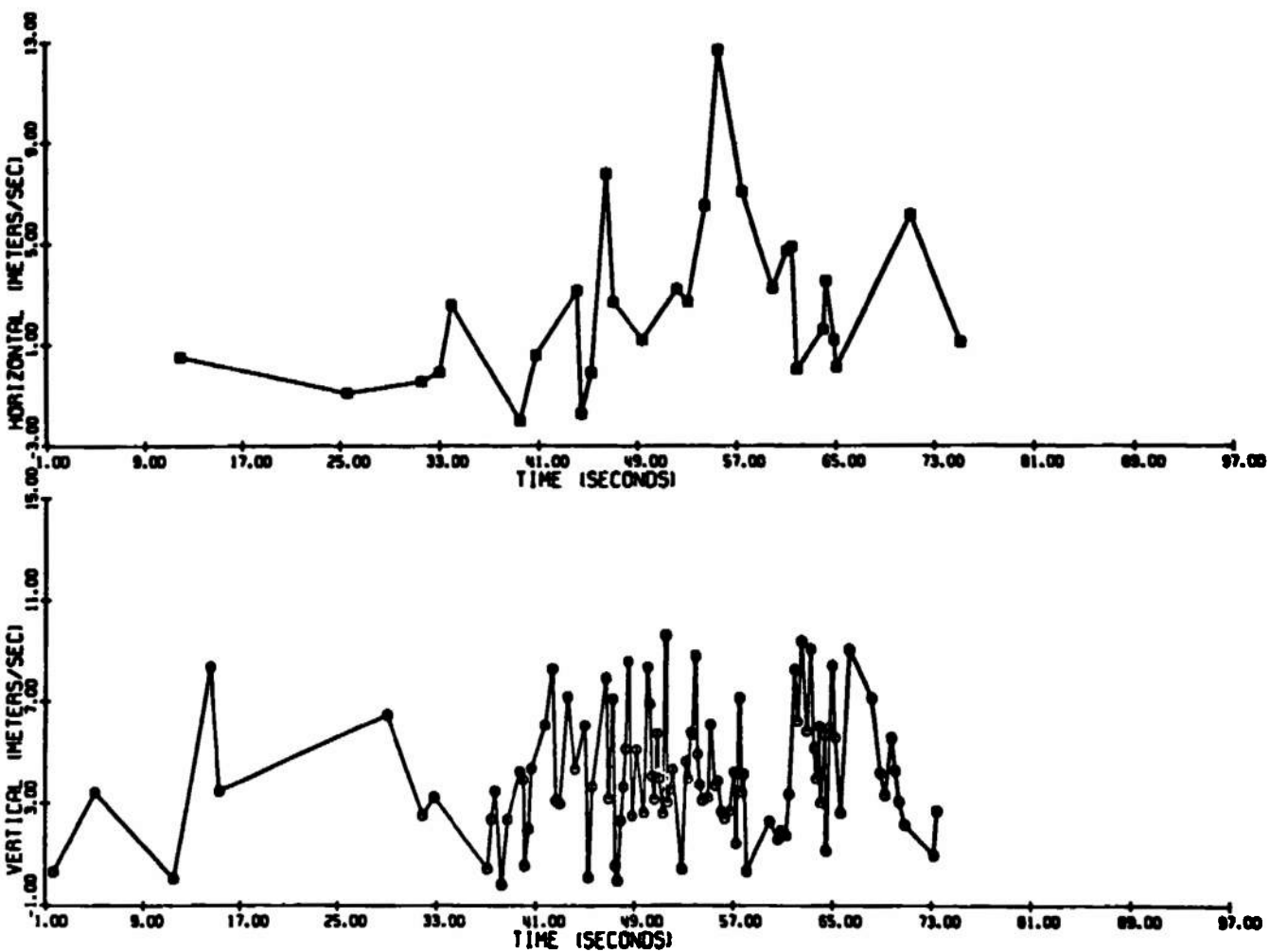


Figure 59. Trailing vortex LV data, run no. 24, 7/27/72.

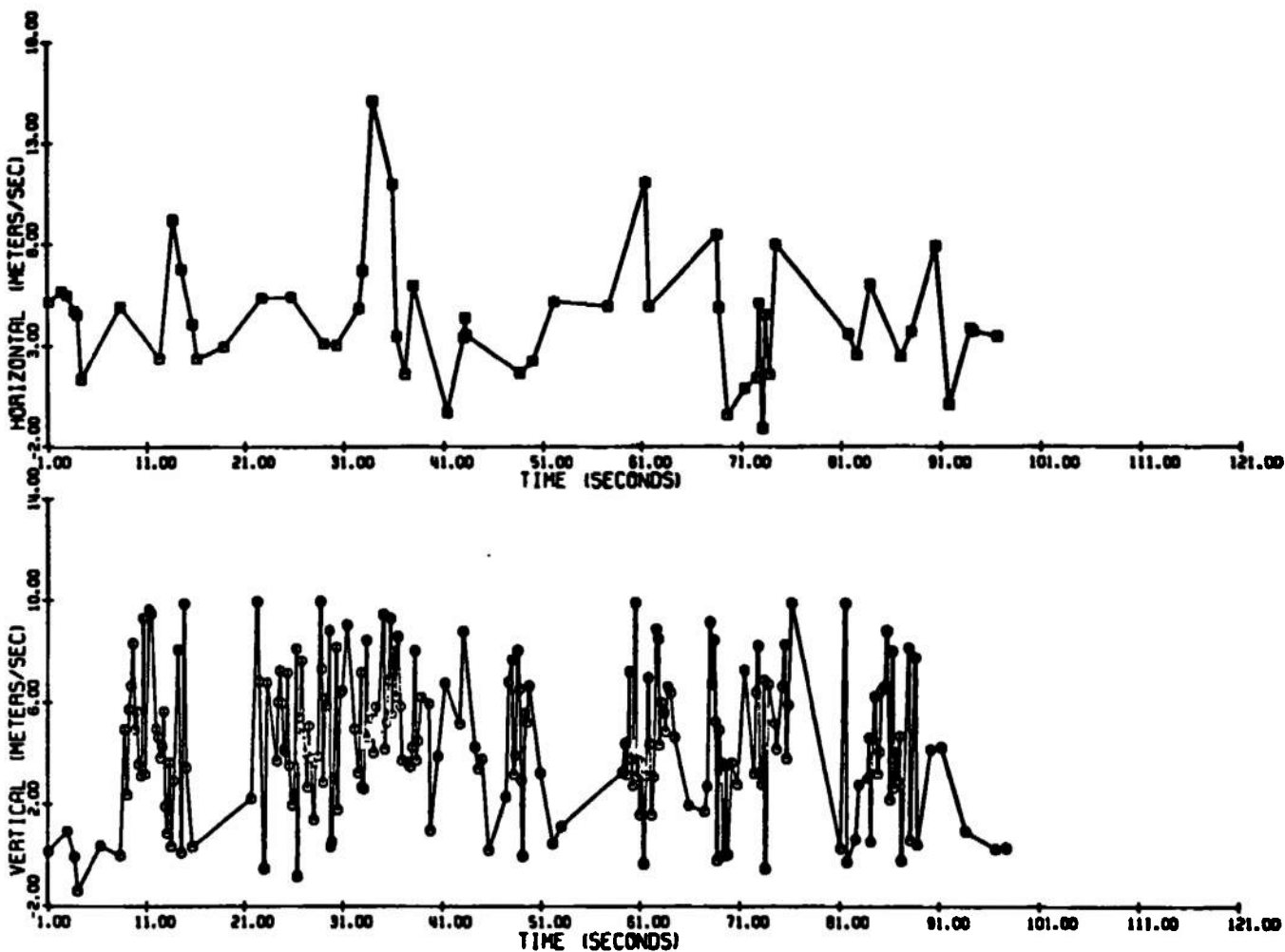


Figure 60. Trailing vortex LV data, run no. 26, 7/27/72.

## 9.0 PROPOSED MOBILE LV SYSTEM

### 9.1 GENERAL DESCRIPTION

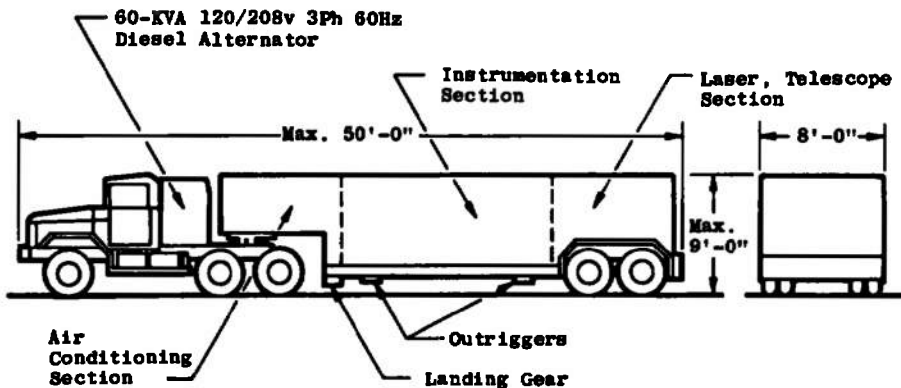
The proposed trailing vortex laser velocimeter system will be completely contained in a trailer towed by a diesel truck. The maximum length of the truck trailer combination is approximately 60 ft. The width of the truck will be a maximum of 8 ft and the height a maximum of 9 ft from the ground. The trailer will contain a 60 KVA diesel power unit to furnish all the necessary electric power required for the LV system. The truck will be located approximately 100 ft from the trailer during LV operation. The LV telescope section will be constructed so that the sides and roof may be removed to permit unobstructed visibility when required. In addition, it will be possible to open the doors on the rear of the truck in the event that horizontal scanning is required. The telescope system is to be shock mounted and the entire trailer section mounted on a floating floor isolated by means of out-riggers.

The overall truck-trailer system is schematically illustrated in Fig. 61. The figure depicts the sectionalization of the trailer with the location of the equipment as indicated. Figure 62 is a schematic of the telescope system compartment located on the trailer with the truck and power supply subsystem remotely located. The entire trailer complex will be designed such that it is capable of being transported by a means of a C-130 type or larger type aircraft.

### 9.2 TELESCOPE REQUIREMENTS

To determine the telescope and laser systems required for a full-scale, operating, remote sensing, laser velocimeter the experimental results discussed in previous sections were used to effect scaling laws.

The laboratory and experimental setup in performing vortex measurement at the AEDC runway in 1972 was used to determine the full-scale requirements. The efficiency of the Bragg Cell subsystem was approximately 80 percent. The efficiency of the 20.32-cm telescope used to position the transmitting beam into the 45.7-cm telescope was approximately 95 percent. The 25.4-cm telescope had an optical efficiency of approximately 95 percent. The efficiency of the 45.7-cm telescope was relatively poor, in comparison with the other two telescopes, and was approximately 60 percent. The overall efficiency of



#### SPECIFICATIONS

1. Tractor is to contain 60-KVA diesel power units to furnish all necessary electrical power to trailer from remote location of 100 feet.
2. Trailer to contain all necessary equipment for operating a trailing vortex and a remote-sensing LV system including:
  - A. Air Conditioning Section - This section will contain not only comfort and equipment cooling systems, but also refrigerated heat exchange system for self-contained laser coolant.
  - B. Instrumentation Section - This section will contain all instrumentation control and power-conditioning equipment for LV.
  - C. LV Telescope Section - This section is to have removable sides and roof to allow unobstructed visibility when required. In addition, the rear section should have removable doors for horizontal scanning application when required.
3. Entire unit is to be constructed so that it is transportable in a C-130 type aircraft or larger aircraft.

Figure 61. Mobile LV for vortices.

the transmitter-receiver telescope system used for scaling the full mobile unit was approximately 43 percent. Invariably, careful system design, specifically for remote sensing applications, should yield an improvement of transmitter-receiver collecting efficiency to 77 percent. A 931A photomultiplier tube was used in the AEDC experiments; quantum efficiency of this tube is approximately 10 percent. Careful selection of photomultiplier tubes to match the requirements will result in a factor of two increase in the quantum efficiency. Figure 63 contains the curves of laser power as function range for different telescope dimensions. From the figure, it is seen that the power requirements for a 48-in. telescope system can be met with state-of-the-art laser systems.

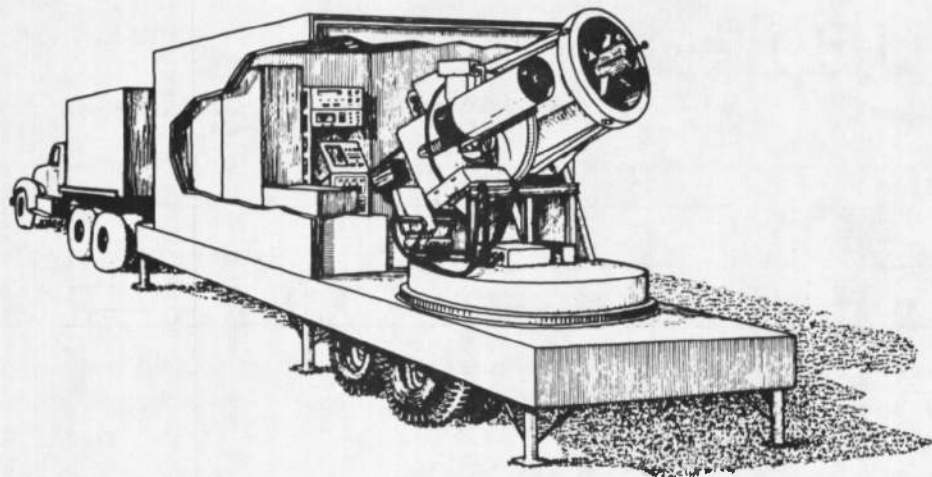


Figure 62. Conceptual design for the remote sensing velocimeter (dual-scatter-LO system).

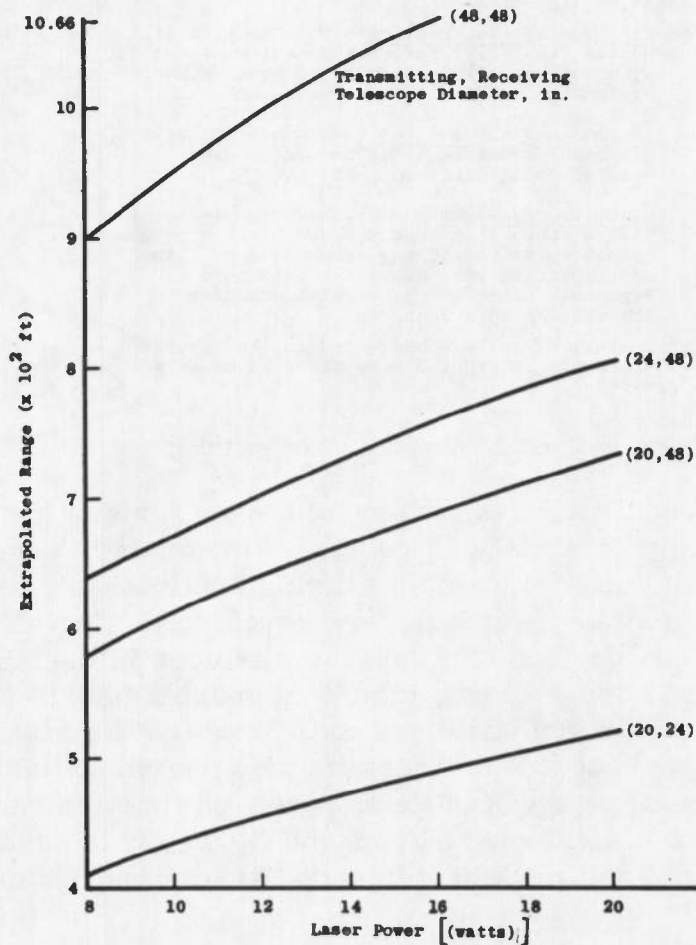


Figure 63. Laser power (watts) range-laser power relationship.

### 9.3 TELESCOPE

The telescope subsystem proposed for the remote sensing of trailing vortices is schematically illustrated in Fig. 64. In this telescope configuration the input of the TDBC velocimeter system, from the collimating optics, is transmitted through the eyepiece of the telescope. The secondary mirror has been cut out in a shape to accommodate the three transmitting beams from the Bragg cell. The secondary mirror is cruciform in shape (Fig. 65) such that the transmitted beam impinges upon the secondary mirror and is reflected to the primary; from the primary it is transmitted to the focal region. The three beams are focused on a common point in space. The scattered radiation is collected by the primary mirror, which is suggested to be a 48-in.-diam Cassegrain system. The radiation collected by the primary mirror is transmitted toward the secondary mirror. Since only a small portion of the secondary exists (this is used strictly for transmitting primary radiation to the focal region), the major portion of the radiation impinges upon a reflecting mirror located forward of the secondary mirror from which the beam passes through a collimating lens onto a package located external to the telescope system. This package is the detector subsystem that collects the radiation from the telescope and by means of a focusing lens places the radiation onto a color separating, or dichoric mirror, such that the  $5145\text{\AA}$  line of radiation impinges upon one of the photomultiplier tubes. Upon passing through signal conditioning and data processing electronics, two components of velocity are determined. The  $4880\text{\AA}$  line is transmitted to a separate PM tube to yield the third component of velocity. In this manner, it is possible to have a compact optical and electronics data collection and processing system. The telescope system has the unique characteristic in that it minimizes the possibility of scattered radiation from the secondary mirror returning to the detector of the coaxial, transmitter-receiver telescope system. The efficiency of the proposed optical system, utilizing highly reflective surfaces, is expected to approach 85 percent.

The focusing will be accomplished by using stepping motors or other servo-controlled systems for zooming the telescope. The scanning length will cover a range of  $\pm 50$  ft from the midpoint of the measuring region. For example, an aircraft flying at approximately 900 ft and with the transmitted focal point positioned 900 ft directly overhead, the system should be able to scan 900 ft  $\pm 50$  ft.

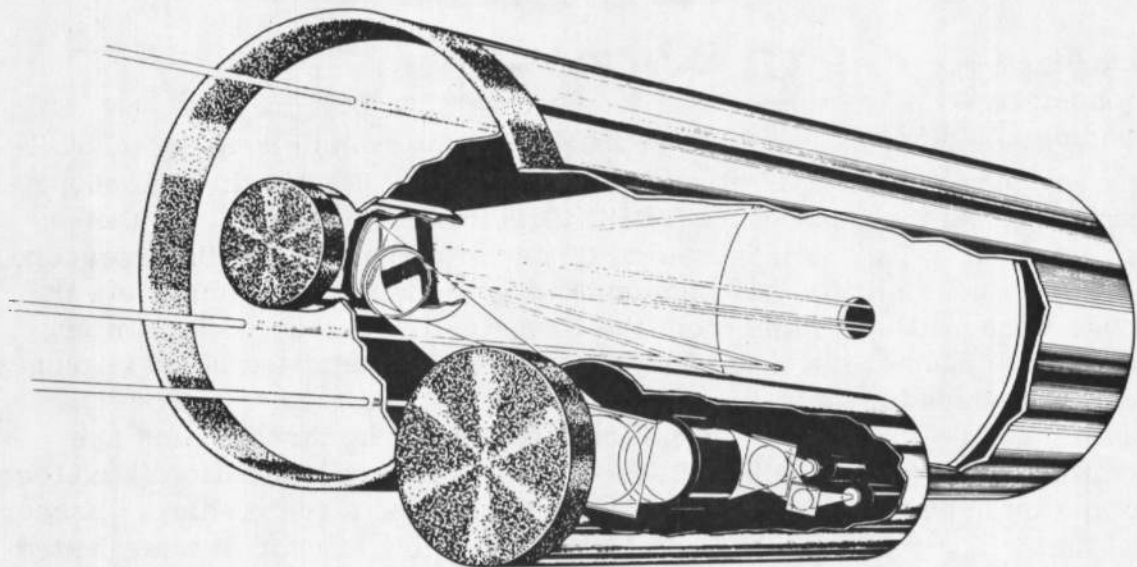


Figure 64. Remote sensing mono-static velocimeter.

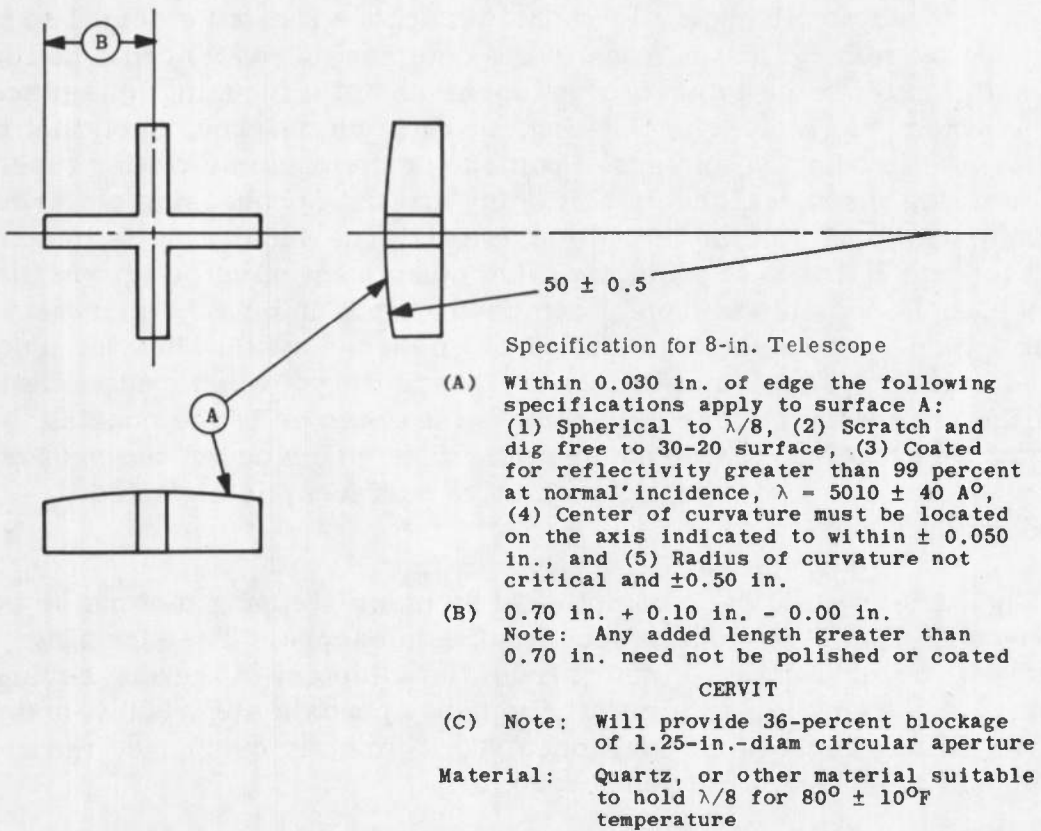


Figure 65. Spherical mirror segment.

Since Bragg cell frequencies will be used in conjunction with a monostatic system, two other parameters, of importance, are the fringe spacing and depth of focus as a function of range.

The fringe spacing  $d_s$  is determined from

$$d_s = \frac{\lambda}{2 \sin \theta/2}$$

The fringe spacing as a function of range and several selected Bragg cell frequencies is plotted in Fig. 66.

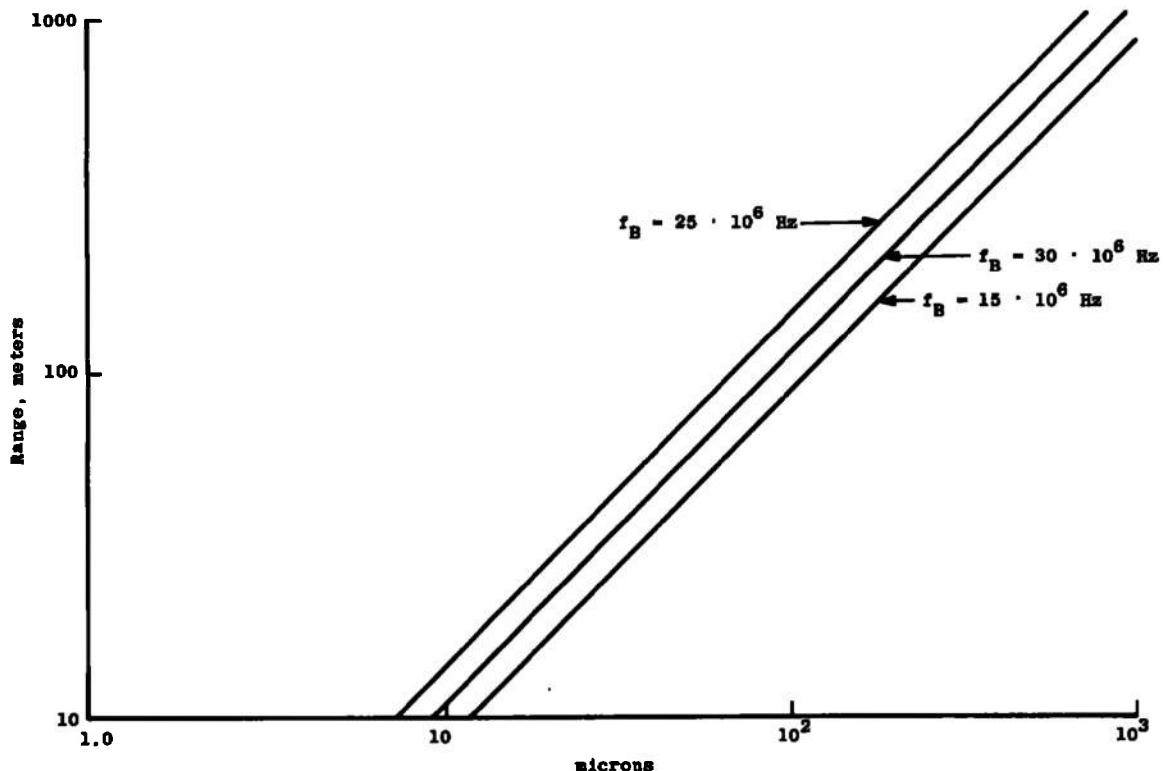


Figure 66. Fringe spacing.

The depth of field, or transmitted probe volume, is obtained from

$$d_f = \frac{\sqrt{2} d_v}{2 \sin \theta/2}$$

where  $d_v$ , the diameter of the focal volume, is determined from

$$d_v = \frac{4}{\pi} \lambda \frac{F.L.}{d_b}$$

F.L. is the focal length of the lens, on the range,  $\lambda$  = the wavelength of the laser, and  $d_b$  the laser beam diameter at the transmitting lens. A plot of the depth of field, as a function of range for the three selected frequencies, is plotted in Fig. 67.

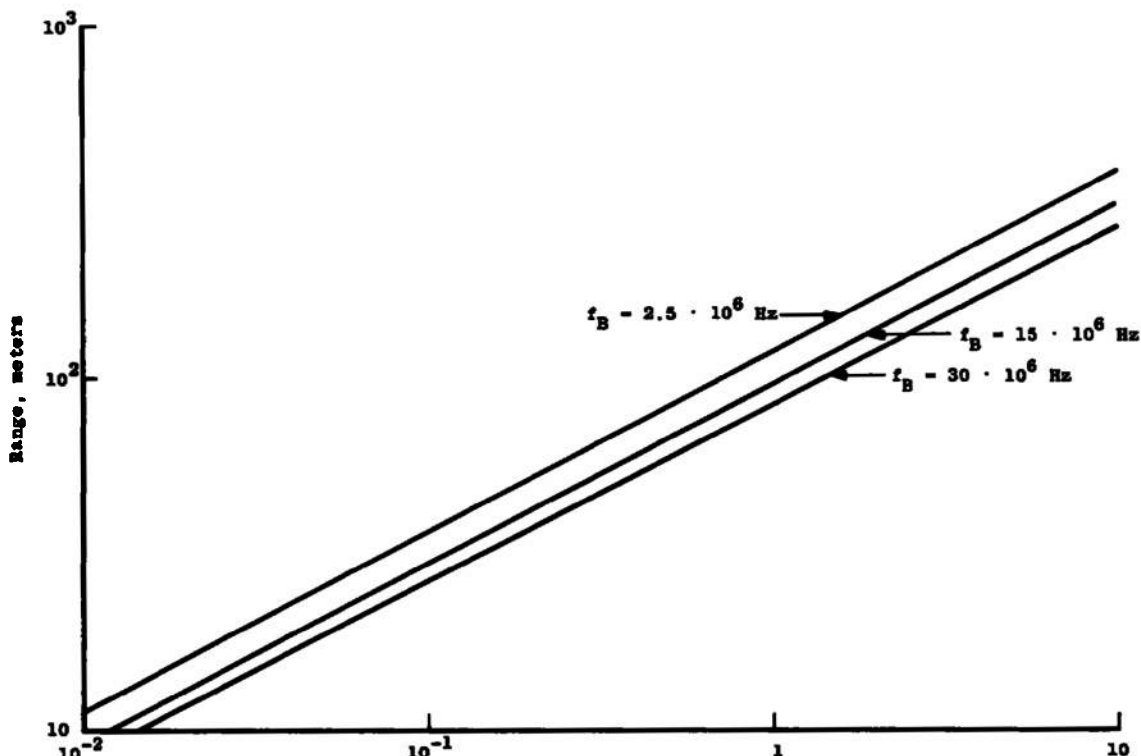


Figure 67. Transmitted probe volume length (cm).

## 10.0 CONCLUSIONS AND RECOMMENDATIONS

### 10.1 CONCLUSIONS

Theoretical analysis and confirming experiments indicate the dual-scatter laser velocimeter is capable of performing remote, trailing vortex flow field measurements. During the course of the experimental program of attempting to measure the trailing vortices at the AEDC runway, in 1972, a number of additional problems were uncovered. These problems must be resolved before the construction of a full-scale, mobile, operational, LV system can be undertaken. Nevertheless, sufficient operational data have been acquired to establish preliminary design criteria for such a system.

The salient problems that were encountered are:

- (1) The data acquisition rate of the horizontal component of velocity was always lower than the vertical component of velocity. The maximum data rate acquired, with the vertical component, was 11 data points per sec. This value was not consistent throughout the measurement period, but was sporadic as evidenced in Figs. 50 through 60. The data rate acquired for the horizontal component was approximately 1 per sec. This, obviously, is entirely too low for evaluating vortex characteristics. There are two main causes for this poor performance; (a) the LV system that was used at the AEDC runway was not optimized for this performance. The data rate could be readily enhanced by (i) a more efficient transmitter-receiver optical system designed specifically for this application and (ii) increasing the power density in the focal volume (higher power laser). (b) More atmospheric impurities were entrained in the rotational velocity field (vertical velocity component) than in the core of the vortex (horizontal component). This problem can be resolved, for a full-scale operational system, by increasing the power density for that particular component.
- (2) There is little significant correlation between the anemometer data and the LV data, as shown in Figs. 54 and 55. During the time span when the anemometer data were available, very little LV data were available; conversely, when LV data were available, anemometer data were not. Nevertheless, it may be presumed that during the latter portion of the experimental run, exhibited in Figs. 54 and 55, considerable data concerning the inner scale of turbulence, and hence vortex breakup, were acquired.
- (3) The three-component, dual-scatter, LV system has been proven feasible in the laboratory and a unit is being constructed, to include the newly developed cruciform secondary mirror, and will be checked out in an operating wind tunnel.
- (4) Performance of the Doppler data processor has been improved and is capable of handling high data acquisition rates quite accurately. Experiments have proven that the unit is capable of processing at least 40,000 data points per sec under favorable operating conditions.

(5) The two-dimensional Bragg cell has been used to provide data for determination of directionality as well as velocity magnitude. Furthermore, the moving fringe technique results in minimizing the "dead zone" characteristic of a stationary fringe system. In addition, the data acquisition time for a particle to traverse a given set of fringes required for a measurement is reduced thereby enhancing the data acquisition rate.

## 10.2 RECOMMENDATIONS

It is recommended that a two-phase program be conducted to acquire sufficient data to establish the validity of analytical techniques for determining trailing vortex characteristics. Model studies should be conducted both in a wind tunnel such as performed in Ref. 52 and in a hydrostatic channel as proposed in Appendix C of this report. In both of these studies, a three-component LV system could easily be used to acquire the data expediently. With the use of the hydrostatic channel an opportunity would be afforded to monitor the wake throughout the measuring period so as to ascertain the vortex decay characteristics. The wind tunnel model studies could yield wake data as a function of distance behind the aircraft.

In both of the model studies the cost, as a function of the amount of data acquired, would be economical as opposed to performing full-scale measurements at this time. When sufficient confidence is acquired in the analytical techniques, developed under the initial phase of the effort, then full-scale experiments can be performed to verify the model studies.

During the initial phase of the program, considerable improvements should be realized in the performance of LV systems. At the present time a two-component, backscatter, Bragg cell LV system is being operated at the AEDC PWT 4-T wind tunnel and considerable design information is being acquired. A three-component, backscatter, Bragg cell LV system is being constructed and its performance will also be evaluated in an operational environment. The Ronchi ruling concept has shown promise and additional effort is required to ascertain its performance. It appears entirely feasible that during the course of the Phase I, Model Study Effort, plans could be initiated for conducting the Phase II portion of the Program.

During the Phase II effort it is recommended, from an overall economic viewpoint, that the NASA-Langley 48- and 24-in. telescope be modified to accommodate a three-component, backscatter, Bragg cell system. A detailed experimental program can be formulated and conducted, at a predetermined site, to substantiate the model studies and scaling laws, using actual aircraft in flight comparable to the experiments previously performed.

## REFERENCES

1. McGowan, William A. "Remote Detection of Turbulence in Clear Air." Air Transportation Society Proceedings of the Conference, Key Biscayne. Vol. II, September 15, 1971, Key Biscayne, Fla.
2. Huffaker, R. M. "Laser Doppler Program for Velocity Turbulence Measurements." Project Squid Proceedings. "The Use of a Laser Doppler Velocimeter for Flow Measurements." March 9-10, 1972, Purdue University, Lafayette, Indiana.
3. Worsing, E. J., et. al. "Feasibility of Wake Vortex Monitoring Systems for Air Terminals." Final Report January 1971 - July 1972, NASA-CR 123821.
4. Farmer, W. M., Hornkohl, J. O., and Brayton, D. B. "A Relative Performance Analysis of Atmospheric Laser Doppler Velocimeter Methods." Optical Engineering Journal of the Society of the Photo-Optical Instrumentation Engineers, Vol. XI, No. 1, January-February 1972.
5. Brayton, D. B. and Goethert, W. H. "A New Dual-Scatter Laser Doppler-Shift Velocity Measuring Technique." ISA Transactions Vol. 10, No. 1, 1971, pp. 40-50.
6. Lennert, A. E., Brayton, D. B., Crosswy, F. L., et. al. "Summary Report of the Development of a Laser Velocimeter to be Used in AEDC Wind Tunnels." AEDC-TR-70-101 (AD871321), July 1970.
7. Lennert, A. E., Smith, F. H., and Parker, R. L. "Application of Dual Scatter Laser Doppler Velocimeters for Wind Tunnel Measurements." AGARD Lecture Series No. 49, Laser Technology in Aerodynamic Measurements. Presented at the von Kármán Institute for Fluid Dynamics, June 14-18, 1971.

8. Lennert, A. E., Hornkohl, J. O., and Kalb, H. T. "The Application of Laser Velocimeters for Flow Measurements." Presented at the Airbreathing Propulsion Conference, Monterey, California, September 19-21, 1972.
9. Massey, G. A. "Photomixing of Diffusely Reflected Light." Applied Optics, Vol. II, 1965.
10. Davis, D. T. "Analysis of Laser Doppler Velocimeter." ISA Transactions, Vol. 7, No. 1, p. 43, 1968.
11. Hugh, A. S., Oliver, C. S., Pike, E. R. and O'Shaughnessy. "Measurements of Wind Velocity by Laser Scattering." Royal Radar Establishment, Newsletter and Research Review, No. 9, 7/i, 1970.
12. Owens, J. C. "Optical Doppler Measurement of Micro-Scale Wind Velocity." Proceedings of the IEEE, Vol. 57, No. 4, 1969.
13. Friedman, J. D., Kinnard, K. F., and Meister, K. "Laser Doppler Instrumentation for the Measurement of Turbulence in Gas and Fluid Flows." Electro-Optical System Design Conference Proceedings, 1969.
14. Rudd, M. J. "A New Theoretical Model for the Laser Doppler-meter." Journal of Scientific Instruments (Journal of Physics E) Series 2, Vol. 2, 1969, p. 55.
15. McCormick, M. P. "Laser Backscatter Measurement of the Low Atmosphere." Ph. D. Thesis, Department of Physics, College of William and Mary, Virginia, 1967.
16. Huffaker, R. M., Jelalion, A. V., and Thomson, J. A. C. "Laser Doppler System in Detection of Aircraft Trailing Vortices." Proceedings of the IEEE, Vol. 58, No. 3, 1970.
17. Friedman, J., Harrisk, A., Jelalian, W., et al. "Remote Detection of Trailing Vortices." NASA-CR-121034, June 1971.
18. Brayton, D. B. "A Simple Laser, Doppler Shift, Velocimeter with Self-Aligning Optics." Presented at the Electro-Optical Systems Design Conference, September 16-18, 1969, New York Coliseum, New York.
19. Farmer, W. M. "Measurement of Particle Size, Number Density, and Velocity Using a Laser Interferometer." Applied Optics, Vol. 11, No. 11, November 1972.

20. Bullrich, K. "Scattered Radiation in the Atmosphere and the Natural Aerosol." Advances in Geophysics, No. 10, p. 99, 1964, Academic Press, New York.
21. Fried, D. L. "Optical Heterodyne Detection of an Atmospherically Distorted Signal Wavefront." Proceedings of the IEEE, January 1967, p. 57.
22. Hodaro, H. "Laser Wave Propagation through the Atmosphere." Proceedings of the IEEE, Vol. 54, March 1966, p. 368.
23. Treacy, E. B. "An Analysis of Some Factors Affecting the Accuracy of the Laser Doppler Velocimetry." Instrumentation in the Aerospace Industry, Vol. 17, p. 165-173, 1971. Published by the ISA.
24. Abramowitz, M., and Stegun, I. A. Handbook of Mathematical Functions, Dover Publication, Inc., New York, 1965, p. 26.
25. Tatarski, V. I. Wave Propagation in a Turbulent Medium, McGraw Hill Publishing Co., New York, 1961.
26. Junge, Christian E. "Vertical Profiles of Condensation Nuclei in the Stratosphere. Journal of Meteorology, Vol. 18, 1961, p. 501.
27. Bullrich, K. "Scattered Radiation in the Atmosphere and the Natural Aerosol." Advances in Geophysics No. 10, Academic Press, New York, 1964, p. 99.
28. Handbook of Geophysics and Space Environments. U.S.A.F. Cambridge Research Laboratories, McGraw-Hill, Inc., N. Y., 1965.
29. Mie, G. "Beitrage zur Optic trüber Medien, Speziell Kolloidaler Metallösungen." Ann. d. Physik, Vol. 25, 1908, p. 377.
30. Yanta, W. S., Gates, D. F., and Brown, F. W. "The Use of a Laser Velocimeter in Supersonic Flow." AIAA Paper No. 71-287, AIAA 6th Aerodynamic Testing Conference, Albuquerque, N. M., March 10-12, 1971.
31. Myers, J. F. "Investigation and Calculation of Basic Parameters for the Application of the Laser Doppler Velocimeter." NASA-TN D-6125, April 1971.
32. Waters, R. C., Jr., Lewis, R. D., and Waters, H. S. "Instruments for Motion Measurements Using Laser Doppler Heterodyning Techniques." ISA Transactions, Vol. 8, p. 20, 1969.

33. Cummins, H. Z., Knable, N., and Yeh, Y. "Observation of Diffusion Broadening of Rayleigh Scattered Light." Physical Review Letters, Vol. 12, 1964, p. 150.
34. Stevenson, W. H. "Optical Frequency Shifting by Means of a Rotating Diffraction Grating." Applied Optics, Vol. 9, p. 649, 1970.
35. Mazumder, M. K. "Laser Doppler Velocity Measurements without Directional Ambiguity by Using Frequency Shifted Incident Beams." Applied Physics Letters, Vol. 16, No. 11, June, 1970, pp. 462-464.
36. Chu, W. P. and Mauldin, L. E. "Bragg Diffraction of Light by Two Orthogonal Ultrasonic Waves in Water." Applied Physics Letters, Vol. 22, No. 11, June 1973.
37. Born, M. and Wolf, E. Principles of Optics, Pergamon Press, New York, p. 593, 1965.
38. Brown, D. and Goodman, J. E. High Intensity Ultrasonics, D. Van Nostrand, Princeton, 1965, p. 94.
39. Richardson, E. G. Ultrasonic Physics, Elsevier Publishing Co., New York, 1952, p. 188.
40. Lennert, A. E., Farmer, W. M., and Hornkohl, J. O. "LDV for Characterizing Aircraft Trailing Vortices." Proceedings of Project Squid Laser Doppler Velocimeter Workshop, Purdue University, March 9-10, 1972.
41. Crosswy, F. L. and Hornkohl, J. O. "Signal-Conditioning Electronics for a Vector Velocity Laser Velocimeter." AEDC-TR-72-192 (AD755842), February 1973; also Review of Scientific Instruments, Vol. 44, No. 9, September 1973.
42. Brayton, D. B., Kalb, H. T., and Crosswy, F. L. "A Two-Component, Dual-Scatter, Laser Doppler Velocimeter with Frequency Burst Readout." Applied Optics, Vol. 12, No. 6, 1973.
43. Farmer, W. M. "The Determination of a Third Orthogonal Velocity Component Using Two Rotationally Displaced Laser Doppler Velocimeter Systems." Applied Optics, Vol. 11, No. 4, April 1972.
44. Dennison, E. B. and Stevenson, W. H. "Oscillatory Flow Measurements with a Directionally Sensitive Laser Velocimeter." The Review of Scientific Instruments, Vol. 41, No. 10, October 1970, pp. 1475-1478.

45. Grant, G. R. and Orloff, K. K. "A Two-Color, Dual Beam, Back-scatter Laser Doppler Velocimeter." NASA TM X-62254, March 1973.
46. Clark, W. J. "Final Technical Report on the Application of Inertial Technique to Surveying." Litton Systems, Inc., Woodland Hills, California, November 1966.
47. Block, M. J. and Milgram, J. H. "Optical Detection of Local Fluid-Flow Velocities by Filtering in Space and Time." Optical Society of America Journal, Vol. 57, No. 5, May 1967, p. 604.
48. Heflinger, I. O., et al. "Portable Laser Velocimeter for Stack Velocity Measurements." PB 213 263, TRW Systems Group, Redondo Beach, California, November, 1972.
49. Willard, G. W. "Criteria for Normal and Abnormal Ultrasonic Light Diffraction Effects." The Journal of the Acoustical Society of America, Vol. 21, No. 2, March 1949, pp. 101-108.
50. Goethert, W. H. "Balanced Detection for the Dual Scatter Laser Doppler Velocimeter." AEDC-TR-71-70 (AD726093), June 1971.
51. Cline, V. A., Jr. "Dust Particle Velocity Measurements Using a Laser Velocimeter." AEDC-TR-72-159 (AD752225), December 1972.
52. Orloff, K. L. and Grant, G. R. "The Application of Laser Doppler Velocimeter to Trailing Vortex Definition and Alleviation." NASA TM X-62243, February 1973.

## APPENDIX A

### DETERMINATION OF A THIRD, DUAL-SCATTER, VELOCITY COMPONENT

It is now a straightforward procedure to determine two orthogonal velocity components in a gas flow using self-aligning dual-scatter LV optical systems developed and applied at the AEDC (Refs. A-1 through 4). The measurements may be made in any convenient coordinate system with respect to that defined by the LV optics, although it has been found most convenient to analyze only the backscattered or forward scattered radiation. In this appendix we will analyze only LV systems which utilize backscatter measurements. The extension to any other system is straightforward.

Measurement of the third velocity component,  $V_z$ , in a self-aligning backscatter system appears simple: a reference beam is mixed with the backscattered radiation to give a velocity component orthogonal to the two dual-scatter components. However, it has been shown that reference beam velocimeter systems tend to give inherently smaller signal-to-noise, S/N, power ratios than dual-scatter systems (Ref. A-1). While there exist a number of applications where the reference beam technique can be used with good results, there are some applications where it is not technically feasible. For example, in long range atmospheric LV systems where the return signal is distorted by turbulence, one would expect, on the basis of previous analysis, that the effective aperture for a heterodyned signal would be so small as to make detection impractical (assuming a real-time signal analyzer) (Ref. A-5).

The proposed dual-scatter method of determining the third velocity component to be discussed utilizes two rotationally separated velocimeter systems. Each system uses self-aligning optics but is not self-aligned with respect to the other system. This presents no real difficulty as long as the point where the velocity being measured is stationary. However, when this point moves the two systems must be synchronized such that they both observe the same point, otherwise obvious errors result. It follows that if the angles between the two systems are made as small as possible, one could possibly effect some type of self-alignment between the two systems--possibly generating the two through the same set of optics. Thus, it is necessary to determine the transformation equation between the two systems and the limitations on their angular separation such that the third velocity component can still be calculated.

For the reader to fully understand the development given here, it will be necessary to digress briefly and discuss a convenient interpretation of the LV (Refs. A-1 and A-6). For clarity, a long range, one-component, dual-scatter, backscatter LV system that has been developed is shown in Fig. A-1. At the point where the focused beams cross, the velocity is measured. The LV signals are generated (where the beams cross) within an ellipsoidal volume called the probe volume (Ref. A-1). Within the probe volume, interference fringes are formed due to the angular tilt of the two beams. A photomicrograph of these fringes at a range of 20 m is shown in Fig. A-2. The fringes define a set of planes which slice the probe volume into a set of bright and dark areas. Each plane is normal to the plane defined by the two crossed beams and parallel to the axis of the system. The output Doppler frequency may then be interpreted in terms of a particle crossing a set of fringes. From this interpretation, it should be clear that the velocity which is measured is only that component of the particle velocity which is normal to the fringe planes. Hence, the necessity of utilizing two rotationally separated velocimeter systems and determining the third component using measurements in each system. One could not, for example, expect to determine the third component by using one two-component velocimeter system and two rotationally separated simultaneous measurements of components generated by that system.

#### Derivation of the transformation equations

In this section, a generalized treatment of the coordinate transformation equations necessary to calculate the third velocity component from a knowledge of velocities measured in two rotationally separated systems is presented. It will be assumed that the velocimeters can specify both the magnitude and direction of the component velocities. The derivation is very similar to that found in standard mechanics texts which treat Euler angles.

Consider Fig. A-3 where we have three velocimeter beams ABC crossing to form a coordinate system  $x, y, z$  with origin 0 in the probe volume. ABO will be taken perpendicular to ACO. The  $x$  coordinates, which serve to define the velocity  $V_x$ , are formed by the fringe planes lying normal to ABO and parallel to AO as previously discussed.\*

---

\*Actually, the planes lie parallel to the bisector of angle ABO.

Since ABO is usually a very small angle, we can simplify the transformation considerably by assuming parallelism to AO.

Similar coordinates are formed for  $y$  and  $V_y$  by ACO. A velocity  $V_z$  cannot be defined by ABC per se. However, we will define a  $z$  coordinate and unit normal vector,  $\bar{e}_3$ , as being the right-handed normal to the coordinates and unit vectors defined by  $x$ ,  $y$ , and  $\bar{e}_1$ ,  $\bar{e}_2$ , respectively. In a similar manner, we use a second set of beams DEF with probe volume at 0, and a coordinate system  $x''', y''', z'''$  with unit vectors  $\bar{e}_1''', \bar{e}_2''', \bar{e}_3'''$ . Observe that plane DEO is required to be perpendicular to DFO in the same manner as the planes defined by ABO and ACO, and that the respective planes lie normal and parallel as discussed for the ABCO system.

Recall that coordinates or vector components in any two-dimensional rectangular coordinate system  $(x, y)$  are related to those obtained by a rotation of  $(x, y)$ , to  $(x', y')$  through some angle  $\theta$  by the matrix equation

$$\begin{bmatrix} x' \\ y' \end{bmatrix} = \begin{bmatrix} \cos(\theta) \pm \sin(\theta) \\ \pm \sin(\theta) \cos(\theta) \end{bmatrix} \times \begin{bmatrix} x \\ y \end{bmatrix} \quad (A-1)$$

where the upper (+) lower (-) signs are chosen for counterclockwise, CCW, rotations. Instead of writing the explicit sign dependence for the angles as in Eq. (A-1), the sign dependence will be assigned to the respective rotation angles. All CCW rotations will be defined as a positive rotation, while all clockwise, CW, rotations will be defined as a negative rotation.

Using transformations of the type in Eq. (A-1), the general transformation equation can be obtained. All rotations will be assumed CCW. First rotate through an angle  $\theta_r$  about DO to make  $e_2'''$  lie in the  $yz$  plane, and thus define a new coordinate system with unit vectors  $e_1''$ ,  $e_2''$ ,  $e_3'''$ ; hence

$$\begin{bmatrix} e_1'' \\ e_2'' \\ e_3''' \end{bmatrix} = \begin{bmatrix} \cos(\theta_r) \sin(\theta_r) & 0 \\ -\sin(\theta_r) \cos(\theta_r) & 0 \\ 0 & 1 \end{bmatrix} \begin{bmatrix} e_1''' \\ e_2''' \\ e_3''' \end{bmatrix} \quad (A-2)$$

Next rotate about  $e_2''$  by  $\theta_p$  to make  $e_3''$  lie in the  $yz$  plane and thus establish a new set of unit vectors  $e_1'$ ,  $e_2'$ ,  $e_3'$ , the required transformation is

$$\begin{bmatrix} e_1' \\ e_2' \\ e_3' \end{bmatrix} = \begin{bmatrix} \cos(\theta_p) 0 \sin(\theta_p) \\ 0 1 0 \\ -\sin(\theta_p) 0 \cos(\theta_p) \end{bmatrix} \begin{bmatrix} e_1'' \\ e_2'' \\ e_3'' \end{bmatrix} \quad (A-3)$$

Finally, we rotate by  $\theta_q$  about  $e_1'$  to obtain coincidence of ABC with DEF. This transformation is

$$\begin{bmatrix} e_1 \\ e_2 \\ e_3 \end{bmatrix} = \begin{bmatrix} 1 & 0 & 0 \\ 0 & \cos(\theta_q) & \sin(\theta_q) \\ 0 & -\sin(\theta_q) & \cos(\theta_q) \end{bmatrix} \begin{bmatrix} e_1' \\ e_2' \\ e_3' \end{bmatrix} \quad (A-4)$$

We obtain the transformation from the  $\bar{e}_i'''$  components and the  $\bar{e}_i$  components using Eq. (A-4). The result is

$$\bar{e} = \hat{R} \bar{e}''' \quad (A-5)$$

where R is the matrix given by

$$\hat{R} = \begin{bmatrix} (\cos(\theta_p) \cos(\theta_q)) & (\sin(\theta_p) \cos(\theta_q)) & (\sin(\theta_q)) \\ (-\sin(\theta_p) \cos(\theta_q) - \sin(\theta_q) \sin(\theta_p) \cos(\theta_q)) & (\cos(\theta_q) \cos(\theta_p) - \sin(\theta_q) \sin(\theta_p)) & (\sin(\theta_q) \cos(\theta_p)) \\ (\sin(\theta_q) \sin(\theta_p) - \sin(\theta_q) \cos(\theta_p) \cos(\theta_q)) & (-\sin(\theta_q) \cos(\theta_p) - \cos(\theta_q) \sin(\theta_p) \sin(\theta_q)) & (\cos(\theta_q) \cos(\theta_p)) \end{bmatrix} \quad (A-6)$$

Now, since  $\hat{R}$  is orthonormal (Determinant of R =  $\pm 1$ ),  $R^{-1} = R$ , where  $\hat{R}^{-1}$  is the matrix of the inverse of  $\hat{R}$ , and  $\hat{R}^T$  is the transpose of  $\hat{R}$ , we can easily transform back and forth between the two velocimeter systems using Eq. (A-5) with

$$\bar{e}''' = \hat{R} \bar{e} \quad (A-7)$$

$\hat{R}$  is the desired transformation whether we want to compare velocity components at a single point by two separate velocimeter systems or we want to relate components of a single velocimeter system to some more convenient coordinate system.

**Minimum Angular Separation Between Two LV Systems for the Calculation of the Third Velocity Component**

For this analysis, it is convenient to assume that  $\theta_r = 0$ , and that  $\theta_p, \theta_q \lesssim 0.1$ . \*\* Thus, the angles may be written as

$$\begin{aligned} \sin \theta_i &= \theta_i & i = p, q \\ \cos \theta_i &= 1 & \theta_i \ll 1 \end{aligned} \quad (A-8)$$

Also, for notational convenience call the  $e'''$  system the  $e'$  system. Then using the notation change and assumptions in Eq. (A-7) the transformation is ( $e' = Re$ )

$$\begin{bmatrix} \bar{e}' \\ \bar{e}'_2 \\ \bar{e}'_3 \end{bmatrix} = \begin{bmatrix} 1 & -\theta_p \theta_q & -\theta_p \\ 0 & 1 & -\theta_q \\ \theta_p & \theta_q & 1 \end{bmatrix} \begin{bmatrix} \bar{e}_1 \\ \bar{e}_2 \\ \bar{e}_3 \end{bmatrix} \quad (A-9)$$

Substituting the respective velocity components for the unit vector components, Eq. (A-9) reduces to

$$V'_x = V_x - \theta_p \theta_q V_y - \theta_p V_z \quad (a)$$

$$V'_y = V_y - \theta_q V_z \quad (b) \quad (A-10)$$

$$V'_z = \theta_p V_x + \theta_q V_y + V_z \quad (c)$$

---

\*\* Maintaining  $\theta_p, \theta_q \lesssim 0.1$  allows the possibility of transmitting both sets of LV beams through the same lens. Ordinarily, optimum use of the lens is made when the component beams are separated at the lens by about 0.8-lens diameters and the input beam diameters are about 0.1-lens diameters. The interference fringe spacing is then the Rayleigh resolution limit of the lens. The beam spacing for three beams set orthogonally to each other for a two-component LV system reduces the optimum beam separation somewhat, the loss being power density in the probe volume. For two two-component beam sets transmitting through the same lens, the component beam spacing becomes even smaller so that  $\theta_p, \theta_q$  must be small for nearly all practical transmitting lens F numbers.

Since  $V'_x$ ,  $V'_y$ ,  $V_x$ ,  $V_y$  are measured with the two systems, only Eqs. (A-10a) and (b) can be used to solve for  $V_z$ . All solutions of Eqs. (A-10a) and (b) will have some form of first or second order differences in the velocities, i.e., solutions will contain forms of  $(V_x - V'_x)$  etc., or  $(V'_x V_y - V_y V_x)$ , etc. The ability of the instrument to measure the velocity components with sufficient accuracy to determine these differences when they are small determines the minimum angles which must separate the two systems in order to calculate  $V_z$ . For example, if the prime system is set at  $\pi/2$  in a one-dimensional CCW rotation about  $x$  then  $V'_y$  is exactly  $V_z$  (see Eq. (A-4)) in the unprimed system, and  $V'_y$  is measured with the same degree of accuracy as  $V_x$ ,  $V_y$ . However, as the angle decreases,  $V_z$  is measured in terms of not only of  $V'_y$  but also  $V'_x$ , whose respective errors are adding, until we can no longer measure  $V_z$  with any accuracy because the instrumental error is too great. In the following analysis this angle and the velocity conditions which allow it to be made small are determined.

Solving Eq. (A-10b) for  $V_z$  in terms of first and second velocity differences yields

$$V_{z_1} = \frac{V_y - V'_y}{\theta_q} \quad (A-11)$$

where  $V_{z_1}$  indicates  $V_z$  is calculated using a first order velocity difference. Using Eqs. (A-10a) and (b),  $V'_x/V'_y$  can be written and solved for  $V_z$ , hence

$$V_{z_2} = \frac{V'_x V_y - V_x V'_y + \theta_p \theta_q V_y V'_y}{\theta_q V'_x - \theta_p V'_y} \quad (A-12)$$

where  $V_{z_2}$  indicates  $V_z$  is calculated using a second order velocity difference. Note, if only first order terms in  $\theta_i$  are kept in Eq. (A-9), all second order velocity differences (e.g.,  $V'_x V'_y - V_x V_y$ ) will all have the same form of solution for  $V_{z_2}$  under the same approximation.

Let the specific error (1 minus the specific accuracy) (Ref. A-7)  $\Delta V_{ij}/V_{ij}$  in a measurement of a first order velocity difference  $V_i - V_j$  be some specified value, say  $\Delta V_{ij}/V_i \leq C$ , before a measurement of  $V_z$  is claimed. Since the errors in the measurements of  $V_i$  are additive, then

$$\frac{\Delta V_{ij}}{V_{ij}} = \frac{\Delta V_i + \Delta V_j}{V_i - V_j} \quad (A-13)$$

or using C directly, Eq. (A-13) becomes

$$V_i - V_j \geq \frac{1}{C} (\Delta V_i + \Delta V_j) \quad (A-14)$$

Let b be the specific error for  $\Delta V_i$ ,  $\Delta V_j$  then Eq. (A-14) becomes

$$V_i - V_j \geq a(V_i + V_j) \quad (A-15)$$

where a has been written for b/C.

Using Eq. (A-15) in Eq. (A-11),  $\theta_{q1}$ , the angle of velocimeter system separation for calculation of  $V_z$  using a first order velocity difference, is given by

$$\theta_{q1} \geq \frac{a(V_y + V'_y)}{V_z} \quad (A-16)$$

It is observed that for small angles in  $\theta_p$ ,  $\theta_q$ ,  $V_x - V'_x$  and  $V_y - V'_y$  then Eq. (A-16) can be written as

$$\theta_{q1} \gtrsim 2a \frac{V_y}{V_z} \quad (A-17)$$

which is the desired result.

To calculate the limits in  $(\theta_p, \theta_q)$  for second order velocity differences, use Eqs. (A-12) and (A-15) and assume that the term to second order in  $(\theta_p, \theta_q)$  is negligible. Setting  $f\theta_{q2} = \theta_{p2}$ ,  $\theta_{q2}$  becomes

$$\theta_{q2} \gtrsim 2a \frac{V_y}{V_z} \left[ \frac{1}{(\pm)_q^1 - (\pm)_p \left[ \frac{V_y}{V_x} \right] f} \right] \quad (A-18)$$

where  $\theta_{q2}$  is the minimum angle of separation for the velocimeter systems in order to calculate  $V_z$  from a second order velocity difference. The sign dependence of the various rotations has been preserved through the notation  $(\pm)_{q,p}$  where the upper (lower) signs are chosen from CCW (CW) rotations and q,p subscripts indicate which angular rotations are being performed,  $\theta_q$  or  $\theta_p$ . There are two cases of Eq. (A-18) which require consideration: case one is where the signs in  $(\pm)_p$  and  $(\pm)_q$  are

opposite; case two is where they are the same. Case one corresponds to a mixture of rotation directions in  $\theta_q$  and  $\theta_p$ , i.e., one CCW rotation and one CW rotation. Case two corresponds to consecutive rotations in the same direction, e.e., either both ( $\theta_q$ ,  $\theta_p$ ) CCW or CW. If Fig. A-3 is examined and the indicated rotations performed for rotating the ABC system into the DEF system for the two cases, the coordinate system octants are found to which these rotations apply. Figure A-4 shows the octant end faces in which the different rotation directions place the ABC system.

For case one, Eq. (A-18) gives

$$\theta_{q2} \geq \pm 2a \frac{V_y}{V_z} \frac{1}{\left(\frac{fV_y}{V_x} + 1\right)} \quad (A-19)$$

On using Eq. (A-17), Eq. (A-19) can be written as

$$\theta_{q2} \geq \theta_{q1} \frac{1}{\frac{fV_y}{V_x} + 1} \quad (A-20)$$

For case two, Eq. (A-18) gives

$$\theta_{q2} \geq \theta_{q1} \left[ \frac{1}{\frac{fV_y}{V_x} - 1} \right] \quad (A-21)$$

Thus, it can be concluded that for case one, second order velocity difference calculations for  $V_z$  require a minimum of the same angular separation as for the first order velocity difference calculation. However, when  $f(V_y/V_x) \gtrsim 1$ , second order velocity difference calculations require significantly smaller angular displacements than for first order calculations. Figure A-5 illustrates this characteristic. From Eqs. (A-20) and (A-21), one can see that for  $f(V_y/V_x) \gg 1$ ,  $\theta_{q2}$  is about the same in both cases. However, when  $f(V_y/V_x) \approx 1$ ,  $\theta_{q2}$  for case two will be much greater than  $\theta_{q1}$  and first order calculations require much smaller angular separations than the second order calculations. This effect is illustrated in Fig. A-6.

This analysis leads to a surprising result. The sizes of the angles through which the two velocimeter systems must be displaced are very sensitive to the direction of the displacement when  $f(V_y/V_x) \approx 1$ . If it occurs that the displacement is in the direction of case two and  $f(V_y/V_x) \approx 1$ , then a second velocimeter system with only one-component capability need be used.

If  $V_y$  or  $V_x$  in Eqs. (A-20) and (A-21) happens to have a negative magnitude (which leads to a left-handed coordinate system in unprimed coordinates), then the values of the two cases are reversed. It follows that unless there is a priori knowledge concerning the direction of the velocities to be measured, the direction and magnitude of the angles of separation of the two systems must be at least as large as  $\theta_{q_1}$ . Under

these circumstances, one needs to measure only one component,  $V_y'$ , the second component,  $V_x'$ , contributing nothing to the determination of  $V_z$ . However, if sufficient knowledge of the relative magnitudes and directions of the respective velocity components exists, then one can always choose an appropriate separation direction such that Eq. (A-21) is satisfied. The separation angles must then be at worst ( $f(V_y/V_x \ll 1)$ ) as large as  $\theta_{q_1}$  and at best ( $f(V_y/V_x) \gg 1$ ) significantly less than  $\theta_{q_1}$ .

It was tacitly assumed that  $f \approx 1$ ; obviously, one could always satisfy  $f(V_y/V_x) \gg 1$  by judiciously choosing  $f$  for any  $V_y$ ,  $V_x$ . However, the goal of making  $\theta_p$ ,  $\theta_q$  as small as possible is endangered if  $f$  is required to be too large. One gains the advantage of using smaller ( $\theta_q$ ,  $\theta_p$ ) by measuring two velocity components in the primed velocimeter system if the rotations are in the directions of case two.

It is interesting to note that in case one when  $V_x \approx V_y \approx V_z$ , and  $f \approx 1$ , that  $\theta_{q_2} \approx a$ . Furthermore, in all cases where  $V_z \gg V_y$ ;  $V_x$ ;  $\theta_{q_1} \ll a$ . It follows that when either  $a$  is small, or  $V_z$  is much larger than  $V_x$  and  $V_y$  that ( $\theta_q$ ,  $\theta_p$ ) can be very small. This leads to the possibility of transmitting both sets of velocimeter system beams through the same set of optics, thereby making the two systems self-aligning with respect to each other.

### Summary and Conclusions

A generalized transformation equation has been developed for components of velocity measured in two rotationally separated two-component velocimeter systems. The transformation allows for mixtures of rotation directions in rotating the coordinate axes from one system to the next. From the measurements in the two systems and the

transformation equation, the third orthogonal component of velocity  $V_z$  in either system can be determined. The transformation may also be used to relate components measured off-axis from a single system to those defined by the system on-axis (axis being defined as the normal to the x and y components).

The minimum separation angles which are required between the two velocimeter systems depend on the specific error of the instrument used to convert the power scattered from the probe volume into velocity information and the relative magnitude of the velocities  $V_y$ ,  $V_z$ . It has been shown that in special cases, depending on the direction the second system has been rotated relative to the first, calculation of  $V_z$  from second order velocity differences can considerably relax the minimum angular separation requirement. To calculate second order velocity differences, a two-component second velocimeter system is required as opposed to a first order difference calculation requiring a one-component second system. Therefore, a system measuring two velocity components can relax the minimum separation angle requirement determined for a one-velocity component system. It has been found that whether or not a two-component second system can relax the angular separation requirements depends on the direction the second system has been rotated relative to the first system, the relative velocity directions in the two systems, and the relative velocity magnitudes.

## REFERENCES

1. Brayton, D. B. and Goethert, W. H. "A New Dual-Scatter Laser Doppler-Shift Velocity Measuring Technique." ISA Transactions, Vol. 10, No. 1, 1971, pp. 40-50.
2. Lennert, A. E., Brayton, D. B., Goethert, W. H., and Smith, F. H. "Laser Applications for Flow Field Diagnostics." Laser Journal, Vol. 2, No. 2, March/April 1970.
3. Smith, F. H. and Parsons, J. A. "Velocity Measurements in the AEDC Low Speed Wind Tunnel (VISTOL) Using a Laser Doppler Velocimeter." AEDC-TR-70-119 (AD 708717), July 1970.
4. Yanta, W. J., Gates, D. F., and Brown, F. W. "The Use of a Laser Doppler Velocimeter in Supersonic Flow." Presented at AIAA 6th Aerodynamics Testing Conference, Albuquerque, New Mexico, March 10-12, 1971.

5. Fried, D. L. "Optical Heterodyne Detection of an Atmospherically Distorted Signal Wave Front." Proceedings of the IEEE, Vol. 55, January 1967, p. 57.
6. Rudd, M. J. "A New Theoretical Model for the Laser Doppler-meter." Journal of Scientific Instruments (Journal of Physics E), Vol. 2, 1969, p. 55.
7. Trimmer, J. D. "Response of Physical Systems." John Wiley and Sons, Inc., New York, 1950, p. 150.

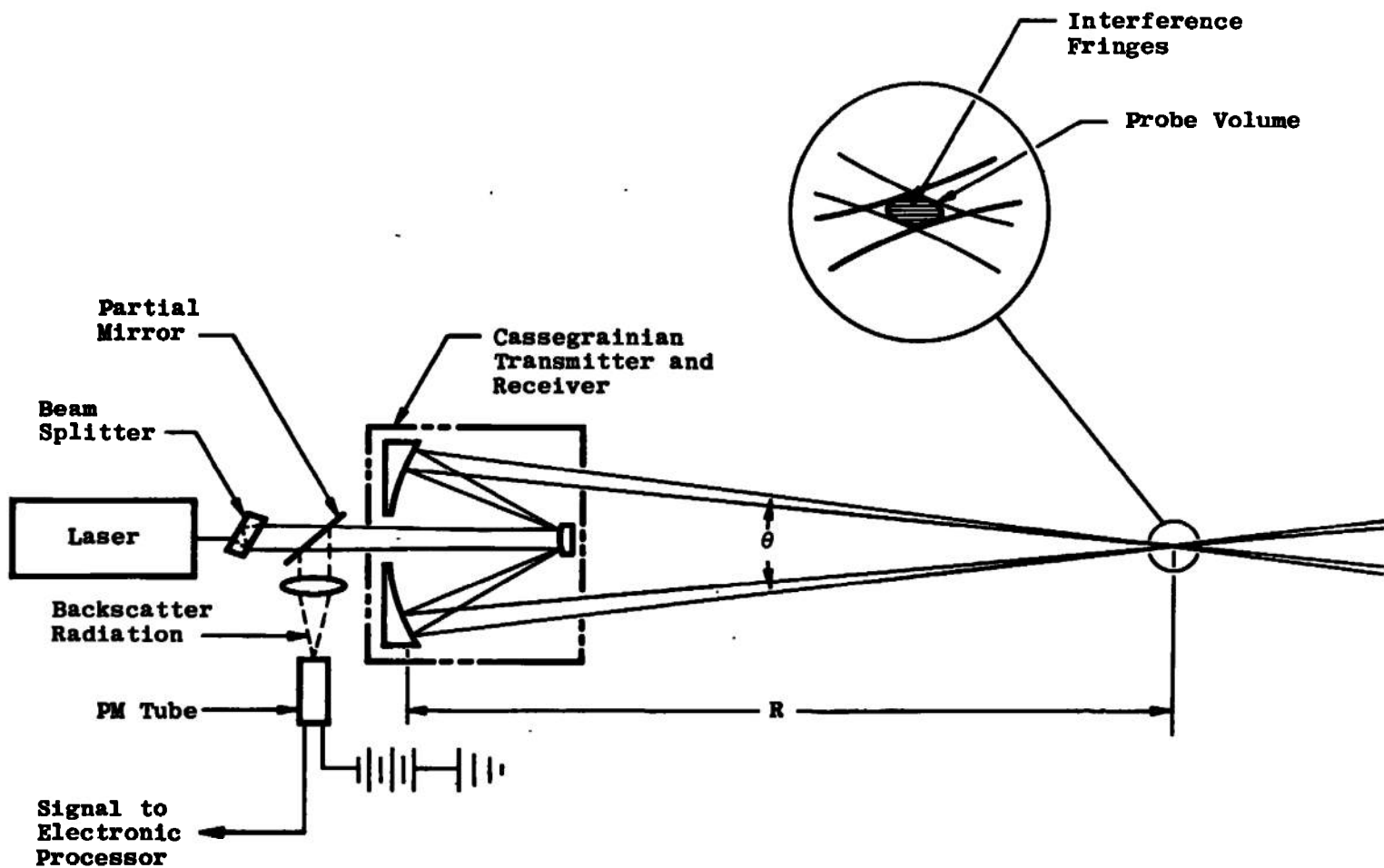
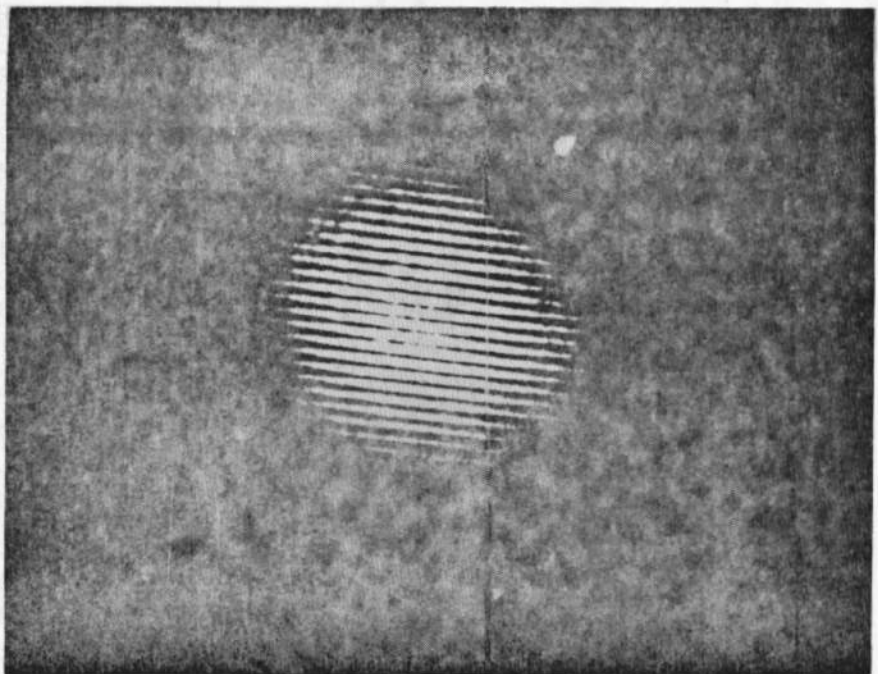


Figure A-1. One velocity component, long range-coaxial dual-scatter backscatter LDV system.



**Figure A-2. Photomicrograph of one-velocity-component interference fringes in the probe volume.**

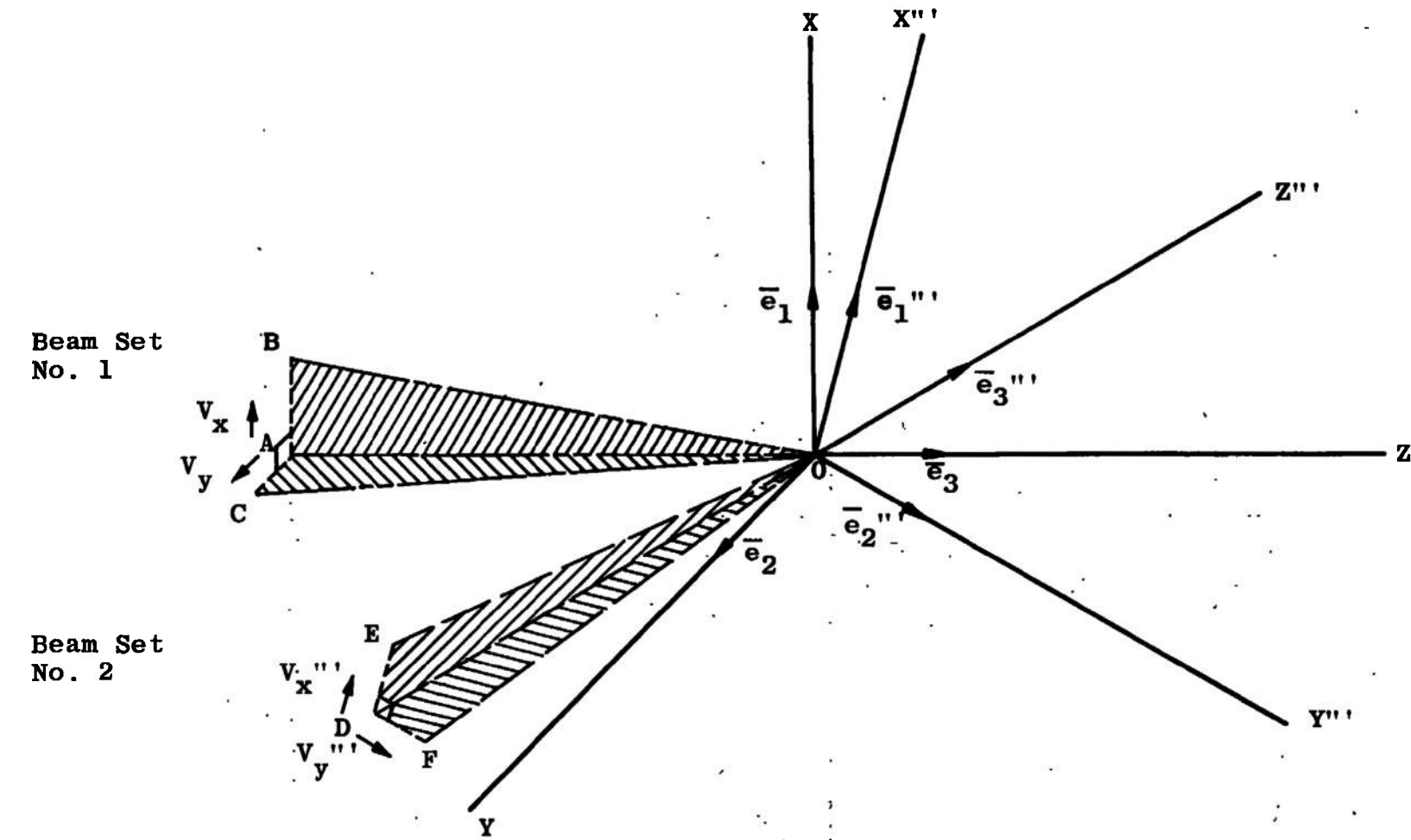


Figure A-3. Geometry for two rotationally separated two-velocity-component LDV systems observing a common point.

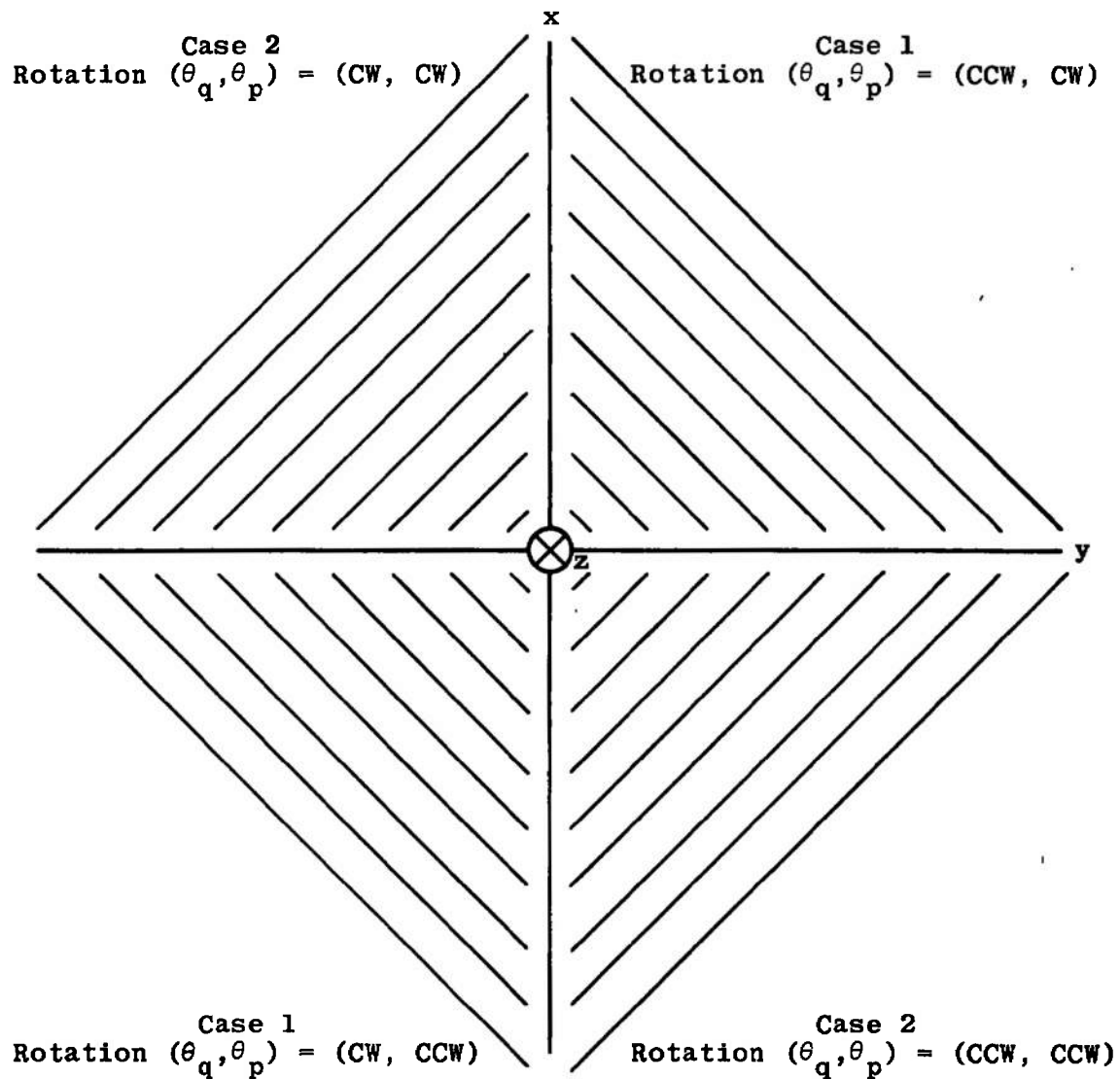


Figure A-4. End view of xyz coordinate system showing  $\theta$  octant end faces which ABC would occupy after the indicated rotation directions for  $\theta_q, \theta_p$ .

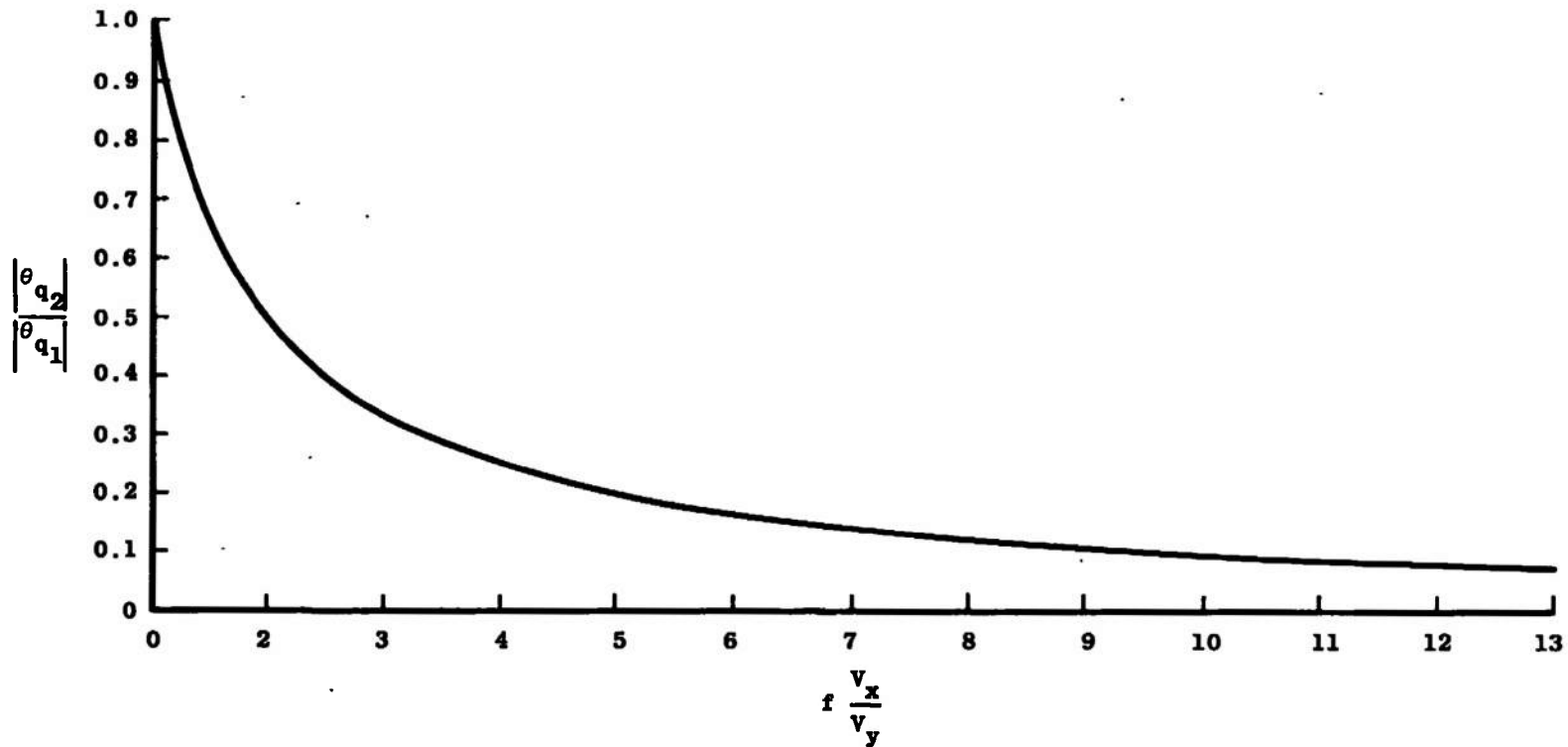


Figure A-5. Relaxation of angular separation requirement for case one rotations.

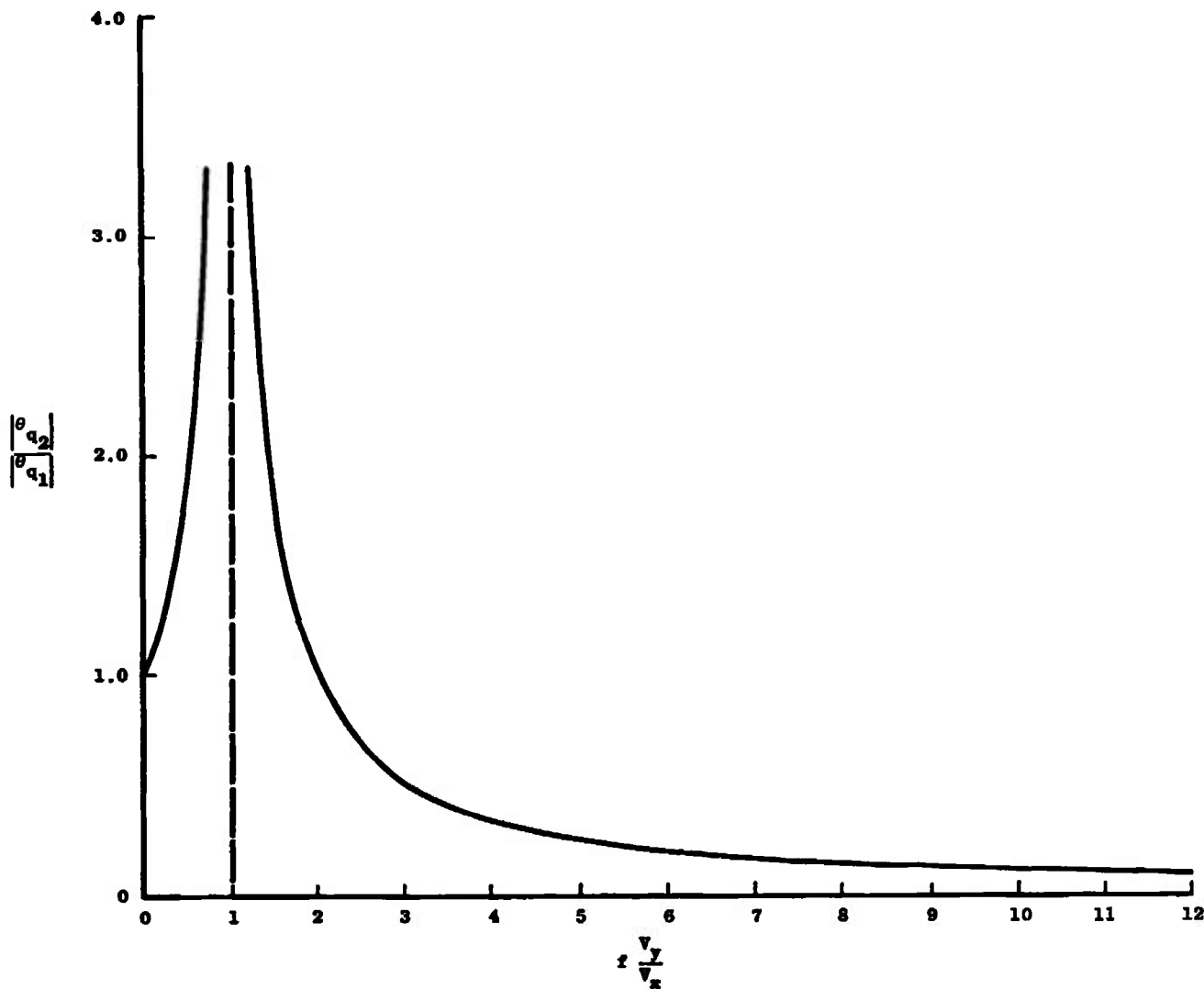


Figure A-6. Relaxation of angular separation requirement for case two rotations.

**APPENDIX B**  
**BRAGG DIFFRACTION OF LIGHT BY TWO ORTHOGONAL ULTRASONIC**  
**WAVES IN WATER**

W. P. Chu  
 Old Dominion University, Norfolk, Virginia 23500

L. E. Mauldin  
 NASA Langley Research Center  
 Hampton, Virginia 23365

It has been shown that an incident laser beam can be simultaneously diffracted into various side and cross orders by the two-dimensional Bragg cell (TDBC) (Refs. B-1 and B-2). In this Appendix the theory and performance of the TDBC will be presented.

The analysis and evaluation of the TDBC is based on the wave equation describing the electromagnetic field within an acoustically excited medium. The acousto-optical interaction geometry is illustrated in Fig. B-1. Two acoustic waves with angular frequencies  $\Omega_1$  and  $\Omega_2$ , and wave numbers  $K_1$  and  $K_2$  are traveling along the  $x$  and  $z$  axes, respectively. Both acoustic waves have a width  $L$  measured along the  $y$  axis. The incident optical wave is characterized by angular frequency  $\omega$ , wave number  $k = 2\pi/\lambda$  measured within the medium, and polarization approximately along the  $z$  axis. The directional cosines of the incident beam are  $\alpha$ ,  $\beta$ ,  $\gamma$ . Assuming the two acoustic waves propagate independently in the medium, the modulation of the dielectric constant can be written in the form

$$\epsilon = \epsilon_0 + \epsilon_1 \cos(K_1 x - \Omega_1 t) + \epsilon_2 \cos(K_2 z - \Omega_2 t) \quad (B-1)$$

where  $\epsilon_1$  and  $\epsilon_2$  are the amplitudes of the fluctuating dielectric constant associated with the two propagating acoustic waves. The magnitudes of  $\epsilon_1$  and  $\epsilon_2$  are directly proportional to the square root of the acoustic wave intensities  $I_1$  and  $I_2$ , respectively. Following the same procedure in deriving the Raman and Nath equation (Ref. B-3) the solution for the electric field amplitude  $E$  within the cell is sought in the form

$$E = \sum_{n,m} U_{n,m}(y) \exp[ik\beta y + i(n+m)\pi/2 + i(ka + nK_1)x + i(ky + mK_2)z - i(\omega + n\Omega_1 + m\Omega_2)t], \quad (B-2)$$

$$n, m = 0, \pm 1, \pm 2, \dots$$

Under the conditions that  $\Omega_1/\omega = \Omega_2/\omega \ll 1$ ,  $\epsilon_1 - \epsilon_2 \ll 1$  and  $\lambda/L \ll 1$  where  $\lambda = \frac{2\pi}{k}$ ,  $U_{n,m}(y)$  will satisfy the following recurrence equation:

$$\begin{aligned} \frac{d}{dx} U_{n,m}(x) + \frac{i\epsilon_0}{(\epsilon_1 + \epsilon_2)k^2} [nK_1(2ka + K_1n) + mK_2(2ky + K_2m)] U_{n,m}(x) \\ + \frac{\epsilon_1}{2(\epsilon_1 + \epsilon_2)} [U_{n+1,m}(x) - U_{n-1,m}(x)] + \frac{\epsilon_2}{2(\epsilon_1 + \epsilon_2)} [U_{n,m+1}(x) - U_{n,m-1}(x)] = 0, \end{aligned} \quad (B-3)$$

where  $x = k(\epsilon_1 + \epsilon_2) y/2\epsilon_0$ . From Eq. (B-2), each of the  $U_{n,m}$  can be considered to be the amplitude of the  $(n,m)$ -th diffracted order with a shift in angular frequency of  $n\Omega_1 + m\Omega_2$ , and a shift in wave vector of amount  $nK_1$  along the  $x$  axis and  $mK_2$  along the  $z$  axis.

A complete solution to Eq. (B-3) has not been achieved. However, a simplified solution can be obtained if one considers the diffraction process to satisfy the Bragg condition (Ref. B-4). Under the Bragg condition, only the zero and the first order predominate in the diffraction process. If it is assumed that the laser beam is incident at the Bragg angle, all other orders except those with  $n,m = 0$  or  $-1$  can be neglected. Thus Eq. (B-3) is reduced to the following four simultaneous first order differential equations

$$\begin{aligned} \frac{d}{dx} U_{0,0}(x) - \frac{\epsilon_1}{2(\epsilon_1 + \epsilon_2)} U_{-1,0}(x) - \frac{\epsilon_2}{2(\epsilon_1 + \epsilon_2)} U_{0,-1}(x) = 0, \\ \frac{d}{dx} U_{-1,0}(x) + \frac{\epsilon_1}{2(\epsilon_1 + \epsilon_2)} U_{0,0}(x) - \frac{\epsilon_2}{2(\epsilon_1 + \epsilon_2)} U_{-1,-1}(x) = 0, \\ \frac{d}{dx} U_{0,-1}(x) - \frac{\epsilon_1}{2(\epsilon_1 + \epsilon_2)} U_{-1,-1}(x) + \frac{\epsilon_2}{2(\epsilon_1 + \epsilon_2)} U_{0,0}(x) = 0, \\ \frac{d}{dx} U_{-1,-1}(x) - \frac{\epsilon_1}{2(\epsilon_1 + \epsilon_2)} U_{0,-1}(x) + \frac{\epsilon_2}{2(\epsilon_1 + \epsilon_2)} U_{-1,0}(x) = 0. \end{aligned} \quad (B-4)$$

Solving these equations with the boundary conditions  $U_{0,0}(0) = 1$ ,  $U_{-1,0}(0) = U_{0,-1}(0) = U_{-1,-1}(0) = 0$  yields

$$\begin{aligned}
 |U_{0,0}(L)|^2 &= \cos^2 \frac{\epsilon_1 \pi L}{2\beta \epsilon_0 \lambda} \cos^2 \frac{\epsilon_2 \pi L}{2\beta \epsilon_0 \lambda}, \\
 |U_{-1,0}(L)|^2 &= \sin^2 \frac{\epsilon_1 \pi L}{2\beta \epsilon_0 \lambda} \cos^2 \frac{\epsilon_2 \pi L}{2\beta \epsilon_0 \lambda}, \\
 |U_{0,-1}(L)|^2 &= \cos^2 \frac{\epsilon_1 \pi L}{2\beta \epsilon_0 \lambda} \sin^2 \frac{\epsilon_2 \pi L}{2\beta \epsilon_0 \lambda}, \\
 |U_{-1,-1}(L)|^2 &= \sin^2 \frac{\epsilon_1 \pi L}{2\beta \epsilon_0 \lambda} \sin^2 \frac{\epsilon_2 \pi L}{2\beta \epsilon_0 \lambda}.
 \end{aligned} \tag{B-5}$$

Under normal experimental conditions in which  $L$  and  $\lambda$  are held constant, Eq. (B-5) describes the variation of intensity for the respective order on parameters  $\epsilon_1$  and  $\epsilon_2$ . In terms of measurable parameters, the  $\epsilon$ 's will be proportional to the respective square root acoustic input powers. Note that when  $\epsilon_1 = \epsilon_2 = \epsilon_0 \beta \gamma / 2L$ , equal intensity in all four diffracted components is predicted.

The TDBC consists of two Bragg cells constructed in a common housing with center lines intersecting and orthogonal to each other. The transducers are made of x-cut quartz crystal with diameters of 2.92 cm. The two crystals are operated at their third-harmonic frequencies of 15 and 25 MHz with L-pad feedthrough to provide terminating impedances of  $50 \Omega$ . Two variable-output rf power supplies operating at 15 and 25 MHz are used to drive the TDBC. In-line wattmeters are used to measure the input power applied to the crystals. A He-Ne laser with an output wavelength of 6328 Å and a beam diameter of 1 mm is used in the experiment. The laser beam traverses the TDBC at the approximate intersection of acoustic center lines, about 1.46 cm from each crystal surface. Alignment for Bragg angle incidence of the laser beam is accomplished by individually monitoring the output of the two diffracted first orders (-1,0 and 0,-1). With only one crystal being driven, the TDBC is rotated about the appropriate axis to achieve maximum intensity in the first order. This procedure is repeated several times for each crystal until no rotation is required to achieve intensity maximum when switching from one crystal to the other. This assures simultaneous Bragg angle incidence of the laser beam to each acoustic wave and maximum efficiency of the laser power diffracted into the minus one orders (Ref. B-5). Figure B-2 shows theoretical curves and experimental data of power diffracted into the four orders versus the square root of input power applied to the 25-MHz crystal. In this case  $\Omega_1 = 15$  MHz and  $\Omega_2 = 25$  MHz. The input power applied to the 15-MHz

crystal fixed at 0.5 w, which corresponds to a fixed value of  $\epsilon_1$ . Good agreement between theory and experiment is obtained with  $\epsilon_1 = 10^{-5} P_{15}^{1/2}$  and  $\epsilon_2 = 8.7 \times 10^{-6} P_{25}^{1/2}$ , where  $P_{15}$  and  $P_{25}$  are the input power in watts applied to the 15- and 25-MHz crystals, respectively. Figure B-3 shows similar theoretical and experimental results when the input power applied to the 15-MHz crystal is held at 1.0 w. The incident laser beam energy is divided evenly among the four diffracted orders when approximately 1.5-w input power is applied to the 25-MHz crystal. According to Eq. (B-5), the modulation amplitudes of the dielectric constant at this point should be  $\epsilon_1 = \epsilon_2 = 10^{-5}$ . It is interesting to observe that the index modulation at 25 MHz is not as efficient as that at 15 MHz. This can be explained in terms of the attenuation coefficient of the acoustic wave in water which is dependent on the frequency squared.

Closer inspection of Figs. B-2 and B-3 shows that theoretical and experimental results start to depart as acoustic input power becomes large. This is caused by an increasing coupling of energy into higher-order components and has been verified by experimental observation. A more complete account of the diffraction process under large modulation would require inclusion of higher-order terms in Eq. (B-4).

## REFERENCES

1. Hornkohl, J. O. and Farmer, W. M. "Two-Component Self-Aligning Laser Vector Velocimeter." Applied Optics, Vol. 12, No. 11, November 1973.
2. Uchida, N. and Iwasaki, H. "Two-Dimensional Acoustooptical Deflector." Japanese Journal of Applied Physics, Vol. 8, No. 6, 1969, p. 811.
3. Born, M. and Wolf, E. "Principles of Optics." 2nd Edition, Pergamon Press, New York, 1964, p. 597.
4. Damon, R. W., Maloney, W. T., and McMahon, D. H. Physical Acoustics, Edited by W. P. Mason and R. N. Thurston, Academic Press, New York, 1970. Vol. 7, Chap. 5, p. 282.
5. Kleinhans, W. and Fired, D. L. "Efficient Diffraction of Light from Acoustic Waves in Water." Applied Physics Letters, Vol. 7, 1965, p. 19.

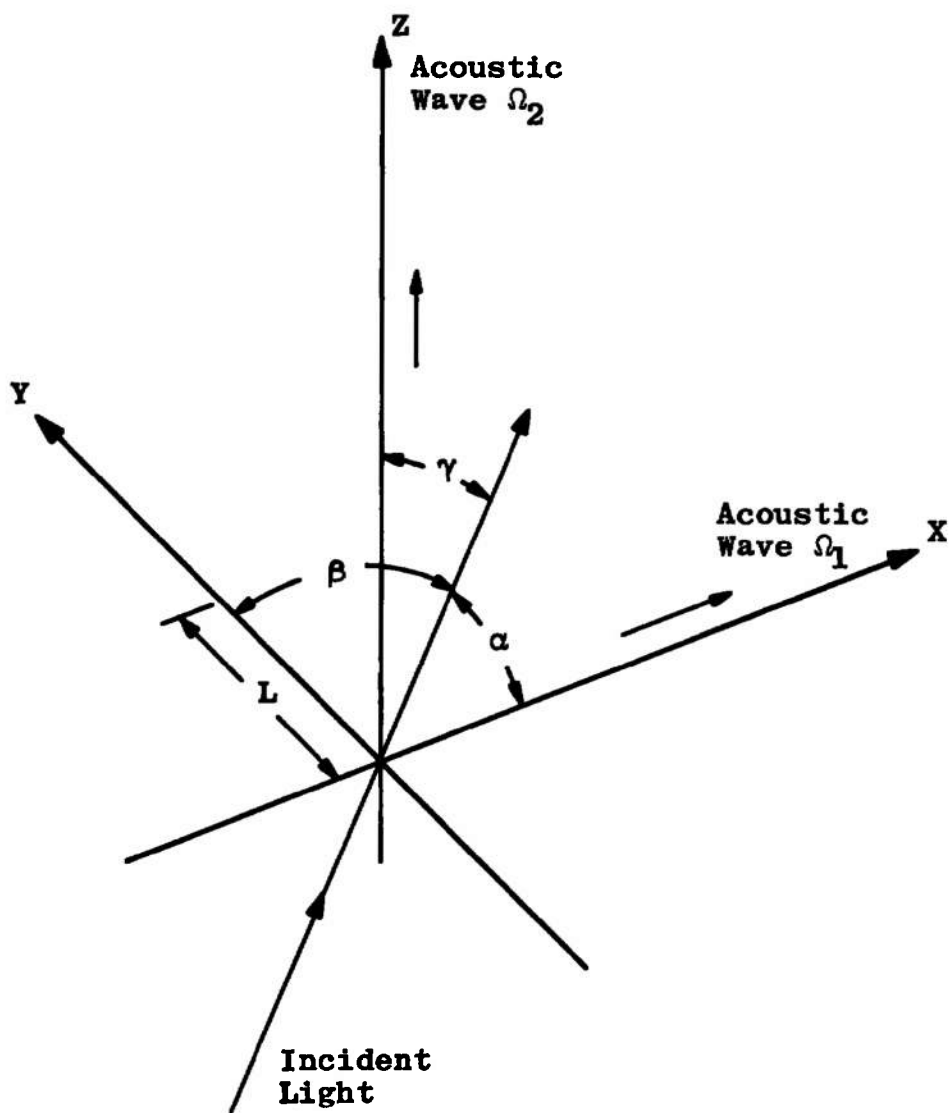
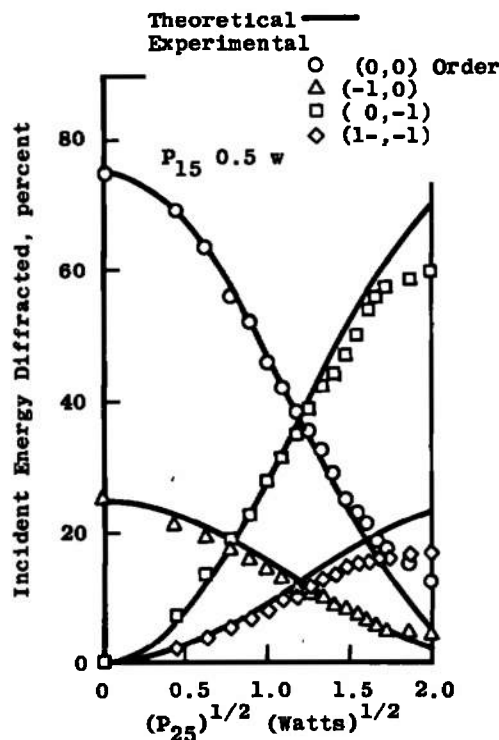
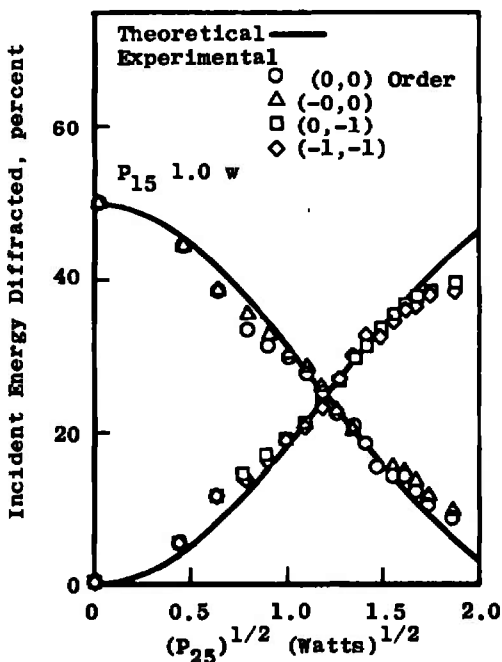


Figure B-1. Acousto-optics interaction geometry.

Figure B-2. Incident diffracted energy versus power<sup>1/2</sup>.Figure B-3. Incident diffracted energy versus power<sup>1/2</sup>.

**APPENDIX C**

**INVESTIGATION OF TRAILING VORTEX WAKE VELOCITIES AND DISSIPATION  
PROPERTIES USING THE LV**

Further study is recommended in both wind tunnels and hydrostatic channels due to the present lack of quantitative knowledge of wake turbulence phenomena. Little is known about the strength of the trailing vortex wake at large distances behind an aircraft. Effects of the viscous forces of the free atmosphere upon dissipation of such wakes have not been clearly defined. Conditions leading to the formation of the high-energy vortex cores, observed by some investigators, are not clearly understood and at present cannot be accurately predicted. The literature contains only limited airborne wake data due to the extreme difficulty of measurement. As long as this lack of information exists the formulation of high-confidence analytical techniques, required to predict the motion of trailing vortex wakes, will remain a difficult task. With the ever increasing number of larger aircraft such predictions are vital to air traffic controllers and pilots in the establishment of adequate traffic separation criteria.

The LV can be used to measure velocity distributions in the turbulent wake at various stations behind a wing. Quantitative wake dissipation information can be obtained by towing a model through a hydrostatic channel. Experiments can be performed to define the vortex formation mechanics and various unsteady phenomena. Tests can be conducted for simulated atmospheric turbulence conditions both in the presence of the ground and in the interference-free environment. Additional flow field information can be obtained through the use of various flow visualization devices.

An attempt can be made to correlate the results of these tests with existing full-scale empirical data to determine the effects of scale. In addition, comparisons can be made with values predicted by state-of-the-art analytical techniques.

**Hydrostatic Channel**

A hydrostatic channel such as shown in Fig. C-1 can be used for the test program. The facility at the AEDC consists of a water-filled tank 30 ft long, 24 in. wide, and 16 in. deep. A traverse cart is capable of propelling the test article along the tank length at precisely

controlled speeds from 0.06 ft/sec to 16.6 ft/sec. The unique cantilever channel support structure in conjunction with the transparent glass sides, bottom, and ends of the channel, permits optical equipment such as cameras or the LV to travel with the test article, viewing it from either side, above, or below the channel. The optical equipment can also be mounted on the tank support structure in situations where ground-fixed data are required.

The wing proposed for study has a cross section approximating a NASA 0012 Model with an aspect ratio of four. As shown in Fig. C-2, the maximum velocity induced normal to the channel walls, by an 8-in. span wing mounted horizontally at 6-deg angle of attack, is less than 0.5 percent of the free-stream velocity. The corresponding wall interference at the model location has been computed by the technique presented in Ref. C-2. The calculations yield an induced angle of attack of 0.053 deg and a downwash error of 0.09 percent of free-stream velocity.

Computations were made to determine the sink rate of the trailing vortex pair using the method described in Ref. C-1, neglecting vortex decay. For the previously mentioned wind, located one and one-half spans above the channel floor, the vortices reach the floor at approximately seventeen spans aft of the trailing edge. For a 6-in. span model mounted at two spans above the floor, the intersection occurs at twenty-nine spans downstream. Rotating the 6-in. span wing 90 deg and placing it three spans from the side wall permits observation of the undisturbed vortices for forty-three spans behind the trailing edge. Longer observation times may be accomplished by further reducing the model scale.

#### **Laser Doppler Velocimeter**

A laser system will be used which is capable of simultaneously providing three components of velocity in the flow field. A schematic of proposed setup is shown in Fig. C-3. The system will employ a three-component, self-aligning, Bragg cell optics system. Electronic readout of the velocity components will be provided to facilitate data acquisition.

Previous experience indicates that normal tap water contains sufficient contaminant particles to make this LV system very useful under the anticipated test conditions. Computations similar to those presented in Ref. C-3 and C-4 were made to determine the dynamics of particles in the flow field aft of the wing. Differences in particle

trajectories and fluid streamlines were found to be negligible under the most severe acceleration conditions expected.

### **Flow Visualization**

A hydrogen bubble generator, designed for use in the hydrostatic channel, is capable of producing streamlines and/or pulsed lateral lines in the fluid. The system can be mounted either on the traverse cart or on the tank depending upon the type data desired.

A collimated light source can be used to illuminate various parts of the flow field. This technique permits the investigation of flow patterns in selected cross sections by illuminating contamination particles in a thin sheet of fluid. The light sheet, in conjunction with dye or hydrogen bubbles emitted from the wing trailing edge, provides an excellent means of defining the shape and position of the wake at various distances behind the wing.

### **REFERENCES**

1. Jones, Lt. Col. Dale N. "Introduction to Jet- Engine Exhaust and Trailing Vortex Wakes." Technical Report 226, Air Weather Service (MAC), United States Air Force, April 1970.
2. Joppa, Robert G. "A Method of Calculating Wind Tunnel Interference Factors for Tunnels of Arbitrary Cross-Section." Report 67-1, University of Washington, February 1967.
3. Kliegel, J. R. "One Dimensional Flow of a Gas Particle System." TR-59-0000-00746 (AD607600), Space Technology Laboratories, Inc., Los Angeles, California, July 8, 1959.
4. Quan, Victor and Kliegel, James R. "Axisymmetric Two-Phase Reacting Gas Nonequilibrium Nozzle Flows Analysis." NASA CR 92058, August 1967.

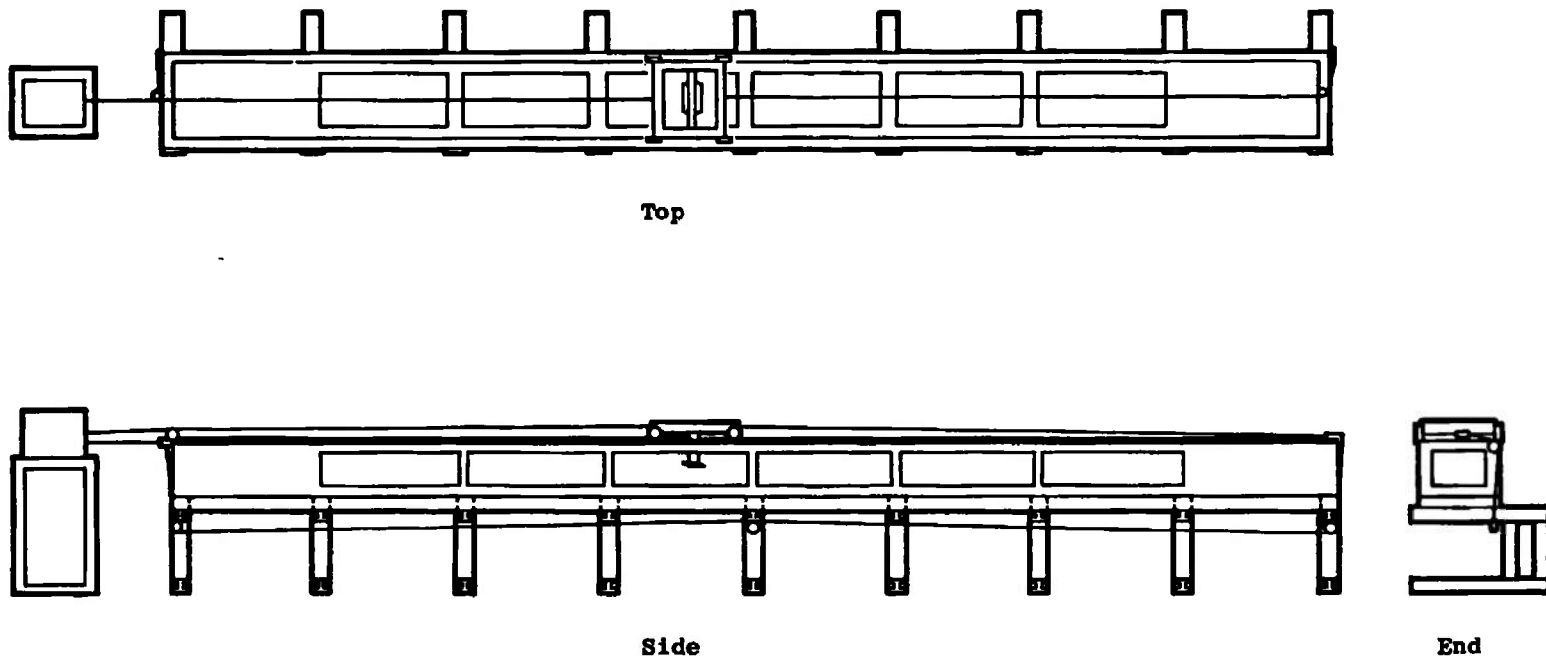
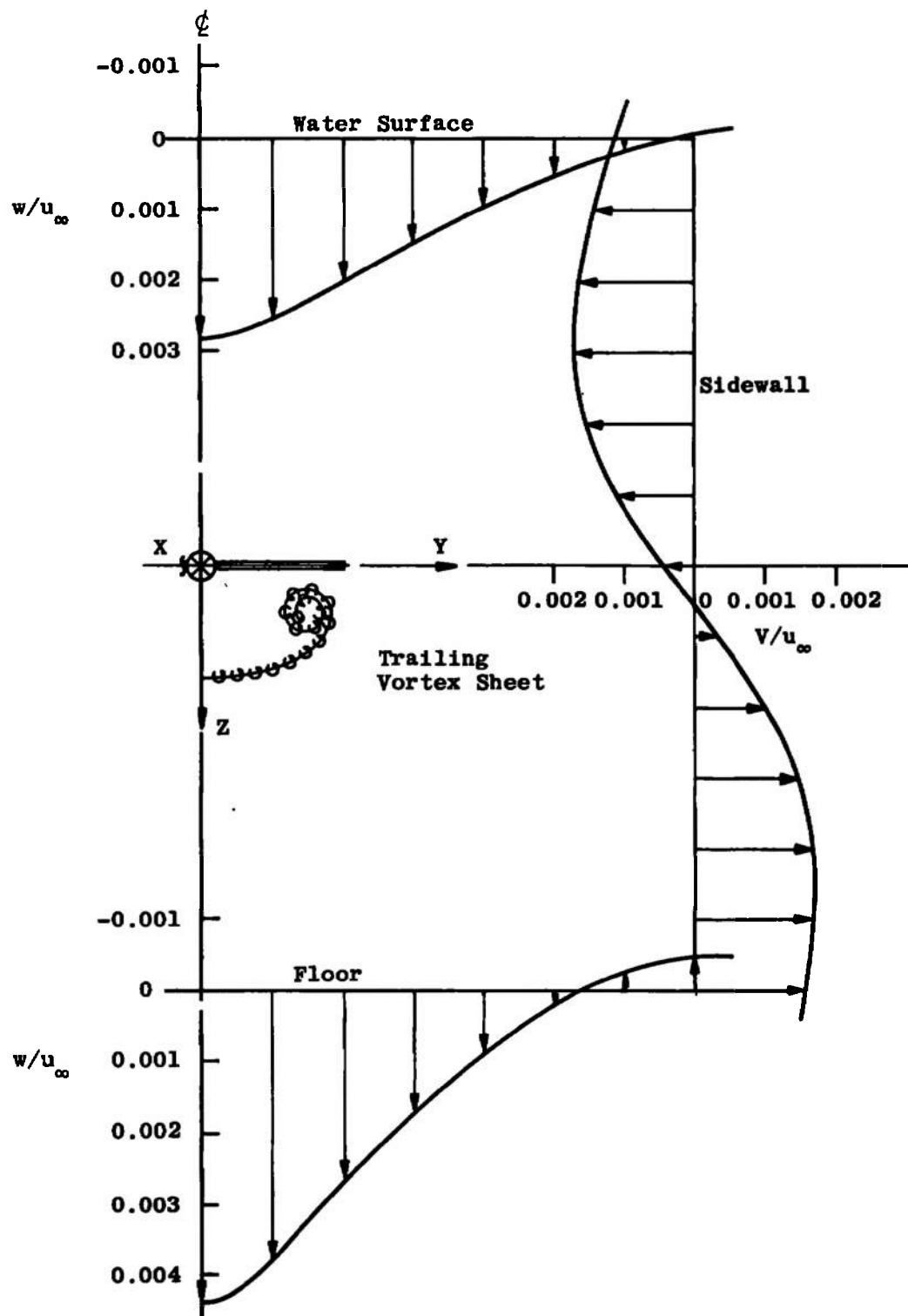
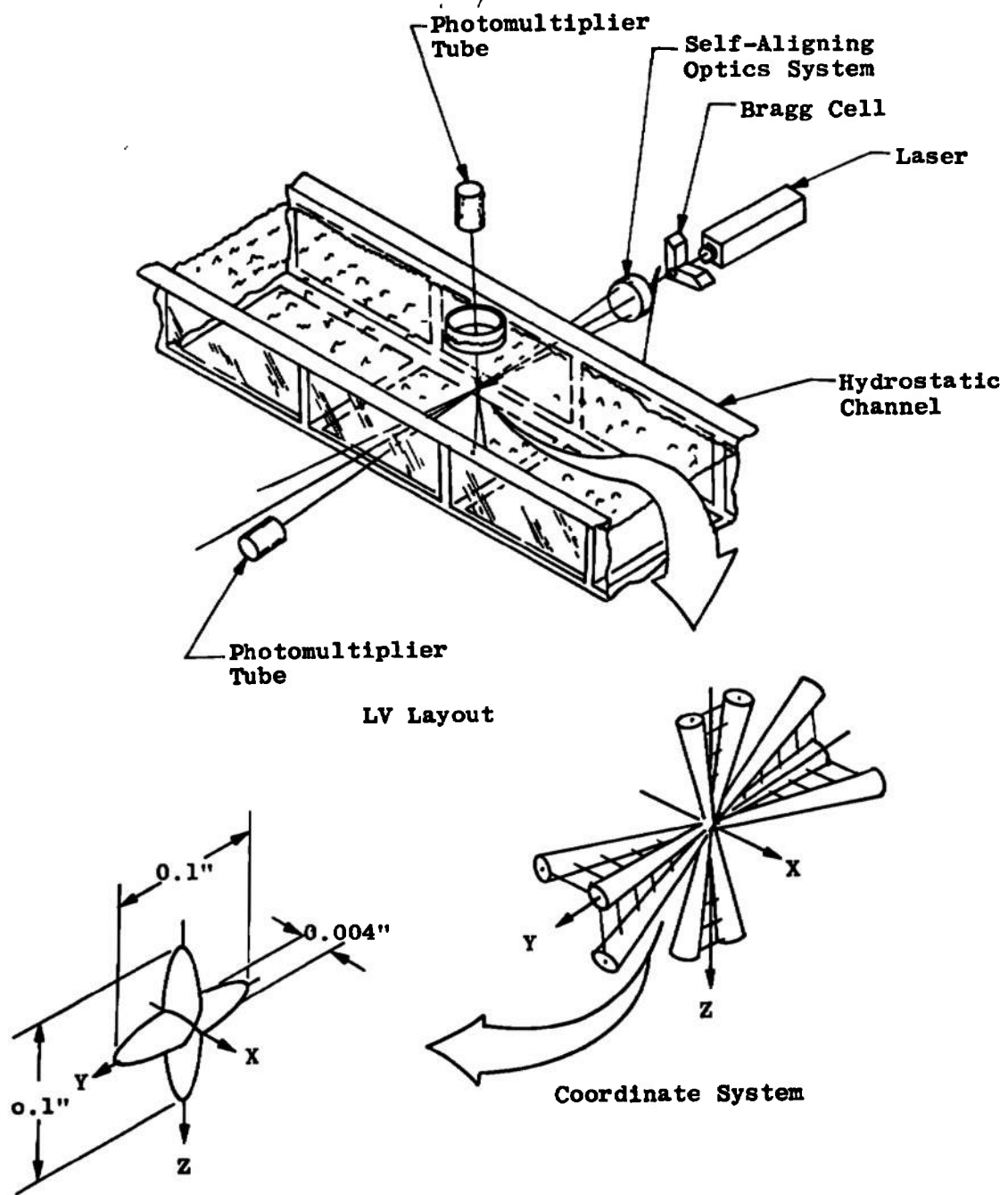


Figure C-1. Hydrostatic channel.



**Figure C-2. Maximum\* velocity induced at the hydrostatic channel wall by an 8-in. span wing at a 6-deg angle of attack.**

\*Computed at two spans aft of the trailing edge.



Focal Volume Dimensions

Figure C-3. Three-dimensional laser velocimeter system.